Beyond the Conventional Quark Model: Using QCD Sum Rules to Explore the Spectrum of Exotic Hadrons

A Thesis Submitted to the

College of Graduate Studies and Research

in Partial Fulfillment of the Requirements

for the degree of Doctor of Philosophy

in the Department of Physics & Engineering Physics

University of Saskatchewan

Saskatoon

By

Jason Ho

Permission to Use

In presenting this thesis in partial fulfilment of the requirements for a Postgraduate degree from the University of Saskatchewan, I agree that the Libraries of this University may make it freely available for inspection. I further agree that permission for copying of this thesis in any manner, in whole or in part, for scholarly purposes may be granted by the professor or professors who supervised my thesis work or, in their absence, by the Head of the Department or the Dean of the College in which my thesis work was done. It is understood that any copying or publication or use of this thesis or parts thereof for financial gain shall not be allowed without my written permission. It is also understood that due recognition shall be given to me and to the University of Saskatchewan in any scholarly use which may be made of any material in my thesis.

Requests for permission to copy or to make other use of material in this thesis in whole or part should be addressed to:

> Department of Physics & Engineering Physics
>
> University of Saskatchewan
>
> 116 Science Place, Rm 163
>
> Saskatoon, SK S7N 5E2
>
> Canada

and

> College of Graduate and Postdoctoral Studies
>
> University of Saskatchewan
>
> 116 Thorvaldson Building, 110 Science Place
>
> Saskatoon, Saskatchewan S7N 5C9
>
> Canada

ABSTRACT

Exotic hadrons are theoretical structures allowed by our current understanding of Quantum Chromodynamics (QCD), lying outside the traditional $q\bar{q}$, qqq, or $\bar{q}\bar{q}\bar{q}$ understanding of mesons and baryons. These exotic hadrons potentially give us a unique window into the properties of the gluon, the nature of color confinement, and the strong interaction. As we progress through the precision-era of particle physics and experiments such as BESIII, Belle, BaBar, LHCb, GlueX, and PANDA amass experimental data across the expected mass ranges of exotic hadrons (such as hybrid mesons with both $\bar{q}q$ quark content and a gluonic component), theoretical predictions of the individual mass states and the overall multiplet structure are crucial in identifying exotic states as well as departures from predicted behaviour. Using the methodology of QCD sum-rules (QCDSRs), we explore the properties of exotic hadrons, and discuss the QCDSR methodology and its extensions.

ACKNOWLEDGEMENTS

When I moved to Saskatoon seven years ago, I quickly learned that Tom, my supervisor, is a serious runner. I remember my first conference in Savannah when (eager to connect and impress my new supervisor) I naïvely agreed to accompany him on a run. A few kilometres later, as the connection between mind and body frayed, the only impression I was worried about was the one I was going to make in the pavement when I passed out. Tom pretended not to notice the strangled suction noises as I tried to avoid asphyxiation, for which I am grateful. Tom and I usually met a couple times a week to talk about research. Near the end of our meetings, Glenn Hussey typically pops his head into the office to confirm that Tom is still on for their afternoon run. Though I highly doubt that I'll ever be a runner, seven years of Tom's stories about his training, and Glenn's dedication to their daily ritual, have made one thing clear to me: running, though ultimately an individual feat, is fundamentally a better experience when done in community. Although I'll never voluntarily run a marathon, I think training for one would have a lot of similarities to graduate school. Some days you're cruising downhill with the wind at your back; some days it's an uphill battle with feral geese lurking around every corner. Yet, every day, it's your coaches and running mates that keep you moving and make it worthwhile.

There's a lot of people in my life that have coached me, cheered me on, kept me hydrated (mostly with beer, but all analogies break down somewhere), and even run alongside for a spell. I'm more than likely to forget someone, but here are just a few of the people who have formed my "running" community over the last seven years.

First, to my coaches: Tom Steele and Derek Harnett. If you would have told me in my first semester of undergrad that I would fall in love with Physics, I wouldn't have believed you (particularly after I failed Derek's first-year physics midterm). Without the coaching and mentorship of Tom and Derek, I would never have made it this far. Thank you both for always having an open door (or Skype window), a friendly ear, and for your care in developing not just physicists but also people.

To my fellow physicists that have ran and trained alongside me, encouraged me, experienced the dry-heaves with me...and still found time to dabble in non-physics shenanigans

To my parents, for their undying belief in me.

To Josha, for pulling me forward when I had nothing left.

To Sara, for her constant love, support, and endless faith
that one day, I *might* have a real job.

CONTENTS

LIST OF TABLES

LIST OF FIGURES

LIST OF ABBREVIATIONS

GSR(s)	Gaussian sum-rule(s)
LSR(s)	Laplace sum-rule(s)
LHS	Left-hand Side
LO	Leading Order
NLO	Next-to-leading Order
OPE	Operator Product Expansion
RHS	Right-hand Side
SSB	Spontaneous Symmetry Breaking
VEV	Vacuum Expectation Value
QCD	Quantum Chromodynamics
QCDSR(s)	QCD sum-rule(s)
LQCD	Lattice QCD
QFT	Quantum Field Theory
CLAS12	CEBAF Large Acceptance Spectrometer
JLAB	Jefferson Lab
PANDA	Anti-Proton Annihilations at Darmstadt
3D	Dimension three
4D	Dimension four
5D	Dimension five
6D	Dimension six

CHAPTER 1

INTRODUCTION

1.1 Motivation

We live in the age of Large Hadron Colliders, big data, and precision physics. The Standard Model of fundamental interactions has withstood every test against it to date, and is our best understanding of how fundamental particles interact with one another. And yet, we know this understanding is incomplete. For example, the Standard Model accounts for only visible matter, approximately 4% of what we observe to be a part of the universe; however this does not mean we understand this fraction completely. Basic questions about the nature of the fundamental degrees of freedom contained in the Standard Model go unanswered to this day. Why are there three generations of quarks? Why are only colourless states observed? How does the strong interaction generalize to bound-states of four or more quarks? Can we observe bound states of gluons? All of these questions and more still lie within the realm of the Standard Model and are fundamental to our understanding of visible matter that we interact with every day, literally the building blocks of our existence.

It wasn't long after the experimental establishment of quarks (following the seminal work of Gell-Mann and Zweig [10, 11]) that theorists began to play with the idea of multi-quark hadrons, or other bound states of quarks and gluons as described by the conventional quark model, a classification of hadronic states characterized by $q\bar{q}$ or $qqq/\bar{q}\bar{q}\bar{q}$ internal quark structure [12, 13]. These novel hadronic states are not precluded by our current understanding of quantum chromodynamics (QCD) and the observation of colour confinement; their existence and structural properties are, in many cases, still an open question. This possibility of novel structures outside of the conventional meson ($q\bar{q}$) or baryon/antibaryon ($qqq/\bar{q}\bar{q}\bar{q}$) paradigm can be seen throughout the history of particle physics as physicists have tried to explain

and categorize new experimental observations such as the scalar meson states [14], Roper resonance [15], or, in recent years, the XYZ resonances [16, 17, 18]. In each of these cases, bound states of quarks were discovered in excess of those predicted by the conventional quark model; these overpopulations of hadronic states is a signal of something different.

Recent experimental observations have elevated multi-quark bound states such as four-quark and five-quark structures out of the realm of theoretical possibility. For example, observation of the $Z_c(3900)$ by BESIII [19], and the later confirmation by Belle [20] experimentally established the existence of a bosonic non-$q\bar{q}$ state at a high degree of statistical certainty with many in the community pointing towards a four-quark interpretation [1]. The surprising observation of two five-quark states at the LHCb [21] and the most recent observation of a third state [22] has yet to be confirmed; however, the GlueX experiment underway at Jefferson Lab expects to provide insight on the lighter five-quark states reported by the LHCb [23, 24].

Perhaps the more peculiar exotic hadron structures beyond the conventional quark model are those that involve the gauge boson of QCD, the gluon. The non-perturbative nature of the strong interaction distinguishes itself from the well-understood theory of Quantum Electrodynamics (QED) through a self-interacting gauge boson; unlike the photon, the gluon carries colour charge, allowing it to self-interact and (theoretically) act as constituents of hadrons. Theoretical predictions of hybrid states (hybrid mesons containing a $q\bar{q}$ pair and a valence gluon or hybrid baryons/antibaryons containing $qqq/\bar{q}\bar{q}\bar{q}$ and a valence gluon) as well as bound states containing only gluons (glueballs) have all been commonly discussed throughout the literature with experimental candidates for both hybrid states and glueballs currently under investigation [1, 25]. While both hybrid mesons and hybrid baryons have been theorized, closed-flavour hybrid mesons tend to occupy the attention of the literature as they can carry quantum numbers that are indisputably outside the conventional quark model ("exotic" J^{PC}); we examine both non-exotic and exotic J^P and J^{PC} hybrid systems in Chapters 3 and 4 respectively. In contrast to the closed-flavour hybrid mesons, hybrid baryons carry J^P quantum numbers indistinguishable from their conventional counterparts. This, coupled with inconclusive understanding of the already crowded conventional spectrum of baryons, makes distinguishing hybrid baryon states an experimental and theoretical chal-

lenge. We review the status of the hybrid baryon literature from a QCDSR perspective in Chapter 6. To date, there are two promising experiments with a primary mandate of exploring hybrid meson states: GlueX, which is well underway at Jefferson Lab [24] and PANDA, currently under construction in Darmstadt, Germany [26]. Additionally, the CLAS12 experiment at JLAB [27] is conducting a search for hybrid baryons based on lattice QCD (LQCD) calculations performed in 2012 [28]. It is an exciting time for exotic hadron spectroscopy, and with precise experimental data being generated, a complementary demand for analysis and modeling by theorists is emerging.

However, the technical challenges corresponding to the non-perturbative nature of QCD often means applying a model-based approximation or calculating under a set of simplifying assumptions. Given this, it is necessary to consult a variety of computational methods in order to ensure an alignment in the theoretical predictions corresponding to a particular experimental prediction; common approaches in the literature include LQCD [28, 29, 30], Dyson-Schwinger Equations (DSE) [31], and chiral Lagrangian methods [14, 32, 33, 34] along with other effective theories [35]. Our approach focuses on a QCD sum rules (QCDSR) methodology which has a long history of successfully predicting properties of QCD bound states [36, 37] (see also Refs. [18, 38, 39, 40] for reviews). As with LQCD, QCDSR is rooted in calculating correlation functions of composite operators,

$$\Pi_\Gamma(q) = i \int \mathrm{d}^4x \, e^{iq\cdot x} \, \langle 0|Tj_\Gamma(x)j_\Gamma^\dagger(0)|0\rangle \,, \tag{1.1}$$

where the composite operators j_Γ are operators constructed from quantum fields describing the valence content and quantum numbers of a particular state Γ. This can be calculated within QCD by addressing non-perturbative effects using an operator product expansion (OPE). The correlation functions calculated in a QCD framework are then connected to low-energy hadronic physics through a dispersion relation such as

$$\Pi(Q^2) = \frac{1}{\pi} \int_{t_0}^\infty \frac{\mathrm{Im}\Pi(t)}{(t+Q^2)} \, \mathrm{d}t + \cdots \,, \quad Q^2 > 0. \tag{1.2}$$

where Q^2 is the euclideanized momentum scale, $\cdots$ represents subtraction constants that will need to be accounted for, and t_0 is an energy threshold for the state described by Π.

In the context of QCDSR, there are a variety of different spectral sum rules that can be used to extract information about this connection between QCD (a natural description of the high-energy physics) and hadronic physics (naturally describing the low-energy regime), but all are derived beginning with a dispersion relation such as this which connects high- and low-energy behaviour. We explore Laplace and Gaussian QCDSRs extensively in our work (see Chapters 3 and 4). This dispersion relation represents one of the challenges inherent in QCD and hadronic physics: because of the phenomenon of confinement, the quark and gluon constituents of hadronic matter are the most fundamental descriptions of hadronic bound states, yet we only directly observe the bound state hadrons. This quark-hadron duality was one of the motivations for our work connecting two theoretical frameworks for the first time, chiral Lagrangians and QCDSR (Chapter 5), in order to better understand the connection between a hadronic framework and a QCD framework.

What follows is my contribution to our understanding of exotic hadrons, a piece of the puzzle in the larger question of how to understand the strong interaction. I begin with a brief overview of the formalism relevant to my research (Chapter 2), and proceed through an analysis of different exotic hadronic systems covering four peer-reviewed publications. In Chapter 3, I discuss open-flavour heavy-light hybrid mesons. My contributions to this work begin with the calculation of the multichannel correlation functions, forming the LSRs for each of the sixteen $J^{P(C)}$ (charm and bottom) channels, analysis of LSRs to extract mass predictions from each of the stable channels, performing the error analyses, and interpreting the overall results. In addition, I performed all of the mixing analysis, designed the figures, and I led in the writing and editing of the final manuscript. In Chapter 4, I move onto closed-flavour light hybrid mesons, Here, my contributions to these works include the analysis of correlator and extraction of sum rule predictions, application of different models within GSR analysis and determination of best fits, the Hölder inequality derivation within GSRs, performing the error analyses, designing the figures, and writing & editing of both manuscripts. Shifting away from hybrid mesons, in Chapter 5 I discuss the light scalar mesons. My contributions to both of these works pertain to the QCDSR analysis. In the case of the isotriplet analysis, I rederived and made corrections to expressions used in the previous work, improved the optimization procedure, explored the inclusion of updated sum rule parameter values within

the analysis, designed Figure 5.4, and edited the manuscript. In the case of the isodoublet analysis, I performed a full analysis and determination of scale factors from GSRs applying the optimization procedure I developed in the isotriplet case, designed the figures, and led in the writing and editing of the manuscript. In Chapter 6, I end with my preliminary work on hybrid baryon systems, and finally, in Chapter 7, I highlight the contributions of this work, and look forward towards the future of exotic hadrons both experimentally and within QCDSRs.

CHAPTER 2

METHODOLOGY

2.1 Quantum Chromodynamics

Quantum Chromodynamics (QCD) in its modern form is described by the classical Lagrangian satisfying an $SU(3)_{\text{colour}}$ local gauge symmetry

$$\mathcal{L}_{\text{QCD}}(x) = \bar{q}(x)(i\slashed{D} - m)q(x) - \frac{1}{4}\left(G^a_{\mu\nu}(x)\right)^2, \qquad (2.1)$$

which, when expanded in terms of the quark fields $q(x)$ and gluon fields $B^a_\mu(x)$, and including the Fadeev-Popov ghosts $\phi^a(x)$ [41] and covariant gauge fixing terms becomes (see e.g., Ref. [42]),

$$\begin{aligned}
\mathcal{L}_{\text{QCD}}(x) = & -\frac{1}{2}\left[\partial_\mu B^a_\nu(x)\right]\left[\partial^\mu B^\nu_a(x) - \partial^\nu B^\mu_a(x)\right] - \frac{1}{2a}\left[\partial_\mu B^\mu_a(x)\right]\left[\partial_\nu B^\nu_a(x)\right] \\
& + \frac{i}{2}\left(\bar{q}_\alpha(x)\slashed{\partial}q_\alpha(x)\right) - \frac{i}{2}\left[\partial_\mu\bar{q}_\alpha(x)\right]\gamma^\mu q_\alpha(x) - m_q\bar{q}_\alpha(x)q_\alpha(x) \\
& + \frac{1}{2}g_s\bar{q}_\alpha(x)\lambda^a_{\alpha\beta}\gamma^\mu q_\beta(x)B^a_\mu(x) - \frac{1}{2}g_s f_{abc}\left[\partial_\mu B^a_\nu(x) - \partial_\nu B^a_\mu(x)\right]B^\mu_b(x)B^\nu_c(x) \quad (2.2) \\
& - \frac{1}{4}g_s^2 f_{abc}f_{ade}B^b_\mu(x)B^c_\nu(x)B^\mu_d(x)B^\nu_e(x) \\
& - \left[\partial_\mu\overline{\phi_a}(x)\right]\partial^\mu\phi_a(x) + g_s f_{abc}\left[\partial_\mu\overline{\phi_a}(x)\right]\phi_b(x)B^\mu_c(x),
\end{aligned}$$

where a sum over quark flavours is implied, and a is a gauge-fixing parameter. The following conventions are used in equations (2.1) and (2.2), and throughout this work unless otherwise

noted:

$$t^a_{\alpha\beta} = \frac{1}{2}\lambda^a_{\alpha\beta} \tag{2.3}$$

$$G_{\mu\nu}(x) = t^a\left(G^a_{\mu\nu}(x)\right) = t^a\left(\partial_\mu B^a_\nu(x) - \partial_\nu B^a_\mu(x) + g_s f^{abc} B_{b\mu}(x) B_{c\nu}(x)\right) \tag{2.4}$$

$$D_\mu(x) = \partial_\mu - ig_s t^a B^a_\mu(x) \tag{2.5}$$

$$\alpha_s = \frac{g_s^2}{4\pi}, \tag{2.6}$$

where g_s is the strong coupling, λ are the Gell-Mann matrices, f^{abc} are the structure constants, and m_q are quark masses. Unless otherwise stated, the metric convention used throughout this work is

$$g_{\mu\nu} = \text{diag}(1, -1, -1, -1), \tag{2.7}$$

and the typical "slash" notation has been implemented, i.e.,

$$\slashed{D} = D_\mu \gamma^\mu \tag{2.8}$$

$$\slashed{p} = p_\mu \gamma^\mu. \tag{2.9}$$

The γ_5 matrix is defined in four spacetime dimensions as

$$\gamma_5 = i\gamma_0\gamma_1\gamma_2\gamma_3, \tag{2.10}$$

and satisfies

$$\{\gamma_5, \gamma^\mu\} = 0 \tag{2.11}$$

$$(\gamma_5)^2 = 1. \tag{2.12}$$

In d-dimensional calculations, we use a γ_5 convention in which (2.11)–(2.12) hold [43].

The QCD Lagrangian in (2.2) is the theoretical foundation for our understanding of the strong interaction today. It is built upon decades of experimental observation and testing (including asymptotic freedom, confinement, and spontaneous symmetry breaking), and encodes a depth of theoretical knowledge within its structure and symmetry. The following

sections very briefly explore some of the experimental motivation behind our understanding of the strong interaction, and the development of the theoretical framework encapsulated in (2.2).

2.1.1 Particles and Interactions

In our current understanding of the Standard Model of particle physics (see Figure 2.1), the strong interaction involves three generations of quark pairs interacting through eight vector gauge bosons, the gluon.
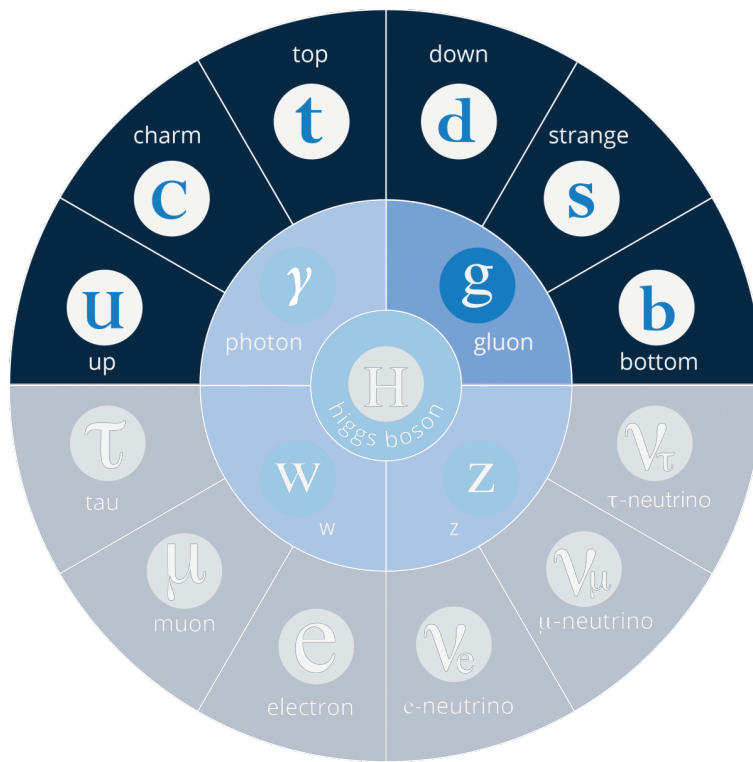
Figure 2.1: The Standard Model of particle physics. Particles considered within QCD are highlighted. Figure modified from [5].

Some consequences of constituent quarks were first observed in Gell-Mann and Ne'eman's individual classification of the known mesons and baryons of the time [12, 13]. The organization of states by electric charge and "strangeness" (a quantity that would later be associated with the constituent strange quark content) formed geometric structures in the space of quantum numbers, such as the hexagonal structure seen in the pseudoscalar nonet of figure 2.2.
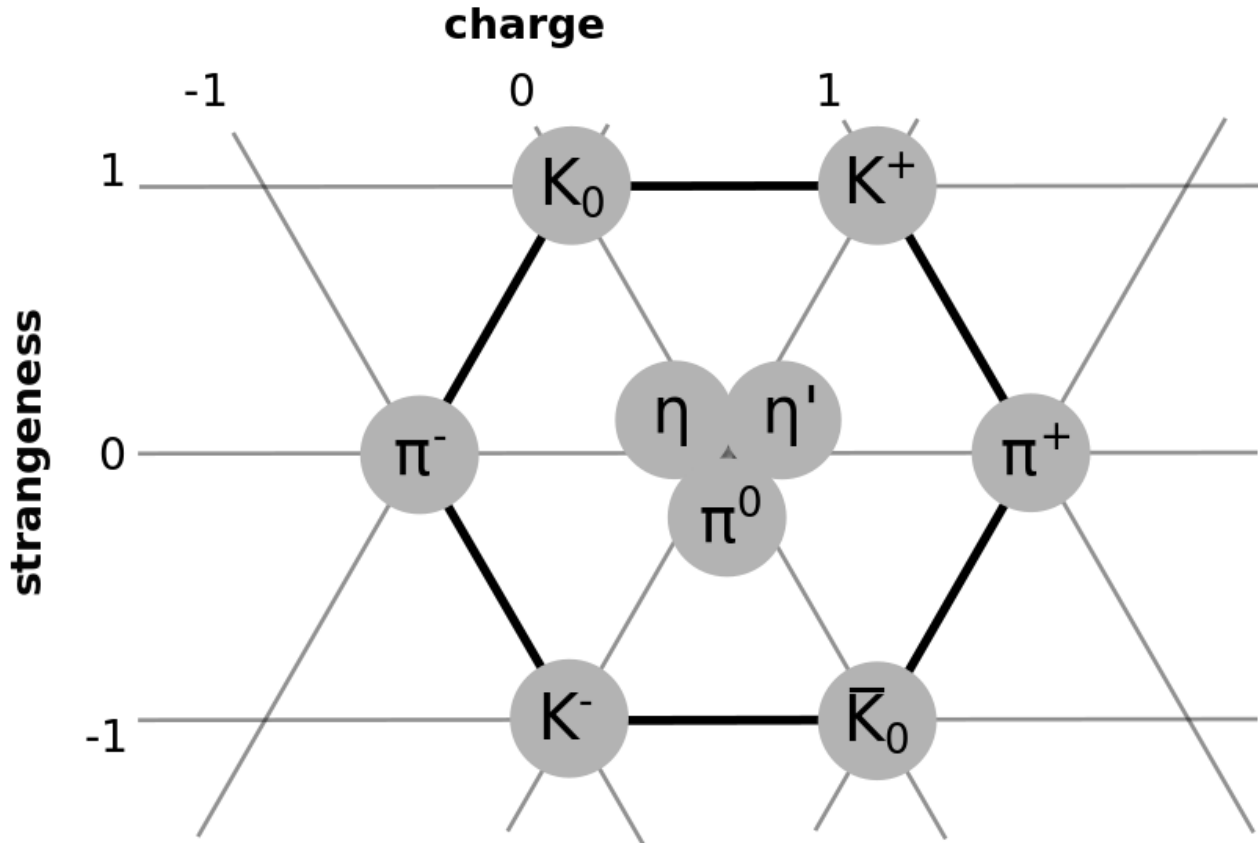
Figure 2.2: Pseudoscalar nonet with electric charge presented in units of e.

This pursuit of an analogue to the periodic table of elements for subatomic particles revealed a pattern that Gell-Mann and Zweig (again, independently) later ascribed to an underlying structure of constituent spin-1/2 particles [10, 11]. However, this model of hadronic structure carried predictions that raised important concerns at the time: these constituents were proposed to carry fractional electric charge, had no experimental evidence of existing outside of hadronic bound states, and in some cases appeared to violate the Pauli exclusion principle. It would take some years until this model would be widely-accepted, with important discoveries in those intervening years that would shed light on these concerns.

2.1.2 Asymptotic Freedom and Confinement

The strength of the strong interaction at the one loop level is characterized by the scale-dependent QCD strong coupling for n_f flavours anchored at a reference energy corresponding

to M,

$$\alpha_s(Q) = \frac{\alpha_s(M)}{1 + \frac{\alpha_s(M)}{2\pi}\left(11 - \frac{2}{3}n_f\right)\log\left(\frac{Q}{M}\right)}. \tag{2.13}$$

Characteristic to QCD is the phenomenon of asymptotic freedom [44, 45]; at high energy scales ($\gtrsim 1\,\mathrm{GeV}$), the strong interaction between quarks and gluons becomes weak, and as the energy scale decreases the coupling between constituents becomes stronger. At low energies ($\lesssim 1\,\mathrm{GeV}$), the phenomenon of colour confinement is observed: experimentally, free quarks or any other coloured states are not observed. Instead of breaking apart into constituent pieces, hadrons involved in collisions of sufficient energy will produce hadronic jets formed through $q\bar{q}$ pair production, discussed in more detail in Section 2.1.3.2. At high energies, perturbation theory is sufficient to describe strong dynamics. It is at these energies where particle colliders have performed important precision tests on the theory of QCD [1]. At lower energies, untangling QCD becomes more complicated. Non-perturbative effects contribute significantly, and as the strength of the coupling at these energies is large, a perturbative expansion is no longer a viable tool. Over time, there have been different approaches to overcoming this challenge in order to gain understanding of the strong interaction; some model the interactions between quarks and gluons using a model potential [46] while other methods exchange the fundamental degrees of freedom of quarks and gluons in favour of effective degrees of freedom, i.e., the bound state hadrons [14, 33, 34]. Methods like QCD sum rules (QCDSR) [36, 37, 47, 48, 49, 50, 51, 52] and lattice QCD (LQCD) [28, 29, 30] attempt to characterize the non-perturbative behaviour directly by using properties of the QCD vacuum or by numerically evaluating the path integral.

2.1.3 Symmetries

At the heart of modern particle physics is the idea of symmetry. Symmetries inform us about conserved physical quantities through Noether's theorem, while deviations from symmetries can signal particle properties (e.g., Nambu-Goldstone bosons). The QCD Lagrangian (2.1) exhibits several important symmetries that inform the properties of the strong interaction.

2.1.3.1 $SU(N_f)_R \times SU(N_f)_L$ **Chiral Symmetry**

The foundation of Gell-Mann and Ne'eman's geometric nonets of the conventional quark model [12, 13] found in Figure 2.2 is the $SU(3)_F$ flavour symmetry of the underlying quark structure of the hadrons, manifesting as patterns in their observable properties. This flavour symmetry is only approximate however, as the light quark flavours that make up the hadronic nonets (up, down, and strange quarks) all carry different masses (Table 2.1).

flavour	mass (GeV)
up	0.00216
down	0.00467
strange	0.093
charm	1.27
bottom	4.18
top	172.9

Table 2.1: Summary of quark masses [1]. Light quark masses (up, down, strange) are referenced to renormalization scale of $2\,\mathrm{GeV}$, while charm and bottom quarks are referenced to a renormalization scale corresponding to the $\overline{\mathrm{MS}}$ masses in question ($\overline{m_c}$ and $\overline{m_b}$ respectively), and the top quark mass is a direct measurement from $t\bar{t}$ event kinematics [1].

However, the three lightest quarks are *much* lighter than the characteristic scale of QCD ($\simeq 1\,\mathrm{GeV}$). These comparably small quark masses point towards an important foundational piece of QCD and hadronic physics. Consider the following parameterization of the quark fields in the QCD Lagrangian (2.1):

$$q_L(x) = \Gamma_L q(x) \tag{2.14}$$

$$q_R(x) = \Gamma_R q(x) \tag{2.15}$$

$$q(x) = q_L(x) + q_R(x) \tag{2.16}$$

where R and L indicate the right- and left-handed chiral representations, and we have defined

11

chiral projection operators $\Gamma_{L,R}$ as

$$\Gamma_L = \frac{1}{2}(1 + \gamma_5) \tag{2.17}$$

$$\Gamma_R = \frac{1}{2}(1 - \gamma_5). \tag{2.18}$$

We note that our chiral operators (2.17) have the properties

$$\Gamma_L + \Gamma_R = 1 \tag{2.19}$$

$$\Gamma_{L,R}\Gamma_{L,R} = \Gamma_{L,R} \tag{2.20}$$

$$\Gamma_L\Gamma_R = \Gamma_R\Gamma_L = 0. \tag{2.21}$$

Under this parameterization, our QCD Lagrangian (2.1) becomes

$$\mathcal{L}(x) = \bar{q}(x)(i\slashed{D} - m)q(x) = \bar{q}_L i\slashed{D} q_L + \bar{q}_R i\slashed{D} q_R - (\bar{q}_L m_q q_R + \bar{q}_R m_q q_L) - \frac{1}{4}\left(G_{\mu\nu}^a\right)^2. \tag{2.22}$$

By considering the chiral limit ($m_q \to 0$), our QCD Lagrangian (2.1) can be parameterized into two unmixed left- and right-handed pieces, eliminating the cross-terms spoiling the chiral symmetry in (2.22)

$$\mathcal{L}(x) = \bar{q}_L i\slashed{D} q_L + \bar{q}_R i\slashed{D} q_R - \frac{1}{4}\left(G_{\mu\nu}^a\right)^2. \tag{2.23}$$

The limit of $m_q \to 0$ reveals the underlying $SU(N_f)_R \times SU(N_f)_L$ chiral symmetry present in (massless) QCD. This chiral symmetry is explicitly broken by the quark masses. We can also see this explicit symmetry breaking in terms of the vector and axial vector currents, which are related to the $SU(N_f)_R \times SU(N_f)_L$ chiral symmetry. If we return to the case where $m_q \neq 0$, we can form the chiral currents,

$$j_L^\mu = \bar{\psi}_L \gamma^\mu \psi_L \tag{2.24}$$

$$j_R^\mu = \bar{\psi}_R \gamma^\mu \psi_R, \tag{2.25}$$

which combine to form the vector (V^μ) and axial vector (A^μ) Noether currents

$$V^\mu = j_L^\mu + j_R^\mu = \bar{\psi}\gamma^\mu\psi \tag{2.26}$$

$$A^\mu = j_L^\mu - j_R^\mu = \bar{\psi}\gamma_5\gamma^\mu\psi. \tag{2.27}$$

We see that while the vector current is conserved, the axial current (2.27) is not, thanks to the anticommutation relation $\{\gamma_\mu, \gamma_5\} = 0$; taking four-divergences, our currents in (2.26) and (2.27) become

$$\partial_\mu V^\mu = 0 \tag{2.28}$$

$$\partial_\mu A^\mu = 2im_q\bar{\psi}\gamma_5\psi. \tag{2.29}$$

Here, we see explicitly that while the vector current V^μ is conserved, the axial current A^μ component of the chiral symmetry is not, and is explicitly broken due to the massive quarks. It is worth mentioning that even in the chiral limit $m_q \to 0$, the axial current is still not conserved; anomalous symmetry breaking occurs due to instanton effects, leading to the $U(1)$ axial anomaly [53].

In addition to the explicit breaking of chiral symmetry, there is also strong evidence for the spontaneous breaking of chiral symmetry in QCD. Examining a few well-defined hadronic states reveals an interesting pattern. Comparing across Tables 2.2 and 2.3, we see that a significant difference in masses exists for states carrying the same quark content. For example, there exists a $\approx 600\,\text{MeV}$ difference between the π^0 and ρ^0 mesons. This mass difference is unusual, and unique to these light quark meson states; a comparison of the pseudoscalar and vector masses of the J/ψ charmonium states show that the masses are nearly degenerate at $2.98\,\text{GeV}$ and $3.10\,\text{GeV}$ for the pseudoscalar and vector states respectively [1].

This large difference in masses in the pseudoscalar nonet signals there is something unique about the light pseudoscalars. Using Nambu-Goldstone's theorem [54, 55], and considering QCD in the chiral limit, the pseudoscalars can be interpreted as Nambu-Goldstone bosons reflecting a spontaneously broken chiral symmetry associated with the axial current [56], i.e., $SU(N_f)_R \times SU(N_f)_L \to SU(N_f)_V$. However, the explicit symmetry breaking resulting

Meson	Quark Content	Isospin, I	Charge	$J^{P(C)}$	Mass (MeV)
π^0	$\frac{1}{\sqrt{2}}\left(u\bar{u} - d\bar{d}\right)$	1	0	0^{-+}	134.9770 ± 0.0005
π^+	$u\bar{d}$	1	+1	0^-	139.57061 ± 0.00024
π^-	$d\bar{u}$	1	-1	0^-	139.57061 ± 0.00024
K_0	$d\bar{s}$	$\frac{1}{2}$	0	0^-	497.611 ± 0.013
$\bar{K}_0$	$s\bar{d}$	$\frac{1}{2}$	0	0^-	497.611 ± 0.013
K^+	$u\bar{s}$	$\frac{1}{2}$	+1	0^-	493.677 ± 0.016
K^-	$s\bar{u}$	$\frac{1}{2}$	-1	0^-	493.677 ± 0.016
η	$\frac{1}{\sqrt{3}}(u\bar{u} + d\bar{d} - 2s\bar{s})$	0	0	0^{-+}	547.862 ± 0.017
η'	$\frac{1}{\sqrt{6}}(u\bar{u} + d\bar{d} + s\bar{s})$	0	0	0^{-+}	957.78 ± 0.06

Table 2.2: Properties of the pseudoscalar nonet depicted in Figure 2.2 [1]. The $J^{P(C)}$ column indicates the total angular momentum J, parity P, and (depending on whether the state carries the symmetry) charge conjugation C. These discrete symmetries are discussed in further detail later on in this chapter.

from the small but nonzero light quark masses means that the spontaneous chiral symmetry breaking is only approximate, generating *pseudo*-Nambu-Goldstone bosons with small masses. The consideration of pseudoscalars as pseudo-Nambu-Goldstone bosons is supported strongly by experimental evidence and multiple theoretical approaches, including the existence of a nonzero vacuum expectation value (VEV) associated with the spontaneously broken chiral symmetry

$$\langle 0| \bar{q}_L q_R + \bar{q}_R q_L |0\rangle = \langle 0| \bar{q}q |0\rangle \neq 0, \tag{2.30}$$

which was predicted before the formulation of QCD, known as the Gell-Mann-Oakes-Renner (GMOR) relation [57],

$$-\frac{1}{2}m_q\langle\bar{q}q\rangle = m_\pi^2 f_\pi^2, \tag{2.31}$$

relating the chiral condensate to the mass of the pion and the pion coupling constant.

Because the u and d masses are much smaller than the s mass, $SU(N_f)_R \times SU(N_f)_L$ chiral symmetry is best realized for the two lightest quark flavours ($N_f = 2$) as evidenced by the relatively smaller pion masses; however, it is generally a good approximation for all three of the light quarks ($N_f = 3$) relative to the characteristic energy scale of QCD ($\approx 1\,\text{GeV}$).

Meson	Quark Content	Isospin, I	Charge	$J^{P(C)}$	Mass (MeV)
$\rho^0(770)$	$\frac{1}{\sqrt{2}}\left(u\bar{u}-d\bar{d}\right)$	1	0	1^{--}	775.26 ± 0.25
$\rho^+(770)$	$u\bar{d}$	1	+1	1^-	775.11 ± 0.34
$\rho^-(770)$	$d\bar{u}$	1	-1	1^-	775.11 ± 0.34
$K_0^*(892)$	$d\bar{s}$	$\frac{1}{2}$	0	1^-	895.55 ± 0.20
$\bar{K}_0^*(892)$	$s\bar{d}$	$\frac{1}{2}$	0	1^-	895.55 ± 0.20
$K^{*+}(892)$	$u\bar{s}$	$\frac{1}{2}$	+1	1^-	891.76 ± 0.25
$K^{*-}(892)$	$s\bar{u}$	$\frac{1}{2}$	-1	1^-	891.76 ± 0.25
$\omega(782)$	$\frac{1}{\sqrt{2}}(u\bar{u}+d\bar{d})$	0	0	1^{--}	782.65 ± 0.12
$\phi(1020)$	$s\bar{s}$	0	0	1^{--}	1019.461 ± 0.019

Table 2.3: Properties of the vector nonet [1]. The $J^{P(C)}$ column indicates the total angular momentum J, parity P, and (depending on whether the state carries the symmetry) charge conjugation C. These discrete symmetries are discussed in further detail later on in this chapter.

2.1.3.2 $SU(3)$ Colour Charge

Gell-Mann and Zweig's conceptualization of quarks [10, 11] required the addition of a quantum number exclusive to the strong interaction, due to the apparent contradiction of the Pauli exclusion principle in experimentally observed flavour-homogenous baryon states such as the Δ^{++} and the Ω^-. This led to the introduction of a "colour charge" by O.W. Greenberg [58], in analogy to additive colour mixing. Experimental evidence since then has supported the consistency of three colour charges within QCD [1]. In the modern context of QCD, the Lagrangian (2.1) is invariant under local $SU(3)$ colour transformations; colour charge manifests as the charge associated with the $SU(3)$ local gauge transformation. Examining just the quark portion of (2.1),

$$\mathcal{L}_{\text{quark}}(x) = \bar{q}_i(x)\left(i\gamma^\mu\left(\partial_\mu - ig_s t_{ij}^a B_\mu^a(x)\right) - m_q\right)q_j(x), \tag{2.32}$$

where the indices on the quark fields indicate colour, i.e.,

$$q(x) = \begin{bmatrix} q_r(x) \\ q_b(x) \\ q_g(x) \end{bmatrix} \tag{2.33}$$

with $\{r, b, g\}$ indicating the different colors of quarks, and where t_{ij}^a are the 3×3 Gell-Mann matrices and the group generators of $SU(3)$. These generators are defined by infinitesimal rotations in quark colour space, and representations of these generators satisfy the same commutation relations as the generators. QCD is built from the fundamental representation, the conjugate of the fundamental representation, and the adjoint representation, which turn out to describe colour dynamics for the quarks, anti-quarks, and gluons respectively. The fundamental representation satisfies the commutator

$$\left[t^a, t^b\right] = i f^{abc} t^c \tag{2.34}$$

where f^{abc} are structure constants, and the 8×8 adjoint representation is defined through the structure constants

$$(t_a)_{bc} = -i f_{abc}. \tag{2.35}$$

Central to this conceptualization of colour charge and the $SU(3)_C$ gauge symmetry is the experimental observation that quarks are not observed outside of a bound state; hadrons must exist in some colour singlet state. This axiom of QCD is called colour confinement, which is an experimentally-driven concept combining what is known about colour charge and the asymptotic freedom of the strong coupling. No analytic formulation of colour confinement exists, however the flux tube model of QCD point towards an overall consistency of this formulation [59]. Figure 2.3 illustrates what happens as the quarks in a hadronic bound state become separated by greater and greater distances due to colour confinement and asymptotic freedom. In $q\bar{q}$ states, the potential between quarks has been shown to be well-approximated by a "Coulomb plus linear" potential model [60, 61, 62], meaning that as a quark-antiquark pair in a meson state is separated, the interaction energy between the $q\bar{q}$ pair linearly increases. At some point, it becomes more energetically favorable for a quark-antiquark pair to be generated from the vacuum through mass-energy equivalence. We see this experimentally through the appearance of hadronic jets: directed showers of hadronic matter generated in high-energy collisions.
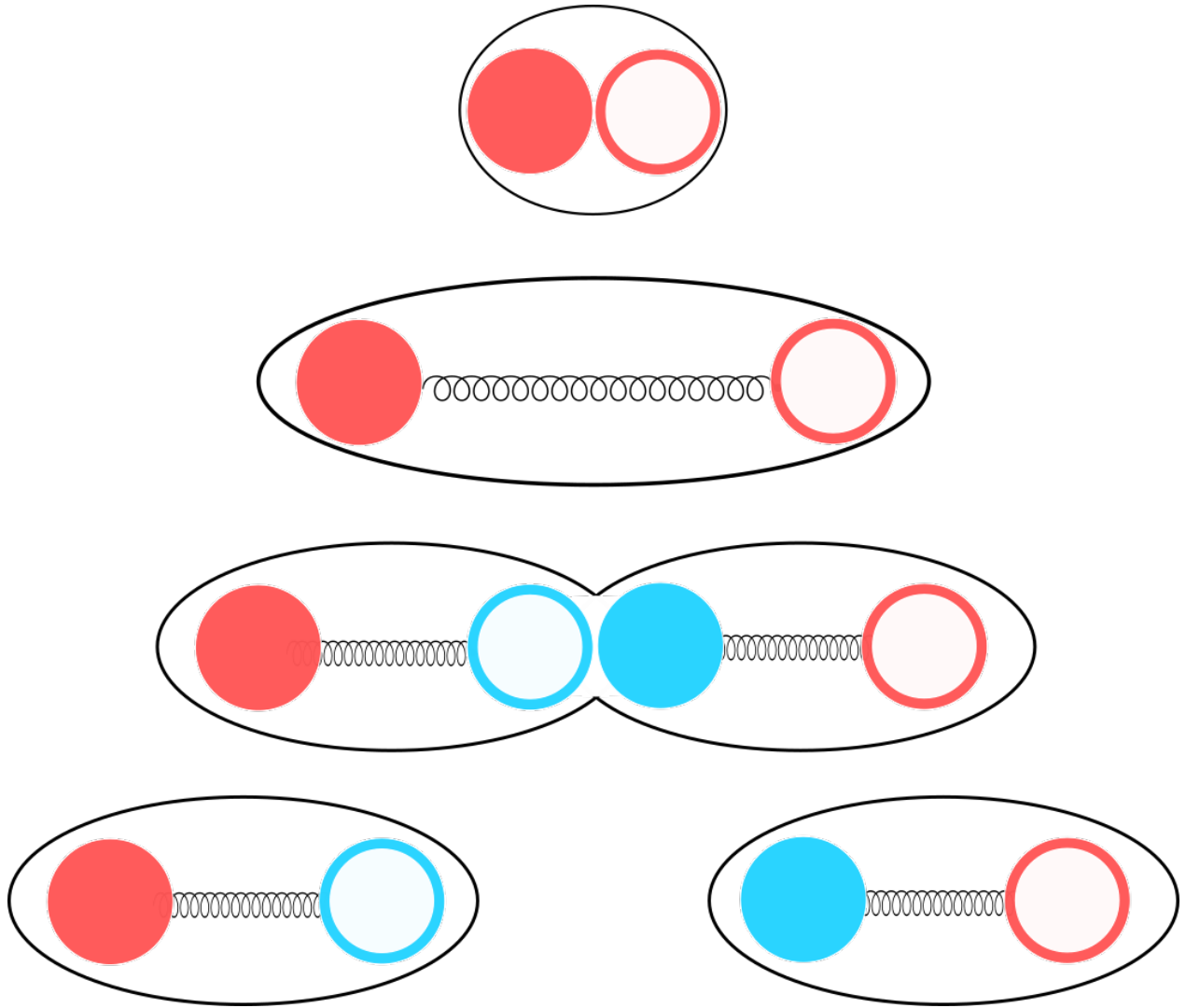
Figure 2.3: Illustration of colour confinement in a meson.

2.1.3.3 J, P, C Quantum Numbers

Important to identifying and categorizing hadronic states are three quantum numbers: the total angular momentum J, the parity P, and the charge parity C. The total angular momentum J is the magnitude of the vector sum of the orbital and spin angular momentum of a quantum system. The parity operator P represents a discrete symmetry in the reversal of spatial orientation (i.e., $\vec{x} \rightarrow -\vec{x}$), and the charge parity operator C represents a discrete symmetry in the exchange of particle to antiparticle ($q \rightarrow \bar{q}$ and vice versa). All hadrons are eigenstates of P, and hadrons that are their own antiparticle are eigenstates of C (such as closed-flavour states).

In his early formulation of the quark model [10], Gell-Mann categorized mesons and baryons according to the nature of their total angular momentum: mesons held integer values of J, and baryons held half-integer values of J. For many years, this has been synonymous with mesons corresponding to $q\bar{q}$ states, and baryons (or antibaryons) corresponding to qqq (or $\bar{q}\bar{q}\bar{q}$) states, forming what we will commonly refer to as the conventional quark model. However with recent observations of tetraquark [20, 63] and pentaquark states [21, 22], Gell-Mann's more general intention for this terminology finds new life. The discrete symmetries P and C have become important for determining whether an observed hadronic states fits within the conventional quark model, or whether it carries some underlying exotic structure. For example, a conventional $q\bar{q}$ meson has a parity given by

$$P = (-1)^{L+1}, \tag{2.36}$$

and a charge parity of

$$C = (-1)^{L+S}, \tag{2.37}$$

where L and S are the orbital and total spin angular momentum quantum numbers respectively. If we consider a scalar state $J = 0$, we can construct a conventional meson state in two ways: an antialigned pair of $q\bar{q}$ spin states with an orbital angular momentum of $L = 0$ or an aligned pair of $q\bar{q}$ spin states with an antialigned oribital excitation of $L = 1$. We can see that this dictates a very predictable set of quantum numbers for a meson within the conventional quark model,

$$J^{PC} \in \left\{0^{-+},\, 0^{++}\right\}. \tag{2.38}$$

However, if the structure deviates from a conventional $q\bar{q}$ paradigm, exotic quantum numbers such as

$$J^{PC} \in \left\{0^{+-},\, 0^{--}\right\} \tag{2.39}$$

are possible due to the extra degrees of freedom. These exotic J^{PC} are important signatures of hadronic structure beyond the quark model (such as hybrid mesons or tetraquark states), and are the focus of experimental efforts such as GlueX [25] and PANDA [26]. However, not all exotic hadrons carry distinct J^{PC} signatures such as these. In systems where C-parity is

not defined, and no symmetry exists in exchanging particles with antiparticles, only a definite J^P may be determined. Baryons are one example where no definite C-parity exists. In these systems, hadronic structures beyond the conventional quark model have no "smoking gun" signal provided by exotic J^{PC}, and signals of exotic states are expected to be mixed with those of conventional states carrying similar quantum numbers. We will see this difficulty explicitly in looking at open-flavour hybrid mesons [49] in Chapter 3, the scalar meson states [33, 34] in Chapter 5, as well as our discussion on hybrid baryons in Chapter 6.

2.2 QCD Sum Rules

Developed by Shifman, Vainshtein, and Zakharov [36, 37] (see also [38, 39, 40] for reviews), QCD sum rules (QCDSR) were developed as a way to access hadronic physics observables from a subatomic description of quarks and gluons (i.e., QCD). Theoretical predictions of correlation functions of composite hadronic operators are constructed using an operator product expansion, and related to phenomenological resonance models through dispersion relations. Through application of a transformation, spectral sum rules may be defined. These sum rules can take on a variety of forms, generally categorized by the weighting of the correlation function against a kernel of some form.

2.2.1 Correlation Functions and Hadronic Currents

Hadronic currents are composite operators conforming to the desired symmetry and valence content requirements of the system in question. For example, in a hybrid meson system composed of light quark-antiquark pairs $\bar{q}(x)$ and $q(x)$, a hadronic current describing the system could take the form

$$j_\mu(x) = ig_s \bar{q}_i(x) t^a \mathcal{G}_{\mu\nu}^a \Gamma_{ij}^\nu q_j(0) \tag{2.40}$$

where Γ^ν represents different combinations of Dirac structures, for example

$$\Gamma^\nu \in \{\gamma^\nu, \gamma^\nu \gamma_5\}, \tag{2.41}$$

19

and $\mathcal{G}_{\mu\nu}^{a}$ represents the gluon field strength tensor or its dual,

$$\mathcal{G}_{\mu\nu}^{a} \in \{G_{\mu\nu}^{a}, \tilde{G}_{\mu\nu}^{a}\}, \tag{2.42}$$

where the dual gluon field strength tensor, $\tilde{G}_{\mu\nu}^{a} = \frac{1}{2}\epsilon_{\mu\nu\rho\sigma}G_{\rho\sigma}^{a}$, and $G_{\rho\sigma}^{a}$ is defined in (2.4). Each combination of Γ^{ν} and $\mathcal{G}_{\mu\nu}^{a}$ describes different parity (P) and charge-parity (C) quantum numbers. This arises from the transformation properties of the Dirac matrices and Levi-Civita tensor from parity and charge-parity transformations [53]. Different combinations of J^{PC} correspond to distinct physical states; by calculating all combinations of J^{PC} available in a system, the multiplet structure of a given set of constituents may be determined. This has been done in early sum rules treatments of hadronic systems [64, 65], and more recently in LQCD frameworks [28, 30], in addition to our own work [49].

2.2.2 Operator Product Expansion

The correlation function is evaluated within QCD through the use of an operator product expansion (OPE). Due to its large coupling constant at low energies, QCD is inherently a non-perturbative theory; this behaviour is described by the inclusion of non-zero vacuum expectation values (VEVs) as operators in the OPE. Given an expectation value of a product of operators $\mathcal{O}_1$ and $\mathcal{O}_2$ acting at different spacetime coordinates, the OPE states that

$$\langle \mathcal{O}_1(x)\mathcal{O}_2(y)\rangle = \lim_{x \to y} \sum_{n} C_n(x-y)\langle O_n(y)\rangle. \tag{2.43}$$

The OPE allows the expansion of the product of nonlocal operators in (2.43) into a sum of local operators $\mathcal{O}_n$ weighted by some perturbative coefficients C_n called Wilson coefficients. Essentially, the energetic behaviour of QCD is partitioned into the high-energy regime (purely perturbative contributions i.e., $\mathcal{O}_n \to \mathbf{1}$) and the low-energy regime (non-perturbative contributions parameterized by nonzero VEVs). For example, for a hadronic current such as (2.40),

$$\langle j_\mu(x)j_\nu^\dagger(0)\rangle = C_1(x)\mathbf{1} + C_3(x)\langle\bar{q}q\rangle + C_4(x)\langle G^2\rangle + C_5(x)\langle\bar{q}\sigma Gq\rangle + \dots. \tag{2.44}$$

Here, each term of the OPE corresponds to a family of Feynman diagrams, where the coefficients $C_n(x)$ are calculated perturbatively, and $\langle \bar{q}q \rangle, \langle G^2 \rangle, \langle \bar{q}\sigma Gq \rangle, \ldots$ are nonzero VEVs parameterizing the QCD vacuum. The subscript represents the mass dimension of the operator such that the series is organized in terms of increasing mass dimension. Forming expressions in terms of each of these local, nonzero VEVs from our composite operators and constituent fields is a matter of considering their symmetry properties; these nonzero VEVs are a property of the QCD vacuum, and as such they must be local, gauge invariant, Lorentz invariant, colourless, and (as a property of the vacuum) be constructed of metrics and Dirac matrices [42]. We also rely on the symmetry properties of the fields in question. For example, the gluon field-strength tensor $G_{\mu\nu}^a(x)$ is antisymmetric under the interchange of Lorentz indices $\mu \leftrightarrow \nu$. Note that no $C_2(x)$ (dimension-two) term exists in (2.44) due to the requirements of Lorentz and gauge symmetry. These symmetry restrictions as well as the QCD equations of motion are sufficient to restrict the form of these nonzero VEVs [66, 64]. The following are lowest-order expansions of nonzero VEVs used throughout this work (a more detailed derivation of the following may be found in [67]). Where necessary, the fixed-point gauge condition at leading order

$$B_\mu(x) = \frac{1}{2}x^\omega G_{\omega\mu}(0), \tag{2.45}$$

has been applied [68, 69, 70].

$$\langle G_{\mu\rho}^a(x)G_{\nu\sigma}^b(0) \rangle = \frac{\langle GG \rangle}{8d(d-1)}\delta^{ab}(g_{\mu\nu}g_{\rho\sigma} - g_{\mu\sigma}g_{\rho\nu}) \tag{2.46}$$

$$\langle \bar{q}_k^{\beta'}(x)q_j^\beta(0) \rangle = \frac{\langle \bar{q}q \rangle}{12}\delta^{\beta\beta'}\delta_{jk} \tag{2.47}$$

$$t_{\beta'\beta}^c\langle \bar{q}_k^{\beta'}(x)B_\lambda^c(y)q_j^\beta(0) \rangle = \frac{\langle \bar{q}\sigma \cdot Gq \rangle}{8id(d-1)g_s}y_\omega(\sigma^{\omega\lambda})_{jk} \tag{2.48}$$

$$t_{\beta'\beta}^c\langle \bar{q}_k^{\beta'}(x)G_{\lambda\kappa}^c(y)q_j^\beta(0) \rangle = \frac{\langle \bar{q}\sigma \cdot Gq \rangle}{4id(d-1)g_s}(\sigma^{\lambda\kappa})_{jk} \tag{2.49}$$

21

$$g_s^3 f^{abc} \langle G_{\eta\tau}^a(x) G_{\sigma\alpha}^c(y) G_{\beta\lambda}^b(0) \rangle = \frac{\langle g^3 G^3 \rangle}{d(d^2 - 4)} \left[(g_{\tau\sigma} g_{\alpha\beta} g_{\lambda\eta} - g_{\eta\sigma} g_{\alpha\beta} g_{\lambda\tau}) \right.$$

$$- (g_{\tau\alpha} g_{\sigma\beta} g_{\lambda\eta} - g_{\eta\alpha} g_{\sigma\beta} g_{\lambda\tau})$$

$$- (g_{\tau\sigma} g_{\alpha\lambda} g_{\beta\eta} - g_{\eta\sigma} g_{\alpha\lambda} g_{\beta\tau})$$

$$\left. + (g_{\tau\alpha} g_{\sigma\lambda} g_{\beta\eta} - g_{\eta\alpha} g_{\sigma\lambda} g_{\beta\tau}) \right] . \tag{2.50}$$

$$\langle [D_{\omega_1}, [D_{\omega_2}, G_{\mu\rho}]] G_{\nu\sigma} \rangle = - \frac{i \langle g^3 G^3 \rangle}{d(d-2)(d+2)} \, g_{\omega_1 \omega_2} \left(g_{\mu\nu} g_{\rho\sigma} - g_{\rho\nu} g_{\mu\sigma} \right)$$

$$- \frac{i \langle g^3 G^3 \rangle}{2d(d-2)(d+2)}$$

$$\times \left[g_{\omega_2 \nu} \left(g_{\omega_1 \mu} g_{\rho\sigma} - g_{\omega_1 \rho} g_{\mu\sigma} \right) - g_{\omega_2 \sigma} \left(g_{\omega_1 \mu} g_{\rho\nu} - g_{\omega_1 \rho} g_{\mu\nu} \right) \right] \tag{2.51}$$

$$+ \frac{3i \langle g^3 G^3 \rangle}{2d(d-1)(d-2)(d+2)}$$

$$\times \left[g_{\omega_1 \nu} \left(g_{\omega_2 \mu} g_{\rho\sigma} - g_{\omega_2 \rho} g_{\mu\sigma} \right) - g_{\omega_1 \sigma} \left(g_{\omega_2 \mu} g_{\rho\nu} - g_{\omega_2 \rho} g_{\mu\nu} \right) \right]$$

where d is spacetime dimension, $\sigma^{\mu\nu} = \frac{i}{2} [\gamma^\mu, \gamma^\nu]$, and the values of the nonzero VEV parameters ($\langle \bar{q}q \rangle$, $\langle GG \rangle$, $\langle \bar{q}\sigma \cdot Gq \rangle$, $\langle g^3 G^3 \rangle$) may be found in the literature (see [40] for a summary of recent values). The OPE is part of the foundation of the QCDSR methodology. Diagrammatically, we represent the non-perturbative contributions to the correlation function as Feynman diagrams with broken lines (see Figure 2.4). These nonzero VEVs are also referred to as condensates; the lowest dimension condensate, $m_q \langle \bar{q}q \rangle$, corresponds to the chiral condensate of QCD manifesting from the spontaneous symmetry breaking of chiral symmetry.

To calculate the Wilson coefficients in the OPE, a coordinate space methodology is used [42]; Wick's theorem is applied to the correlator of interest, leaving uncontracted fields corresponding to the nonzero VEV associated with the Wilson coefficient of interest. If necessary, a fixed-point gauge is applied to uncontracted fields [68, 69], and the uncontracted fields are expressed in terms of the local nonzero VEVs shown in (2.44). Note that it has been shown that the use of a fixed-point gauge does not conflict with the covariant gauge used for gauge-fixing and quantization in the QCD Lagrangian [70]. Finally, after Fourier transforming to momentum space, any coordinate terms from the VEV expansion become momentum derivative operators and zero-momentum insertions; from here, we can apply loop momentum methods to finish evaluating the Wilson coefficient.
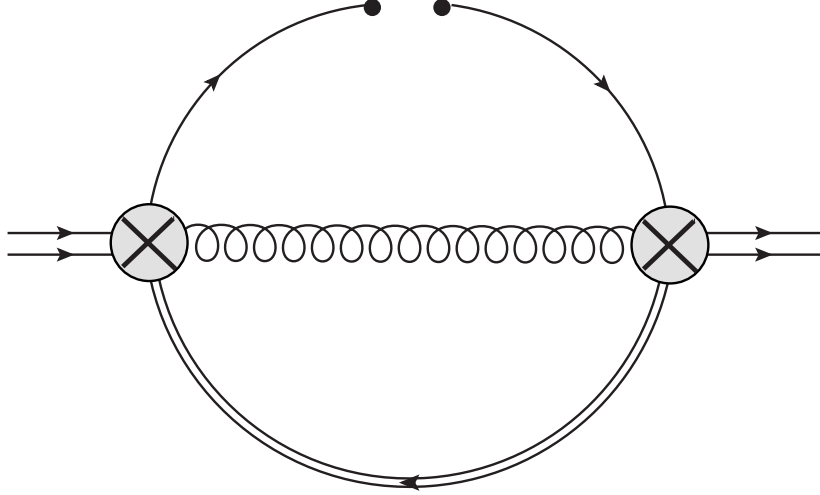
Figure 2.4: An example of a non-perturbative condensate diagram within QCDSR. This depicts a quark condensate characterized by the chiral condensate vacuum expectation value $m_q \langle \overline{q} q \rangle$.

2.2.3 Dispersion Relations and Spectral Sum-Rules

The methodology of QCDSR begins with a dispersion relation [71, 72] (see also [47]),

$$\Pi(Q^2) = \int_{t_0}^{\infty} \frac{\rho^{\text{had}}(t)}{(t + Q^2)} \, \mathrm{d}t + \cdots , \quad Q^2 > 0, \tag{2.52}$$

defined in terms of the euclideanized momentum Q^2, and where t_0 represents the physical threshold of the system. This expression relates the QCD description of hadrons found through calculating correlation functions of composite operators (LHS) to the phenomenological side described by experimental hadronic physics (RHS). This is commonly described as quark-hadron duality; the energy regime describing the degrees of freedom within QCD (quarks and gluons) does not naturally connect with the regime describing the degrees of freedom of experimental hadronic physics (mesons and baryons, for example). The dispersion relation (2.52) connects these low- and high-energy regimes. The hadronic spectral function, $\rho^{\text{had}}(t)$, is often described using some model corresponding to an appropriate resonance shape. The right side also contains low-energy constants (polynomials in Q^2, denoted by the $\cdots$ in (2.52)) which are not always well-known. In order to evaluate (2.52), typically some sort of integral transform $\mathcal{T}$ is considered which eliminates these unknown polynomials. In

general, this turns (2.52) into the form

$$\mathcal{T}\left[\Pi(Q^2)\right] = \int_{t_0}^{\infty} \mathrm{d}t \, t^k K(\tau_i, t) \rho^{\mathrm{had}}(t), \tag{2.53}$$

where $K(\tau_i, t)$ is some kernel associated with a particular category of spectral sum rule, dependant on some set of characteristic energy scales τ_i.

2.2.3.1 Laplace Sum Rules

Laplace sum rules (LSRs), also known as Borel sum rules, are named due to the resulting kernel $K(\tau, t) = e^{-\tau t}$, and lead to (2.53) becoming

$$\mathcal{R}_k(\tau) = \int_{t_0}^{\infty} t^k e^{-t\tau} \rho^{\mathrm{had}}(t) \, \mathrm{d}t. \tag{2.54}$$

The derivation of these sum rules starts with the application of a Borel transform to the dispersion relation (2.52), where the Borel transform operator is defined as

$$\hat{\mathcal{B}} = \lim_{\substack{N,Q^2 \to \infty \\ \tau = N/Q^2}} \frac{(-Q^2)^N}{\Gamma(N)} \left(\frac{d}{dQ^2}\right)^N. \tag{2.55}$$

Applying (2.55) to (2.52), weighted with $(-Q^2)^k$ for $k \geq 0$ (alongside a convenient factor of $\frac{1}{\tau}$), gives

$$\frac{1}{\tau}\hat{\mathcal{B}}\left[(-Q^2)^k \Pi(Q^2)\right] = \frac{1}{\tau} \int_{t_0}^{\infty} \rho^{\mathrm{had}}(t) \, \hat{\mathcal{B}}\left[\frac{(-Q^2)^k}{(t+Q^2)}\right] \mathrm{d}t \tag{2.56}$$

$$= \frac{1}{\tau} \int_{t_0}^{\infty} \rho^{\mathrm{had}}(t) \, t^k \left(\tau e^{-t\tau}\right) \mathrm{d}t, \tag{2.57}$$

where t_0 is the physical threshold for the hadronic system of interest. The application of the Borel operator in (2.55) eliminates all purely polynomial structures in Q^2, which simplifies the dispersion relation through removal of the (unknown) low-energy constants. From Ref. [42], we use the identity $\hat{\mathcal{B}}\left[\frac{Q^{2k}}{(t+Q^2)}\right] = (-1)^k t^k \tau e^{-t\tau}$ to evaluate the transform on the RHS. Phenomenologically, the resulting Laplace kernel weights the hadronic spectral function $\rho^{\mathrm{had}}(t)$, and preferentially amplifies lower-energy states. Figure 2.5 shows this demonstrated on a toy
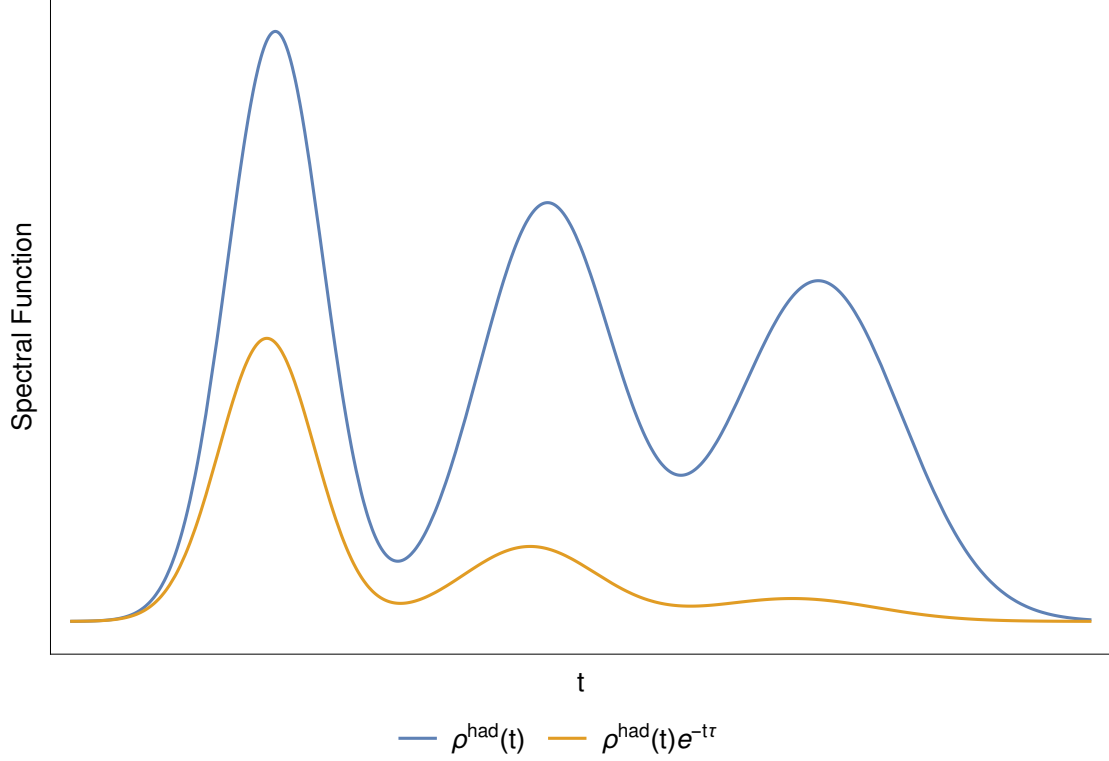
Figure 2.5: Weighting of the Laplace kernel on a toy spectral function.

spectral function. By suppressing resonances lying at higher energies, LSRs are well-suited for probing the ground state of hadronic systems, and reduce the dependence on high-energy continuum-like features.

To evaluate the transform applied to the correlation function on the LHS of (2.56), we note that the Borel transform may be related to the inverse Laplace transform [42] by

$$\frac{1}{\tau} \hat{\mathcal{B}} \left[f \left(Q^2 \right) \right] = \mathcal{L}^{-1} \left[f \left(Q^2 \right) \right], \tag{2.58}$$

and the problem of evaluating the transform of the correlation function on the LHS of (2.56) becomes a matter of evaluating the contour integral defined by the inverse Laplace transform. The inverse Laplace transform is defined by

$$\mathcal{L}^{-1} \left[f \left(Q^2 \right) \right] = \frac{1}{2\pi i} \int_{b-i\infty}^{b+i\infty} \mathrm{d}Q^2 \, e^{-\tau Q^2} f \left(Q^2 \right), \tag{2.59}$$

where the integration is performed along a contour in the complex plane, where b is defined

to the right of any complex branch and pole structure in $f(Q^2)$.
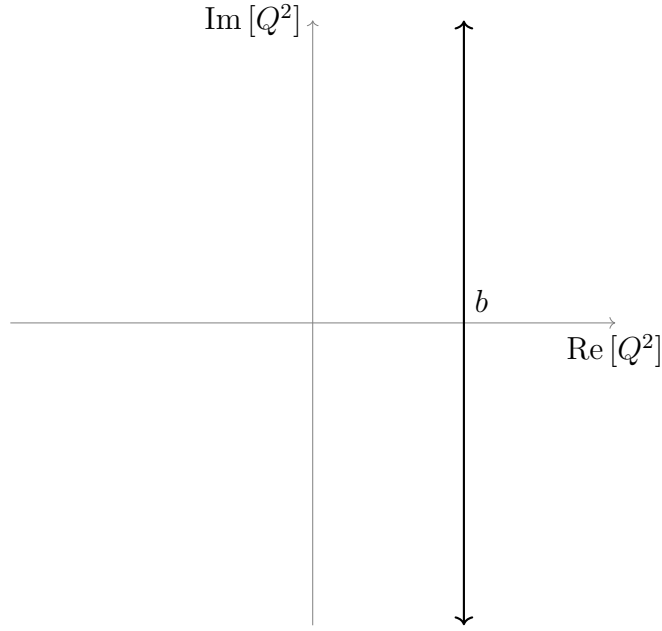
Figure 2.6: Integration contour for inverse Laplace transform

Consider the contour of integration Γ for (2.59) shown in Figure 2.6. Using Cauchy's integral theorem, we instead evaluate the integral along the closed contour $\sum_{i=1}^{6} \Gamma_i$ depicted in Figure 2.7,

$$\oint_{\Gamma_1+\Gamma_2+\Gamma_3+\Gamma_4+\Gamma_5+\Gamma_6} (\cdots)\mathrm{d}Q^2 = 0. \tag{2.60}$$

By taking the radius of the semicircular contour $R \to \infty$, we can recover the result of (2.59) by relating the contour Γ to the branch structure in the deformed contour depicted in Figure 2.7, that is,

$$\int_{b-i\infty}^{b+i\infty} (\cdots)\mathrm{d}Q^2 = \lim_{R\to\infty} \int_{\Gamma_1} (\cdots)\mathrm{d}Q^2 = -\lim_{R\to\infty} \int_{\Gamma_2+\Gamma_3+\Gamma_4+\Gamma_5+\Gamma_6} (\cdots)\mathrm{d}Q^2 \tag{2.61}$$

In evaluating the contour integral as shown, the LHS of equation (2.56) typically reduces to the following form (depending on the complex structure of the problem at hand)

$$\frac{1}{\tau}\hat{\mathcal{B}}\left[\Pi(Q^2)\right] \equiv \mathcal{L}^{-1}\left[\Pi(Q^2)\right] = \int_{t_0}^{\infty} e^{-t\tau}\frac{1}{\pi}\mathrm{Im}\Pi^{\mathrm{OPE}}(t)\,\mathrm{d}t \tag{2.62}$$

$$+ f(\tau), \tag{2.63}$$
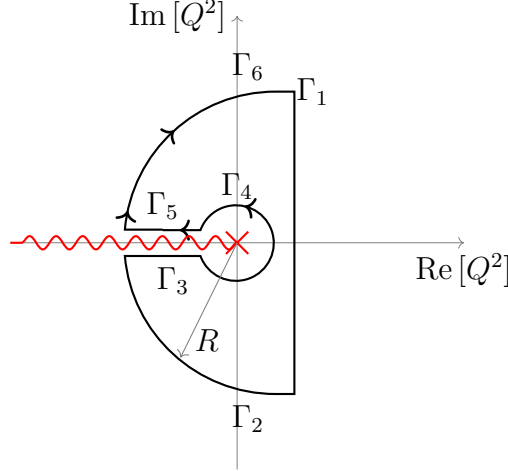
Figure 2.7: Deformed contour around branch structure in red.

where $f(\tau)$ represents the contributions coming from the pole structure, and where we have explicitly labeled $\frac{1}{\pi}\mathrm{Im}\Pi^{\mathrm{OPE}}(t)$ to emphasize that this describes the QCD side of the dispersion relation, calculated through application of the OPE; the imaginary part of Π^{OPE} results from using the Schwarz reflection principle in the evaluation of the contour integral. For the hadronic side of the dispersion relation, we must propose an appropriate model for the hadronic spectral function. Perhaps the simplest model we can consider is a narrow resonance plus continuum model [36, 37, 73],

$$\rho^{\mathrm{had}}(t) = f_H^2 m_H^8 \delta(t - m_H^2) + \theta(t - s_0)\frac{1}{\pi}\mathrm{Im}\Pi^{\mathrm{OPE}}(t), \tag{2.64}$$

where f_H is the dimensionless coupling strength, m_H is the hadronic mass (we have assumed our correlator is of mass dimension six), θ is the Heaviside step function, and s_0 is the onset of the continuum in GeV^2. At high energies characterized by the onset of the continuum, perturbation theory dominates the strong interaction, and so our OPE is a good description of the high-energy behaviour. At lower energies, we are interested in extracting the properties of the ground state, which we model with a Dirac delta distribution. If there were any width effects present, they have been shown to scale like $m_H\Gamma\tau$ [74], where m_H is the hadronic mass, Γ is the resonance width, and τ is our introduced Borel parameter. Applying this

model to the RHS of (2.56) gives us

$$\int_{t_0}^{\infty} \rho^{\text{had}}(t)\, e^{-t\tau}\, \mathrm{d}t = f_H^2 m_H^8 e^{-m_H^2 \tau} + \int_{s_0}^{\infty} e^{-t\tau} \frac{1}{\pi} \mathrm{Im}\Pi^{\text{OPE}}(t)\mathrm{d}t \tag{2.65}$$

and so, with (2.63) and (2.65), (2.56) becomes

$$\int_{t_0}^{\infty} e^{-t\tau} \frac{1}{\pi} \mathrm{Im}\Pi^{\text{OPE}}(t)\, \mathrm{d}t + f(\tau) = f_H^2 m_H^8 e^{-m_H^2 \tau} + \int_{s_0}^{\infty} e^{-t\tau} \frac{1}{\pi} \mathrm{Im}\Pi^{\text{OPE}}(t)\mathrm{d}t. \tag{2.66}$$

Grouping the terms that depend on the OPE into an expression coming solely from QCD, we arrive at a final formulation of our LSR expression that we define to be $\mathcal{R}_0(\tau, s_0)$

$$\mathcal{R}_0(\tau, s_0) \equiv \int_{t_0}^{s_0} e^{-t\tau} \frac{1}{\pi} \mathrm{Im}\Pi^{\text{OPE}}(t)\, \mathrm{d}t + f(\tau) = f_H^2 m_H^8 e^{-m_H^2 \tau}. \tag{2.67}$$

Strictly speaking, this expression generalizes to a family of sum rules with different weights characterized by an integer $k \geq 0$, where more generally,

$$\mathcal{R}_k(\tau, s_0) \equiv \int_{t_0}^{s_0} t^k e^{-t\tau} \frac{1}{\pi} \mathrm{Im}\Pi^{\text{OPE}}(t)\, \mathrm{d}t + f(k, \tau) = f_H^2 m_H^{8+2k} e^{-m_H^2 \tau}. \tag{2.68}$$

Using a combination of different weights, the hadronic mass can be extracted from the QCD side of equation (2.68)

$$\frac{\mathcal{R}_{k+1}(\tau, s_0)}{\mathcal{R}_k(\tau, s_0)} = m_H^2, \tag{2.69}$$

where τ is the Borel parameter characterizing the sum rule window where the OPE is convergent, and s_0 is the continuum onset, characterizing the region of the spectral function where perturbative QCD dominates.

2.2.3.2 Gaussian Sum Rules

Much like LSRs, Gaussian sum rules (GSRs) are also named by the form of their kernel, taking a slightly more complicated form than their LSR counterpart, where

$$G_k(\hat{s}, \tau) = \int_{t_0}^{\infty} t^k \left(\frac{e^{-\frac{(\hat{s}-t)^2}{4\tau}}}{\sqrt{4\pi\tau}} \right) \rho^{\text{had}}(t)\, \mathrm{d}t. \tag{2.70}$$

The derivation for these sum rules is similar to that of the LSRs with some notable deviations; a detailed description of the derivation may be found in Refs. [9, 75, 76]. Unlike the LSR, the GSR is defined with an extra degree of freedom $\hat{s}$ as well as a parameter τ. It should be explicitly noted that the parameter τ within the GSR construction has no relationship to the Borel parameter τ defined in a LSR context. Contrasted with the preferential weighting of the spectral function in the case of the LSR, the Gaussian kernel in the GSR (2.70) weights the spectral function $\rho^{\mathrm{had}}(t)$ equally when $t = \hat{s}$, allowing the GSR methodology to probe a wide range of energies by scanning through the energy parameter $\hat{s}$. While it can be problematic to examine resonance width effects or mixing using LSR given higher energy states are supressed by design, the Gaussian weighting of the GSR as well as the capacity to scan through different energy scales makes this formulation of QCDSR a natural choice to explore more complex resonance models and quantum mechanical mixing, particularly in states with conventional J^{PC} or states with undefined C-parity.

2.2.4 Optimizing Sum Rules

By forming the Gaussian and Laplace spectral sum rules, the parameter τ is introduced as a result of applying the transform. In the case of GSRs, there is an additional parameter $\hat{s}$ allowing the exploration of a wide range in energies. In order to ensure the accuracy of the resulting sum rule predictions, a few restrictions must be considered.

2.2.4.1 LSR Constraints

Because our analysis of QCDSR relies on both perturbative calculations and the properties of the OPE (2.43) truncated at a particular order, we must check that any predicted results within the sum rules framework ensures convergence of the OPE; that is, the correlation function must have a dominant contribution from perturbation theory, with higher dimensional condensate terms contributing less and less to the overall result. Ensuring that the nonperturbative contributions to the calculation are controlled gives us a low-energy bound on our analysis, or an upper-bound on the value of τ within LSRs [36, 37]. A set of typical

constraints would look like

$$\left| \frac{\mathcal{R}_k^{\mathrm{4D}}(\tau)}{\mathcal{R}_k^{\mathrm{pert}}(\tau)} \right| \leq \frac{1}{3} \tag{2.71}$$

$$\left| \frac{\mathcal{R}_k^{\mathrm{6D}}(\tau)}{\mathcal{R}_k^{\mathrm{4D}}(\tau)} \right| \leq \frac{1}{3}. \tag{2.72}$$

To fix an upper bound on τ, a nominal requirement of $\sim 30\%$ is set for the upper bound on the contribution of dimension four condensates ($m_q\langle \bar{q}q \rangle$ and $\langle G^2 \rangle$) relative to the expected dominant contribution from perturbation theory, as well as that of the dimension six condensates ($m_q\langle \bar{q}\sigma Gq \rangle$, $\langle g^3 G^3 \rangle$, and $\langle \bar{q}\bar{q}qq \rangle$) relative to the dimension four condensates. Similar conditions for higher-dimensional condensates could be applied if necessary.

For a high-energy bound on the LSRs analysis (or a lower-bound on τ), we require that the mass prediction of the ground state energy is not contaminated by the QCD continuum or suppressed excited resonances [36, 37]. This can be thought of as a "signal-to-noise" condition; we impose a minimum threshold of an acceptable level of signal (the ground state resonance) against the background (the QCD continuum). That is, the ratio of integrals

$$\mathrm{PC}\left(s_0, \tau \right) = \frac{\int_{M_Q^2}^{s_0} e^{-t\tau} \mathrm{Im}\Pi(t)\mathrm{d}t}{\int_{M_Q^2}^{\infty} e^{-t\tau} \mathrm{Im}\Pi(t)\mathrm{d}t}. \tag{2.73}$$

Typically the value of the pole contribution (2.73) is constrained to be $\geq 10\%$ [77]. The combination of these two requirements on the value of τ form a range of values where a τ-independent solution for the hadronic mass may be found. This is commonly referred to as the Borel window.

2.2.4.2   GSR Constraints

The introduction of the energy parameter $\hat{s}$ as well as the shape of the Gaussian kernel make applying the same constraints as considered in the case of LSRs difficult. While convergence of the OPE and matters of pole dominance remain important, an approach more natural to the GSRs is applied.

When initially derived and proposed [75], a parallel between the GSRs and the classical

one-dimensional heat equation was drawn. The GSR $G_k(\hat{s}, \tau)$ satisfies

$$\frac{\partial^2 G_k(\hat{s}, \tau)}{\partial \hat{s}^2} = \frac{\partial G_k(\hat{s}, \tau)}{\partial \tau}, \tag{2.74}$$

where $\hat{s}$ and τ take the place of position and time in the classical case, respectively. Through this lens, we find a soft upper bound on the value of τ; the time-asymmetric nature of the heat equation reveals to us that larger values of τ will "wash out" the original GSR. It serves us best then to extract predictions from the GSRs at as low of a value of τ as can be managed. While this doesn't provide an explicit upper-bound on the parameter τ, it does allow us to compare the behaviour across multiple values of τ and take the lowest value possible. But what then, of the lower bound on τ? Due to the renormalization-group invariance of (2.40), previous applications of GSRs [9] have determined the natural renormalization scheme for a GSR analysis with logarithmic dependence in the perturbative contribution to be

$$\int_0^\infty \log^n \left(\frac{t}{\nu^2}\right) \exp\left(-\frac{(t-\hat{s})^2}{4\tau}\right) dt = \nu^2 \int_0^\infty dx \, \log^n(x) \exp\left[-\left(\frac{\nu^2 x}{2\sqrt{\tau}} - \frac{\hat{s}}{2\sqrt{\tau}}\right)^2\right], \tag{2.75}$$

that is, the renormalization-group equation is satisfied with the running coupling constant $\alpha(\nu)$ and the renormalization scale of $\nu^2 = \sqrt{\tau}$. This provides us a natural lower bound on the value of the GSR parameter τ; depending on the system of interest, the value of τ will depend on what the appropriate scale of interest is. We will see this carried out when examining light hybrid states with GSRs in Chapter 4.

There have been efforts to develop alternative methods of extracting predictions from QCD sum rules without the need of a Borel window, which can be difficult to determine [78]. In the case of the GSRs, there is no standard methodology for ensuring OPE convergence and enforcing the pole contribution as there is in the LSRs; the parameter τ is distinct in each methodology, and the idea of a Borel window is not well-defined in a GSR approach. With this in mind, we can look towards a more fundamental way of constraining our sum rules. A more general form of the Cauchy-Schwarz inequality, called the Hölder inequality, states

$$\left|\int_{t_1}^{t_2} f(t) g(t) \, d\mu\right| \le \left(\int_{t_1}^{t_2} |f(t)|^p d\mu\right)^{\frac{1}{p}} \left(\int_{t_1}^{t_2} |g(t)|^q d\mu\right)^{\frac{1}{q}}, \tag{2.76}$$

provided that

$$\frac{1}{p} + \frac{1}{q} = 1. \tag{2.77}$$

Using the positivity of the spectral function ρ to define the integration measure, this can be related to both the LSR and GSR expressions. For LSRs, provided $0 \leq \omega \leq 1$ and $\tau_{\max} - \tau_{\min} > 0$), equations (2.76) and (2.77) result in [78, 79]

$$\mathcal{L}_0 \left(\omega \tau_{\min} + (1 - \omega)\tau_{\max}, s_0 \right) \leq \mathcal{L}_0^\omega \left(\tau_{\min}, s_0 \right) \mathcal{L}_0^{1-\omega} \left(\tau_{\max}, s_0 \right). \tag{2.78}$$

In Chapter 4, equations (2.76) and (2.77) are applied to the GSRs for the first time, resulting in

$$\left| G_0 \left(\frac{\tau_1 \tau_2}{\omega \tau_2 + (1 - \omega)\tau_1}, \hat{s}, s_0 \right) \right| \leq \left(\frac{\omega \tau_2 + (1 - \omega)\tau_1}{\tau_2} \right)^{\frac{\omega}{2}} \left(\frac{\omega \tau_2 + (1 - \omega)\tau_1}{\tau_1} \right)^{\frac{1-\omega}{2}}$$
$$\times G_0^\omega \left(\tau_1, \hat{s}, s_0 \right) G_0^{1-\omega} \left(\tau_2, \hat{s}, s_0 \right). \tag{2.79}$$

assuming $0 \leq \omega \leq 1$. A full derivation of (2.79) may be found in Appendix A.

2.3   Regularization

To extract meaningful finite results from a QFT, typically a regularization procedure of some kind must be implemented. Regularization is the process of parameterizing divergences within a QFT such that we can perform the resulting loop integrals without being hindered by the infinities that might arise [53]. Typically, regularization is followed by a systematic renormalization procedure (discussed in the next section) which eliminates the divergent terms, resulting in a finite prediction. Throughout this work, we use the process of dimensional regularization [80]: by evaluating our integrals in a $d = 4 + 2\epsilon$ dimensional spacetime, divergences are parameterized by $\frac{1}{\epsilon^n}$ terms (for an integer $n > 0$). In applying dimensional regularization to a QCDSR calculation, we must ensure that all aspects of the calculations are represented in terms of d dimensions. Integrals for two-point functions involving light quarks for the most part are well known and tabulated (see Ref. [42]). For two-loop calculations with arbitrary masses, we rely on the *Mathematica* package TARCER [81] which uses

recursion relationships [82, 83] to reduce two-point function two-loop integrals to a set of known master integrals ,

$$
\begin{aligned}
\mathbf{A}^d_{\{\nu_1, m_1\}} &\equiv \mathrm{TAI}[d,\, 0,\, \{\{\nu_1,\, m_1\}\}] \\
&= \frac{1}{\pi^{d/2}} \int \frac{d^d k_1}{(k_1^2 - m_1^2)^{\nu_1}}, \\
\mathbf{B}^d_{\{\nu_1, m_1\}, \{\nu_2, m_2\}} &\equiv \mathrm{TBI}[d,\, q^2,\, \{\{\nu_1,\, m_1\},\, \{\nu_2,\, m_2\}\}] \\
&= \frac{1}{\pi^{d/2}} \int \frac{d^d k_1}{(k_1^2 - m_1^2)^{\nu_1} \left((k_1 - q)^2 - m_2^2\right)^{\nu_2}}, \\
\mathbf{J}^d_{\{\nu_1, m_1\}, \{\nu_2, m_2\}, \{\nu_3, m_3\}} &\equiv \mathrm{TJI}[d,\, q^2,\, \{\{\nu_1,\, m_1\},\, \{\nu_2,\, m_2\},\, \{\nu_3,\, m_3\}\}] \\
&= \frac{1}{\pi^d} \int \frac{d^d k_1 d^d k_2}{(k_1^2 - m_1^2)^{\nu_1} \left((k_1 - k_2)^2 - m_2^2\right)^{\nu_2} \left((k_2 - q)^2 - m_3^2\right)^{\nu_3}}.
\end{aligned}
\tag{2.80}
$$

By using dimensionally regularized results for the master integrals in (2.80), we obtain dimensionally regulated results for our two-loop, two-point correlation function. For example, results necessary to evaluate the correlation function of the heavy-light hybrid case are [42, 84, 85, 86]

$$
\mathbf{A}^d_{\{1, m\}} = -i \left(m^2\right)^{\frac{d}{2}-1} \Gamma\left(1 - \frac{d}{2}\right),
\tag{2.81}
$$

$$
\mathbf{B}^d_{\{\beta, m\}, \{\alpha, 0\}} = i(-1)^{-\beta-\alpha} \left(m^2\right)^{\frac{d}{2}-\beta-\alpha} \frac{\Gamma\left(\frac{d}{2}-\beta\right)\Gamma\left(\beta+\alpha-\frac{d}{2}\right)}{\Gamma\left(\frac{d}{2}\right)\Gamma(\alpha)}
$$
$$
\times \; {}_2F_1\left[\begin{matrix} \beta,\, \beta+\alpha-\frac{d}{2} \\ \frac{d}{2} \end{matrix} \, \Big| \, \frac{q^2}{m^2} \right],
\tag{2.82}
$$

$$
\mathbf{J}^d_{\{\nu, m\}, \{1, 0\}, \{1, 0\}} = (-1)^{1-\nu}(m^2)^{d-2-\nu} \frac{\Gamma\left(\frac{d}{2}-1\right)^2 \Gamma(\nu+2-d)\Gamma\left(2-\frac{d}{2}\right)}{\Gamma\left(\frac{d}{2}\right)\Gamma(\nu)}
$$
$$
\times \; {}_2F_1\left[\begin{matrix} 2-\frac{d}{2},\, \nu+2-d \\ \frac{d}{2} \end{matrix} \, \Big| \, \frac{q^2}{m^2} \right],
\tag{2.83}
$$

where the hypergeometric function ${}_2F_1$ is defined by

$$
{}_2F_1\left[\begin{matrix} a,\, b \\ c \end{matrix} \, \Big| \, z \right] = \sum_{n=0}^{\infty} \frac{(a)_n (b)_n}{(c)_n} \frac{z^n}{n!},
\tag{2.84}
$$

and where the Pochhammer symbol defining (2.84) is expressed in terms of Gamma functions

$$(a)_n = \frac{\Gamma(a+n)}{\Gamma(a)}. \tag{2.85}$$

Whether or not a calculation can be done analytically depends on whether appropriate dimensionally regularized integral results are available for the loop topology of the calculation in question. For multi-loop light quark systems such as the light hybrid baryons, the absence of a mass term simplifies the calculation such that it can be done iteratively using results for the integrals of two-point functions containing light quarks [42]. Other topologies such as three-point functions can be more difficult to solve analytically (particularly in the case of massive quarks); numerical methods using sector decomposition [87, 88, 89] may be useful in these cases.

2.4 Renormalization

In QCD, as we move past tree-level calculations and explore higher and higher orders of loop calculations, the need for a renormalization prescription becomes apparent; loop integrals exhibit ultraviolet and infrared (UV and IR) divergent behaviour that hampers a physical interpretation. This renormalization formally manifests in the inclusion of renormalization coefficients in the renormalized Lagrangian. The guiding principle of renormalization is simple: observable quantities should be finite and calculable from the underlying Lagrangian. Following that, the divergent behaviour of these integrals may be removed by including counterterm diagrams that serve to cancel the divergent behaviour of the calculation. In general, we can think of the Lagrangian as three different pieces

$$\mathcal{L} = \mathcal{L}_0 + \mathcal{L}_{\mathrm{int}} + \mathcal{L}_{\mathrm{ct}}. \tag{2.86}$$

Here, the Lagrangian $\mathcal{L}$ has been broken into the free Lagrangian $\mathcal{L}_0$ describing the kinematics of the theory, the interaction Lagrangian describing the dynamics of the theory $\mathcal{L}_{\mathrm{int}}$, and the counterterm Lagrangian $\mathcal{L}_{\mathrm{ct}}$. For example, in a simple ϕ^4 scalar theory, the bare Lagrangian

expressed in terms of bare fields and parameters is

$$\mathcal{L}_0 = \frac{1}{2} \left(\partial_\mu \phi_0 \right)^2 - \frac{\mu_0^2}{2} \phi_0^2, \tag{2.87}$$

and the (bare) interaction piece is

$$\mathcal{L}_{\text{int}} = -\frac{\lambda_0}{4!} \phi_0^4, \tag{2.88}$$

where a subscript "0" indicates a bare quantity. For a theory to be considered renormalizable, only a finite number of terms may be added to the Lagrangian corresponding to terms in the original bare Lagrangian. The counterterm piece of the Lagrangian for the case of ϕ^4 theory is

$$\mathcal{L}_{\text{ct}} = -\frac{C_\phi}{2} \left(\partial_\mu \phi_0 \right)^2 + \frac{C_\mu \mu_0^2}{2} \phi_0^2 + \frac{C_\lambda \lambda_0}{4!} \phi_0^4, \tag{2.89}$$

where the values of the C's are such that any divergences of the form $\frac{1}{\epsilon^n}$ for n a positive integer arising from our dimensional regularization are cancelled and a finite prediction remains. Typically, the renormalization coefficients are defined as

$$Z_i \equiv (1 - C_i) \tag{2.90}$$

such that

$$\mathcal{L} = Z_\phi \frac{1}{2} \left(\partial_\mu \phi_0 \right)^2 - Z_\mu \frac{\mu_0^2}{2} \phi_0^2 - Z_\lambda \frac{\lambda_0}{4!} \phi_0^4, \tag{2.91}$$

and finally, renormalized fields and couplings are defined to be

$$\phi_R = Z_\phi^{1/2} \phi_0 \tag{2.92}$$

$$\mu_R = Z_\mu^{1/2} Z_\phi^{-1/2} \mu_0 \tag{2.93}$$

$$\lambda_R = Z_\lambda Z_\phi^{-2} \lambda_0. \tag{2.94}$$

This renormalization can be generalized in order to leverage the Feynman diagram formalism; counterterm diagrams associated with a loop divergence may be included in a calculation as shown in Figure 2.8. Although this formalism has been generalized to the fields and couplings of QCD, a detailed look at the renormalization of QCD is beyond the scope of this work, and

may be found in Ref. [42], for example.

Figure 2.8: An example of a counterterm contribution and its associated divergent diagram in a ϕ^4 self-energy.

In calculating correlation functions of currents, when confronted with divergences that cannot be renormalized with the inclusion of a Lagrangian counterterm (i.e., a non-local divergence [90]), a composite operator renormalization procedure must be applied to the constructed current, and operator mixing with appropriate lower-dimensional currents must be considered [48]. Recall that, in renormalizing the operators and parameters in a QFT, new fields and physical parameters were defined in terms of the bare fields and parameters and the necessary renormalization coefficients. In these cases, the integrals resulting from the Feynman diagrams in question contained overall divergences that could be subtracted. However, in forming local composite operators such as (2.40), we take the product of these renormalized fields. Unfortunately, constructing a composite operator as a product of renormalized fields does not mean the result will also be renormalized. If we consider our OPE (2.43),

$$\langle \mathcal{O}_1(x)\mathcal{O}_2(y)\rangle = \sum_n C_n(x - y)\langle \mathcal{O}_n(y)\rangle \tag{2.95}$$

$$= C_1(x - y)\langle \mathcal{O}_1(y)\rangle + C_2(x - y)\langle \mathcal{O}_2(y)\rangle + \dots,$$

we can imagine a product of two operators at x and y that are well-defined, but diverge as $x \to y$. This necessitates a formalism for renormalizing composite operators. Given some composite operator J, the renormalized operator (distinguished by square brackets) is

expressed formally as

$$[J] = \sum_A Z_{JA} A, \tag{2.96}$$

where A represent all possible unrenormalized composite operators that carry the same symmetries and quantum numbers as J. This describes operator mixing within the formalism of composite operator renormalization; as a general result, a composite operator J may mix with other composite operators A provided they have the same quantum numbers and carry dimension equal to or less than that of J [90]. This is directly tied to the renormalizability of the theory being considered; Z_{JA} in equation (2.96) must have dimensions $\dim(Z_{JA}) \geq 0$, and by dimensional analysis this implies that the currents A must have $\dim(A) \leq \dim(Z_{JA})$ [90]. These renormalized composite operators will generate additional diagrams that must be considered for a calculation to be finite. For example, consider a correlation function built from a renormalized vector current $[J_\mu] = Z_{J1} J_\mu + Z_{J2} \tilde{J}_\mu$,

$$\begin{aligned}
\langle \Omega | [J_\mu(x)] [J_\nu(0)]^\dagger | \Omega \rangle =& |Z_{J1}|^2 \langle \Omega | J_\mu J_\nu^\dagger | \Omega \rangle + |Z_{J2}|^2 \langle \Omega | \tilde{J}_\mu \tilde{J}_\nu^\dagger | \Omega \rangle \\
&+ Z_{J1} Z_{J2}^* \langle \Omega | J_\mu \tilde{J}_\nu^\dagger | \Omega \rangle + Z_{J1}^* Z_{J2} \langle \Omega | \tilde{J}_\mu J_\nu^\dagger | \Omega \rangle,
\end{aligned} \tag{2.97}$$

where $\tilde{J}_\mu$ is an operator that mixes with the composite operator in question J_μ. We see on the RHS of (2.97) that the complete renormalized calculation requires the consideration of off-diagonal correlation functions as well as a contribution from the diagonal correlator of $\tilde{J}_\mu$. The complete process has been done for some hybrid currents such as the light exotic vector hybrid meson [91], but as such calculations can be complex, in general limited results are available for other composite operators.

2.5 Mixing

While we have briefly discussed the mathematical necessity of operator mixing above in the context of renormalization, there is another important consideration of mixing distinct from the composite operator formalism discussed in Section 2.4. In Section 2.1.3.3, we reviewed how exotic J^{PC} are considered a clean signal of exotic structure beyond the conventional quark model, making these primary targets for observation by experiments such as GlueX

[25]. However, exotic hadrons can still be constructed with conventional quantum numbers. As with any quantum mechanical system, we must account for all possible outcomes, and, as such, we must consider quantum mechanical mixing between states carrying the same quantum numbers. Due to this mixing, a current with a particular set of J^{PC} may non-trivially probe other states carrying the same quantum numbers. For example, in the absence of mixing, for a hypothetical pure hybrid current $j_\mu^h(x)$ we would expect

$$\langle 0|j_\mu^h|h\rangle \neq 0 \tag{2.98}$$

$$\langle 0|j_\mu^h|c\rangle = 0, \tag{2.99}$$

where $|h\rangle$ represents some hybrid state and $|c\rangle$ represents a conventional state. When mixing occurs, the operator probes both states such that

$$\langle 0|j_\mu^h|h\rangle \neq 0 \tag{2.100}$$

$$\langle 0|j_\mu^h|c\rangle \neq 0. \tag{2.101}$$

Within the framework of QCDSR, by generalizing our resonance plus continuum model (2.64) to a distributed resonance model, we can consider mixing between states that are widely-separated. A variety of mixing models may be tested to discern what best characterizes the hadronic mixing; available options include a square wave (or a single wide resonance)

$$\rho^{\text{had}}(t) = \frac{\pi f}{2m_H \Gamma} \left[\theta\left(t - m_H^2 + m_H \Gamma\right) - \theta\left(t - m_H^2 - m_H \Gamma\right) \right], \tag{2.102}$$

a double narrow resonance model,

$$\rho^{\text{had}}(t) = f_1^2 m_1^8 \delta(t - m_1^2) + f_2^2 m_2^8 \delta(t - m_2^2), \tag{2.103}$$

or some combination of the two, such as a wide plus narrow resonance model

$$\rho^{\text{had}}(t) = \frac{\pi f}{2m_1 \Gamma} \left[\theta\left(t - m_1^2 + m_1 \Gamma\right) - \theta\left(t - m_1^2 - m_1 \Gamma\right) \right] + f_2^2 m_2^8 \delta(t - m_2^2). \tag{2.104}$$

While it is possible to consider mixing within a LSR methodology [50], because of the suppression of higher energies characteristic of the LSRs, a GSR approach may be preferred when analyzing systems that exhibit mixing [9, 51] as GSRs treat the ground and excited state resonances with similar sensitivity.

Chapter 3

Heavy-Light Hybrids

3.1 Open-Flavour Hybrids

3.1.1 Motivation and Background

The previously discussed quarkonium-like light hybrid mesons carry flavour-paired constituent quarks ("closed" meson states due to symmetry in valence quark flavour content), giving some of them unique experimental signatures due to exotic J^{PC} combinations not seen in the conventional quark model spectrum. Because of the possibility of these clean experimental signals and their energetic accessibility, they have attracted much attention and study. Less-studied in the literature are states that bridge the spectrum between the light and the heavy quarkonium-like states, states that carry a flavour asymmetry in their valence quark content. We borrow the language found in previous studies of hybrid mesons with similar valence quark structure [92, 93], and call these open-flavour hybrid meson states.

The consequence of considering open-flavour hybrid meson states is that, because of the asymmetric flavour structure of the valence quarks, these states do not carry a well-defined charge-parity quantum number C. As such, to experimentally determine whether an observed open-flavour state is a conventional or hybrid meson, it is necessary to carefully identify the $\bar{q}q$ meson spectrum and determine theoretical predictions of any exotics carrying similar properties in the same mass range. An overpopulation of states observed in in the conventional meson spectrum would be a signal of other exotic states.

While the mass spectra of closed flavour hybrid meson states have been carefully investigated using a variety of methodologies [30, 64, 65, 94, 95], open flavour hybrid meson states have attracted considerably less attention. This is likely because of the relative difficulty in
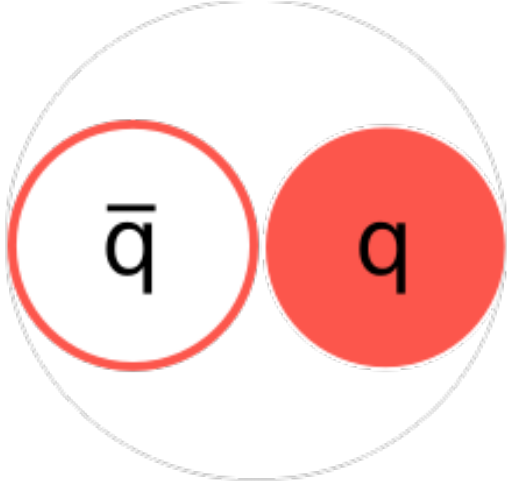
(a) Closed-flavour conventional meson structure
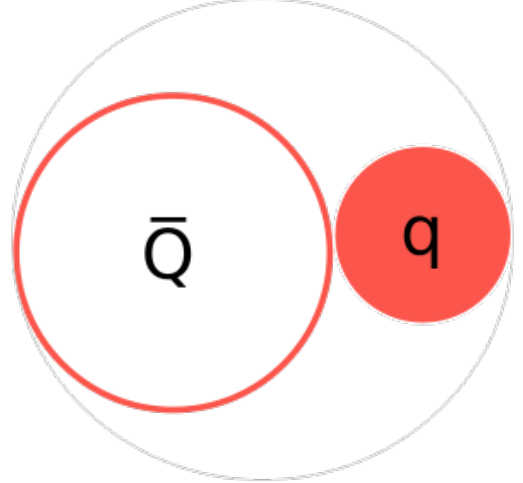
(b) Open-flavour conventional structure

experimentally observing these states. In contrast, the resources for experimental searches of hybrid mesons (both closed and open-flavour) are at an all-time high, with two experiments being of notable interest to our work. The first, GlueX, is currently searching for signals of light closed-flavour hybrid candidates [23]. The second experimental collaboration, PANDA, is currently under construction and aims to examine exotic states in the mass range containing open-charm and closed-charm conventional mesons, as well as provide a precision analysis of the conventional spectrum [26]. In anticipation of its launch and in awareness of the need for theoretical predictions to investigate the nature of exotics of open-flavour structure, we were motivated to pursue a systematic multi-channel analysis of heavy-strange and heavy-nonstrange hybrid mesons. In this way, we could not only provide mass predictions for the states in question, but multiplet structures as well.

In the process of calculating the open-flavour heavy-light spectrum, several aspects of the calculation came to our attention: consequences from calculating with composite operators, conventional J^P opening the door to meson-hybrid mixing, and the nature of distinct hadronic currents carrying identical J^P. My contributions to this work begin with the calculation of the multichannel correlation functions, forming the LSRs for each of the sixteen $J^{P(C)}$ (charm and bottom) channels, analysis of LSRs to extract mass predictions from each of the stable channels, performing the error analyses, and interpreting the overall results. In addition, I performed all of the mixing analysis, designed the figures, and I led in the writing and editing

of the final manuscript.

The following work may be found published in:

3.2 Manuscript: Masses of open-flavour heavy-light hybrids from QCD sum rules

Abstract: We use QCD Laplace sum-rules to predict masses of open-flavour heavy-light hybrids where one of the hybrids constituent quarks is a charm or bottom and the other is an up, down, or strange. We compute leading-order, diagonal correlation functions of several hybrid interpolating currents, taking into account QCD condensates up to dimension-six, and extract hybrid mass predictions for all $J^P \in \{0^\pm, 1^\pm\}$, as well as explore possible mixing effects with conventional quark-antiquark mesons. Within theoretical uncertainties, our results are consistent with a degeneracy between the heavy-nonstrange and heavy-strange hybrids in all J^P channels. We find a similar mass hierarchy of 1^+, 1^-, and 0^+ states (a 1^+ state lighter than essentially degenerate 1^- and 0^+ states) in both the charm and bottom sectors, and discuss an interpretation for the 0^- states. If conventional meson mixing is present the effect is an increase in the hybrid mass prediction, and we estimate an upper bound on this effect.

3.2.1 Introduction

Hybrids are hypothesized, beyond-the-quark-model hadrons that exhibit explicit quark, anti-quark, and gluonic degrees of freedom. They are colour singlets and so should be permissible within quantum chromodynamics (QCD); thus, the question of their existence provides us with a key test of our characterization of confinement. Despite nearly four decades of searching, hybrids have not yet been conclusively identified in experiment. There are, however, a number of noteworthy candidates. For example, the Particle Data Group (PDG) [2] lists a pair of tentative resonances, the $\pi_1(1400)$ and the $\pi_1(1600)$, both with exotic $J^{PC} = 1^{-+}$, a combination inaccessible to conventional quark-antiquark mesons [73, 94]. There are several non-exotic hybrid prospects as well. For instance, each of the resonances $\phi(2170)$, X(3872), Y(3940), and Y(4260) has been singled out as a possible hybrid or at least as a mixed hadron

containing a hybrid component [96, 97, 98, 99, 100, 101].

Definitively assigning a hybrid interpretation to an observed resonance would be greatly facilitated by agreement between theory and experiment concerning the candidate hybrid's mass. Previous calculations aimed at predicting hybrid masses have been made using a constituent gluon model [102], the MIT bag model [103, 104], and the flux tube model [46, 105, 106] as well as through the QCD-based approaches of QCD sum-rules [73, 77, 95, 100, 107, 108, 109, 110, 111, 112, 113, 114, 115, 116], lattice QCD [29, 117, 118, 119], and Heavy Quark Effective Theory [120]. Unfortunately, as of yet, there is little consensus concerning hybrid masses.

To date, closed-flavour (hidden-flavour or quarkonium) hybrids have received more attention than open-flavour hybrids likely because most promising hybrid candidates are closed. Furthermore, closed-flavour hybrids allow for exotic J^{PC} quantum numbers; open-flavour hybrids, on the other hand, are not eigenstates of C-parity, and so are characterized by non-exotic J^P quantum numbers. However, the recent observation of the fully-open-flavour X(5568) containing a heavy (bottom) quark [121, 122] may be a precursor to additional open-flavour discoveries that do not have a simple quark-model explanation (e.g., the X(5568) has been studied as a $\bar{b}\bar{d}su$ tetraquark [123]). Hence, computing masses of open hybrids containing heavy quarks is timely and of phenomenological relevance.

Ground state masses of bottom-charm hybrids were recently computed using QCD sum-rules in [93]; therefore, we focus on a QCD sum-rules analysis of open-flavour heavy-light hybrids i.e., hybrids containing one heavy quark (charm or bottom) and one light quark (up, down, or strange).

The seminal application of QCD Laplace sum-rules to open-flavour hybrids was performed by Govaerts, Reinders, and Weyers [124] (hereafter referred to as GRW). Therein, they considered four distinct currents covering $J \in \{0, 1\}$ in an effort to compute a comprehensive collection of hybrid masses. Their QCD correlator calculations took into account perturbation theory as well as mass-dimension-three (i.e., 3d) quark and 4d gluon condensate contributions. Precisely half of the analyses stabilized and yielded viable mass predictions. However, for all heavy-light hybrids, the ground state hybrid mass was uncomfortably close to the continuum threshold (with a typical separation of roughly 10 MeV), so that even a modest hadron width

would result in the resonance essentially merging with the continuum [124].

In this article, we extend the work of GRW by including both 5d mixed and 6d gluon condensate contributions in our correlator calculations. As noted in GRW, for open-flavour heavy-light hybrids, condensates involving light quarks could be enhanced by a heavy quark mass allowing for the possibility of a numerically significant contribution to the sum-rules. By this reasoning, the 5d mixed condensate should also be included. As for the 6d gluon condensate, recent sum-rules analyses of closed-flavour heavy hybrids [77, 100, 115, 116] have demonstrated that it is important and can have a stabilizing effect on what were, in the pioneering work [64, 125], unstable analyses. We also consider the possibility that conventional quark-antiquark mesons couple to the hybrid current, and demonstrate that this leads to an increase in the predicted value of the hybrid mass. A methodology is developed to estimate an upper bound on this mass increase in each channel.

This paper is organized as follows: in Section 3.2.2, we define the currents that we use to probe open-flavour heavy-light hybrids and compute corresponding correlation functions; in Section 3.2.3, we generate QCD sum-rules for each of the correlators; in Section 3.2.4, we present our analysis methodology as well as our mass predictions for those channels which stabilized; in Section 3.2.5 we consider the effects of mixing; and, in Section 3.2.6, we discuss our results and compare them to GRW and to contemporary predictions made using lattice QCD.

3.2.2   Currents and Correlators

Following GRW, we define open-flavour heavy-light hybrid interpolating currents

$$j_\mu = \frac{g_s}{2}\overline{Q}\Gamma^\rho\lambda^a q \mathcal{G}_{\mu\rho}^a \tag{3.1}$$

where g_s is the strong coupling and λ^a are the Gell-Mann matrices. The field Q represents a heavy charm or bottom quark with mass M_Q whereas q represents a light up, down, or strange quark with mass m_q. The Dirac matrix Γ^ρ satisfies

$$\Gamma^\rho \in \{\gamma^\rho, \gamma^\rho\gamma_5\}, \tag{3.2}$$

44

and the tensor $\mathcal{G}^a_{\mu\rho}$ satisfies

$$\mathcal{G}^a_{\mu\rho} \in \{G^a_{\mu\rho}, \tilde{G}^a_{\mu\rho}\} \tag{3.3}$$

where $G^a_{\mu\rho}$ is the gluon field strength and

$$\tilde{G}^a_{\mu\rho} = \frac{1}{2}\epsilon_{\mu\rho\nu\sigma}G^a_{\nu\sigma} \tag{3.4}$$

is its dual defined using the totally antisymmetric Levi-Civita symbol $\epsilon_{\mu\rho\nu\sigma}$.

For each of the four currents defined through (3.1)–(3.3), we consider a diagonal correlation function

$$\Pi_{\mu\nu}(q) = i \int \mathrm{d}^4x \, e^{iq\cdot x} \, \langle 0|\tau j_\mu(x)j^\dagger_\nu(0)|0\rangle \tag{3.5}$$

$$= \frac{q_\mu q_\nu}{q^2}\Pi^{(0)}(q^2) + \left(\frac{q_\mu q_\nu}{q^2} - g_{\mu\nu}\right)\Pi^{(1)}(q^2), \tag{3.6}$$

where $\Pi^{(0)}$ probes spin-0 states and $\Pi^{(1)}$ probes spin-1 states. Each of $\Pi^{(0)}$ and $\Pi^{(1)}$ couples to a particular parity value, and, in the case of closed-flavour hybrids, also to a particular C-parity value; however, as noted in Section 3.2.1, open-flavour hybrids are not C-parity eigenstates. Regardless, we will refer to $\Pi^{(0)}$ and $\Pi^{(1)}$ using the J^{PC} assignments they would have if we were investigating closed- rather than open-flavour hybrids. But, to stress that the C-value cannot be taken literally, we will enclose it in brackets (a notation employed in [31, 93]). In Table 3.1, we provide a breakdown of which currents couple to which $J^{P(C)}$ combinations.

Table 3.1: The $J^{P(C)}$ combinations probed through different choices of Γ^ρ (3.2) and $\mathcal{G}^a_{\mu\rho}$ (3.3).

Γ^ρ	$\mathcal{G}^a_{\mu\rho}$	$J^{P(C)}$
γ^ρ	$G^a_{\mu\rho}$	$0^{+(+)}, 1^{-(+)}$
γ^ρ	$\tilde{G}^a_{\mu\rho}$	$0^{-(+)}, 1^{+(+)}$
$\gamma^\rho\gamma_5$	$G^a_{\mu\rho}$	$0^{-(-)}, 1^{+(-)}$
$\gamma^\rho\gamma_5$	$\tilde{G}^a_{\mu\rho}$	$0^{+(-)}, 1^{-(-)}$

We calculate the correlators (3.5) within the operator product expansion (OPE) in which perturbation theory is supplemented by a collection of non-perturbative terms, each of which

is the product of a perturbatively computed Wilson coefficient and a non-zero vacuum expectation value (VEV) corresponding to a QCD condensate. We include condensates up to 6d:

$$\langle \bar{q}q \rangle = \langle \bar{q}_i^\alpha q_i^\alpha \rangle \tag{3.7}$$

$$\langle \alpha G^2 \rangle = \langle \alpha_s G_{\mu\nu}^a G_{\mu\nu}^a \rangle \tag{3.8}$$

$$\langle g\bar{q}\sigma Gq \rangle = \langle g_s \bar{q}_i^\alpha \sigma_{ij}^{\mu\nu} \lambda_{\alpha\beta}^a G_{\mu\nu}^a q_j^\beta \rangle \tag{3.9}$$

$$\langle g^3 G^3 \rangle = \langle g_s^3 f^{abc} G_{\mu\nu}^a G_{\nu\rho}^b G_{\rho\mu}^c \rangle\,, \tag{3.10}$$

respectively referred to as the 3d quark condensate, the 4d gluon condensate, the 5d mixed condensate, and the 6d gluon condensate. Superscripts on light quark fields are colour indices whereas subscripts are Dirac indices, and $\sigma^{\mu\nu} = \frac{i}{2}[\gamma^\mu, \gamma^\nu]$. The Wilson coefficients (including perturbation theory) are computed to leading-order (LO) in g_s using coordinate-space fixed-point gauge techniques (see [42, 126], for example). Note that LO contributions to (3.5) associated with 6d quark condensates are $\mathcal{O}(g_s^4)$; our calculation is actually $\mathcal{O}(g_s^3)$, and so 6d quark condensates have been excluded from (3.7)–(3.10). (In Ref. [77] the numerical effect of the 6d quark condensates has been shown to be small compared to the 6d gluon condensate). Light quark mass effects are included in perturbation theory through a next-to-leading-order light quark mass expansion, and at leading-order in all other OPE terms. The contributing Feynman diagrams are depicted in Figure 3.2[1] where we follow as closely as possible the labeling scheme of [95]. (Note that there is no Diagram IV in Figure 3.2 because, in [95], Diagram IV corresponds to an OPE contribution stemming from 6d quark condensates that is absent in the open-flavour heavy-light systems.) The $\overline{\text{MS}}$-scheme with the $D = 4 + 2\epsilon$ convention is used, and μ is the corresponding renormalization scale. We use the program TARCER [81], which implements the recurrence algorithm of [82, 83], to express each diagram in terms of a small collection of master integrals, all of which are well-known. Following [43], we employ a dimensionally regularized γ_5 that satisfies $\gamma_5^2 = 1$ and $\{\gamma_5, \gamma^\mu\} = 0$. Note that the imaginary parts of Diagrams I–III were actually first computed between [64] and GRW; for these three diagrams, we were able to successfully bench-mark

---

[1]All Feynman diagrams are drawn using JaxoDraw [6]

our results against that original work.

Diagram XII, a 5d mixed condensate contribution, generates some complications. Focusing on the lower portion of the diagram, we see a heavy quark propagator carrying momentum q multiplied by a divergent, one-loop sub-graph. Correspondingly, Diagram XII contributes to the correlator a non-local divergence proportional to

$$\frac{1}{(q^2 - M_Q^2)\epsilon}.$$ (3.11)

Following [97], this divergence is eliminated by renormalization of the composite operators (3.1) which induces mixing with either $\overline{Q}\gamma_\mu q$ or $\overline{Q}\gamma_\mu\gamma_5 q$. Specifically, for those operators with $\Gamma^\rho = \gamma^\rho$ (recall (3.2)), this mixing results in

$$j_\mu \to j_\mu + k\frac{M_Q^2\alpha_s}{\pi\epsilon}\overline{Q}\gamma_\mu q$$ (3.12)

whereas, for those with $\Gamma^\rho = \gamma^\rho\gamma_5$, we have

$$j_\mu \to j_\mu + k\frac{M_Q^2\alpha_s}{\pi\epsilon}\overline{Q}\gamma_\mu\gamma_5 q$$ (3.13)

where k is an as yet undetermined constant emerging from renormalization. For currents that mix according to (3.12), the VEV under the integral on the right-hand side of (3.5) gets modified as follows:

$$\langle 0|\tau j_\mu(x)j_\nu^\dagger(0)|0\rangle \to \langle 0|\tau j_\mu(x)j_\nu^\dagger(0)|0\rangle$$
$$+ k\frac{M_Q^2\alpha_s}{\pi\epsilon}\langle 0|\tau\overline{Q}(x)\gamma_\mu q(x)j_\nu^\dagger(0)|0\rangle + k^*\frac{M_Q^2\alpha_s}{\pi\epsilon}\langle 0|\tau j_\mu(x)\overline{q}(0)\gamma_\mu Q(0)|0\rangle \quad (3.14)$$

with an analogous expression for operators that mix according to (3.13). The first term on the right-hand side of (3.14) corresponds to the diagrams of Figure 3.2 whereas the last two terms give rise to new, renormalization-induced contributions to the OPE. Almost all of these new contributions are sub-leading in g_s, however, and so are ignored. The only exceptions are those containing the 5d mixed condensate (3.9); these give rise to the pair of diagrams depicted in Figure 3.3. Both of these tree-level diagrams contain a heavy quark propagator

47
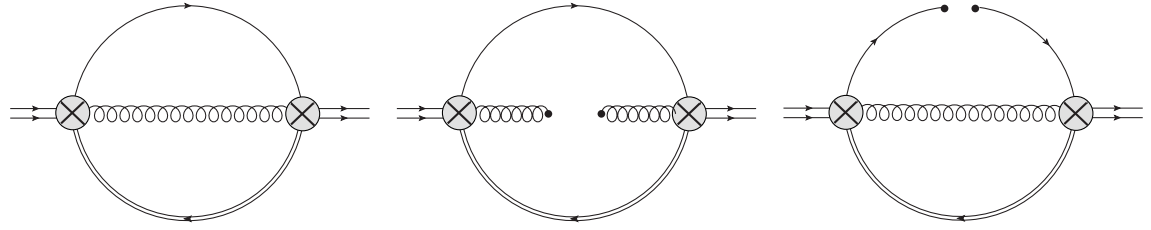
(a) Diagram I (LO perturbation theory)

(b) Diagram II (dimension-four)

(c) Diagram III (dimension-four)
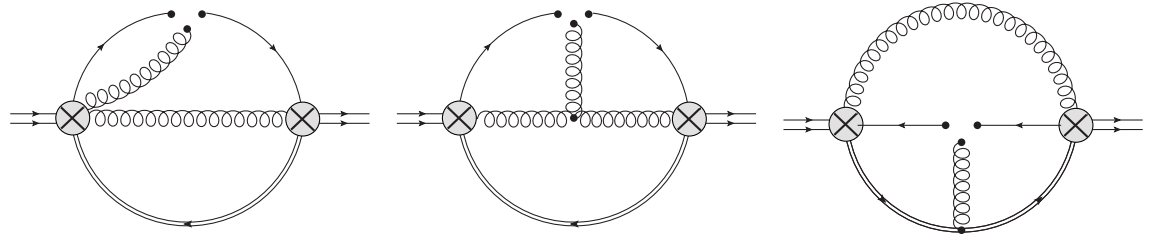
(d) Diagram VII (dimension-five)

(e) Diagram VIII (dimension-five)

(f) Diagram IX (dimension-five)
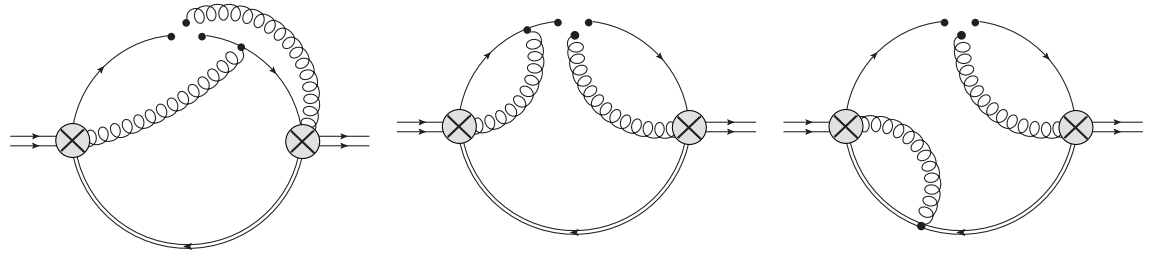
(g) Diagram X (dimension-five)

(h) Diagram XI (dimension-five)

(i) Diagram XII (dimension-five)
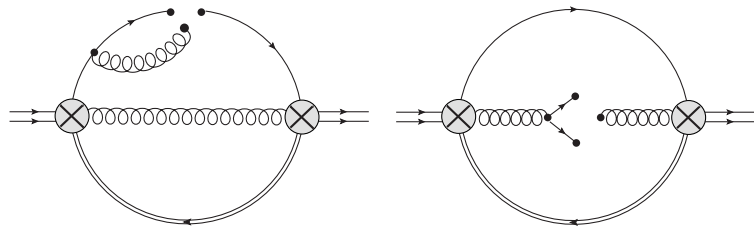
(j) Diagram XIII (dimension-five)

(k) Diagram XIV (dimension-five)

Figure 3.2: The Feynman diagrams calculated for the correlator (3.5). Single solid lines correspond to light quark propagators whereas double solid lines correspond to heavy quark propagators.

48

with momentum q and are multiplied by a factor of $\frac{1}{\epsilon}$ in (3.14), precisely what is needed to cancel the non-local divergence (3.11)
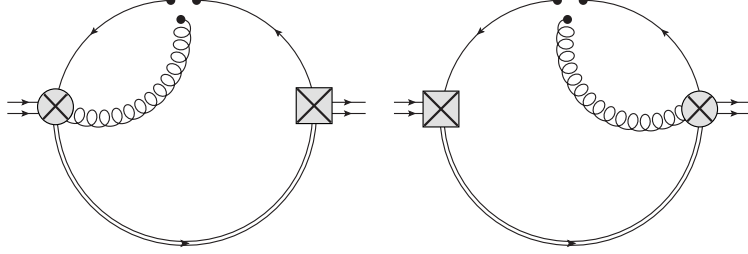
Figure 3.3: Renormalization-induced Feynman diagrams. Square insertion represents the mixing current.

Summing the diagrams from Figures 3.2 and 3.3, and then determining the constant k from (3.12) or (3.13) such that all non-local divergences are eliminated, we find for either $\Pi^{(0)}$ or $\Pi^{(1)}$ from (3.6) that

$$
\begin{aligned}
\Pi(q^2) = {} & \frac{M_Q^6 \alpha_s}{960\pi^3 z^2} \left[f_1^{(\text{pert})}(z) \log(1-z) + f_2^{(\text{pert})}(z) \text{Li}_2(z) + c^{(\text{pert})} z \right] \\
& + \frac{M_Q^5 m_q \alpha_s}{\pi^3 z^2} \left[f_1^{(m)}(z) \log(1-z) + f_2^{(m)}(z) \text{Li}_2(z) + c^{(m)} z \right] \\
& + \frac{M_Q^3 \alpha_s \langle \bar{q} q \rangle}{6\pi z^2} \left[f^{(qq)}(z) \log(1-z) + c^{(qq)} z \right] \\
& + \frac{M_Q^2 \langle \alpha G^2 \rangle}{144\pi z^2} \left[f^{(GG)}(z) \log(1-z) + c^{(GG)} z \right] \\
& + \frac{M_Q \alpha_s \langle g\bar{q}\sigma Gq \rangle}{3456\pi z^2} \left[f_1^{(qGq)}(z) \log(1-z) + f_2^{(qGq)}(z) \frac{z^2}{1-z} \log\left(\frac{M_Q^2}{\mu^2}\right) + f_3^{(qGq)}(z) \frac{z}{(1-z)} \right] \\
& + \frac{\langle g^3 G^3 \rangle}{192\pi^2 z^2} \left[f^{(GGG)}(z) \log(1-z) + c^{(GGG)} z \right]
\end{aligned}
$$

(3.15)

where

$$
z = \frac{q^2}{M_Q^2}
$$

(3.16)

and where $\text{Li}_2(z)$ is the dilogarithm function defined by

$$
\text{Li}_2(z) = \int_z^\infty \frac{\ln(1-t)}{t} \, dt.
$$

(3.17)

Table 3.2: The polynomials and constants of perturbation theory.

J	$f_1^{(\text{pert})}(z)$	$f_2^{(\text{pert})}(z)$	$c^{(\text{pert})}$
0	$-3 + 30z + 20z^2 - 60z^3 + 15z^4 - 2z^5$	$-60z^2$	-3
1	$-1 - 140z^2 + 100z^3 + 45z^4 - 4z^5$	$60z^2(1 + 2z)$	-1

Table 3.3: The polynomials and constants of the light quark mass correction to perturbation theory.

$J^{P(C)}$	$f_1^{(m)}(z)$	$f_2^{(m)}(z)$	$c^{(m)}$
$0^{+(+)}$	$3(1 - 6z + 18z^2 - 10z^3 - 3z^4)$	$-36z^3$	3
$0^{-(-)}$	$-3(1 - 6z + 18z^2 - 10z^3 - 3z^4)$	$36z^3$	-3
$0^{-(+)}$	$3(1 - 6z + 18z^2 - 10z^3 - 3z^4)$	$-36z^3$	3
$0^{+(-)}$	$-3(1 - 6z + 18z^2 - 10z^3 - 3z^4)$	$36z^3$	-3
$1^{+(+)}$	$1 - 6z + 18z^2 - 10z^3 - 3z^4$	$-12z^3$	1
$1^{-(-)}$	$-(1 - 6z + 18z^2 - 10z^3 - 3z^4)$	$12z^3$	-1
$1^{-(+)}$	$1 - 6z + 18z^2 - 10z^3 - 3z^4$	$-12z^3$	1
$1^{+(-)}$	$-(1 - 6z + 18z^2 - 10z^3 - 3z^4)$	$12z^3$	-1

The remaining quantities in (3.15) are listed in Tables 3.2–3.7 for the distinct $J^{P(C)}$ combinations under consideration. Also, in Table 3.8, we give the values determined for the renormalization parameter k. Finally, we note that, for the sake of brevity, we have omitted all polynomials in z corresponding to dispersion-relation subtractions from (3.15) and Tables 3.2 to 3.7. As discussed in Section 3.2.3, these subtraction constants do not contribute to the Laplace sum-rules.

Table 3.4: The polynomials and constants of the 3d quark condensate contribution.

$J^{P(C)}$	$f^{(qq)}(z)$	$c^{(qq)}$
$0^{+(+)}$	$-(1 - z)^3$	-1
$0^{-(-)}$	$(1 - z)^3$	1
$0^{-(+)}$	$-(1 - z)^3$	-1
$0^{+(-)}$	$(1 - z)^3$	1
$1^{+(+)}$	$-\frac{1}{3}(1 - z)^3$	$-\frac{1}{3}$
$1^{-(-)}$	$\frac{1}{3}(1 - z)^3$	$\frac{1}{3}$
$1^{-(+)}$	$-\frac{1}{3}(1 - z)^3$	$-\frac{1}{3}$
$1^{+(-)}$	$\frac{1}{3}(1 - z)^3$	$\frac{1}{3}$

Table 3.5: The polynomials and constants of the 4d gluon condensate contribution.

$J^{P(C)}$	$f^{(GG)}(z)$	$c^{(GG)}$
$0^{+(+)}$	$3(1-z)^2(1+2z)$	3
$0^{-(-)}$	$3(1-z)^2(1+2z)$	3
$0^{-(+)}$	$-3(1-z)^2(1+2z)$	-3
$0^{+(-)}$	$-3(1-z)^2(1+2z)$	-3
$1^{+(+)}$	$-(1-z)^2(1-4z)$	-1
$1^{-(-)}$	$-(1-z)^2(1-4z)$	-1
$1^{-(+)}$	$(1-z)^2(1-4z)$	1
$1^{+(-)}$	$(1-z)^2(1-4z)$	1

Table 3.6: The polynomials and constants of the 5d mixed condensate contribution.

$J^{P(C)}$	$f_1^{(qGq)}(z)$	$f_2^{(qGq)}(z)$	$f_3^{(qGq)}(z)$
$0^{+(+)}$	$18(1-z)(13+2z)$	$-36(17-z)$	$9(26+27z-21z^2)$
$0^{-(-)}$	$-18(1-z)(13+2z)$	$36(17-z)$	$-9(26+27z-21z^2)$
$0^{-(+)}$	$-18(1-z)(27+2z)$	$-36(7+z)$	$-3(162-351z+29z^2)$
$0^{+(-)}$	$18(1-z)(27+2z)$	$36(7+z)$	$3(162-351z+29z^2)$
$1^{+(+)}$	$-6(1-z)(27-38z)$	$12(21+19z)$	$-(162+369z+205z^2)$
$1^{-(-)}$	$6(1-z)(27-38z)$	$-12(21+19z)$	$162+369z+205z^2$
$1^{-(+)}$	$6(1-z)(13-38z)$	$12(51-19z)$	$78-999z+569z^2$
$1^{+(-)}$	$-6(1-z)(13-38z)$	$-12(51-19z)$	$-(78-999z+569z^2)$

Table 3.7: The polynomials and constants of the 6d gluon condensate contribution.

$J^{P(C)}$	$f^{(GGG)}(z)$	$c^{(GGG)}$
$0^{+(+)}$	-3	-3
$0^{-(-)}$	-3	-3
$0^{-(+)}$	3	3
$0^{+(-)}$	3	3
$1^{+(+)}$	$1-2z$	1
$1^{-(-)}$	$1-2z$	1
$1^{-(+)}$	$-(1-2z)$	-1
$1^{+(-)}$	$-(1-2z)$	-1

Table 3.8: The renormalization parameter k from (3.12) and (3.13).

$J^{P(C)}$	k
$0^{+(+)}$	$-\frac{2i}{3}$
$0^{-(-)}$	$-\frac{2i}{3}$
$0^{-(+)}$	$-\frac{1}{3}$
$0^{+(-)}$	$-\frac{1}{3}$
$1^{+(+)}$	$-\frac{5}{9}$
$1^{-(-)}$	$-\frac{5}{9}$
$1^{-(+)}$	$-\frac{4i}{9}$
$1^{+(-)}$	$-\frac{4i}{9}$

3.2.3 QCD Laplace Sum-Rules

Viewed as a function of Euclidean momentum $Q^2 = -q^2$, each of $\Pi^{(0)}$ and $\Pi^{(1)}$ from (3.6) satisfies a dispersion relation

$$\Pi(Q^2) = \frac{Q^8}{\pi} \int_{t_0}^{\infty} \frac{\mathrm{Im}\Pi(t)}{t^4(t + Q^2)} \, \mathrm{d}t + \cdots , \quad Q^2 > 0 \tag{3.18}$$

where $\cdots$ represents subtractions constants, collectively a third degree polynomial in Q^2, and t_0 represents the appropriate physical threshold. The quantity Π on the left-hand side of (3.18) is identified with the OPE result (3.15) while $\mathrm{Im}\Pi$ on the right-hand side of (3.18) is the hadronic spectral function. To eliminate the (generally unknown) subtraction constants and enhance the ground state contribution to the integral, the Borel transform

$$\hat{\mathcal{B}} = \lim_{\substack{N,Q^2 \to \infty \\ \tau = N/Q^2}} \frac{(-Q^2)^N}{\Gamma(N)} \left(\frac{d}{dQ^2} \right)^N \tag{3.19}$$

is applied to (3.18) weighted by $(-Q^2)^k$ for $k \geq 0$ to yield the kth-order Laplace sum-rule (LSR) [36, 37]

$$\mathcal{R}_k(\tau) = \int_{t_0}^{\infty} t^k e^{-t\tau} \frac{1}{\pi} \mathrm{Im}\Pi(t) \, \mathrm{d}t, \ \ \mathcal{R}_k(\tau) = \frac{1}{\tau} \hat{\mathcal{B}} \left\{ (-Q^2)^k \Pi(Q^2) \right\}. \tag{3.20}$$

The Borel transform annihilates polynomials in Q^2 which eliminates dispersion-relation subtraction constants and justifies our omission of polynomials (divergent or not) from (3.15). The exponential kernel on the right-hand side of (3.20) suppresses contributions from excited

resonances and the continuum relative to the ground state.

In a typical QCD sum-rules analysis, the hadronic spectral function is parametrized using a small number of hadronic quantities, predictions for which are then extracted using a fitting procedure. We employ the "single narrow resonance plus continuum" model [36, 37]

$$\frac{1}{\pi}\text{Im}\Pi(t) = f_H^2 m_H^8 \delta(t - m_H^2) + \theta(t - s_0)\frac{1}{\pi}\text{Im}\Pi^{\text{OPE}}(t) \tag{3.21}$$

where m_H is the ground state resonance mass, f_H is its coupling strength, θ is a Heaviside step function, s_0 is the continuum threshold and $\text{Im}\Pi^{\text{OPE}}$ is the imaginary part of the QCD expression for Π given in (3.15). Substituting (3.21) into (3.20) gives

$$\mathcal{R}_k(\tau) = f_H^2 m_H^{8+2k} e^{-m_H^2 \tau} + \int_{s_0}^{\infty} t^k e^{-t\tau} \frac{1}{\pi}\text{Im}\Pi^{\text{OPE}}(t)\mathrm{d}t, \tag{3.22}$$

and, defining continuum-subtracted LSRs by

$$\mathcal{R}_k(\tau, s_0) = \mathcal{R}_k(\tau) - \int_{s_0}^{\infty} t^k e^{-t\tau} \frac{1}{\pi}\text{Im}\Pi^{\text{OPE}}(t)\mathrm{d}t, \tag{3.23}$$

we find, between (3.22) and (3.23), the result

$$\mathcal{R}_k(\tau, s_0) = f_H^2 m_H^{8+2k} e^{-m_H^2 \tau}. \tag{3.24}$$

Finally, using (3.24), we obtain

$$\frac{\mathcal{R}_1(\tau, s_0)}{\mathcal{R}_0(\tau, s_0)} = m_H^2, \tag{3.25}$$

the central equation of our analysis methodology.

To develop an OPE expression for $\mathcal{R}_k(\tau, s_0)$, we exploit a relationship between the Borel transform and the inverse Laplace transform $\hat{\mathcal{L}}^{-1}$ [36, 37]

$$\frac{1}{\tau}\hat{\mathcal{B}}\left\{f(Q^2)\right\} = \hat{\mathcal{L}}^{-1}\left\{f(Q^2)\right\}$$
$$= \frac{1}{2\pi i}\int_{c-i\infty}^{c+i\infty} f(Q^2)e^{Q^2\tau}\mathrm{d}Q^2 \tag{3.26}$$

where c is chosen such that $f(Q^2)$ is analytic to the right of the integration contour in the

Table 3.9: The constants a and b from (3.27).

$J^{P(C)}$	a	b
$0^{+(+)}$	-18	9
$0^{-(-)}$	18	-9
$0^{-(+)}$	9	-15
$0^{+(-)}$	-9	15
$1^{+(+)}$	15	-23
$1^{-(-)}$	-15	23
$1^{-(+)}$	12	-11
$1^{+(-)}$	-12	11

complex Q^2-plane. Applying definitions (3.20) and (3.23) to (3.15) and using (3.26), it is straightforward to show that

$$\mathcal{R}_0(\tau,\,s_0) = M_Q^2 \int_1^{\frac{s_0}{M_Q^2}} e^{-xM_Q^2\tau} \frac{1}{\pi} \text{Im}\Pi^{\text{OPE}}(xM_Q^2)\,\mathrm{d}x$$
$$+ \frac{e^{-M_Q^2\tau} M_Q^3 \alpha_s \langle g\bar{q}\sigma Gq\rangle}{108\pi} \left[a \log\left(\frac{M_Q^2}{\mu^2}\right) + b\right] \quad (3.27)$$

and

$$\mathcal{R}_1(\tau,\,s_0) = -\frac{d}{d\tau}\mathcal{R}_0(\tau,\,s_0) \quad (3.28)$$

where a, b are constants given in Table 3.9 for each $J^{P(C)}$ combination under investigation. Note that the definite integral in (3.27) can be evaluated exactly; however, the result is rather long and not particularly illuminating, and so is omitted for brevity.

Renormalization-group (RG) improvement [127] dictates that the coupling constant and quark masses in (3.27) be replaced by their (one-loop, $\overline{\text{MS}}$) running counterparts. The running coupling is given by

$$\alpha_s(\mu) = \frac{\alpha_s(M_X)}{1 + \frac{1}{12\pi}(33 - 2N_F)\alpha_s(M_X)\log\left(\frac{\mu^2}{M_X^2}\right)} \quad (3.29)$$

where N_F is the number of active quark flavors and M_X is a reference scale for experimental values of α_s. In addition, the running heavy quark mass can be expressed as

$$M(\mu) = M(\overline{M})\left[\frac{\alpha_s(\mu)}{\alpha_s(\overline{M})}\right]^{\frac{12}{33-2N_f}} \quad (3.30)$$

where $\overline{M}$ is defined by $M(\overline{M}) = \overline{M}$, and the running light quark mass can be expressed as

$$m(\mu) = m(2 \text{ GeV}) \left[\frac{\alpha_s(\mu)}{\alpha_s(2 \text{ GeV})} \right]^{\frac{12}{33-2N_f}}, \tag{3.31}$$

in anticipation of using the Ref. [2] light-quark mass values at 2 GeV. For charm systems, we use the renormalization scale $\mu = \overline{M} = M_c$ while for bottom systems $\mu = \overline{M} = M_b$ with PDG values [2]

$$M_c = (1.275 \pm 0.025) \text{ GeV}, \ M_b = (4.18 \pm 0.03) \text{ GeV}. \tag{3.32}$$

We then evaluate α_s via (3.29) within the relevant flavour thresholds using appropriate Ref. [2] reference values at the τ and Z masses

$$\alpha_s(M_\tau) = 0.330 \pm 0.014, \ \alpha_s(M_Z) = 0.1185 \pm 0.0006. \tag{3.33}$$

Lastly, we use the following values for the light quark masses [2]

$$m_n(2 \text{ GeV}) = \frac{1}{2} \left[m_u(2 \text{ GeV}) + m_d(2 \text{ GeV}) \right] = (3.40 \pm 0.25) \text{ MeV}, \tag{3.34}$$

$$m_s(2 \text{ GeV}) = (93.5 \pm 2.5) \text{ MeV}. \tag{3.35}$$

The QCD predictions (3.15) have isospin symmetry because $\langle \bar{u}u \rangle = \langle \bar{d}d \rangle = \langle \bar{n}n \rangle$ and the subleading effect of nonstrange quark masses is negligible (i.e., we are effectively in the chiral limit for nonstrange systems).

In addition to specifying expressions for the running coupling and quark masses, we must also specify the numerical values of the condensates (3.7)–(3.10). Because of the form of (3.15), for $\langle \bar{q}q \rangle$ we consider the product

$$M\langle \bar{q}q \rangle = \left(\frac{M}{m} \right) \langle m\bar{q}q \rangle \tag{3.36}$$

as both $\frac{M}{m}$ and $\langle m\bar{q}q \rangle$ are RG-invariant quantities. From PCAC [57] (using Ref. [47] conven-

tions), we have

$$\langle m_n \bar{n} n \rangle = -\frac{1}{2} f_\pi^2 m_\pi^2 \tag{3.37}$$

$$\langle m_s \bar{s} s \rangle = -\frac{1}{2} f_K^2 m_K^2 \tag{3.38}$$

where PDG values are used for the meson masses [2] and the decay constants are [128]

$$f_\pi = 92.2 \pm 3.5 \text{ MeV} , \ f_K = 110.0 \pm 4.2 \text{ MeV}. \tag{3.39}$$

The quark mass ratios of strange to light and charm to strange quarks are given in [2]; however, in order to consider the RG-invariant product (3.36) for all open-flavor combinations of interest, we must combine results from [2] with bottom-flavoured ratios obtained on the lattice [129]. The resulting ratios and their errors (treated in quadrature) are

$$\frac{M_c}{m_n} = \left(\frac{M_c}{m_s}\right)\left(\frac{m_s}{m_n}\right) = 322.6 \pm 13.6, \qquad \frac{M_c}{m_s} = 11.73 \pm 0.25, \tag{3.40}$$

$$\frac{M_b}{m_n} = \left(\frac{M_b}{M_c}\right)\left(\frac{M_c}{m_n}\right) = 1460.7 \pm 64.0, \qquad \frac{M_b}{m_s} = 52.55 \pm 1.30. \tag{3.41}$$

For the purely gluonic condensates (3.8) and (3.10), we use values from [130, 131, 132]:

$$\langle \alpha G^2 \rangle = (0.075 \pm 0.020) \text{ GeV}^4 \tag{3.42}$$

$$\langle g^3 G^3 \rangle = \left((8.2 \pm 1.0) \text{ GeV}^2\right) \langle \alpha G^2 \rangle. \tag{3.43}$$

The 5d mixed condensate can be related to the 3d quark condensate through [109, 133, 132, 134]

$$\frac{\langle g \bar{q} \sigma G q \rangle}{\langle \bar{q} q \rangle} \equiv M_0^2 = (0.8 \pm 0.1) \text{ GeV}^2. \tag{3.44}$$

Because we are using (3.36) to specify the chiral-violating condensates, in the analysis below, the $\langle \bar{q} q \rangle$ effects are subsumed within dimension-four contributions and $\langle g \bar{q} \sigma G q \rangle$ effects within dimension-six contributions. As noted above, we choose the central value of the renormalization scale μ to be M_c for the charm systems and M_b for the bottom systems.

3.2.4 Analysis Methodology and Results

In order to extract stable mass predictions from the QCD sum-rule, we require a suitable range of values for our Borel scale (τ) within which our analysis can be considered reliable. Within this range, we perform a fitting (i.e., minimization) procedure to obtain an optimized value of the continuum onset (s_0) associated with our resulting mass prediction. We determine the bounds of our Borel scale by examining two conditions: the convergence of the OPE, and the pole contribution to the overall mass prediction, mirroring our previous work done in charmonium and bottomonium systems [77]. To enforce OPE convergence and obtain an upper-bound on our Borel window (τ_{max}), we require that contributions to the dimension-four condensate be less than one-third that of the perturbative contribution, and the dimension-six gluon condensate contribute less than one-third of the dimension-four condensate contributions. (See Figure 3.4 for an example.)

To determine a lower bound for our Borel window, we examine the pole contribution defined as

$$\text{PC}\left(s_0, \tau\right) = \frac{\int_{M_Q^2}^{s_0} e^{-t\tau} \text{Im}\Pi(t) \mathrm{d}t}{\int_{M_Q^2}^{\infty} e^{-t\tau} \text{Im}\Pi(t) \mathrm{d}t}. \tag{3.45}$$

The pole contribution constraint can also be understood as a suppression of excited state contributions. To extract a lower bound for our Borel window (τ_{min}), we must first provide a reasonable estimate of the continuum s_0 as a seed value for the minimization. To do this, we look for stability in the hadronic mass prediction as a function of s_0 with variations in τ (Figure 3.5).

We optimize the initial s_0 and m_H predictions by minimizing

$$\chi^2 = \sum_{i=1}^{20} \left(\frac{1}{m_H} \sqrt{\frac{\mathcal{R}_1(\tau_i, \, s_0)}{\mathcal{R}_0(\tau_i, \, s_0)}} - 1 \right)^2, \tag{3.46}$$

where we sum over an equally-spaced discretized τ range inside the Borel window.

Minimizing (3.46) results in an optimized values for the continuum s_0. Once s_0 is found, we may use (3.45) to determine a lower bound on τ by requiring a pole contribution of at least 10%. Note that this procedure involving (3.45) should be iterated to ensure that the values

of s_0 and τ_{min} are self-consistent. Once the hadronic mass prediction has been extracted, we may return to (3.24) to solve for the hybrid coupling from the τ critical point of f_H using the optimized continuum value and hadronic mass prediction.

We present results for the Borel window, continuum, and predicted hybrid mass and couplings for open-charm and open-bottom hybrids in Tables 3.10 through 3.13, and in Figs. 3.6 and 3.7. Channels that do not stabilize have been omitted from the tables. The errors presented encapsulate contributions added in quadrature from the heavy quark masses, quark mass ratios, α_s reference values, and the condensate values. We also include estimations of the error due to truncation of the OPE series by comparing mass predictions with and without 6d contributions and due to variations in the τ window of 10%. Uncertainties associated with the renormalization scale follow the methodology established in Ref. [135] which doubled the resulting uncertainty associated with variations in the renormalization scale of $\delta\mu = \pm 0.1\,\mathrm{GeV}$ (charm systems) and $\delta\mu = \pm 0.5\,\mathrm{GeV}$ (bottom systems).

Table 3.10: QCD sum-rules analysis results for ground state charm-nonstrange hybrids.

J^{PC}	$\tau_{\min}$ (GeV^{-2})	$\tau_{\max}$ (GeV^{-2})	$s_0 \pm \delta s_0$ (GeV^2)	$m_H \pm \delta m_H$ (GeV)	$f_H^2 \times 10^6$
$0^{+(+)}$	0.08	0.25	26.1 ± 6.0	4.55 ± 0.43	7.47
$0^{-(-)}$	0.07	0.17	31.8 ± 4.2	5.07 ± 0.31	7.28
$1^{-(-)}$	0.09	0.29	24.7 ± 2.5	4.40 ± 0.19	12.4
$1^{+(-)}$	0.15	0.35	14.7 ± 1.6	3.39 ± 0.18	9.87

Table 3.11: QCD sum-rules analysis results for ground state charm-strange hybrids.

J^{PC}	$\tau_{\min}$ (GeV^{-2})	$\tau_{\max}$ (GeV^{-2})	$s_0 \pm \delta s_0$ (GeV^2)	$m_H \pm \delta m_H$ (GeV)	$f_H^2 \times 10^6$
$0^{+(+)}$	0.08	0.24	25.2 ± 5.2	4.49 ± 0.40	7.36
$0^{-(-)}$	0.07	0.17	30.4 ± 5.2	4.98 ± 0.39	2.03
$1^{-(-)}$	0.10	0.30	23.1 ± 2.4	4.28 ± 0.19	11.0
$1^{+(-)}$	0.18	0.34	12.5 ± 1.1	3.15 ± 0.14	8.45

As a validation of our analysis, we also consider ratios of higher-weight sum-rules which serve as a generalization of (3.25):

$$\frac{\mathcal{R}_{k+1}(\tau,\, s_0)}{\mathcal{R}_k(\tau,\, s_0)} = m_H^2 \ . \tag{3.47}$$

In Table 3.14, Table 3.15 and Figure 3.8 we compare the nonstrange sum-rule ratios for

Table 3.12: QCD sum-rules analysis results for ground state bottom-nonstrange hybrids.

J^{PC}	$\tau_{\min}$ (GeV^{-2})	$\tau_{\max}$ (GeV^{-2})	$s_0 \pm \delta s_0$ (GeV^2)	$m_H \pm \delta m_H$ (GeV)	$f_H^2 \times 10^6$
$0^{+(+)}$	0.03	0.12	92.5 ± 15.6	8.57 ± 0.51	1.28
$0^{-(+)}$	0.05	0.09	59.1 ± 3.9	7.01 ± 0.21	0.516
$1^{-(-)}$	0.03	0.10	94.7 ± 7.5	8.74 ± 0.25	1.76
$1^{+(-)}$	0.03	0.14	86.7 ± 11.1	80.30 ± 0.41	1.66

Table 3.13: QCD sum-rules analysis results for ground state bottom-strange hybrids.

J^{PC}	$\tau_{\min}$ (GeV^{-2})	$\tau_{\max}$ (GeV^{-2})	$s_0 \pm \delta s_0$ (GeV^2)	$m_H \pm \delta m_H$ (GeV)	$f_H^2 \times 10^6$
$0^{+(+)}$	0.04	0.11	79.9 ± 13.0	8.14 ± 0.49	0.817
$0^{-(+)}$	0.06	0.10	55.1 ± 4.0	6.79 ± 0.22	0.434
$1^{-(-)}$	0.03	0.10	87.6 ± 9.9	8.46 ± 0.32	1.24
$1^{+(-)}$	0.04	0.15	81.7 ± 15.7	8.02 ± 0.59	1.39

$k = 0, 1, 2$. Although the higher-weight ratios have greater sensitivity to the high-energy region of the spectral function (excited states and QCD continuum), the hadronic mass scales emerging from the various weights are remarkably consistent, indicating that the sum-rule window has been well-chosen to emphasize the lightest hybrid state via the pole contribution criterion (3.45).

3.2.5 Mixing Effects

As noted in Section 3.2.1, the open-flavor structure of the hybrid systems in question precludes the possibility of explicitly exotic J^{PC} states. As such, we might expect a degree of mixing with conventional mesonic states. In our previous work on heavy quarkonium hybrids [77], this possibility of mixing was examined through the addition of a conventional meson to the

Table 3.14: Charm-Nonstrange Masses from Higher-Weight Sum-Rules (GeV)

$J^{P(C)}$	$\sqrt{\frac{R_1}{R_0}}$	$\sqrt{\frac{R_2}{R_1}}$	$\sqrt{\frac{R_3}{R_2}}$
$0^{+(+)}$	4.54	4.54	4.59
$0^{-(-)}$	5.07	5.07	5.12
$1^{-(-)}$	4.40	4.39	4.45
$1^{+(-)}$	3.39	3.39	3.45

Table 3.15: Bottom-Nonstrange Masses from Higher-Weight Sum-Rules (GeV)

$J^{P(C)}$	$\sqrt{\frac{R_1}{R_0}}$	$\sqrt{\frac{R_2}{R_1}}$	$\sqrt{\frac{R_3}{R_2}}$
$0^{+(+)}$	8.57	8.52	8.60
$0^{-(+)}$	7.01	7.01	7.06
$1^{-(-)}$	8.74	8.71	8.80
$1^{+(-)}$	80.30	8.20	8.29

single narrow resonance model (3.21) such that (3.24) becomes

$$\mathcal{R}_k(\tau,\, s_0) = f_H^2 m_H^{8+2k} e^{-m_H^2 \tau} + f_{conv}^2 m_{conv}^{8+2k} e^{-m_{conv}^2 \tau} \tag{3.48}$$

where the parameters f_{conv} and m_{conv} are the coupling constant and mass of the ground state conventional meson sharing the same J^P values. By including these terms, we can form a sum-rule coupled to the conventional state,

$$m_H^2 = \frac{\mathcal{R}_1(\tau,\, s_0) - f_{conv}^2 m_{conv}^{10} e^{-m_{conv}^2 \tau}}{\mathcal{R}_0(\tau,\, s_0) - f_{conv}^2 m_{conv}^8 e^{-m_{conv}^2 \tau}} \tag{3.49}$$

which can be used to investigate the dependence of the hybrid mass on the coupling to the conventional state by using known values of conventional meson masses to specify m_{conv}. We see in the resulting Figure 3.9 that increasing the coupling to the conventional state tends to increase the hybrid mass prediction, indicating our results presented here may correspond to a lower bound on the hybrid mass if mixing with conventional states is substantial. From Figure 3.9, we estimate an upper bound on the increased hybrid mass by implementing the condition that the coupling of the hybrid current to the conventional state f_{conv} be no more than half the coupling of the hybrid current to the hybrid state f_H (Tables 3.10 to 3.13). In the simplest mixing scenario this limit on f_{conv} corresponds to a mixing angle of approximately half that of a maximal mixing between conventional and hybrid mesons. The estimated effect of mixing on the hybrid mass prediction is summarized in Table 3.16, and shows interesting dependence on J^P.

Table 3.16: Effect on hybrid mass prediction from mixing with conventional meson states. Masses from Tables 3.10 to 3.13 are summarized with δm_{mix} expressing increased mass range with mixing up to $\left| \frac{f_{conv}}{f_H} \right| = \frac{1}{2}$ due to coupling to the lowest-lying conventional state with appropriate quantum numbers according to PDG [2]. Entries have been omitted where no conventional meson state has been tabulated.

Flavour	J^P	m_H (GeV)	PDG State	m_{conv}(GeV)	$+\delta m_{mix}$ (GeV)
Charm-nonstrange	0^+	4.54	$D_0^*(2400)^0$	2.318	0.02
	0^-	5.07	D^0	1.865	0.00
	1^-	4.40	$D^*(2007)^0$	2.007	0.01
	1^+	3.39	$D_1(2420)^0$	2.420	0.05
Charm-strange	0^+	4.49	$D_{s0}^*(2317)^\pm$	2.318	0.02
	0^-	4.98	$D_s^\pm$	1.969	0.00
	1^-	4.28	$D_s^{*\pm}$	2.112	0.02
	1^+	3.15	$D_{s1}(2460)^\pm$	2.460	0.06
Bottom-nonstrange	0^+	8.57	-	-	-
	0^-	7.01	B_0	5.279	0.19
	1^-	8.74	B^*	5.324	0.32
	1^+	80.30	$B_1(5721)^0$	5.726	0.74
Bottom-strange	0^+	8.14	-	-	-
	0^-	6.79	B_s^0	5.367	0.44
	1^-	8.46	B_s^*	5.416	0.35
	1^+	8.02	$B_{s1}(5830)^0$	5.828	0.72

Table 3.17: Comparison of central values against GRW mass predictions for $\bar{c}qG$ hybrids ($q = \{u, d\}$).

J^P	$m_{\mathrm{GRW}}(\mathrm{GeV})$	m_{H} (GeV)
0^+	4.0	4.54
0^-	4.5	5.07
1^-	3.6	4.40
1^+	3.4	3.39

3.2.6 Discussion

For each open-flavour heavy-light hybrid combination under consideration, we performed a LSRs analysis of all eight $J^{P(C)}$ combinations defined according to Table 3.1. As can be inferred from Tables 3.10–3.13 as well as Figure 3.7, half of the analyses stabilized; the other half did not. In particular, the $J^{P(C)} \in \{0^{+(+)}, 1^{-(-)}, 1^{+(-)}\}$ analyses were stable while the $J^{P(C)} \in \{0^{+(-)}, 1^{+(+)}, 1^{-(+)}\}$ were unstable. For charm-light hybrids, the $0^{-(-)}$ sector stabilized whereas the $0^{-(+)}$ sector did not. For bottom-light hybrids, this situation was reversed: the $0^{-(+)}$ sector stabilized while the $0^{-(-)}$ sector did not. This should be contrasted with GRW for which the stable channels were $J^{P(C)} \in \{0^{+(+)}, 0^{-(-)}, 1^{+(+)}, 1^{-(-)}\}$ for all heavy-light flavour hybrids. Comparing to GRW by truncating our additional condensate terms, we find that this change in stability originates from the addition of the 5d and 6d condensate terms. Note that, for all heavy-light quark combinations considered, we did arrive at a unique mass prediction for each J^P. GRW found something similar, but, as can be seen from Tables 3.17 and 3.18, the central value of our mass predictions differ significantly from that of GRW in all channels except the 1^+ charm-nonstrange. However, we note that GRW observed a change in the C value for currents that stabilized as the heavy quark mass increased, a feature shared in our analysis where the charm 0^{--} and bottom 0^{-+} channels stabilized.

In all stable channels, the most significant non-perturbative contribution to the LSRs is the 4d gluon condensate term of the OPE. At the corresponding optimized value of s_0 and over the Borel window indicated in Tables 3.10–3.13, the 4d gluon condensate term accounts for roughly 10–30% of the area underneath the $\mathcal{R}_0(\tau, s_0)$ curve. The second most significant contribution comes from the 3d quark condensate term which accounts for roughly 10% of

Table 3.18: Comparison of central values against GRW mass predictions for $\bar{b}qG$ hybrids ($q = \{u, d\}$).

J^P	m_{GRW}(GeV)	m_{H} (GeV)
0^+	6.8	8.57
0^-	7.7	7.01
1^-	6.7	8.74
1^+	6.5	8.26

the area while the 5d mixed and 6d gluon condensate contributions each account for $\lesssim 5\%$. Light quark mass corrections to massless perturbation theory are numerically insignificant leading to isospin invariance of our results.

The dominant contributions to the error in both the charm and bottom systems come from the gluon condensates, and the truncation of the OPE. All channels are relatively insensitive to uncertainties in the quark condensate, the heavy quark masses, the quark mass ratios, the reference values of α_s, and variations in the τ range and renormalization scales.

Within computational uncertainty, we cannot preclude degeneracy between the mass spectra of the heavy-nonstrange hybrid systems and their heavy-strange counterparts. (Compare Tables 3.10 and 3.11 as well as Tables 3.12 and 3.13. Also, see Figure 3.7.) This can be attributed to the small size of the light quark mass correction to massless perturbation theory and to the presence of a heavy quark mass factor as opposed to a light quark mass factor in the 3d quark and 5d mixed condensate contributions to the OPE.

Apart from the 0^- states, both the charm and bottom cases share a mass hierarchy pattern for the 1^+, 1^- and 0^+ states where the 1^+ state is lighter than essentially degenerate 1^- and 0^+ states. The 0^- states have different roles in the mass hierarchies in the charm and bottom sector, which we hypothesize as originating from the differing C quantum numbers associated with their currents. Although open-flavour systems do not have a well-defined C quantum number, Ref. [31] attributes physical meaning to C in the internal structures of hybrids and finds that the $0^{-(-)}$ structure is heavier than the $0^{-(+)}$, identical to the pattern we observe in Fig. 3.7.

In GRW, for each heavy-light hybrid channel whose LSR analysis was stable, the authors pointed out that the difference between the square of the predicted resonance mass and the continuum threshold parameter was small, typically a couple of hundred MeV which

did not seem to allow for much in the way of resonance width. In our updated analysis, Tables 3.10–3.13 shows that even a relatively wide resonance would be well-separated from the continuum.

We can compare our negative parity charm hybrid results to those computed on the lattice in [119]. In general, our predictions are heavier and show a larger mass splitting between states.

In summary, we have performed a QCD LSR analysis of spin-0,1, heavy-light open flavour hybrids. In the OPE, we included condensates up to dimension-six as well as leading-order light quark mass corrections to massless perturbation theory. For all flavour combinations, we extracted a single mass prediction for each $J^P \in \{0^\pm, 1^\pm\}$ (see Tables 3.10–3.13). Our results were isospin-invariant and within theoretical uncertainties, we could not preclude degeneracy under the exchange of light nonstrange and strange quarks. We find similar mass hierarchy patterns in the charm and bottom sectors for the $1^\pm$ and 0^+ states, and that Ref. [31] provides a natural interpretation for our 0^- mass predictions. Finally, given that open-flavour hybrids cannot take on exotic J^{PC}, mixing with conventional mesons could be important; our analysis suggests that such mixing would tend to increase the hybrid mass predictions, and we have estimated an upper bound on this effect.

Acknowledgments
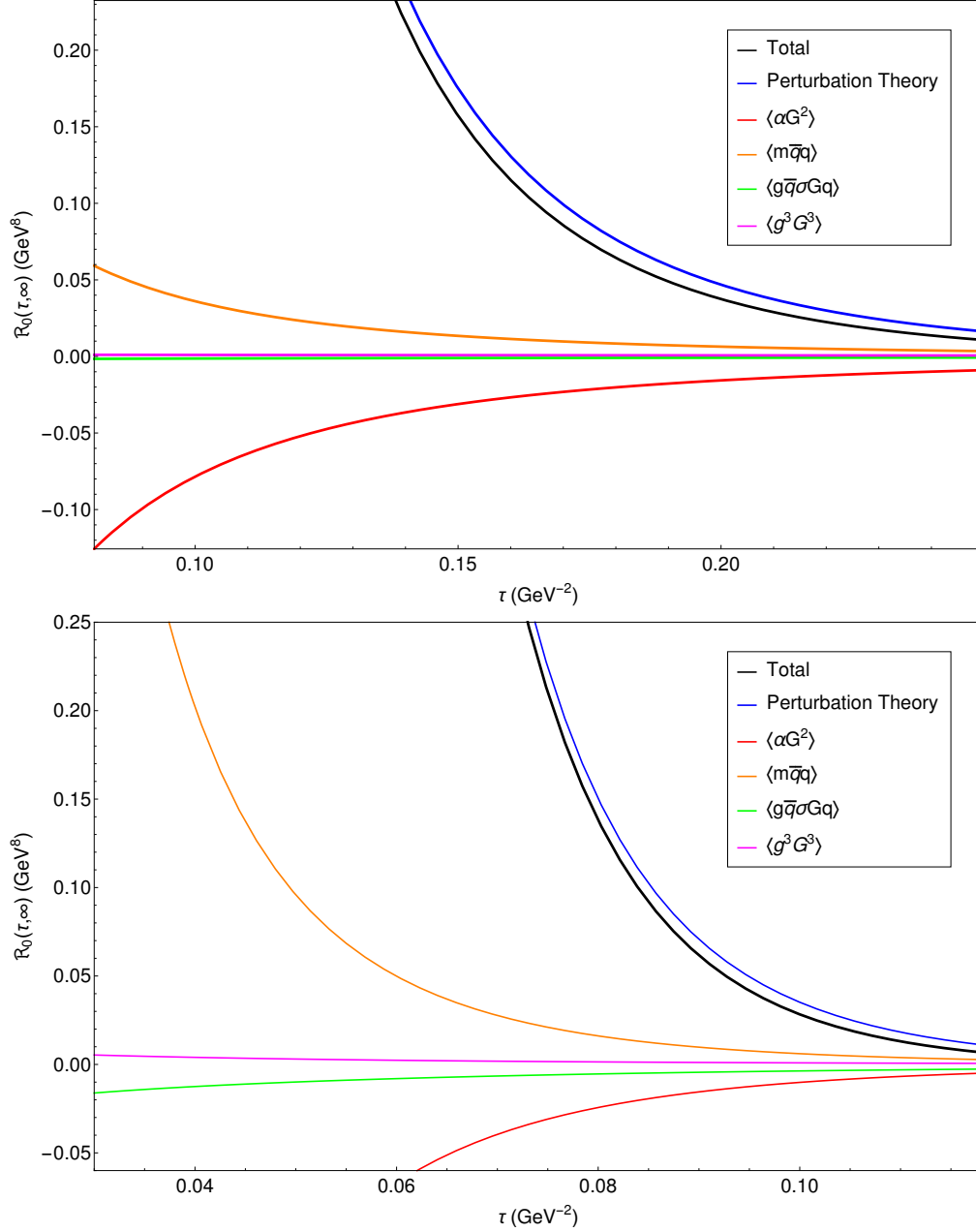
Figure 3.4: OPE convergence for $0^{+(+)}$ charm-nonstrange and bottom-nonstrange channels.
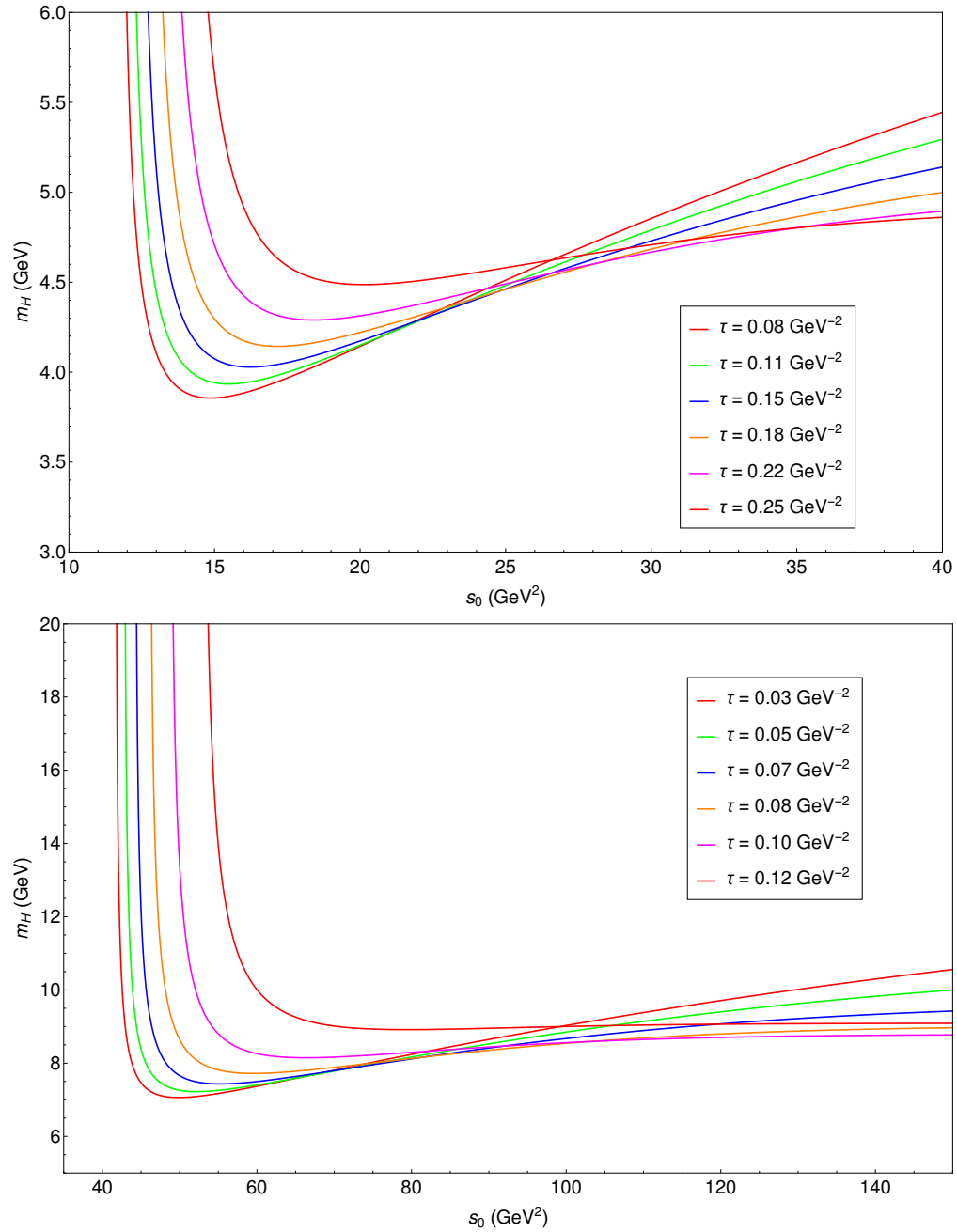
Figure 3.5: Plots of hybrid mass m_H as a function of continuum threshold s_0 for various values of the Borel parameter τ for $0^{+(+)}$ charm-nonstrange and bottom-nonstrange channels.
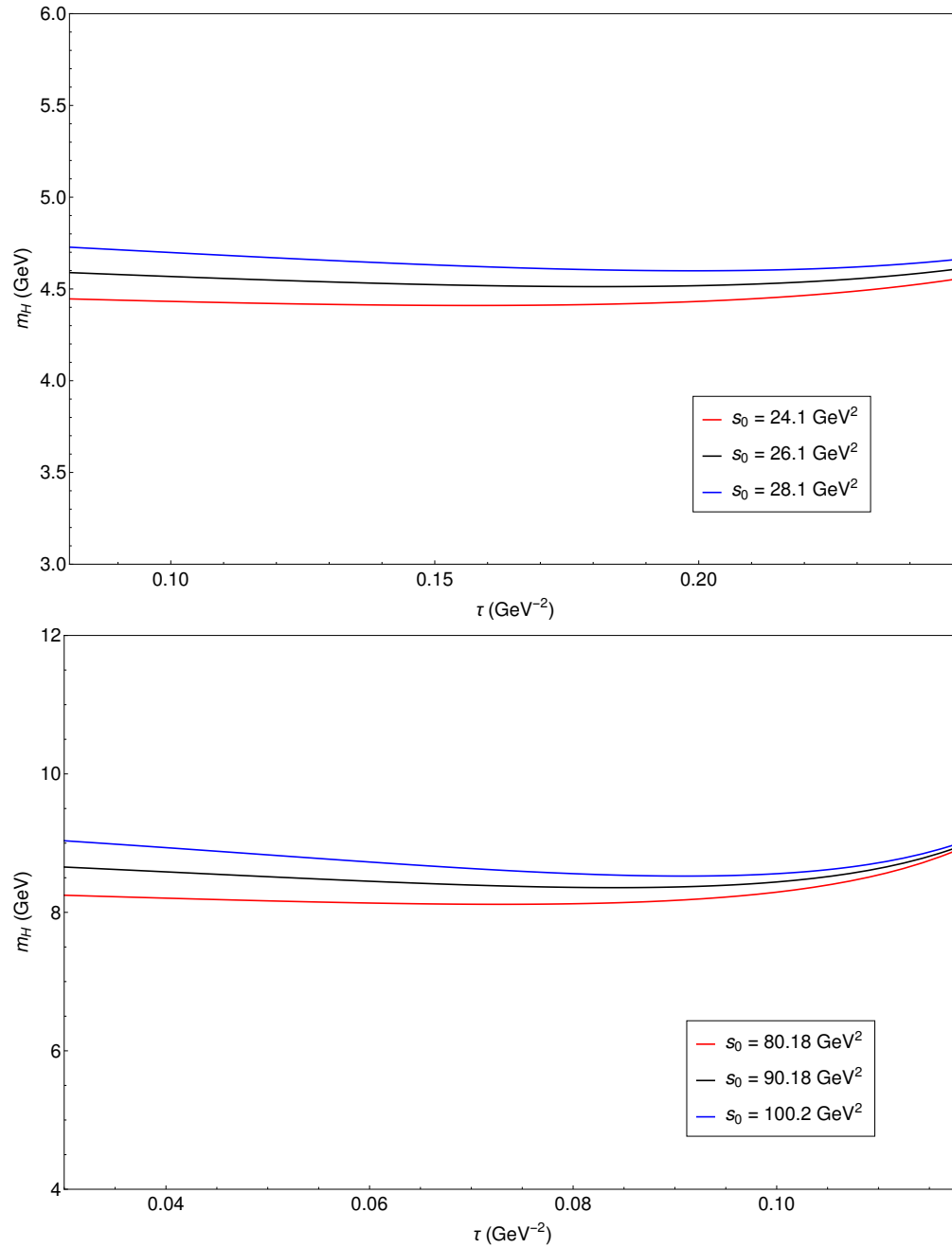
Figure 3.6: Plots illustrating the stability of mass predictions for $0^{+(+)}$ charm-nonstrange and bottom-nonstrange channels.
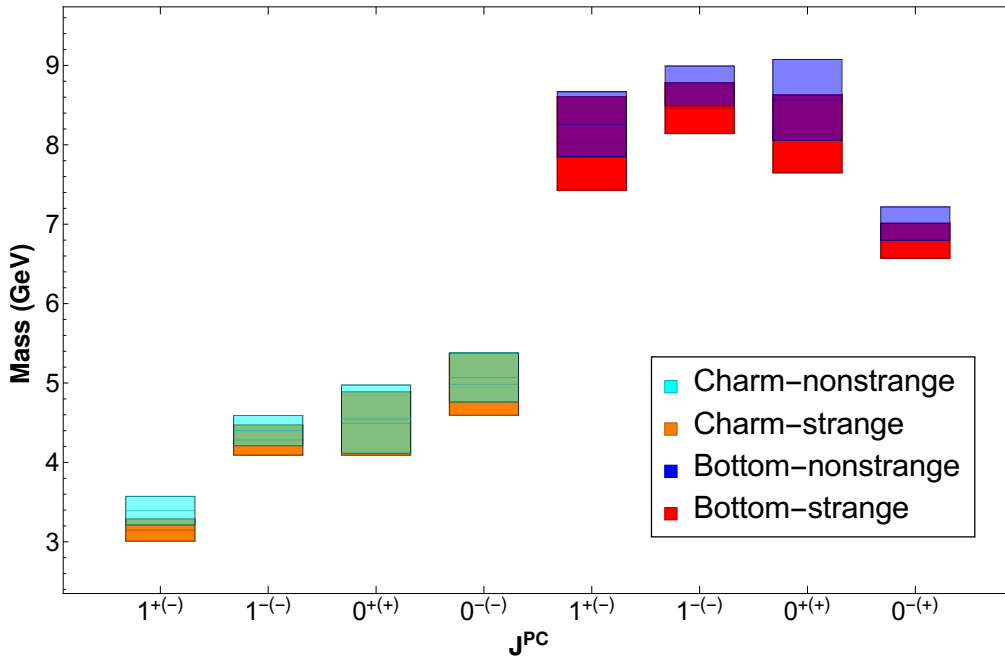
Figure 3.7: Summary of mass predictions in charm and bottom systems with uncertainties. The overlap between the heavy-nonstrange and heavy-strange predictions is denoted by the green tone in the charm sector and purple in the bottom sector.
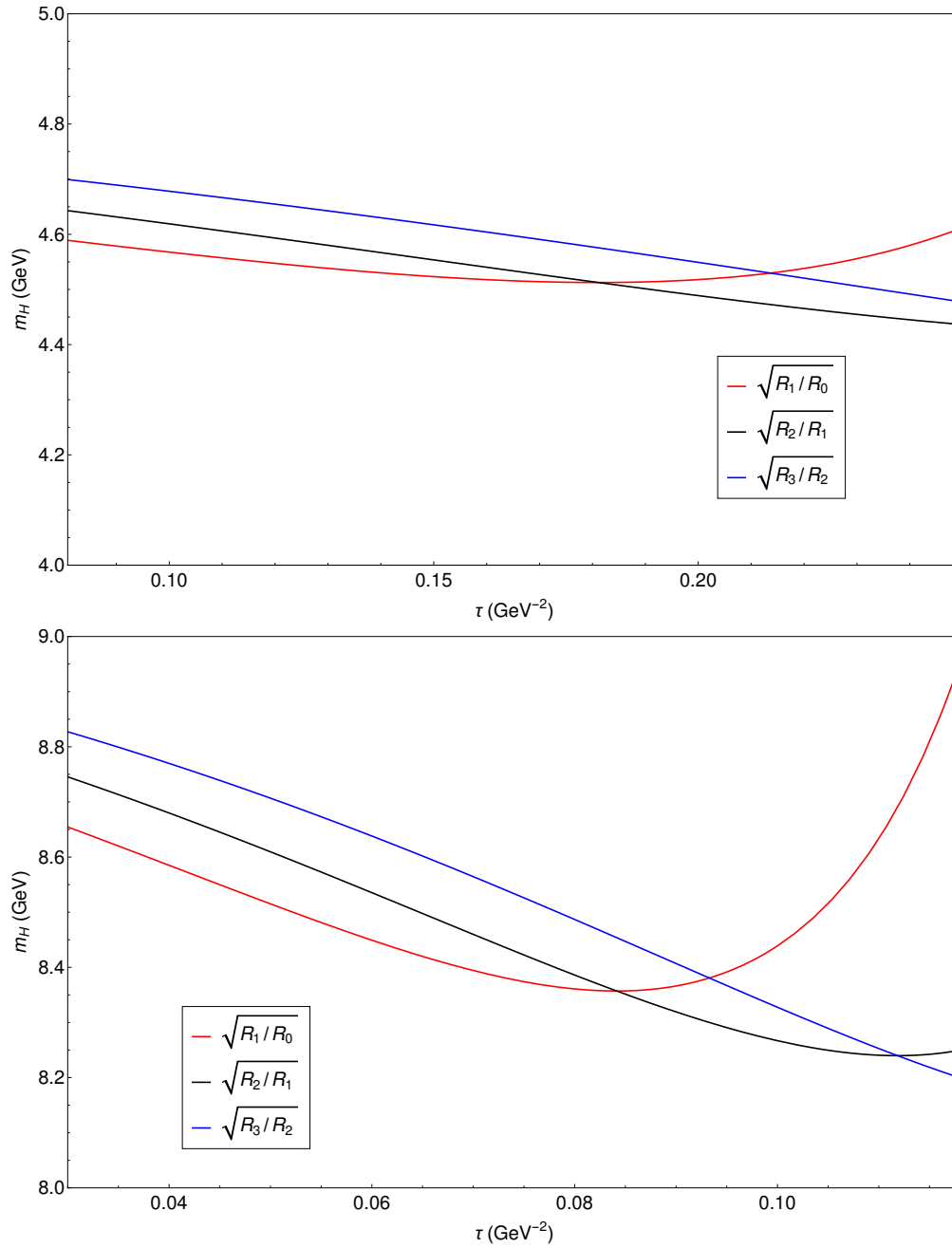
Figure 3.8: Plots illustrating higher-weight sum-rule ratios in $0^{+(+)}$ charm-nonstrange and bottom-nonstrange channels.
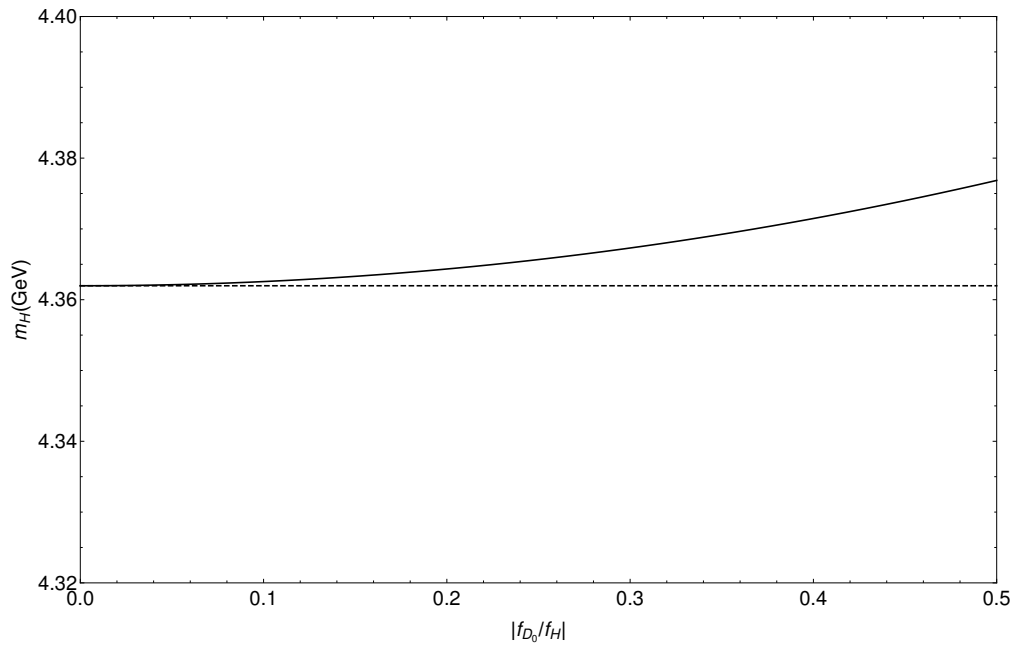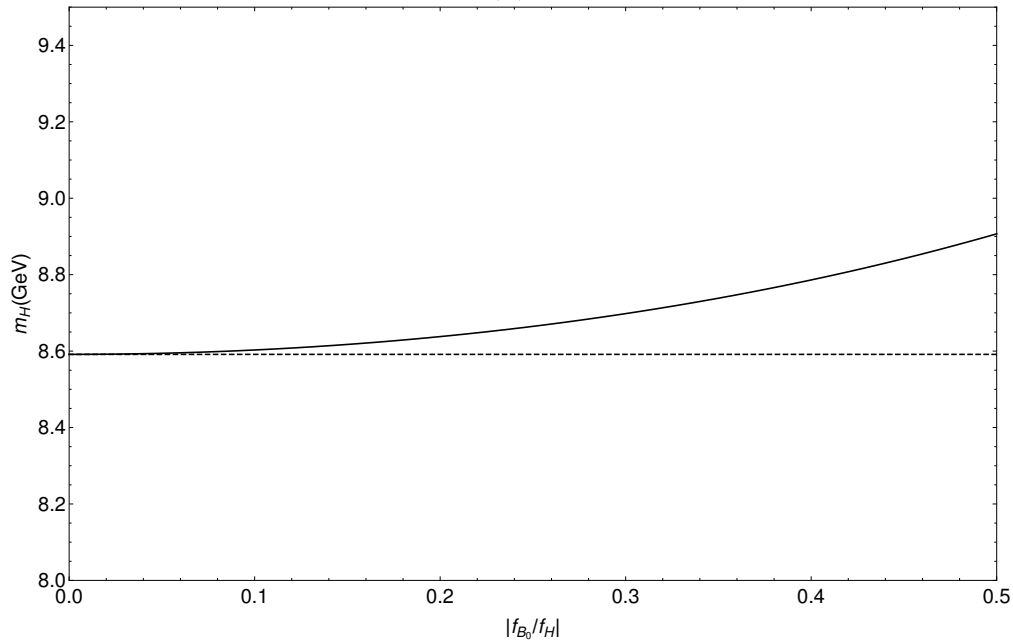
Figure 3.9: Dependence of hybrid mass m_H defined in (3.49) on the conventional state coupling constant f_{conv} for $1^{-(-)}$ (a) charm-nonstrange and (b) bottom-nonstrange states taken at the central τ values from Tables 3.10 and 3.12. Dashed lines indicate the mass prediction associated with the channel. An upper bound has been placed on the mixing effect by considering that the coupling of conventional states to the hybrid current is restricted to $\left| \frac{f_{conv}}{f_H} \right| \leq \frac{1}{2}$.

CHAPTER 4

LIGHT HYBRID MESONS

4.1 Light Hybrid Mesons

A considerable mountain of literature has been dedicated to the search for hybrid mesons, particularly those containing light valence quarks (i.e., up, down, or strange) [30, 64, 65, 95]. In general, matching an experimentally observed state to a phenomenological model requires the consideration of hadron mass, decay paths, resonance widths, and coupling strengths. However, the novel structure of hybrid mesons and multiquark states provides an additional possibility—exotic quantum numbers. These signals are unambiguous signs of hadronic structures not described within the conventional quark model. This is advantageous, particularly in the range of $\sim 1 - 2\,\mathrm{GeV}$ where (as we will discuss in Chapter 5) many resonances remain unidentified.

4.1.1 Exotic Light $J^{PC} = 0^{+-}$ Hybrid Meson

As reviewed in Section 2.1.3.3, exotic J^{PC} are phenomenologically exciting signals, pointing towards physics not described by the conventional quark model. Not only is the possibility of contamination through mixing greatly reduced, but exotic J^{PC} demands a novel hadron structure; only hybrid mesons and evenly-populated multiquarks may carry these distinct quantum numbers. A large body of predictions from QCD sum rules, lattice QCD, and other methodologies [94] supporting a light exotic vector hybrid meson with $J^{PC} = 1^{-+}$ existing between $1.5 - 1.8\,\mathrm{GeV}$ [94], and a broader multiplet structure is predicted from lattice QCD [30]. The 1^{-+} exotic hybrid is expected to be the lightest close-flavoured hybrid meson, but, while the theoretical literature is full of predictions around the properties of

the 1^{-+}, calculations on other exotic light hybrids has been sparse. In particular, the 0^{+-} light hybrid meson has been previously studied in the framework of QCD sum rules, but a stable analysis has only been found for higher-dimension currents using an estimate for the low-energy theorem [136, 137]. In an early analysis of the 0^{+-}, the authors noted that distributed resonance strength could help stabilize the analysis [136]; in GSRs, the weighting of the spectral function is distinct from the LSR approach, opening the possibility of a stable analysis. We explored a number of different distributed models, and found that a double-narrow resonance fit the QCDSR predictions best, predicting the masses of two hadronic states coupling to the hybrid current [51].

4.1.2 The $Y(2175)$ and exotic candidates

Without the constraint of exotic quantum numbers, identification of hadronic states beyond the conventional quark model becomes more complicated. In the case of conventional quantum numbers, it becomes possible for exotic states to mix with conventional states. Additionally, the mass spectrum must contend with the addition of radially excited states. Many observed resonances remain unidentified, waiting for more experimental data or more sophisticated analyses to untangle their nature. This is true throughout the energy spectrum; at low energies below $\sim 2\,\mathrm{GeV}$, an overpopulation of scalar mesons and long-predicted (but yet unidentified) gluonium states crowd the spectrum, and theoretical methods are challenged by the importance of non-perturbative dynamics at these scales. At higher energies above $2\,\mathrm{GeV}$, the XYZ resonances and their analogues begin to appear [16, 17]. While the conventional quark model is well-understood at these higher energies, and excited states are better identified than in the light domain, there still exists a multitude of states not explained by the conventional quark model yet to be identified. Some of these states have been confirmed as exotic four-quark states [20, 63], opening the door for exotic explanations of other members of these mysterious XYZ resonances. Though below the charmonium threshold, the $Y(2175)$ is among these unidentified states [138]. With production modes similar to the $Y(4260)$ [1, 138], it has been suggested to be similar in structure [139], which is favoured to be a charmonium hybrid candidate. The $J^{PC} = 1^{--}$ resonance carries conventional quantum numbers, and has been proposed as a hybrid meson, four-quark, or radially-excited strangeonium-like state, to

name a few [29, 96, 106, 124, 140, 141, 142, 143, 144, 145, 146, 147, 148, 149, 150, 151, 152]. Using a similar GSR methodology as for the 0^{+-} system, we investigated how the phenomenological inputs from experiment fit with the predictions from QCDSRs, and (assuming mixing with a hybrid state) to what degree the $Y(2175)$ coupled to a hybrid current [52]. We found that the $Y(2175)$ did not display a particularly strong hybrid character, and put bounds on the coupling to the hybrid current. My contributions to these works include the analysis of correlator and extraction of sum rule predictions, application of different models within GSR analysis and determination of best fits, the Hölder inequality derivation within GSRs, performing the error analyses, designing the figures, and writing & editing of both manuscripts.

The following works may be found published in:

> *Mass calculations of light quarkonium, exotic $J^{PC} = 0^{+-}$ hybrid mesons from Gaussian sum rules,*
> J. Ho, R. Berg, T.G. Steele, W. Chen, and D. Harnett Phys. Rev. D 98, 096020 doi:10.1103/PhysRevD.98.096020

and

> *Is the $Y(2175)$ a Strangeonium Hybrid Meson?,*
> J. Ho, R. Berg, T.G. Steele, W. Chen, and D. Harnett Phys. Rev. D 100, 034012 doi:10.1103/PhysRevD.100.034012

4.2 Manuscript: Mass Calculations of Light Quarkonium, Exotic $J^{PC} = 0^{+-}$ Hybrid Mesons from Gaussian Sum-Rules

Abstract: We extend previous calculations of leading-order correlation functions of spin-0 and spin-1 light quarkonium hybrids to include QCD condensates of dimensions five and six, with a view to improving the stability of QCD sum-rules analyses in previously unstable channels. Based on these calculations, prior analyses in the literature, and its experimental importance, we identify the exotic $J^{PC} = 0^{+-}$ channel as the most promising for detailed study. Using Gaussian sum rules constrained by the Hölder inequality, we calculate masses of light (nonstrange and strange) quarkonium hybrid mesons with $J^{PC} = 0^{+-}$. A model-independent analysis of the hadronic spectral function indicates that there is distributed resonance strength in this channel. Hence,

we study two hadronic models with distributed resonance strength: a single wide resonance model and a double narrow resonance model. The single wide resonance model is disfavored as it leads to an anomalously large resonance width (greater than 1 GeV). The double narrow resonance model yields excellent agreement between QCD and phenomenology: in both nonstrange and strange cases, we find hybrid masses of 2.60 GeV and 3.57 GeV.

4.2.1 Introduction

It has long been conjectured that hadrons could exist beyond the conventional quark model of quark-antiquark ($q\bar{q}$) mesons and three-quark (qqq, $\bar{q}\bar{q}\bar{q}$) baryons. In particular, colour-singlet hybrid mesons consisting of a quark, antiquark, and explicit gluonic degree of freedom have a long history [35]. While evidence of hadronic structures outside of the conventional model has been accumulating with experimental observations and confirmations of tetraquarks [63, 20, 19] and pentaquarks [21], an experimental confirmation of hybrid mesons has eluded observation. Designed to search for light hybrid mesons (particularly those with exotic J^{PC} that do not exist in the conventional quark model), the GlueX experiment at Jefferson Lab [25] is currently underway, and is anticipated to give crucial insight into the existence and structure of light hybrids.

The characterization of light hybrid states within the framework of QCD is important. Identifying the spectrum of the lightest hybrid supermultiplet ($J^{PC} \in \{1^{--}, (0, 1, 2)^{-+}\}$, where the $q\bar{q}$ are in an S-wave configuration) and the neighbouring larger supermultiplet ($J^{PC} \in \{0^{+-}, 1^{+-}, 2^{+-}, 3^{+-}, (0, 1, 2)^{++}\}$, where the $q\bar{q}$ are in a P-wave configuration) is of particular interest from an experimental perspective, and is aligned with the mandate of the GlueX experiment [25]. There have been numerous studies done on light quark hybrids covering a range of quantum numbers using QCD Laplace sum-rules (LSRs) [73, 91, 95, 107, 108, 109, 112, 136, 137, 153, 154, 155, 156, 157, 158, 159, 160], lattice QCD [29, 30], the Schwinger-Dyson formalism [92, 161, 162], the flux tube model [105, 106], and the MIT bag model [163, 104]. In particular, Reference [136] contains a comprehensive LSRs analysis of light hybrids for all J^{PC} with $J \in \{0, 1\}$ that takes into account condensates up to dimension four (i.e., 4d). Analyses of the 0^{++}, 0^{--}, 1^{++}, and 1^{--} sectors were stable; analyses of the 0^{+-}, 0^{-+}, 1^{+-}, and 1^{-+} sectors were unstable. Expected to be the lightest hybrid with exotic

quantum numbers, the 1^{-+} has been the subject of much additional study. Reference [95] contains a (error-free) 1^{-+} hybrid correlator that includes condensates up to 6d. By analyzing lower-weight LSRs than those used in [136], the authors arrived at a stable mass prediction. Subsequently, a variety of improvements (e.g., radiative corrections and higher dimension condensates) were included in the 1^{-+} hybrid correlator, and the LSRs analyses were updated accordingly [73, 91, 112, 157, 158, 159]. In the LSRs analysis of [137], a stable mass prediction for the 0^{-+} was found using a current different from that of [136]. The only stable LSRs analysis of the 0^{+-} channel [155] used higher-dimension currents and required estimation of the low-energy theorem term from other channels, introducing multiple sources of theoretical uncertainty. Thus, further QCD sum-rules studies of the 0^{+-} channel are necessary.

In [93, 100, 116, 164], it was found that the inclusion of higher-dimension condensates stabilized previously unstable LSRs analyses from [136] of hybrids containing heavy quarks. Therefore, in Section 4.2.2 we provide a systematic computation of leading-order (LO) 5d and 6d condensate contributions for all light quarkonium hybrids of spin-zero and spin-one. Unfortunately, as discussed in Section 4.2.3, these higher-dimension condensates do not stabilize the unstable light hybrid LSRs analyses as they do for heavy hybrids. However, in [136], it was proposed that the instability in the LSRs might be resolved by accounting for finite width effects, an issue also raised in [155]. As we show in Section 4.2.5, a model-independent analysis of the 0^{+-} hadronic spectral function indicates that there is distributed (as opposed to concentrated) resonance strength in this channel. To explore width effects and the possibility of excited states, we depart from previous LSRs methods. Gaussian sum-rules (GSRs) [75] are sensitive probes of width effects and both ground and excited states, and have been shown to be a powerful and versatile analysis methodology [9, 165, 166, 167]. In particular, the QCD sum-rules paradigm of the ρ meson was used to benchmark and validate these GSR methodologies [9]. Thus, in this article, we use GSRs to investigate the possibility of distributed resonance strength in the exotic 0^{+-} light hybrid channel.

In Section 4.2.2, we calculate LO spin-0 and spin-1 correlation functions of light quarkonium hybrid currents, including condensates up to 6d. Section 4.2.3 includes a review of the GSRs formalism, and a theoretical constraint on the GSRs based on the Hölder inequality is developed in Section 4.2.4. The GSRs analysis methodology and results for the 0^{+-} channel

are presented in Section 4.2.5 with concluding remarks in Section 4.2.6.

4.2.2 Hybrid Currents and Correlation Functions

To investigate light quarkonium hybrids, we use currents of the form

$$j_\mu = g_s \bar{q} \Gamma^\nu t^a \mathcal{G}^a_{\mu\nu} q, \tag{4.1}$$

where q is a light (nonstrange or strange) quark field and t^a are generators of the fundamental representation of SU(3). Each combination of $\mathcal{G}^a_{\mu\nu} \in \left\{ G^a_{\mu\nu}, \ \tilde{G}^a_{\mu\nu} = \frac{1}{2}\epsilon^{\mu\nu\rho\sigma} G^a_{\rho\sigma} \right\}$ and Dirac structure Γ^ν together corresponds to particular values of J^{PC} [95, 136]; these combinations are summarized in Table 4.1.

Γ^ν	$\mathcal{G}^a_{\mu\nu}$	J^{PC}
γ^ν	$G^a_{\mu\nu}$	0^{++}, 1^{-+}
γ^ν	$\tilde{G}^a_{\mu\nu}$	0^{-+}, 1^{++}
$\gamma^\nu\gamma_5$	$G^a_{\mu\nu}$	0^{--}, 1^{+-}
$\gamma^\nu\gamma_5$	$\tilde{G}^a_{\mu\nu}$	0^{+-}, 1^{--}

Table 4.1: The J^{PC} combinations probed through different choices of Γ^ν and $\mathcal{G}^a_{\mu\nu}$ in (4.1).

For each current (4.1), we calculate and decompose a diagonal correlation function as follows:

$$\Pi_{\mu\nu}(q) = i \int d^4x \, e^{iq\cdot x} \, \langle 0| \tau j_\mu(x) j_\nu^\dagger(0)|0\rangle \tag{4.2}$$

$$= \frac{q_\mu q_\nu}{q^2} \Pi^{(0)}(q^2) + \left(\frac{q_\mu q_\nu}{q^2} - g_{\mu\nu} \right) \Pi^{(1)}(q^2) \tag{4.3}$$

where $\Pi^{(0)}$ probes spin-0 states and $\Pi^{(1)}$ probes spin-1 states.

The calculation of (4.2) is performed in the framework of the operator product expansion (OPE),

$$\langle \Omega | \tau \left\{ \mathcal{O}(x)\mathcal{O}(0) \right\} |\Omega\rangle = \sum_n C_n(x)\langle \Omega | :\mathcal{O}_n(0): |\Omega\rangle. \tag{4.4}$$

In (4.4), the vacuum expectation value (VEV) of a time-ordered, non-local product of com-

posite operators is expanded in a series, each term of which is a product of a perturbative Wilson coefficient $C_n(x)$ and a nonzero VEV of a local composite operator $\mathcal{O}_n(0)$, i.e., a condensate. The condensates parameterize the nonperturbative nature of the QCD vacuum, and we include in our correlator calculations the following set:

$$\langle \bar{q}q \rangle = \langle \bar{q}_i^\alpha q_i^\alpha \rangle \tag{4.5}$$

$$\langle \alpha G^2 \rangle = \langle \alpha_s G_{\mu\nu}^a G_{\mu\nu}^a \rangle \tag{4.6}$$

$$\langle g\bar{q}\sigma Gq \rangle = \langle g_s \bar{q}_i^\alpha \sigma_{ij}^{\mu\nu} \lambda_{\alpha\beta}^a G_{\mu\nu}^a q_j^\beta \rangle \tag{4.7}$$

$$\langle g^3 G^3 \rangle = \langle g_s^3 f^{abc} G_{\mu\nu}^a G_{\nu\rho}^b G_{\rho\mu}^c \rangle \tag{4.8}$$

$$\langle \bar{q}q\bar{q}q \rangle = \langle \bar{q}_i^\alpha q_i^\alpha \bar{q}_j^\beta q_j^\beta \rangle, \tag{4.9}$$

respectively the 3d quark condensate, the 4d gluon condensate, the 5d mixed condensate, the 6d gluon condensate, and the 6d quark condensate. In (4.5)–(4.9), superscripts on quark fields are colour indices whereas subscripts are Dirac indices and $\sigma^{\mu\nu} = \frac{i}{2}[\gamma^\mu, \gamma^\nu]$. Regarding Wilson coefficients, we consider LO calculations in α_s, and we compute $\mathcal{O}(m^2)$ light quark mass corrections to perturbation theory as a way to distinguish between the nonstrange- and strange-flavored cases, similar to [49]. Also, the values of (4.5), (4.7), and (4.9) depend on whether the light quarks are nonstrange or strange. The diagrams representative of the correlation function calculation are displayed in Figure 4.1.

We use dimensional regularization in $D = 4 + 2\epsilon$ dimensions at $\overline{\text{MS}}$ renormalization scale μ. The program TARCER [168] is utilized to reduce the resulting integrals to a selection of well-known master integrals using the Tarasov recurrence relations [82, 83].

All of the correlators defined between (4.1) and Table 4.1 can be written in general as

(a) Diagram I (LO perturbation theory)

(b) Diagram II (dimension-three)

(c) Diagram III (dimension-four)

(d) Diagram IV (dimension-six)

(e) Diagram V (dimension-six)

(f) Diagram VI (dimension-six)

(g) Diagram VII (dimension-five)

(h) Diagram VIII (dimension-five)

(i) Diagram IX (dimension-five)

(j) Diagram X (dimension-five)

(k) Diagram XI (dimension-five)

(l) Diagram XII (dimension-five)

(m) Diagram XIII (dimension-five)

(n) Diagram XIV (dimension-five)

Figure 4.1: The Feynman diagrams calculated for the correlator (4.2). Feynman diagrams were created using JaxoDraw [6].

$$\Pi\left(q^2\right) = \alpha_s \left(A_1 q^6 + A_2 m^2 q^4\right) \left\{\log\left(\frac{-q^2}{\mu^2}\right) + \frac{1}{2\epsilon}\right\}$$

$$+ \left(A_4 q^2 \langle \alpha G^2 \rangle + \alpha_s (A_3 q^2 m \langle \bar{q} q \rangle + A_5 \langle \bar{q} q \rangle^2 + A_6 \langle g^3 G^3 \rangle + A_7 m \langle g \bar{q} \sigma G q \rangle)\right)$$

$$\times \left\{\log\left(\frac{-q^2}{\mu^2}\right) + \frac{1}{\epsilon}\right\} \qquad (4.10)$$

$$+ \alpha_s \left(B_1 q^6 + B_2 m^2 q^4 + B_3 q^2 m \langle \bar{q} q \rangle + B_4 q^2 \langle \alpha G^2 \rangle\right.$$

$$\left. + B_5 \langle \bar{q} q \rangle^2 + B_6 \langle g^3 G^3 \rangle + B_7 m \langle g \bar{q} \sigma G q \rangle\right)$$

where we have suppressed the superscript (J) on the left-hand side. The coefficients A_i and B_j contained in (4.10) are given in Tables 4.2 and 4.3 respectively. We note that, as Diagram IV has no loops, A_5 is trivially zero. In all channels, perturbation theory, the 3d quark condensate term, and the 4d gluon condensate term were benchmarked against [136]. The 0^{--} and 1^{-+} correlators were benchmarked against [95].

Table 4.2: Coefficients of the logarithmic and divergent terms of the perturbative and condensate contributions to the correlation function (4.10) for the J^{PC} summarized in Table 4.1.

	0^{++}	1^{-+}	0^{--}	1^{+-}	0^{-+}	1^{++}	0^{+-}	1^{--}
A_1	$-\frac{1}{480\pi^3}$	$-\frac{1}{240\pi^3}$	$-\frac{1}{480\pi^3}$	$-\frac{1}{240\pi^3}$	$-\frac{1}{480\pi^3}$	$-\frac{1}{240\pi^3}$	$-\frac{1}{480\pi^3}$	$-\frac{1}{240\pi^3}$
A_2	0	$\frac{1}{12\pi^3}$	$\frac{1}{16\pi^3}$	$\frac{5}{48\pi^3}$	0	$\frac{1}{12\pi^3}$	$\frac{1}{16\pi^3}$	$\frac{5}{48\pi^3}$
A_3	$\frac{1}{3\pi}$	$-\frac{2}{9\pi}$	$-\frac{1}{3\pi}$	$-\frac{4}{9\pi}$	$\frac{1}{3\pi}$	$-\frac{2}{9\pi}$	$-\frac{1}{3\pi}$	$-\frac{4}{9\pi}$
A_4	$\frac{1}{24\pi}$	$-\frac{1}{36\pi}$	$\frac{1}{24\pi}$	$-\frac{1}{36\pi}$	$-\frac{1}{24\pi}$	$\frac{1}{36\pi}$	$-\frac{1}{24\pi}$	$\frac{1}{36\pi}$
A_5	0	0	0	0	0	0	0	0
A_6	0	0	0	0	0	0	0	0
A_7	$\frac{1}{9\pi}$	0	$\frac{11}{72\pi}$	$-\frac{19}{72\pi}$	$-\frac{1}{9\pi}$	0	$-\frac{11}{72\pi}$	$\frac{19}{72\pi}$

4.2.3   QCD Sum Rules

Each function $\Pi^{(J)}(q^2)$ defined in (4.3) satisfies a dispersion relation at Euclidean momentum $Q^2 = -q^2 > 0$,

$$\Pi\left(Q^2\right) = Q^8 \int_{t_0}^{\infty} \frac{\frac{1}{\pi}\text{Im}\Pi(t)}{t^4 (t + Q^2)} \, dt + \cdots, \qquad (4.11)$$

Table 4.3: Coefficients of the finite terms of the perturbative and condensate contributions to the correlation function (4.10) for the J^{PC} summarized in Table 4.1.

	0^{++}	1^{-+}	0^{--}	1^{+-}	0^{-+}	1^{++}	0^{+-}	1^{--}
B_1	$\frac{97}{19200\pi^3}$	$\frac{39}{3200\pi^3}$	$\frac{97}{19200\pi^3}$	$\frac{39}{3200\pi^3}$	$\frac{19}{6400\pi^3}$	$\frac{77}{9600\pi^3}$	$\frac{19}{6400\pi^3}$	$\frac{77}{9600\pi^3}$
B_2	$\frac{1}{32\pi^3}$	$-\frac{7}{32\pi^3}$	$-\frac{55}{384\pi^3}$	$-\frac{109}{384\pi^3}$	$\frac{1}{32\pi^3}$	$-\frac{13}{96\pi^3}$	$-\frac{31}{384\pi^3}$	$-\frac{23}{128\pi^3}$
B_3	$-\frac{1}{2\pi}$	$\frac{7}{27\pi}$	$\frac{1}{6\pi}$	$\frac{17}{27\pi}$	$\frac{1}{6\pi}$	$-\frac{5}{27\pi}$	$-\frac{1}{2\pi}$	$-\frac{7}{27\pi}$
B_4	$-\frac{13}{144\pi}$	$\frac{11}{216\pi}$	$-\frac{13}{144\pi}$	$\frac{11}{216\pi}$	$-\frac{5}{144\pi}$	$\frac{7}{216\pi}$	$-\frac{5}{144\pi}$	$\frac{7}{216\pi}$
B_5	$-\frac{4\pi}{3}$	$\frac{4\pi}{9}$	$\frac{4\pi}{3}$	$-\frac{4\pi}{9}$	0	$-\frac{8\pi}{9}$	0	$-\frac{8\pi}{9}$
B_6	$-\frac{1}{192\pi^2}$	$\frac{1}{192\pi^2}$	$-\frac{1}{192\pi^2}$	$\frac{1}{192\pi^2}$	$\frac{5}{192\pi^2}$	$-\frac{5}{192\pi^2}$	$\frac{5}{192\pi^2}$	$-\frac{5}{192\pi^2}$
B_7	$-\frac{461}{1728\pi}$	$-\frac{83}{1728\pi}$	$\frac{731}{1728\pi}$	$\frac{1019}{1728\pi}$	$-\frac{217}{1728\pi}$	$\frac{265}{1728\pi}$	$\frac{41}{1728\pi}$	$\frac{71}{1728\pi}$

where we have again suppressed the superscript (J). In (4.11), t_0 is a hadron production threshold and $\cdots$ are subtraction constants, together a third degree polynomial in Q^2. Equation (4.11) connects theoretical predictions of QCD, i.e., $\Pi(Q^2)$ on the left-hand side, to properties of hadrons contained in $\mathrm{Im}\Pi(t)$, the hadronic spectral function, on the right-hand side.

Regarding (4.11), to eliminate subtraction constants and to accentuate the low-energy region of the integral on the right-hand side, some transformation is typically applied. A popular choice is to formulate unsubtracted LSRs of (usually nonnegative) integer weight k,

$$\mathcal{R}_k(M_B) = M_B^2 \lim_{\substack{N, Q^2 \to \infty \\ M_B^2 = Q^2/N}} \frac{(-Q^2)^N}{\Gamma(N)} \left(\frac{d}{dQ^2}\right)^N \left\{(-Q^2)^k \Pi(Q^2)\right\}, \tag{4.12}$$

at Borel parameter M_B [36, 37, 47, 169]. Details on how to evaluate (4.12) for a correlator such as (4.10), denoted Π^{QCD} from here on to emphasize that it is a quantity calculated using QCD, can be found in the literature (e.g., [36]). The result is

$$\mathcal{R}_k(M_B) = \int_0^\infty t^k e^{-t/M_B^2} \frac{1}{\pi} \mathrm{Im}\Pi^{\mathrm{QCD}}(t)\, \mathrm{d}t \tag{4.13}$$

for $k \in \{0, 1, 2, \ldots\}$ and where

$$\frac{1}{\pi}\text{Im}\Pi^{\text{QCD}}(t) = -A_1 \alpha_s t^3 - A_2 \alpha_s m^2 t^2$$
$$- A_3 \alpha_s t \langle m\bar{q}q \rangle - A_4 t \langle \alpha G^2 \rangle \tag{4.14}$$
$$- A_7 \alpha_s m \langle g\bar{q}\sigma Gq \rangle.$$

Recall, the A_i are given in Table 4.2.

In (4.11), we impose on $\text{Im}\Pi(t)$ a general resonances-plus-continuum model with onset of the QCD continuum at threshold s_0,

$$\text{Im}\Pi(t) = \rho^{\text{had}}(t) + \theta\left(t - s_0\right)\text{Im}\Pi^{\text{QCD}}(t), \tag{4.15}$$

where $\rho^{\text{had}}(t)$ represents the resonance content of the hadronic spectral function and $\theta(t)$ is the Heaviside step function. To isolate the resonance contributions to the LSRs, we consider (continuum-) subtracted LSRs

$$\mathcal{R}_k(M_B, s_0) = \mathcal{R}_k(M_B) - \int_{s_0}^{\infty} t^k e^{-t/M_B^2} \frac{1}{\pi}\text{Im}\Pi^{\text{QCD}}(t)\, \mathrm{d}t. \tag{4.16}$$

Then, Equations (4.11)–(4.13), (4.15), and (4.16) together imply that

$$\mathcal{R}_k(M_B, s_0) = \int_{t_0}^{\infty} t^k e^{-t/M_B^2} \frac{1}{\pi}\rho^{\text{had}}(t)\, \mathrm{d}t \tag{4.17}$$

where

$$\mathcal{R}_k(M_B, s_0) = \int_0^{s_0} t^k e^{-t/M_B^2} \frac{1}{\pi}\text{Im}\Pi^{\text{QCD}}(t)\, \mathrm{d}t \tag{4.18}$$

and (again) $\text{Im}\Pi^{\text{QCD}}(t)$ is given in (4.14).

There are a number of interesting observations we can make concerning the LSRs of light quarkonium hybrids. In particular, the 6d gluon condensate terms do not contain a logarithm, i.e., $A_6 = 0$ for all J^{PC} values considered (see Table 4.2), and hence do not contribute to the imaginary part (4.14). This result is surprising: both Diagrams V and VI (see Figure 4.1) have logarithmic contributions, but they cancel when the two diagrams are added together. Thus, the LO 6d gluon condensate terms cannot stabilize light quarkonium hybrid LSRs

analyses as they have done in some heavy quarkonium hybrid analyses [93, 100, 116, 164].

Another observation relates to the mixed condensate contributions. Using (4.12), if we try to formulate $k = -1$ (i.e., lower-weight) unsubtracted LSRs, we get a piece that formally looks like the right-hand side of (4.13) at $k = -1$ and another piece:

$$- B_5 \langle \bar{q} q \rangle^2 - B_6 \langle g^3 G^3 \rangle - \left(\frac{A_7}{\epsilon} + B_7 \right) m \langle g \bar{q} \sigma G q \rangle. \tag{4.19}$$

If $A_7 \neq 0$, then neither piece is well-defined: the integral from (4.13) diverges and (4.19) contains a ϵ^{-1} field theory divergence. But for $J^{PC} \in \{1^{-+}, 1^{++}\}$, we find that $A_7 = 0$ which allows for the construction of lower-weight LSRs in these two channels. Unlike the $k = 0$ LSRs, the $k = -1$ LSRs do receive contributions from the 6d quark and gluon condensates as both B_5 and B_6 are nonzero. An analysis of these $k = -1$ LSRs does require some knowledge of the subtraction constants in (4.11).

As noted in Section 4.2.1, in the multi-channel LSRs analysis of [136], the 0^{+-}, 0^{-+}, 1^{+-}, and 1^{-+} sectors were unstable. The 1^{-+} has since been stabilized using lower-weight LSRs [95], and the 0^{-+} has been stabilized [137] using a different current than that used in [136]. That leaves the non-exotic 1^{+-} and the exotic 0^{+-} channels. Given the GlueX emphasis on exotics and the possible complicated features of mixing between hybrids and conventional quark mesons in the 1^{+-} channel, we focus our attention on 0^{+-} light quarkonium hybrids. Attempts to stabilize the 0^{+-} channel have involved higher-dimension currents combined with lower-weight sum-rules requiring estimation of the dispersion-relation low-energy constant within the analysis [155]. Because higher-dimension currents tend to enhance the continuum, the mass determination combined with an estimated low-energy term merits further study.

As in [136], we perform a conventional single narrow resonance (SNR) LSRs analysis of the 0^{+-} channel by letting

$$\rho^{\text{had}}(t) = \pi f^2 \delta(t - m_H^2) \tag{4.20}$$

in (4.17) where f is the resonance coupling and m_H is its mass. We include our higher-dimension condensate contributions as well as updated QCD parameter values, yet the analysis remains unstable. The 5d mixed condensate term in the LSRs is small, and, as noted

above, the 6d condensates do not contribute at all. In [136], it was suggested that the instability in this channel could be related to a distribution of resonance strength. To investigate this possibility, we use GSRs, an alternative to LSRs which provide a fundamentally different weighting of the hadronic spectral function that makes them well-suited to analyzing distributed resonance strength hadron models. Unsubtracted GSRs of integer weight k are defined as [75]

$$
G_k(\hat{s},\,\tau) = \sqrt{\frac{\tau}{\pi}} \lim_{\substack{N,\Delta^2 \to \infty \\ \tau=\Delta^2/(4N)}} \frac{\left(-\Delta^2\right)^N}{\Gamma(N)}
$$
$$
\times \left(\frac{d}{d\Delta^2}\right)^N \left\{ \frac{(\hat{s}+i\Delta)^k \Pi(-\hat{s}-i\Delta) - (\hat{s}-i\Delta)^k \Pi(-\hat{s}+i\Delta)}{i\Delta} \right\}. \quad (4.21)
$$

Details on how to evaluate (4.21) for a correlator such as (4.10) can be found in [9, 75, 165]. The result is

$$
G_k(\hat{s},\,\tau) = \frac{1}{\sqrt{4\pi\tau}} \int_0^\infty t^k e^{-\frac{(\hat{s}-t)^2}{4\tau}} \frac{1}{\pi} \mathrm{Im}\Pi^{\mathrm{QCD}}(t)\,\mathrm{d}t \quad (4.22)
$$

for $k \in \{0,\,1,\,2,\,\ldots\}$ and where $\frac{1}{\pi}\mathrm{Im}\Pi^{\mathrm{QCD}}(t)$ is given in (4.14). Subtracted GSRs are defined in much the same way as subtracted LSRs leading to the following GSRs analogues of (4.17) and (4.18):

$$
G_k(\hat{s},\,\tau,\,s_0) = \frac{1}{\sqrt{4\pi\tau}} \int_{t_0}^\infty t^k e^{-\frac{(\hat{s}-t)^2}{4\tau}} \frac{1}{\pi} \rho^{\mathrm{had}}(t)\,\mathrm{d}t \quad (4.23)
$$

where

$$
G_k(\hat{s},\,\tau,\,s_0) = \frac{1}{\sqrt{4\pi\tau}} \int_0^\infty t^k e^{-\frac{(\hat{s}-t)^2}{4\tau}}
$$
$$
\times \frac{1}{\pi}\mathrm{Im}\Pi^{\mathrm{QCD}}(t)\,\mathrm{d}t. \quad (4.24)
$$

The difference between (4.17)–(4.18) and (4.23)–(4.24) is in the kernel of the integrals: a decaying exponential for LSRs and a Gaussian for GSRs. The two sum-rules represent fundamentally different weightings of the spectral function $\rho^{\mathrm{had}}(t)$; whereas in the LSRs have a duality interval of width $\sim 1/M_B^2$ near the low-energy threshold of the spectral function,

the GSRs have a duality interval of width $\sim \sqrt{2\tau}$ near $\hat{s}$ (4.23). In the $\tau \to 0^+$ limit, we have

$$\lim_{\tau \to 0^+} \frac{1}{\sqrt{4\pi\tau}} e^{-\frac{(\hat{s}-t)^2}{4\tau}} = \delta\left(\hat{s} - t\right), \tag{4.25}$$

which, when applied to (4.23), yields

$$\lim_{\tau \to 0^+} G_k(\hat{s},\, \tau,\, s_0) = \hat{s}^k \frac{1}{\pi} \rho^{\text{had}}(\hat{s}) \text{ for } \hat{s} > t_0. \tag{4.26}$$

Hence, at least in principle, $\rho^{\text{had}}(t)$ can be extracted directly from GSRs. Realistically, the $\tau \to 0^+$ limit cannot be achieved, however, because, through renormalization-group (RG) improvement (see Section 4.2.5), the renormalization scale at which α_s is evaluated decreases with decreasing τ [75]. Nevertheless, it is desirable to use low values of τ to minimize the smearing of $\rho^{\text{had}}(t)$ by the kernel of the GSRs. To further emphasize this, we draw upon an analogy introduced in the seminal GSRs paper [75]. Gaussian sum-rules satisfy the classical heat equation

$$\frac{\partial^2 G_k\left(\hat{s},\, \tau,\, s_0\right)}{\partial \hat{s}^2} = \frac{\partial G_k\left(\hat{s},\, \tau,\, s_0\right)}{\partial \tau}, \tag{4.27}$$

reinterpreting the parameter $\hat{s}$ as "position", the Gaussian width τ as "time", and the GSRs $G_k(\hat{s},\, \tau,\, s_0)$ as "temperature". The smaller the value of τ (i.e. the less "time" that has passed), the better we may assess the original (i.e., $\tau \to 0^+$) "temperature" distribution (i.e., $\hat{s}^k \frac{1}{\pi} \rho^{\text{had}}(\hat{s})$).

Compared to LSRs, GSRs permit greater access to the structure of $\rho^{\text{had}}(t)$. The LSRs methodology is specifically formulated to accentuate the ground state region of the hadronic spectral function while suppressing higher energies. With GSRs, this need not be the case as $\hat{s}$, the position of the Gaussian kernel's peak, is a free parameter. By varying $\hat{s}$, GSRs can probe a wide region of the hadronic spectral function with the same sensitivity as the ground state region. As such, GSRs are generally preferable to LSRs when studying distributed resonance strength models, as demonstrated in the successful analysis of the ρ meson using GSRs methodology [9]. Integrating (4.23) with respect to $\hat{s}$ gives

$$\int_{-\infty}^{\infty} G_k(\hat{s},\, \tau,\, s_0)\, \mathrm{d}\hat{s} = \int_{t_0}^{\infty} t^k \frac{1}{\pi} \rho^{\text{had}}(t)\, \mathrm{d}t \tag{4.28}$$

84

from which we recognize the quantity on the left-hand side as the finite-energy sum-rule of weight k. As shown in [75], a resonance plus continuum model evolved through the diffusion equation only reproduces the QCD prediction at large energy scales if s_0 is constrained by (4.28). To isolate the information contained in the GSRs formalism that is independent of (4.28), we consider normalized Gaussian sum-rules (NGSRs) [9]

$$N_k \left(\hat{s}, \tau, s_0 \right) = \frac{G_k \left(\hat{s}, \tau, s_0 \right)}{M_{k,0} \left(\tau, s_0 \right)}, \tag{4.29}$$

i.e., GSRs scaled by their 0th-order moments $M_{k,0}(\hat{s}, \tau)$ where, in general,

$$M_{k,n} \left(\tau, s_0 \right) = \int_{-\infty}^{\infty} \hat{s}^n G_k \left(\hat{s}, \tau, s_0 \right) \, \mathrm{d}\hat{s}. \tag{4.30}$$

Combining (4.23), (4.28), and (4.29), we get a NGSRs analogue of (4.23),

$$N_k(\hat{s}, \tau, s_0) = \frac{\frac{1}{\sqrt{4\pi\tau}} \int_{t_0}^{\infty} t^k e^{-\frac{(\hat{s}-t)^2}{4\tau}} \frac{1}{\pi} \rho^{\text{had}}(t) \, \mathrm{d}t}{\int_{t_0}^{\infty} t^k \frac{1}{\pi} \rho^{\text{had}}(t) \, \mathrm{d}t}. \tag{4.31}$$

Finally, to emphasize the low-energy region of the spectral function, we work with the lowest-weight sum-rules (i.e., $k = 0$) as in previous applications of GSRs to the prediction of resonance properties [9, 165].

4.2.4 Hölder Inequality

Previous investigations of hadronic systems using LSRs have employed Hölder inequalities to restrict the set of allowed τ and s_0 values [170, 171, 172]. The Hölder Inequality is expressed generally as

$$\left| \int_{t_1}^{t_2} f(t) \, g(t) \, \mathrm{d}\mu \right| \leq \left(\int_{t_1}^{t_2} |f(t)|^p \, \mathrm{d}\mu \right)^{\frac{1}{p}}$$
$$\times \left(\int_{t_1}^{t_2} |g(t)|^q \, \mathrm{d}\mu \right)^{\frac{1}{q}} \tag{4.32}$$

under the condition

$$\frac{1}{p} + \frac{1}{q} = 1 \tag{4.33}$$

and where $d\mu$ is an arbitrary integration measure. From positivity of the hadronic spectral function for diagonal correlators, we can use $\mathrm{Im}\Pi^{\mathrm{QCD}}(t) > 0$ to form an integration measure. Substituting this integration measure into (4.32) leads to restrictions on the allowed values of $\hat{s}$, τ, and s_0 in the GSRs. We consider the inequality (4.32) with the assignments

$$\mathrm{d}\mu = \mathrm{Im}\Pi^{\mathrm{QCD}}(t)\mathrm{d}t \tag{4.34}$$

$$f(t) = t^\alpha \left(\frac{e^{-\frac{(\hat{s}-t)^2}{4\tau}}}{\sqrt{4\pi\tau}} \right)^a \tag{4.35}$$

$$g(t) = t^\beta \left(\frac{e^{-\frac{(\hat{s}-t)^2}{4\tau}}}{\sqrt{4\pi\tau}} \right)^b \tag{4.36}$$

$$t_1 = t_0, \ t_2 = s_0 \tag{4.37}$$

$$a + b = 1 \tag{4.38}$$

where $\alpha + \beta$ is a non-negative integer. Defining

$$\tau_1 = \frac{\tau}{ap} \text{ and } \tau_2 = \frac{\tau}{bq}, \tag{4.39}$$

the inequality (4.32) becomes

$$G_{\alpha+\beta}(\tau, \hat{s}, s_0) \leq \left(\frac{\tau_1}{\tau} \right)^{\frac{1}{2p}} \left(\frac{\tau_2}{\tau} \right)^{\frac{1}{2q}} \\ \times G_{\alpha p}^{\frac{1}{p}}(\tau_1, \hat{s}, s_0) G_{\beta q}^{\frac{1}{q}}(\tau_2, \hat{s}, s_0) \tag{4.40}$$

where we have used $G_k(\tau, \hat{s}, s_0) > 0$, the weakest constraint on the GSRs that emerges from positivity of the spectral function. We define ω as follows:

$$\omega = \frac{1}{p} \Longleftrightarrow 1 - \omega = \frac{1}{q}, \ 0 < \omega < 1 \tag{4.41}$$

and consider (4.40) with zero-weight GSRs (i.e., $\alpha = \beta = 0$),

$$G_0\left(\tau,\ \hat{s},\ s_0\right) \le \left(\frac{\tau_1}{\tau}\right)^{\frac{\omega}{2}} \left(\frac{\tau_2}{\tau}\right)^{\frac{1-\omega}{2}}$$

$$\times G_0^\omega\left(\tau_1,\ \hat{s},\ s_0\right) G_0^{1-\omega}\left(\tau_2,\ \hat{s},\ s_0\right). \tag{4.42}$$

Equations (4.38), (4.39), and (4.41) together imply that

$$\tau = \frac{\tau_1\tau_2}{(1-\omega)\tau_1 + \omega\tau_2} \tag{4.43}$$

which, when substituted into (4.42), gives

$$G_0\left(\frac{\tau_1\tau_2}{(1-\omega)\tau_1 + \omega\tau_2},\ \hat{s},\ s_0\right) \le \left(\frac{(1-\omega)\tau_1 + \omega\tau_2}{\tau_2}\right)^{\frac{\omega}{2}} \left(\frac{(1-\omega)\tau_1 + \omega\tau_2}{\tau_1}\right)^{\frac{1-\omega}{2}}$$

$$\times G_0^\omega\left(\tau_1,\ \hat{s},\ s_0\right) G_0^{1-\omega}\left(\tau_2,\ \hat{s},\ s_0\right). \tag{4.44}$$

Following [172], we set

$$\tau_1 = \tau \tag{4.45}$$

$$\tau_2 = \tau + \delta\tau \tag{4.46}$$

which implies

$$0 \le G_0\left(\frac{\tau(\tau + \delta\tau)}{\omega(\tau + \delta\tau) + (1-\omega)\tau},\ \hat{s},\ s_0\right) - \left(\frac{\omega(\tau + \delta\tau) + (1-\omega)\tau}{(\tau + \delta\tau)}\right)^{\frac{\omega}{2}} \left(\frac{\omega(\tau + \delta\tau) + (1-\omega)\tau}{\tau}\right)^{\frac{1-\omega}{2}}$$

$$\times G_0^\omega\left(\tau,\ \hat{s},\ s_0\right) G_0^{1-\omega}\left(\tau + \delta\tau,\ \hat{s},\ s_0\right). \tag{4.47}$$

We can perform a local analysis of (4.47) by expanding about $\delta\tau = 0$,

$$0 \leq \frac{\omega(\omega - 1)\left(1 - 2\tau^2 \left(\frac{G_0'(\hat{s}, \tau, s_0)}{G_0(\hat{s}, \tau, s_0)}\right)^2 + 2\tau \left(2\left(\frac{G_0'(\hat{s}, \tau, s_0)}{G_0(\hat{s}, \tau, s_0)}\right) + \tau \left(\frac{G_0''(\hat{s}, \tau, s_0)}{G_0(\hat{s}, \tau, s_0)}\right)\right)\right)(\delta\tau)^2}{4\tau^2}$$

$$+ \mathcal{O}\left((\delta\tau)^3\right), \quad (4.48)$$

where primes indicate τ-derivatives. Then, (4.41) and (4.48) together imply

$$H(\hat{s}, \tau, s_0) \equiv 1 - 2\tau^2 \left(\frac{G_0'(\hat{s}, \tau, s_0)}{G_0(\hat{s}, \tau, s_0)}\right)^2 + 2\tau\left(2\left(\frac{G_0'(\hat{s}, \tau, s_0)}{G_0(\hat{s}, \tau, s_0)}\right) + \tau\left(\frac{G_0''(\hat{s}, \tau, s_0)}{G_0(\hat{s}, \tau, s_0)}\right)\right) \geq 0. \quad (4.49)$$

At some $(\tau, \hat{s}, s_0)$, if the GSR $G_0(\hat{s}, \tau, s_0)$ is to be consistent with a positive hadronic spectral function, then it must satisfy the inequality (4.49).

4.2.5   Analysis Methodology and Results

Before we can analyze 0^{+-} light quarkonium hybrids using (4.31), we need to discuss the QCD parameters appearing in (4.10), i.e., the coupling, the quark mass, and the QCD condensates.

To implement RG improvement we replace α_s and m in (4.10) by one-loop, $\overline{\text{MS}}$ running quantities [75]. In our analysis, we use the QCD running coupling anchored at the τ-lepton mass,

$$\alpha_s(\mu) = \frac{\alpha_s(M_\tau)}{1 + \frac{\alpha_s(M_\tau)}{12\pi}(33 - 2n_f)\log\left(\frac{\mu^2}{M_\tau^2}\right)}, \quad (4.50)$$

where we use PDG [173] values for the τ mass and

$$\alpha_s(M_\tau) = 0.325 \pm 0.015. \quad (4.51)$$

For the light quark masses, we use

$$m(\mu) = m(2 \text{ GeV})\left(\frac{\alpha_s(\mu)}{\alpha_s(2 \text{ GeV})}\right)^{\frac{12}{33 - 2n_f}}, \quad (4.52)$$

88

where

$$m(2 \text{ GeV}) = \frac{1}{2} \left(m_u(2 \text{ GeV}) + m_d(2 \text{ GeV}) \right)$$
$$= 3.5^{+0.7}_{-0.3} \text{ MeV} \tag{4.53}$$

for nonstrange quarks and

$$m(2 \text{ GeV}) = 96^{+8}_{-4} \text{ MeV} \tag{4.54}$$

for strange quarks [173]. In both (4.50) and (4.52), we set $n_f = 4$.

Renormalization-group arguments identify our renormalization scale as $\mu = \tau^{1/4}$ [9, 75], putting a lower bound on our choice of τ restricted by the reliability of perturbation theory. A related issue associated with τ is reliability of the GSRs as quantified by the relative contributions of perturbative versus non-perturbative effects and the relative contributions of the resonance versus continuum. We therefore restrict our analysis to $\tau \geq M_\tau^4$, approximately equivalent to $\tau > 10 \, \text{GeV}^4$ as discussed in Section 4.2.5. We also work with an upper bound $\tau \leq 20 \, \text{GeV}^4$ emerging from the Hölder inequality constraint (4.49), as presented in detail in Section 4.2.5.

Turning to the condensates, the value of the RG-invariant quantity $\langle m\bar{q}q \rangle$ is well-known from PCAC [57]. Using the conventions of [47], we have

$$\langle m\bar{q}q \rangle = \begin{cases} -\frac{1}{2} f_\pi^2 m_\pi^2, & \text{for nonstrange } q \\ -\frac{1}{2} f_K^2 m_K^2, & \text{for strange } q \end{cases} \tag{4.55}$$

where PDG values are used for the meson masses [173] and the decay constants are [128]

$$f_\pi = (92.2 \pm 3.5) \text{ MeV} , \ f_K = (110.0 \pm 4.2) \text{ MeV}. \tag{4.56}$$

We use the following value for the 4d gluon condensate [174]:

$$\langle \alpha G^2 \rangle = (0.075 \pm 0.020) \, \text{GeV}^4. \tag{4.57}$$

The nonstrange- and strange-flavored 5d mixed condensates are estimated by [175, 176] to

be

$$\frac{m\langle g\bar{q}\sigma Gq\rangle}{\langle m\bar{q}q\rangle} \equiv M_0^2 = (0.8 \pm 0.1)\,\text{GeV}^2. \tag{4.58}$$

Finally, we note that while the 6d quark and gluon condensates were included in the correlator calculation (4.10), Table 4.2 shows that neither contributes to the $k = 0$ GSRs (4.24) or NGSRs (4.29).

As noted in Section 4.2.3, a SNR analysis of 0^{+-} light quarkonium hybrids fails within the LSRs methodology, and so we turn our attention to models with distributed resonance strength using GSRs. As confirmation of the consistency between the LSRs and GSRs methodology, we analysed the original stabilizing channels in the LSRs methodology $J^{PC} \in \{0^{\pm\pm},\ 1^{\pm\pm}\}$ [136] and found excellent agreement between the results for both mass predictions and continuum onsets. To confirm the need for a distributed resonance model in the case of $J^{PC} = 0^{+-}$, we consider the quantity [165]

$$\sigma_0^2(\tau,\ s_0) \equiv \frac{M_{0,2}(\tau,\ s_0)}{M_{0,0}(\tau,\ s_0)} - \left(\frac{M_{0,1}(\tau,\ s_0)}{M_{0,0}(\tau,\ s_0)}\right)^2 \tag{4.59}$$

where the QCD moments, $M_{k,n}(\tau,\ s_0)$, were defined in (4.30). Combining (4.23) and (4.59) gives

$$\begin{aligned}\sigma_0^2(\tau,\ s_0) =& \frac{\int_{t_0}^{\infty}(t^2 + 2\tau)\rho^{\text{had}}(t)\,\mathrm{d}t}{\int_{t_0}^{\infty}\rho^{\text{had}}(t)\,\mathrm{d}t}\\ &- \left(\frac{\int_{t_0}^{\infty}t\rho^{\text{had}}(t)\,\mathrm{d}t}{\int_{t_0}^{\infty}\rho^{\text{had}}(t)\,\mathrm{d}t}\right)^2. \end{aligned} \tag{4.60}$$

For a SNR model, substituting (4.20) into (4.60) yields

$$\sigma_0^2(\tau,\ s_0) = 2\tau. \tag{4.61}$$

Hence, the quantity $\sigma_0^2(\tau,\ s_0) - 2\tau$ provides a QCD-calculated, model-independent way to assess the suitability of representing a particular hadronic spectral function as a single narrow resonance. If $\sigma_0^2(\tau,\ s_0) - 2\tau \approx 0$, then a single narrow resonance model is appropriate. On the other hand, if $\sigma_0^2(\tau,\ s_0) - 2\tau \not\approx 0$, then the hadronic spectral function has distributed

resonance strength. And so, in Figure 4.2, we plot the QCD prediction $\sigma_0^2(\tau,\,s_0) - 2\tau$ versus τ for nonstrange quarks at several values of s_0 over the range $10 \text{ GeV}^2 \leq s_0 \leq 30 \text{ GeV}^2$. Clearly, $\sigma_0^2(\tau,\,s_0) - 2\tau \not\approx 0$, providing further motivation to consider models other than the SNR. An analogous analysis for strange quarks leads to the same conclusion.
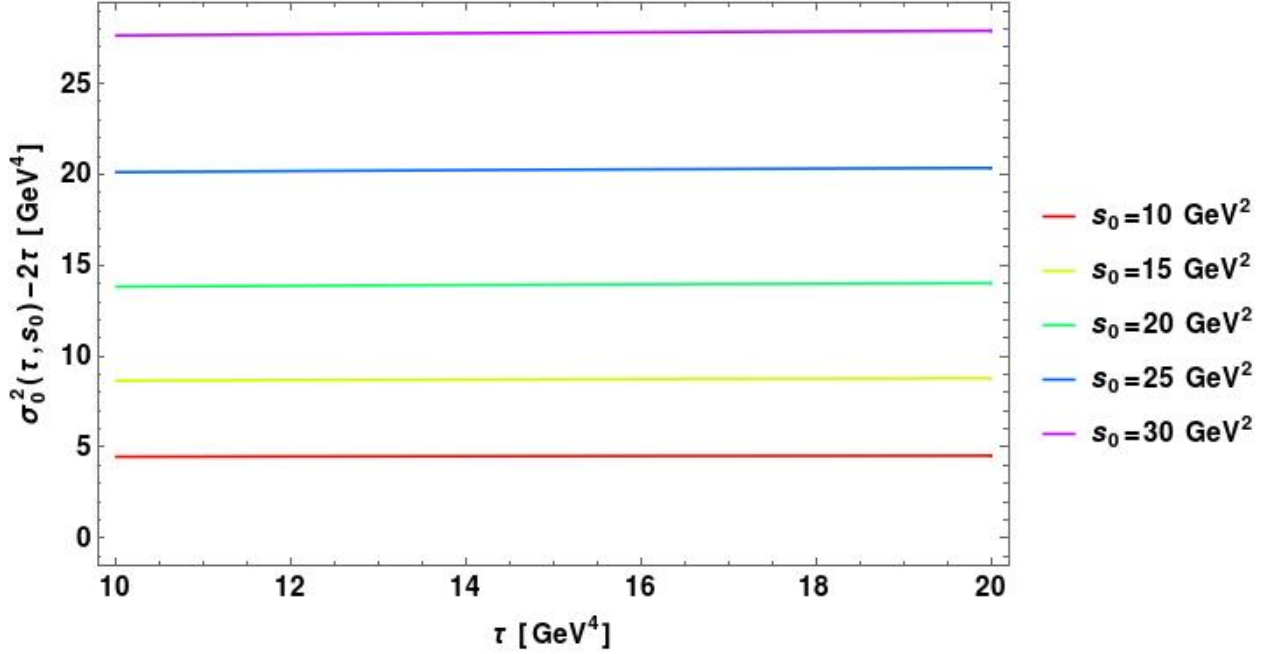
Figure 4.2: The QCD prediction for the quantity $\sigma_0^2 - 2\tau$ (where σ_0^2 is defined in (4.59)) for nonstrange quarks versus τ at several values of the continuum threshold s_0.

If the distributed resonance strength indicated by Figure 4.2 is due to a single wide resonance (SWR), then we can determine a rough lower bound on the resonance's width using a rectangular pulse resonance model,

$$\rho^{\text{had}}(t) = \frac{\pi f}{2 m_H \Gamma} \left[\theta \left(t - m_H^2 + m_H \Gamma \right) - \theta \left(t - m_H^2 - m_H \Gamma \right) \right], \tag{4.62}$$

where f is the resonance's coupling, Γ is its width, and m_H is its mass. Substituting (4.62) into (4.60) gives

$$\sigma_0^2(\tau,\,s_0) = 2\tau + \frac{1}{3} m_H^2 \Gamma^2 \tag{4.63}$$

$$\implies \Gamma = \frac{1}{m_H} \sqrt{3 \left(\sigma_0^2(\tau,\,s_0) - 2\tau \right)}. \tag{4.64}$$

From (4.64), we see that Γ decreases as m_H increases. However, to ensure that the resonance does not merge with the continuum, we require

$$m_H^2 + m_H\Gamma < s_0 \tag{4.65}$$

which implies that the largest possible resonance mass for a particular s_0 is given by

$$m_{H,\,\mathrm{max}}(\tau,\, s_0) = \sqrt{s_0 - \sqrt{3(\sigma_0^2(\tau,\, s_0) - 2\tau)}} \tag{4.66}$$

where we have used (4.63). By letting $m_H \to m_{H,\,\mathrm{max}}$ in (4.64), we find that the smallest possible resonance width for a particular s_0 is given by

$$\Gamma_{\mathrm{min}}(\tau,\, s_0) = \sqrt{\frac{3(\sigma_0^2(\tau,\, s_0) - 2\tau)}{s_0 - \sqrt{3(\sigma_0^2(\tau,\, s_0) - 2\tau)}}}. \tag{4.67}$$

From Figure 4.2, we see that $\sigma_0^2(\tau,\, s_0) - 2\tau$ shows almost no τ-dependence; hence, the same can be said about $\Gamma_{\mathrm{min}}(\tau,\, s_0)$. In Figure 4.3, we plot $\Gamma_{\mathrm{min}}(\tau,\, s_0)$ versus s_0 at $\tau = 10 \ \mathrm{GeV}^4$ for nonstrange quarks. An analogous plot for strange quarks looks nearly identical. At $s_0 = 10 \ \mathrm{GeV}^2$, we find that $\Gamma_{\mathrm{min}} \approx 1.46 \ \mathrm{GeV}$, far larger than a typical hadron width. As s_0 increases, so too does Γ_{min}. For these reasons, we abandon SWR models in favour of a multi-resonance model.

We consider a double narrow resonance (DNR) model

$$\rho^{\mathrm{had}}(t) = \pi\left(f_1^2\delta\left(t - m_1^2\right) + f_2^2\delta\left(t - m_2^2\right)\right), \tag{4.68}$$

where f_1, f_2 and m_1, m_2 are the resonances' couplings and masses respectively. Substituting (4.68) into (4.31) gives

$$N_0\left(\hat{s},\, \tau,\, s_0\right) = \frac{\left(re^{-\frac{(\hat{s}-m_1^2)^2}{4\tau}} + (1-r)e^{-\frac{(\hat{s}-m_2^2)^2}{4\tau}}\right)}{\sqrt{4\pi\tau}} \tag{4.69}$$
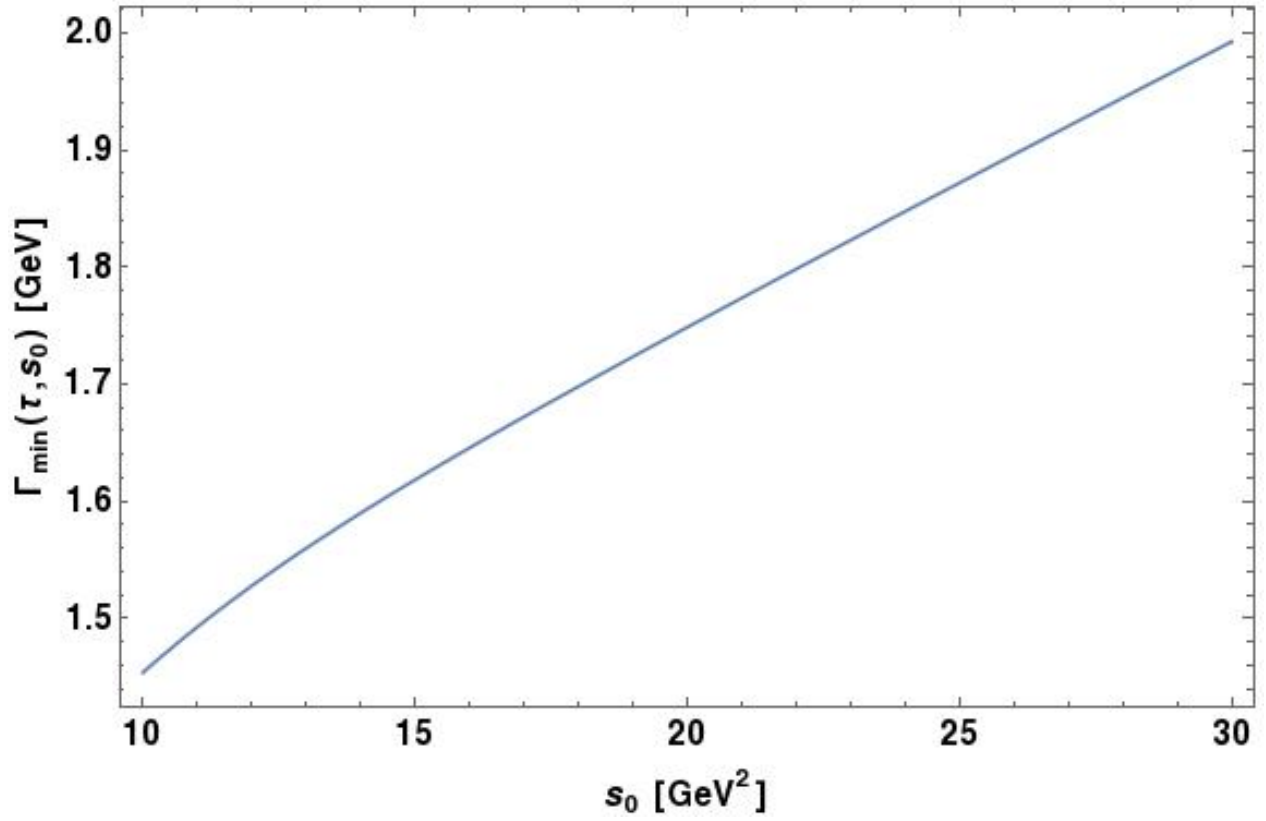
Figure 4.3: Minimum rectangular pulse resonance width, $\Gamma_{\min}$ from (4.67), at $\tau = 10 \text{ GeV}^4$ for nonstrange quarks versus the continuum threshold, s_0.

where

$$r = \frac{f_1^2}{f_1^2 + f_2^2} \iff 1 - r = \frac{f_2^2}{f_1^2 + f_2^2}. \tag{4.70}$$

At fixed values of τ and s_0, we perform a fit of (4.69) over $\hat{s}$ [1] to find best fit parameters for r, m_1, and m_2. In Figure 4.4, we plot the best fit r versus s_0 at $\tau = 10 \, \text{GeV}^4$ for nonstrange quarks. Again, an analogous plot for strange quarks looks nearly identical. From the s_0-stability in r versus s_0, we determine an optimized continuum onset for both the nonstrange- and strange-flavored cases as

$$s_0^{\text{opt}} = (14.5 \pm 1.2) \, \text{GeV}^2 \tag{4.71}$$

where the uncertainties originate from the QCD input parameters; details of the uncertainty analysis are discussed below. Then, a fit to (4.69) at $s_0 = 14.5 \, \text{GeV}^2$ and $\tau = 10 \, \text{GeV}^4$, leads to DNR model parameters

$$r = 0.712 \pm 0.005 \tag{4.72}$$

$$m_1 = 3.57 \pm 0.15 \, \text{GeV} \tag{4.73}$$

$$m_2 = 2.60 \pm 0.14 \, \text{GeV} \tag{4.74}$$

in the nonstrange-flavored case and

$$r = 0.711 \pm 0.005 \tag{4.75}$$

$$m_1 = 3.57 \pm 0.13 \, \text{GeV} \tag{4.76}$$

$$m_2 = 2.60 \pm 0.14 \, \text{GeV} \tag{4.77}$$

in the strange-flavored case. Figure 4.5 shows negligible τ dependence in the mass predictions. Figure 4.6 shows comparisons between the the NGSRs and the DNR model (respectively the left- and right-hand sides of (4.69)) for parameters (4.72)-(4.74) at $\tau = 10 \, \text{GeV}^4$ and $\tau = 20 \, \text{GeV}^4$. We note that the strange and nonstrange 0^{+-} hybrid mass predictions are degenerate within the uncertainties of our analysis; we find this to be consistent with other recent SR analyses [49, 177]. We note that the correlator terms that contain the strange quark

---

[1]using the Mathematica v11 command NonlinearModelFit

mass and condensates are numerically small in our calculation, and do not significantly impact the resulting mass prediction. The relatively small numerical difference between strange and non-strange 0^{+-} hybrids could suggest a dominance of constituent gluonic effects in these systems.
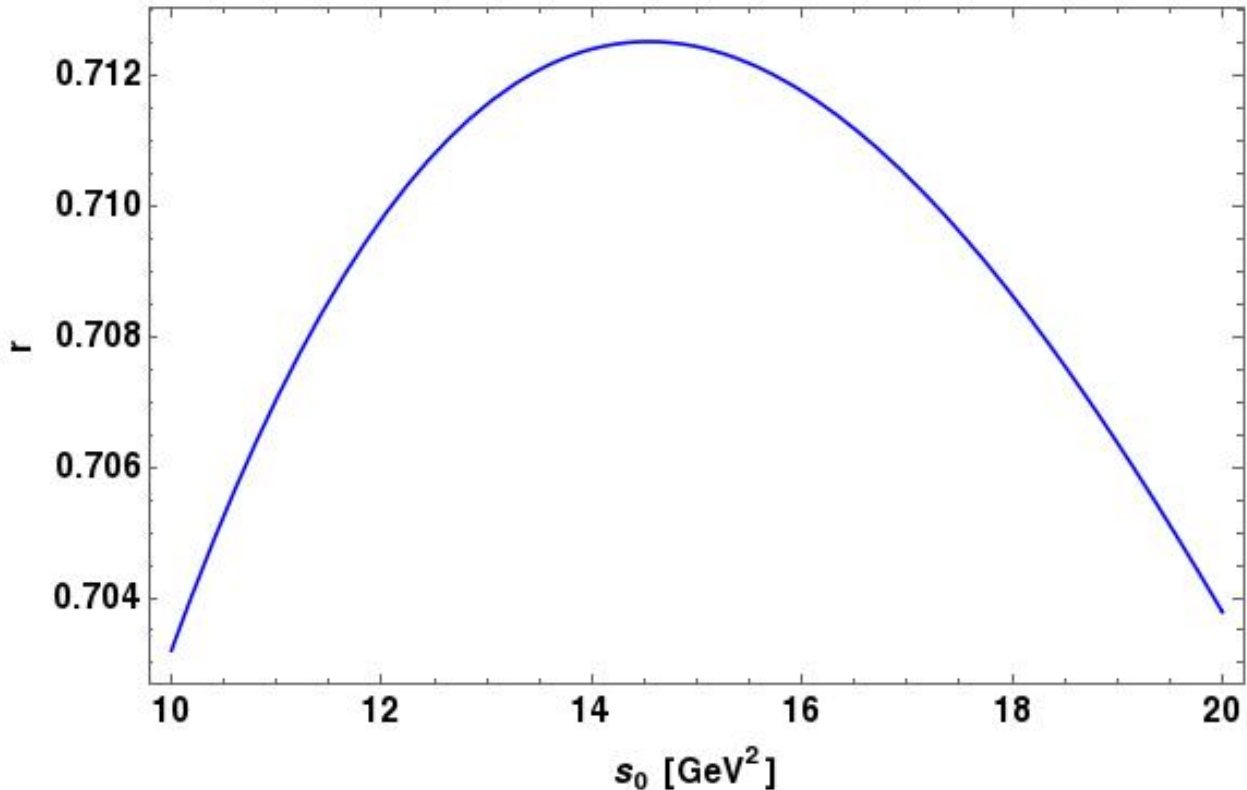
Figure 4.4: Plot of the best fit r (defined in (4.70)) to (4.69) at $\tau = 10$ GeV^4 as a function of continuum threshold, s_0.

Utilizing the Hölder Inequality test (4.49), we can perform a consistency check on our analysis. To determine whether (4.49) is satisfied within the expected uncertainties of the GSRs, we examine the inequality at $s_0^{\text{opt}} = 14.5$ GeV^2 for various values of τ. Because our QCD calculations of Wilson coefficients are truncated perturbative series in α_s, in addition to the QCD parameter uncertainties, we use the 1^{-+} channel [91] to provide an estimated next-order perturbative correction characteristic of hybrid correlators. We find that the Hölder inequality constraint (4.49) is violated for $\tau \gtrsim 20$ GeV^4, and the inequality test for the minimum value $\tau = 10$ GeV^4 is shown in Figure 4.7. Thus, the τ range used in our analysis, 10 GeV$^4 < \tau < 20$ GeV^4, is consistent with the Hölder inequality.
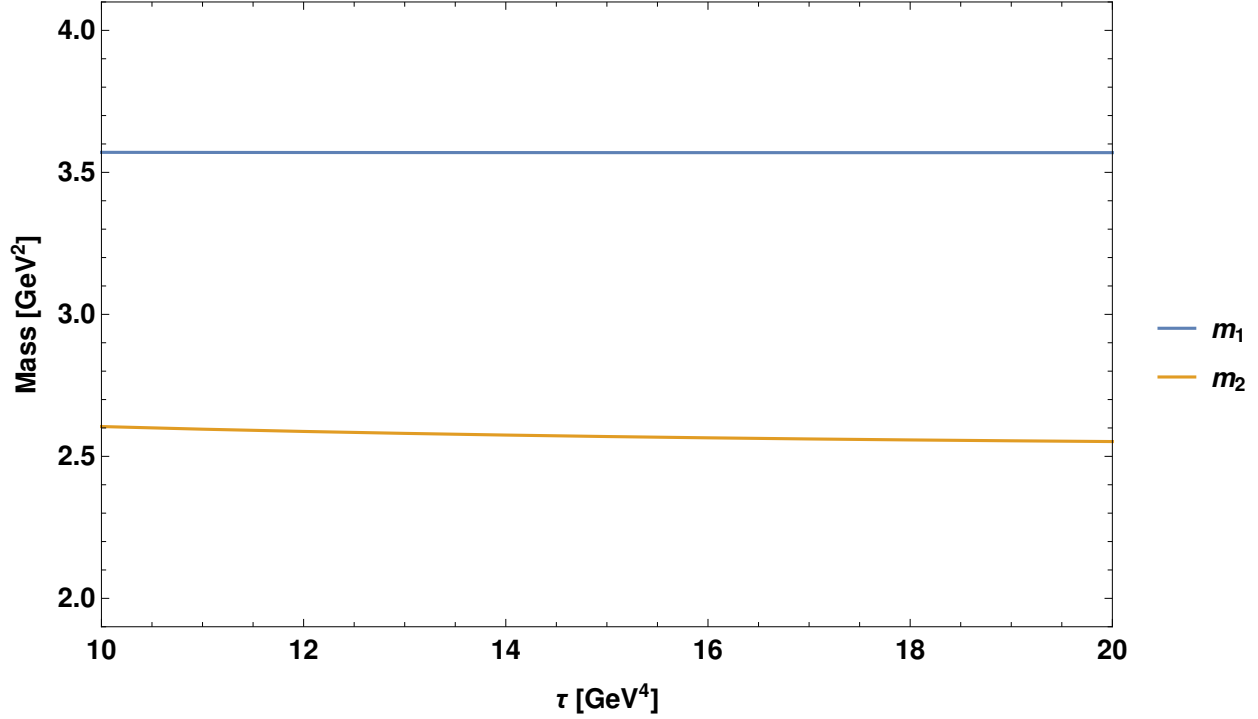
Figure 4.5: Plot of 0^{+-} light quarkonium hybrid masses $m_1(\tau, s_0^{\text{opt}})$ and $m_2(\tau, s_0^{\text{opt}})$ of the DNR model (4.68) at continuum threshold $s_0^{\text{opt}} = 14.5\,\text{GeV}^2$.
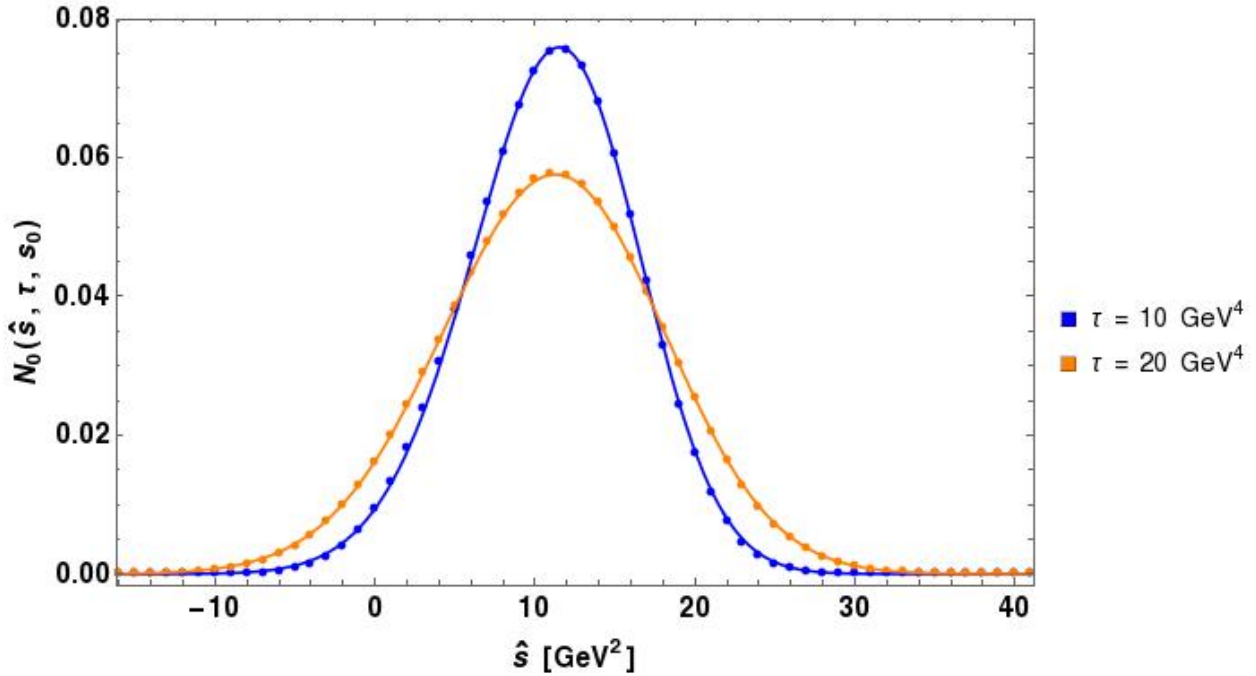
Figure 4.6: Comparison of the two sides of (4.69) for nonstrange DNR parameters (4.72)–(4.74) and for $\tau = 10\,\text{GeV}^4$ and $\tau = 20\,\text{GeV}^4$ at $s_0^{\text{opt}} = 14.5\,\text{GeV}^2$. Solid curves correspond to the left-hand side of (4.69); dots correspond to the right-hand side at selected values of $\hat{s}$.

To explore the lower bound on τ in more detail, we consider OPE convergence and resonance dominance in the GSR. As in LSRs, a reliable GSR analysis requires that perturbation theory dominates power-law corrections and that the resonance contributions dominate the continuum. The average relative contribution of the non-perturbative terms is calculated over the region $10\,\mathrm{GeV}^2 - \sqrt{2\tau} < \hat{s} < 10\,\mathrm{GeV}^2 + \sqrt{2\tau}$ to encompass the peak in Figure 4.6. For $\tau = 10\,\mathrm{GeV}^4$, the $\hat{s}$-averaged non-perturbative contributions are less than 20% of the total and are thus safely controlled. As τ decreases, the relative non-perturbative contribution increases (e.g., to 25% at $\tau = 5\,\mathrm{GeV}^4$). The relative contribution of the resonance versus continuum contribution is much more sensitive to τ. For $\tau = 10\,\mathrm{GeV}^4$ the $\hat{s}$-averaged ratio of resonance to continuum effects is 50% but for $\tau = 5\,\mathrm{GeV}^4$ the ratio decreases to 30%. We thus conclude that the criteria of OPE convergence and resonance dominance requires $\tau > 10\,\mathrm{GeV}^4$ for a reliable GSR analysis. The combination of the Hölder inequality, OPE convergence, and resonance dominance constrains our GSR window of analysis to $10\,\mathrm{GeV}^4 < \tau < 20\,\mathrm{GeV}^4$.

We verify the s_0 optimization (4.71) obtained from Figure 4.4 by looking at an independent analysis developed in [165] based on the properties of the $\hat{s}$ peak position (maximum) of the NGSRs. For the SNR model (4.20) the $\hat{s}$-peak occurs at $\hat{s} = m^2$, independent of τ. Thus, an alternative s_0-optimization criterion for the SNR is minimizing the τ-dependence of the peak position $\hat{s}_{\mathrm{peak}}(\tau, s_0)$ defined implicitly from

$$\frac{\partial}{\partial \hat{s}} N_0^{\mathrm{QCD}}(\hat{s}, \tau, s_0)\bigg|_{\hat{s}=\hat{s}_{\mathrm{peak}}(\tau, s_0)} = 0. \tag{4.78}$$

For the DNR model (4.68), the peak position acquires τ-dependence modeled by

$$\hat{s}_{\mathrm{peak}}(\tau, s_0) = A + \frac{B}{\tau} + \frac{C}{\tau^2} + \frac{D}{\tau^3} \tag{4.79}$$

where the unknown parameters $\{A, B, C, D\}$ are constrained by minimizing the χ^2

$$\chi^2(A, B, C, D, s_0) = \sum_{\tau=10\,\mathrm{GeV}^4}^{20\,\mathrm{GeV}^4} \left(\frac{A + \frac{B}{\tau} + \frac{C}{\tau^2} + \frac{D}{\tau^3}}{\hat{s}_{\mathrm{peak}}(\tau, s_0)} - 1\right)^2. \tag{4.80}$$

By minimizing (4.80) with respect to A, B, C, D, and s_0, we find an optimum continuum
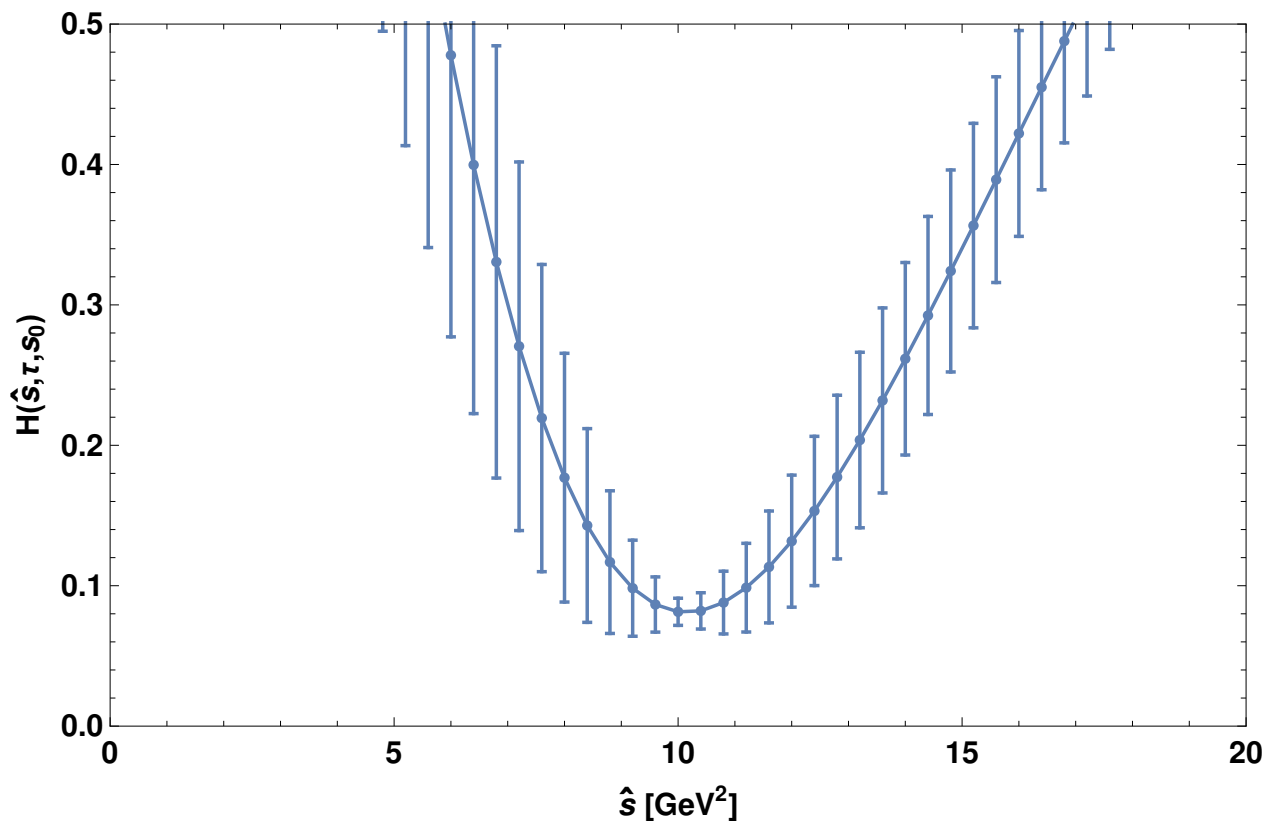
Figure 4.7: Plot of inequality test (4.49) for $\tau = 10$ GeV^4 with error bars displayed. Errors are due to variations in the condensate parameters, variations in α_s, and uncertainties in s_0^{opt} (4.71).

threshold $s_0^{\text{opt}} = 14.0 \, \text{GeV}^2$ in excellent agreement with the value obtained in (4.71).

To obtain errors in s_0^{opt}, r, m_1, and m_2, we examine how the errors in the QCD parameters impact the values of these optimized parameters by varying each independently and examining the impact on the model parameters. Additionally, there exists a methodological error in determining s_0^{opt} as the variance in the QCD parameters will affect the stability point of r. Contributions to the error in s_0^{opt} are summarized in Table 4.4 and contributions to the error in the DNR model parameters are summarized in Tables 4.5-4.7. The dominant error in s_0^{opt} comes from the variation in $\langle \alpha G^2 \rangle$; in determining errors in the DNR parameters, the error in r is driven by the variation in $\langle \alpha G^2 \rangle$ while the dominant errors in the masses m_1 and m_2 arise from variations in s_0^{opt}, followed by $\langle \alpha G^2 \rangle$. Errors in $\langle \overline{q}q \rangle$ and $\langle g\overline{q}\sigma Gq \rangle$ contribute negligibly in the error of all DNR parameters. Adding the values summarized in Tables 4.4-4.7 in quadrature gives us a conservative error estimate summarized in Table 4.8; as the driving errors in each parameter are approximately equivalent for the upper and lower bounds of the corresponding QCD parameters, we express our DNR parameters (4.71)-(4.77) with symmetric error, taking the most conservative bound.

Table 4.4: Contributions to s_0^{opt} error at $\tau = 10 \, \text{GeV}^4$ due to variations in QCD parameter error. Columns $\pm\delta$ indicate variations in DNR parameters at the upper $(+\delta)$ and lower $(-\delta)$ bounds of the corresponding QCD parameters.

Error Source	Nonstrange		Strange	
	$+\delta$	$-\delta$	$+\delta$	$-\delta$
$\langle m\overline{q}q \rangle$	5.62×10^{-3}	-6.74×10^{-4}	9.38×10^{-3}	3.09×10^{-3}
$\langle \alpha G^2 \rangle$	-9.20×10^{-1}	1.18×10^{0}	-9.16×10^{-1}	1.18×10^{0}
$\langle g\overline{q}\sigma Gq \rangle$	1.11×10^{-4}	1.00×10^{-3}	3.66×10^{-3}	4.77×10^{-3}
α_s	1.70×10^{-1}	-1.86×10^{-1}	1.74×10^{-1}	-1.82×10^{-1}

4.2.6 Discussion

We have calculated 5d and 6d QCD condensate contributions to all spin-0 and spin-1 light quarkonium hybrid correlators with the goal of obtaining QCD LSRs mass predictions in the previously-unstable channels of [136]. However, the 6d gluon and quark condensate

Table 4.5: Contributions to r error at $\tau = 10\,\mathrm{GeV}^4$ due to variations in QCD parameter error. Columns $\pm\delta$ indicate variations in DNR parameters at the upper $(+\delta)$ and lower $(-\delta)$ bounds of the corresponding QCD parameters.

Error Source	Nonstrange		Strange	
	$+\delta$	$-\delta$	$+\delta$	$-\delta$
$\langle m\bar{q}q \rangle$	-2.86×10^{-6}	2.76×10^{-6}	-2.58×10^{-6}	3.04×10^{-6}
$\langle \alpha G^2 \rangle$	4.79×10^{-3}	-4.66×10^{-3}	4.79^{-3}	-4.66×10^{-3}
$\langle g\bar{q}\sigma Gq \rangle$	1.43×10^{-6}	-1.34×10^{-6}	1.70×10^{-6}	-1.06×10^{-6}
α_s	-7.93×10^{-4}	8.73×10^{-4}	-7.93×10^{-4}	8.73×10^{-4}
s_0^{opt}	5.09×10^{-4}	3.53×10^{-4}	3.57×10^{-4}	4.81×10^{-4}

Table 4.6: Contributions to m_1 error at $\tau = 10\,\mathrm{GeV}^4$ due to variations in QCD parameter error. Columns $\pm\delta$ indicate variations in DNR parameters at the upper $(+\delta)$ and lower $(-\delta)$ bounds of the corresponding QCD parameters.

Error Source	Nonstrange		Strange	
	$+\delta$	$-\delta$	$+\delta$	$-\delta$
$\langle m\bar{q}q \rangle$	-6.84×10^{-6}	6.58×10^{-6}	-7.06×10^{-6}	6.35×10^{-6}
$\langle \alpha G^2 \rangle$	5.79×10^{-3}	-7.02×10^{-3}	5.79×10^{-3}	-7.02×10^{-3}
$\langle g\bar{q}\sigma Gq \rangle$	-3.07×10^{-6}	3.01×10^{-6}	-3.29×10^{-6}	2.79×10^{-6}
α_s	-1.06×10^{-3}	1.13×10^{-3}	-1.06×10^{-3}	1.13×10^{-3}
s_0^{opt}	1.48×10^{-1}	-1.21×10^{-1}	1.49×10^{-1}	-1.20×10^{-1}

contributions do not have an imaginary part and hence do not contribute to the LSRs. Also, the 5d mixed condensate contributions turn out to be small. We therefore focused on the suggestion of References [136, 155] that a distribution of resonance strength could be the source of instability, a scenario ideally suited to GSRs methods [9, 75, 165]. The 0^{+-} channel was chosen for detailed investigation because of its phenomenological significance in light of the GlueX experiment. Furthermore, a model-independent analysis of the 0^{+-} hadronic spectral function implies that there is a distribution of resonance strength in this channel.

In examining the SWR (4.62) and DNR (4.68) models, we found that the DNR model provided excellent agreement between QCD and phenomenology. (See Figure 4.6.) The SWR model was rejected on the basis of an atypically large resonance width. In the DNR

Table 4.7: Contributions to m_2 error at $\tau = 10\,\mathrm{GeV}^4$ due to variations in QCD parameter error. Columns $\pm\delta$ indicate variations in DNR parameters at the upper $(+\delta)$ and lower $(-\delta)$ bounds of the corresponding QCD parameters.

Error Source	Nonstrange		Strange	
	$+\delta$	$-\delta$	$+\delta$	$-\delta$
$\langle m\bar{q}q \rangle$	-3.72×10^{-5}	3.58×10^{-5}	-3.79×10^{-5}	3.51×10^{-5}
$\langle \alpha G^2 \rangle$	2.81×10^{-2}	-3.64×10^{-2}	2.81×10^{-2}	-3.64×10^{-2}
$\langle g\bar{q}\sigma Gq \rangle$	-2.01×10^{-5}	1.99×10^{-5}	-2.08×10^{-5}	1.93×10^{-5}
α_s	-5.36×10^{-3}	5.63×10^{-3}	-5.36×10^{-3}	5.63×10^{-3}
s_0^{opt}	1.40×10^{-1}	-1.12×10^{-1}	1.40×10^{-1}	-1.11×10^{-1}

Table 4.8: Calculated total errors in s_0^{opt}, r, m_1, m_2 from contributions in Tables 4.4 - 4.7.

Parameter	Value	
	Nonstrange	Strange
s_0^{opt}	$14.5^{+1.2}_{-0.9}$	$14.5^{+1.2}_{-0.9}$
r	0.712 ± 0.005	0.711 ± 0.005
m_1	$3.57^{+0.15}_{-0.12}$	$3.57^{+0.13}_{-0.12}$
m_2	$2.60^{+0.14}_{-0.12}$	$2.60^{+0.14}_{-0.12}$

model, we find degenerate predictions in the case of both nonstrange and strange quark states from the 0^{+-} current: a $2.60 \pm 0.14\,\mathrm{GeV}$ state ($2.60 \pm 0.14\,\mathrm{GeV}$ in the strange case) with 29% relative coupling, and a state at $3.57 \pm 0.15\,\mathrm{GeV}$ ($3.57 \pm 0.13\,\mathrm{GeV}$) with 71% relative coupling. The smaller coupling of the light state suggests the possibility of mixing with a tetraquark because the expected tetraquark mass range is above $2\,\mathrm{GeV}$ [178].

The lighter state is consistent with recent lattice results that find a predominantly non-strange state around 2.4 GeV and a predominantly strange state around 2.5 GeV in the 0^{+-} channel with $m_\pi = 391$ MeV [30]. Our lighter-state mass determination is somewhat larger than the 2.1–2.5 GeV range of central values in [155]. The literature does not provide a clear interpretation of the heavier 0^{+-} state; however lattice studies [30] of the lightest hybrid meson supermultiplet suggest that the 0^{+-} state exists as part of an excited hybrid supermultiplet with radially-excited $q\bar{q}$ pair (i.e., quark total angular momentum $L_{q\bar{q}} = 1$).

We suggest that this heavier second state arising in the GSRs is a manifestation of an excited hybrid state.

In conclusion, we investigated light quarkonium, exotic ($J^{PC} = 0^{+-}$) hybrid mesons with SWR and DNR models using a GSRs analysis. We disfavoured the SWR model as the predicted resonance width was too large. The double-narrow resonance model yielded two 0^{+-} hybrid states: (2.60 ± 0.14) GeV and (3.57 ± 0.15) GeV ((2.60 ± 0.14) GeV and (3.57 ± 0.13) GeV in the strange case). Additionally, we explored using the Hölder inequality derived for the GSRs as a consistency check on our analysis.

Acknowledgments

4.3 Manuscript: Is the $Y(2175)$ a Strangeonium Hybrid Meson?

Abstract: QCD Gaussian sum-rules are used to explore the vector ($J^{PC} = 1$) strangeonium hybrid interpretation of the $Y(2175)$. Using a two-resonance model consisting of the $Y(2175)$ and an additional resonance, we find that the relative resonance strength of the $Y(2175)$ in the Gaussian sum-rules is less than 5% that of a heavier 2.9 GeV state. This small relative strength presents a challenge to a dominantly-hybrid interpretation of the $Y(2175)$.

4.3.1 Introduction

The initial state radiation (ISR) process in e^+e^- annihilation is a very useful technique to search for vector states (*i.e.*, $J^{PC} = 1^{--}$) in B-factories. In 2006, the BaBar Collaboration studied the cross sections for the ISR processes $e^+e^- \to K^+K^-\pi^+\pi^-$ and $e^+e^- \to K^+K^-\pi^0\pi^0$ up to $4.5\,\text{GeV}$, aiming to confirm the existence of the $Y(4260)$ in the $\phi\pi\pi$ channels. Instead of observing the $Y(4260)$, however, they found a new resonance structure in the $\phi(1020)f_0(980)$ channel, which was named the $Y(2175)$ [179]. (It is also known as the $\phi(2170)$ [1]). This resonance was later confirmed by BaBar [180, 181, 182], BES [138], and Belle [183] and recently by BESIII [184, 185]. Its mass and decay width are $M = (2188 \pm 10)\,\text{MeV}$ and $\Gamma = (83 \pm 12)\,\text{MeV}$ and its quantum numbers are $I^G J^{PC} = 0^- 1^{--}$ [1].

To date, the nature of the $Y(2175)$ is still unknown. Based on strange quarkonium mass predictions using a relativized potential model, only the $3\,^3S_1$ and $2\,^3D_1$ $s\bar{s}$ states are expected to have masses close to that of the $Y(2175)$ [140]. However, both interpretations are disfavoured as the corresponding resonance width predictions are significantly larger than the width of the $Y(2175)$. The width of the $3\,^3S_1$ $s\bar{s}$ state was predicted to be $378\,\text{MeV}$ using the $^3P_0$ decay model [141] whereas the width of the $2\,^3D_1$ $s\bar{s}$ state was predicted to be $167\,\text{MeV}$ in the $^3P_0$ model and $212\,\text{MeV}$ in the flux tube breaking model [142]. Another possible interpretation of the $Y(2175)$ is that of a strangeonium hybrid meson (*i.e.*, $\bar{s}gs$). Masses of vector strangeonium hybrid mesons have been computed using several methodologies including the flux tube model [59, 106, 143, 186], lattice QCD [29], and QCD Laplace sum-rules (LSRs) [187]. The flux tube model calculation of [106] found a vector strangeonium

hybrid mass of 2.1–2.2 GeV. The lattice QCD analysis of [29] found a vector strangeonium hybrid mass between 2.4 GeV and 2.5 GeV while the LSRs calculation of [187] found a heavier mass of (2.9 ± 0.3) GeV. Yet another possible interpretation of the $Y(2175)$ is that of a $ss\bar{s}\bar{s}$ tetraquark. In [144], the masses of vector $ss\bar{s}\bar{s}$ tetraquarks were investigated. Two states were predicted with respective masses (2.34 ± 0.17) GeV and (2.41 ± 0.25) GeV. Other LSRs analyses of $ss\bar{s}\bar{s}$ tetraquarks can be found in [145, 146]. Furthermore, the $Y(2175)$ has also been proposed as a molecular state of $\Lambda\bar{\Lambda}$ [147, 148]. In [147], a chromomagnetic interaction Hamiltonian was used to predict a hexaquark of mass 2.184 GeV that is strongly coupled to the $\Lambda\bar{\Lambda}$ channel. In [148], a one-boson-exchange potential model was used to predict a $\Lambda\bar{\Lambda}$ mass between 2.149 GeV and 2.181 GeV. Also, the $Y(2175)$ has been interpreted as a dynamically generated resonance of $\phi f_0(980)$ [149, 150, 151, 152].

Decay modes and rates will be crucial to determining the nature of the $Y(2175)$. In [141], it was predicted using the $^3P_0$ model that the most important decay modes of the $3\,^3S_1$ $s\bar{s}$ meson would be K^*K^*, $KK^*(1410)$, and $KK_1(1270)$ whereas the KK mode would be very weak. In [142], it was predicted using the $^3P_0$ model that the most important decay modes of the $2\,^3D_1$ $s\bar{s}$ meson would be $KK(1460)$, $KK^*(1410)$, $KK_1(1270)$, and K^*K^*. While not dominant, the KK decay mode was predicted to have a partial width of about 0.06. In [96], it was predicted using flux tube and constituent gluon models that the most important decay modes of a vector strangeonium hybrid would be $KK_1(1400)$, $KK_1(1270)$, $KK^*(1410)$, and $KK_2(1430)$, each containing a S-wave meson plus a P-wave meson, due to the $S + P$ selection rule [46, 96, 188]. Also, it was noted that the $\phi f_0(980)$ mode could be significant. Of particular interest are the KK, K^*K^* and $KK(1460)$ modes which are predicted to be zero for a strangeonium hybrid interpretation (the usual rule that suppresses or even forbids hybrid decays to pairs of S-wave mesons [46, 105, 189]). For the $ss\bar{s}\bar{s}$ tetraquark interpretation, it has been suggested that the $\eta\phi$ channel should be one of the dominant decay modes due to the large phase space in the fall-apart mechanism [96]. However, in [190], it was argued that the $\eta\phi$ decay mode would be greatly suppressed and that the $\phi f_0(980)$, $h_1\eta$, and $h_1\eta'$ modes would be most important. For the $\Lambda\bar{\Lambda}$ interpretation of the $Y(2175)$, the KK decay mode was predicted to dominate [191]. At present, the data concerning decay modes and rates of the $Y(2175)$ is incomplete, making it difficult to draw any definitive conclusions [1].

As they are both observed in ISR processes, the $Y(4260)$ and $Y(2175)$ states have the same quantum numbers, and are often considered as analogous states in the hidden-charm and hidden-strange sectors respectively [179, 192, 193]. Perhaps determining the nature of one will shed light on the other. Since the $Y(4260)$ has been identified as a good candidate for charmonium hybrid $\bar{c}gc$ [50, 98, 194] or hidden-charm tetraquark state $qc\bar{q}\bar{c}$ [195], the $Y(2175)$ meson may also be interpreted as a hybrid or tetraquark candidate.

In this work, we use QCD Gaussian sum-rules (GSRs) methods to study the strangeonium hybrid possibility for $Y(2175)$. In contrast to previous analyses of strangeonium hybrids using LSRs [187], the use of GSRs enables an exploration of the possibility of multiple states with hybrid components, allowing us to examine the scenario of a hybrid component of the $Y(2175)$. We find little evidence in support of the $Y(2175)$ having a significant strangeonium hybrid component.

4.3.2 The Correlator and Gaussian Sum-Rules

We investigate vector strangeonium hybrids through the correlator

$$\Pi(q^2) = \frac{i}{D-1}\left(\frac{q_\mu q_\nu}{q^2} - g_{\mu\nu}\right)\int d^D x\, e^{iq\cdot x}\langle\Omega|\tau j_\mu(x) j_\nu(0)|\Omega\rangle \tag{4.81}$$

where D is spacetime dimension and where the current j_μ is given by

$$j_\mu = \frac{g_s}{2}\bar{s}\gamma^\rho\gamma_5\lambda^a\widetilde{G}^a_{\mu\rho}s. \tag{4.82}$$

In (4.82), s is a strange quark field and $\tilde{G}^a_{\mu\rho}$ is the dual gluon field strength tensor,

$$\widetilde{G}^a_{\mu\rho} = \frac{1}{2}\epsilon_{\mu\rho\omega\zeta}G^a_{\omega\zeta}, \tag{4.83}$$

defined in terms of the Levi-Civita symbol, $\epsilon_{\mu\rho\omega\zeta}$.

Between [187] and [51], the quantity $\Pi(q^2)$ from (4.81) has been computed to leading-order (LO) in $\alpha_s = \frac{g_s^2}{4\pi}$ within the operator product expansion (OPE). In [187], the perturbative and dimension-four (*i.e.* 4d) quark and gluon condensate contributions were calculated. In [51], the 5d mixed, 6d quark, and 6d gluon condensate contributions were calculated as well as

$\mathcal{O}(m_s^2)$ corrections to perturbation theory where m_s is the strange quark mass. Denoting the result as $\Pi^{\text{QCD}}(q^2)$ to emphasize that it is a QCD calculation, we have

$$\Pi^{\text{QCD}}(q^2) = \left(\frac{\alpha_s}{\pi} \left(-\frac{q^6}{240\pi^2} + \frac{5m_s^2 q^4}{48\pi^2} - \frac{4q^2}{9}\langle m_s \bar{s}s \rangle \right) \right.$$
$$\left. + \frac{q^2}{36\pi}\langle \alpha G^2 \rangle + \frac{19\alpha_s m_s}{72\pi}\langle g\bar{q}\sigma Gq \rangle \right) \log\left(\frac{-q^2}{\mu^2} \right) \quad (4.84)$$

where

$$\langle m_s \bar{s}s \rangle = \langle m_s \bar{s}_i^\alpha s_i^\alpha \rangle \quad (4.85)$$

$$\langle \alpha G^2 \rangle = \langle \alpha_s G_{\mu\nu}^a G_{\mu\nu}^a \rangle \quad (4.86)$$

$$\langle g\bar{q}\sigma Gq \rangle = \langle g_s \bar{s}_i^\alpha \sigma_{ij}^{\mu\nu} \lambda_{\alpha\beta}^a G_{\mu\nu}^a s_j^\beta \rangle \quad (4.87)$$

are respectively the 4d strange quark condensate, the 4d gluon condensate, and the 5d mixed strange quark condensate. In (4.85)–(4.87), subscripts on strange quarks are Dirac indices, superscripts are colour indices, and $\sigma^{\mu\nu} = \frac{i}{4}[\gamma^\mu, \gamma^\nu]$. In computing (4.84), divergent integrals were handled through dimensional regularization in $D = 4 + 2\epsilon$ dimensions at $\overline{\text{MS}}$-renormalization scale μ. A dimensionally regularized γ_5 satisfying $\{\gamma_5, \gamma^\mu\} = 0$ and $\gamma_5^2 = 1$ was used following the prescription of [196]. Also, TARCER [168], a Mathematica implementation of the recurrence relations of [82, 83], was employed to reduce the set of needed integral results to a small, well-known collection. An irrelevant polynomial in q^2 has been omitted from (4.84) as it ultimately does not contribute to the GSRs used in this article (see below). Included in this omitted polynomial are the 6d quark and gluon condensate contributions, both of which are constant for this channel as discussed in [51].

The quantity $\Pi(q^2)$ in (4.81) is related to its imaginary part, *i.e.*, the hadronic spectral function, through a dispersion relation

$$\Pi(Q^2) = \frac{Q^8}{\pi} \int_{t_0}^\infty \frac{\text{Im}\Pi(t)}{t^4(t + Q^2)}\, \mathrm{d}t + \cdots \quad (4.88)$$

at Euclidean momentum $Q^2 \equiv -q^2 > 0$. In (4.88), t_0 is a hadron production threshold and $\cdots$ represents subtraction constants, collectively a third degree polynomial in Q^2. On

the left-hand side of (4.88), we identify Π with Π^{QCD} of (4.84). On the right-hand side, we partition the hadronic spectral function using a resonance-plus-continuum decomposition,

$$\frac{1}{\pi}\mathrm{Im}\Pi(t) = \rho^{\mathrm{had}}(t) + \theta(t - s_0)\frac{1}{\pi}\mathrm{Im}\Pi^{\mathrm{QCD}}(t), \qquad (4.89)$$

where $\rho^{\mathrm{had}}(t)$ represents the resonance contribution to $\mathrm{Im}\Pi(t)$ and $\theta(t - s_0)$ is a Heaviside step function shifted to the continuum threshold parameter s_0.

In (4.88), to eliminate subtraction constants as well as the aforementioned polynomials omitted from (4.84) and to enhance the resonance contribution relative to the continuum contribution to the integral on the right-hand side, some transform is typically applied leading to some corresponding variant of QCD sum-rules. Laplace sum-rules, for example, are a common choice (*e.g.*, see [36, 37, 47, 169]). Here, we instead choose to work with (lowest-weight) GSRs defined as [197]

$$G(\hat{s}, \tau) = \sqrt{\frac{\tau}{\pi}} \lim_{\substack{N,\Delta^2 \to \infty \\ \tau = \Delta^2/(4N)}} \frac{(-\Delta^2)^N}{\Gamma(N)} \left(\frac{d}{d\Delta^2}\right)^N \left\{\frac{\Pi(-\hat{s} - i\Delta) - \Pi(-\hat{s} + i\Delta)}{i\Delta}\right\}. \qquad (4.90)$$

Discussions of how to evaluate definition (4.90) for a correlator such as (4.84) can be found in [197, 9, 165]. Substituting (4.89) into (4.88) and applying (4.90), we find

$$G^{\mathrm{QCD}}(\hat{s}, \tau) \equiv \frac{1}{\sqrt{4\pi\tau}} \int_0^\infty e^{-\frac{(\hat{s}-t)^2}{4\tau}} \frac{1}{\pi}\mathrm{Im}\Pi^{\mathrm{QCD}}(t)\,\mathrm{d}t \qquad (4.91)$$

$$\implies G^{\mathrm{QCD}}(\hat{s}, \tau) = \frac{1}{\sqrt{4\pi\tau}} \int_{t_0}^\infty e^{-\frac{(\hat{s}-t)^2}{4\tau}} \rho^{\mathrm{had}}(t)\,\mathrm{d}t + \frac{1}{\sqrt{4\pi\tau}} \int_{s_0}^\infty e^{-\frac{(\hat{s}-t)^2}{4\tau}} \frac{1}{\pi}\mathrm{Im}\Pi^{\mathrm{QCD}}(t)\,\mathrm{d}t. \qquad (4.92)$$

Subtracting the continuum contribution,

$$\frac{1}{\sqrt{4\pi\tau}} \int_{s_0}^\infty e^{-\frac{(\hat{s}-t)^2}{4\tau}} \frac{1}{\pi}\mathrm{Im}\Pi^{\mathrm{QCD}}(t)\,\mathrm{d}t, \qquad (4.93)$$

from (4.91) and (4.92) leads to subtracted GSRs

$$G^{\mathrm{QCD}}(\hat{s},\,\tau,\,s_0) \equiv \frac{1}{\sqrt{4\pi\tau}} \int_0^{s_0} e^{-\frac{(\hat{s}-t)^2}{4\tau}} \frac{1}{\pi} \mathrm{Im}\Pi^{\mathrm{QCD}}(t)\,\mathrm{d}t \tag{4.94}$$

$$\implies G^{\mathrm{QCD}}(\hat{s},\,\tau,\,s_0) = \frac{1}{\sqrt{4\pi\tau}} \int_{t_0}^{\infty} e^{-\frac{(\hat{s}-t)^2}{4\tau}} \rho^{\mathrm{had}}(t)\,\mathrm{d}t. \tag{4.95}$$

Finally, calculating $\mathrm{Im}\Pi^{\mathrm{QCD}}(t)$ from (4.84) and substituting the result into the right-hand side of (4.94), we find

$$G^{\mathrm{QCD}}(\hat{s},\,\tau,\,s_0) \equiv \frac{1}{\sqrt{4\pi\tau}} \int_0^{s_0} e^{-\frac{(\hat{s}-t)^2}{4\tau}} \left(\frac{\alpha_s}{\pi} \left(-\frac{t^3}{240\pi^2} + \frac{5m_s^2 t^2}{48\pi^2} - \frac{4t}{9}\langle m_s \overline{s} s \rangle \right) \right.$$
$$\left. + \frac{t}{36\pi}\langle \alpha G^2 \rangle + \frac{19\alpha_s m_s}{72\pi}\langle g\overline{q}\sigma G q \rangle \right) \mathrm{d}t. \tag{4.96}$$

Note that the definite integral in (4.96) can be evaluated in terms of error functions. The kernel of the subtracted GSRs is a Gaussian of width $\sqrt{2\tau}$ centred at $\hat{s}$. As discussed in [9, 51, 165, 167], GSRs are particularly well-suited to the study of multi-resonance hadron models as, by varying $\hat{s}$, excited and ground state resonances can be probed with similar sensitivity.

Renormalization-group (RG) improvement of (4.96) amounts to replacing α_s and m_s by running quantities at the scale $\mu^2 = \sqrt{\tau}$ (e.g., [197, 198]). The one-loop, $\overline{\mathrm{MS}}$ running coupling at $n_f = 4$ active quark flavours is

$$\alpha_s(\mu) = \frac{\alpha_s(M_\tau)}{1 + \frac{25}{12\pi}\alpha_s(M_\tau)\log\left(\frac{\mu^2}{M_\tau^2}\right)} \tag{4.97}$$

where [1]

$$M_\tau = 1.77686 \pm 0.00012\,\mathrm{GeV} \tag{4.98}$$

$$\alpha_s(M_\tau) = 0.325 \pm 0.015. \tag{4.99}$$

Since the previous analysis of strangeonium hybrid mesons using QCD sum-rules [187], the condensate parameters and quark masses are now known more precisely. In addition to the inclusion of higher-dimensional condensates terms in (4.84), we update the values and

uncertainties in the QCD parameters used in [187]. The running strange quark mass is

$$m_s(\mu) = m_s(2 \text{ GeV}) \left(\frac{\alpha_s(\mu)}{\alpha_s(2 \text{ GeV})} \right)^{\frac{12}{25}} \tag{4.100}$$

where [1]

$$m_s(2 \text{ GeV}) = 96^{+8}_{-4} \text{ MeV}. \tag{4.101}$$

The value of the RG-invariant 4d strange quark condensate is known from PCAC,

$$\langle m_s \bar{s}s \rangle = -\frac{1}{2} f_K^2 m_K^2, \tag{4.102}$$

where [1, 128]

$$m_K = (493.677 \pm 0.016) \text{ MeV} \tag{4.103}$$

$$f_K = (110.0 \pm 4.2) \text{ MeV} \tag{4.104}$$

For the 4d gluon condensate, we use the value from [174],

$$\langle \alpha G^2 \rangle = (0.075 \pm 0.020) \text{ GeV}. \tag{4.105}$$

For the 5d mixed strange quark condensate, we use the estimate from [175, 176],

$$\frac{m_s \langle g\bar{q}\sigma Gq \rangle}{\langle m_s \bar{s}s \rangle} \equiv M_0^2 = (0.8 \pm 0.1) \text{ GeV}^2. \tag{4.106}$$

Integrating (4.95) with respect to $\hat{s}$ gives

$$\int_{-\infty}^{\infty} G^{\text{QCD}}(\hat{s}, \tau, s_0) \, \mathrm{d}\hat{s} = \int_{t_0}^{\infty} \rho^{\text{had}}(t) \, \mathrm{d}t. \tag{4.107}$$

The quantity on the LHS of (4.107) is the lowest-weight finite energy sum-rule (FESR), and, as shown in [197], the spectral function decomposition (4.89) only reproduces the QCD prediction at high energy scales if s_0 is constrained by (4.107). To isolate the information in the GSRs that is independent of the FESR constraint (4.107), we define normalized GSRs

(NGSRs) [9],

$$N^{\mathrm{QCD}}(\hat{s},\,\tau,\,s_0) \equiv \frac{G^{\mathrm{QCD}}(\hat{s},\,\tau,\,s_0)}{\int_{-\infty}^{\infty} G^{\mathrm{QCD}}(\hat{s},\,\tau,\,s_0)\,\mathrm{d}\hat{s}} \tag{4.108}$$

which, from (4.95) and (4.107), implies that

$$N^{\mathrm{QCD}}(\hat{s},\,\tau,\,s_0) = \frac{\frac{1}{\sqrt{4\pi\tau}}\int_{t_0}^{\infty} e^{-\frac{(\hat{s}-t)^2}{4\tau}}\rho^{\mathrm{had}}(t)\,\mathrm{d}t}{\int_{t_0}^{\infty} \rho^{\mathrm{had}}(t)\,\mathrm{d}t}. \tag{4.109}$$

4.3.3 Analysis Methodology and Results

Previous work using LSRs used a single-narrow resonance model and resulted in a strangeonium hybrid mass prediction significantly heavier than the $Y(2175)$ [187]. Compared with that analysis, we include 5d and 6d condensate terms in the OPE and use updated QCD parameter values. Also, as outlined above, Gaussian sum-rules have the ability to probe multiple states in the spectral function. We can therefore update and extend the analysis of Ref. [187] and test the hypothesis of a $Y(2175)$ hybrid component by using a double-narrow resonance model for the hadronic spectral function

$$\rho^{\mathrm{had}}(t) = f_1^2 \delta\left(t - m_1^2\right) + f_2^2 \delta\left(t - m_2^2\right). \tag{4.110}$$

This double narrow-resonance model in (4.95) provides the hadronic contribution, *i.e.,* the right-hand side, to the NGSRs (4.109),

$$N^{\mathrm{had}}(\hat{s},\,\tau) = \frac{1}{\sqrt{4\pi\tau}}\left(r e^{-\frac{(\hat{s}-m_1^2)^2}{4\tau}} + (1-r)e^{-\frac{(\hat{s}-m_2^2)^2}{4\tau}}\right), \tag{4.111}$$

where the normalized couplings are defined as

$$r = \frac{f_1^2}{f_1^2 + f_2^2},\, 1 - r = \frac{f_2^2}{f_1^2 + f_2^2},\, 0 \leq r \leq 1. \tag{4.112}$$

We fix one of our modelled resonances (m_1) using the experimental value given in Refs. [1, 199],

$$m_1 = m_{Y(2175)} = 2.188 \text{ GeV}, \tag{4.113}$$

and the additional resonance (m_2) provides the necessary degrees of freedom in the model for the possibility that the $Y(2175)$ decouples (*i.e.,* that m_1 has normalized coupling $r \approx 0$).

We choose the width of the Gaussian kernel to be $\tau = 10\,\mathrm{GeV}^4$, in line with our previous GSRs analysis of light hybrids [51]. Since this resolution is much larger than the experimental width of the $Y(2175)$ (*i.e.,* $\sqrt{\tau} \gg m_1\Gamma$), the narrow width model is an excellent approximation for the $Y(2175)$. For the undetermined resonance m_2, we assume that it is similarly narrow compared to the Gaussian kernel resolution; this assumption is revisited in the results of our analysis presented below. To determine the remaining unknown quantities $\{m_2, r, s_0\}$ in our model we seek the best fit of the the $\hat{s}$ dependence of the QCD prediction and hadronic model by minimizing the χ^2,

$$\chi^2\left(r, m_2, s_0\right) = \sum_{\hat{s}_{min}}^{\hat{s}_{max}} \left[N^{\mathrm{had}}\left(\hat{s},\,\tau\right) - N^{\mathrm{QCD}}\left(\hat{s},\,\tau\, s_0\right)\right]^2, \qquad (4.114)$$

where we use 161 equally spaced $\hat{s}$ points with $\hat{s}_{\mathrm{min}} = -10\,\mathrm{GeV}^4$ and $\hat{s}_{\mathrm{max}} = 30\,\mathrm{GeV}^4$. This region safely encloses the resonances resulting from our analysis as outlined below. Note that the minimization is constrained by the physical condition $0 \le r \le 1$ in (4.112). The resulting prediction of the resonance parameters and continuum onset is

$$s_0^{\mathrm{opt}} = 9.7 \pm 1.0\,\mathrm{GeV}^2 \qquad (4.115)$$

$$m_2 = m_{\mathrm{fit}} = 2.90 \pm 0.16\,\mathrm{GeV} \qquad (4.116)$$

$$r \le 0.033\,. \qquad (4.117)$$

The uncertainties in (4.115)–(4.117) are obtained by varying the values of the QCD input parameters, and calculating the deviation from the central values in quadrature. Errors are dominated by the variation in $\langle \alpha G^2 \rangle$. An upper bound on r is provided because of the $r \ge 0$ constraint. Figure 4.8 shows that the fit between the QCD prediction and hadronic model is excellent; there is no evidence of any deviations that would suggest a need to refine the model (*e.g.,* inclusion of a numerically-large width $\sqrt{\tau} \sim m_2\Gamma$ for m_2). Figure 4.8 also shows that the fitted region $-10\,\mathrm{GeV}^2 < \hat{s} < 30\,\mathrm{GeV}^2$ encloses the regions where the NGSRs are numerically significant. As a further validation of our results, we note that our mass
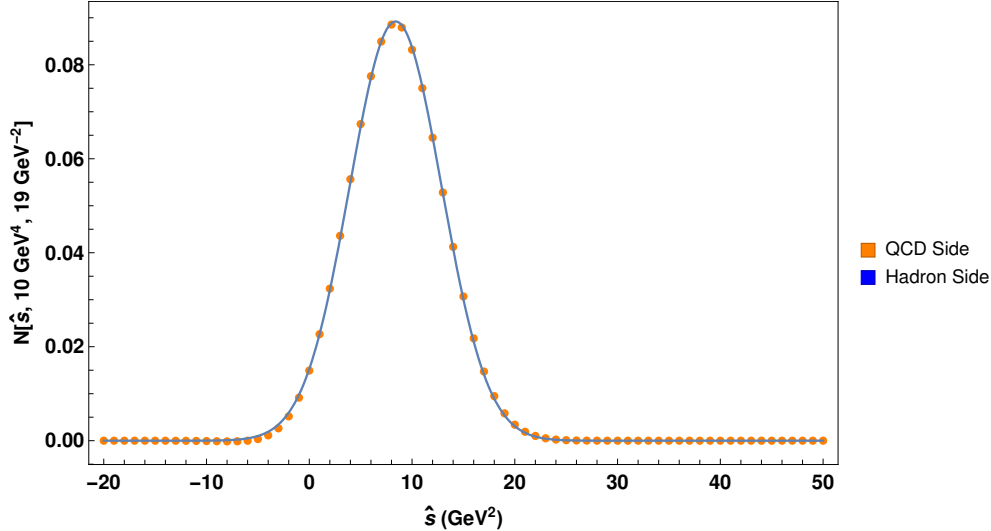
Figure 4.8: Double-narrow resonance model $N^{\text{had}}(\hat{s}, \tau)$ (solid blue curve) and compared to QCD prediction $N^{\text{QCD}}(\hat{s}, \tau, s_0)$ (orange points) for $\tau = 10\,\text{GeV}^4$. Central values of the QCD condensates and the corresponding fitted parameters have been used.

prediction for m_2 is consistent with previous LSRs analyses [187].

The key aspect of our results (4.115)–(4.117) is the small relative resonance strength $r \leq 3.3\%$ of the $Y(2175)$ compared to m_2, which seems to preclude a predominant hybrid component of the $Y(2175)$. We can obtain a more conservative bound on r by calculating the s_0 dependence of r (*i.e.,* choosing s_0 and only fitting r and m_2) and then considering the variation of r within the region of uncertainty in s_0 from (4.115). The result of this analysis leads to the bound $r \leq 5\%$ as shown in Figure 4.9. A similar analysis for m_2 is shown in Figure 4.10.

4.3.4 Discussion

In summary, we have used QCD GSRs to study the strangeonium hybrid interpretation of the $Y(2175)$. Compared to a previous LSRs analysis of vector strangeonium hybrids [187], our calculation includes 5d and 6d condensate contributions, strange quark mass corrections to perturbation theory, and updated QCD parameter values. Furthermore, the advantage of the GSRs approach over the LSRs approach is its comparable sensitivity to multiple states in a hadronic spectral function. This allowed us to explore the relative coupling to
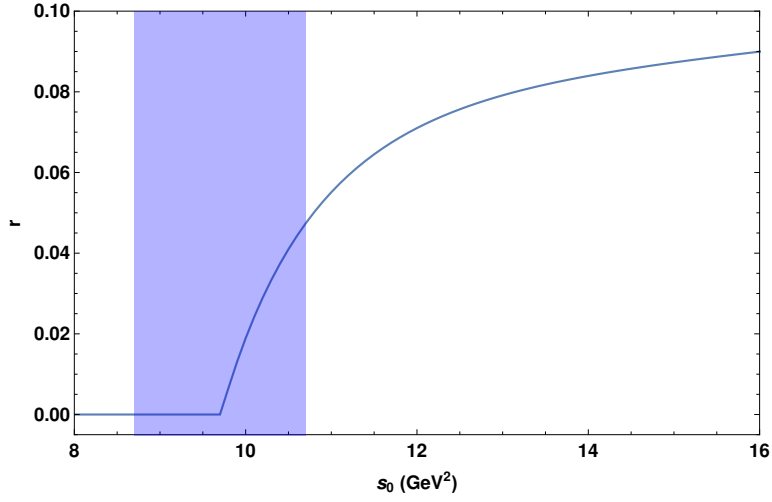
Figure 4.9: Predicted coupling r to $Y(2175)$ state as a function of the continuum onset s_0. The vertical band highlights the optimized value of continuum onset s_0^{opt} with corresponding error (4.115). The physical constraint $r > 0$ has been imposed in the analysis.
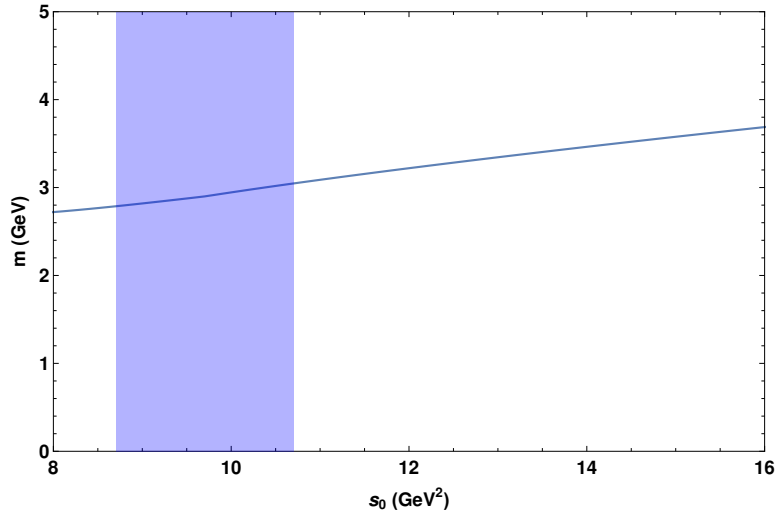
Figure 4.10: Predicted vector strangeonium hybrid mass m_2 as a function of the continuum onset s_0. The vertical band highlights the optimized value of continuum onset s_0^{opt} with corresponding error (4.115).

the hybrid current (4.82) of the $Y(2175)$ and an additional unknown resonance. We found excellent agreement between the QCD prediction and hadronic model, and determined an upper bound $r \leq 5\%$ for the relative coupling strength of the $Y(2175)$. In other words, we found no evidence for a significant strangeonium hybrid component of the $Y(2175)$.

Recently, a structure of mass (2239 ± 13.3) MeV and width (139.8 ± 24.0) MeV (where we have combined statistical and systematic uncertainties) was observed in $e^+ e^- \rightarrow K^+ K^-$ with the BES III detector [200]. If the structure can be identified with the $Y(2175)$, then the observed KK decay mode would disfavour the $3\,^3S_1$ strangeonium meson, strangeonium hybrid, and $ss\bar{s}\bar{s}$ tetraquark interpretations. On the other hand, if the structure can not be identified with the $Y(2175)$, then the lack of observed KK decay mode would disfavour the $2\,^3D_1$ strangeonium meson and $\Lambda\bar{\Lambda}$ interpretations. Clearly, further experimental and theoretical studies are needed.

Acknowledgments

CHAPTER 5

CHIRAL LAGRANGIANS AND QCD SUM RULES

5.1 The Scalar Meson Puzzle

While the focus of Chapters 3 and 4 has been on hybrid mesons in a wide energy range, they are one member of several exotic hadrons that are of experimental interest, all in an attempt to characterize and understand the strong interaction. The notion of exotic hadrons is not a new one; in the same paper over fifty years ago that Gell-Mann proposed his theory of quarks [10], he suggested a redefinition of mesons and baryons to include similarly-spinned and yet to be observed hadrons containing four and five quarks.

5.1.1 Scalar Mesons

The light scalar mesons have been motivating research and questions about the nature of the strong interaction for decades. In the limit of equal quark mass, Gell-Mann and Ne'eman constructed the Eightfold Way [12, 13], which constructed a geometric representation of mesons and baryons using the underlying $SU(3)_F$ quark flavour symmetry present. Figures 5.1a and 5.1b show the pseudoscalar and vector meson representations originating from their work. Similar constructions can be made for the spin 1/2 and 3/2 baryons.

However, classifying the scalar meson states ($J^P = 0^+$) in the same way has proven to be challenging. To date, there exists an overpopulation of experimentally observed scalar mesons at the energies where a nonet is expected to emerge [1]; further, these states do not follow the same mass hierarchy as the pseudoscalar and vector states, leading many to believe a number of these states belong to a second nonet—a grouping of four-quark states [14]. Figure 5.2 shows a prediction of what the four-quark nonet is predicted to look
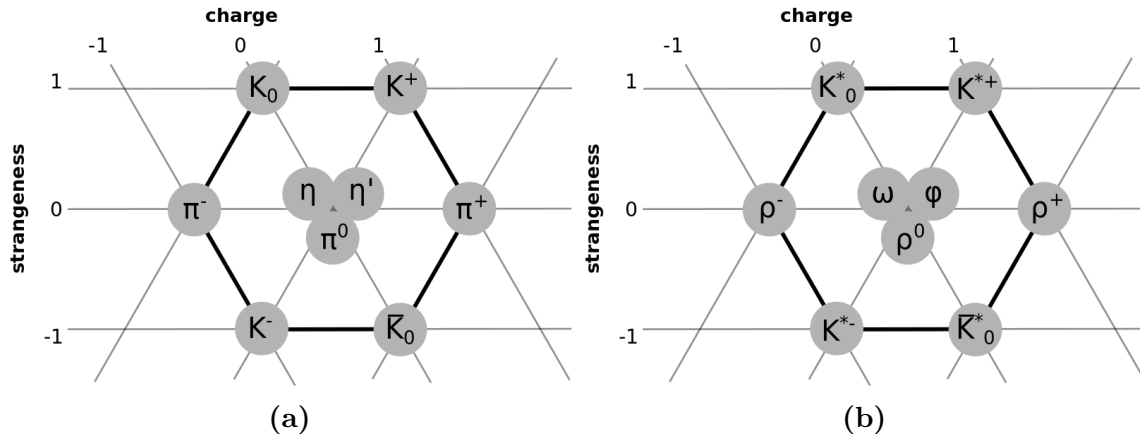
Figure 5.1: Geometric groupings of (a) pseudoscalar and (b) vector meson nonets according to strange quark content and electric charge presented in units of e.

like using known scalar meson states [14], while Figures 5.3a and 5.3b show maps of the pseudoscalar nonet mass hierarchy compared with that of the proposed scalar nonet mass hierarchy shown in Figure 5.2. A similar prediction of a nonet structure for the scalar mesons is more difficult; candidates include the $a_0(1430)$, $f_0(1370)$, $K_0(1430)$, $f_0(1500)$, and the $f_0(1710)$, which leaves one state as excess. However, the $f_0(1500)$ and $f_0(1710)$ states are glueball candidates; identifying the glueball from these states could resolve the excess and clarify which of the remaining states belong to the lowest-lying scalar meson nonet. [14, 201].

To complicate matters, a gluonium state is also predicted in the same range, and significant mixing with meson states has also been predicted [48, 202]. The difficulty in identifying the structure of these states lies not only in the theoretical difficulties in describing non-perturbative dynamics at these lower energies, but also in the distinctly broad resonance widths these states exhibit, and the need for more precise experimental data on them [14].

5.1.2   Chiral Lagrangians and QCD Sum Rules

As a way of approaching the inherent non-perturbative nature of the strong interaction, some have traded the fundamental quark degrees of freedom for a description of strong dynamics using the experimentally observed hadronic degrees of freedom; chiral Lagrangians are one such approach. In the papers that follow, we considered two unmixed scalar nonets S and
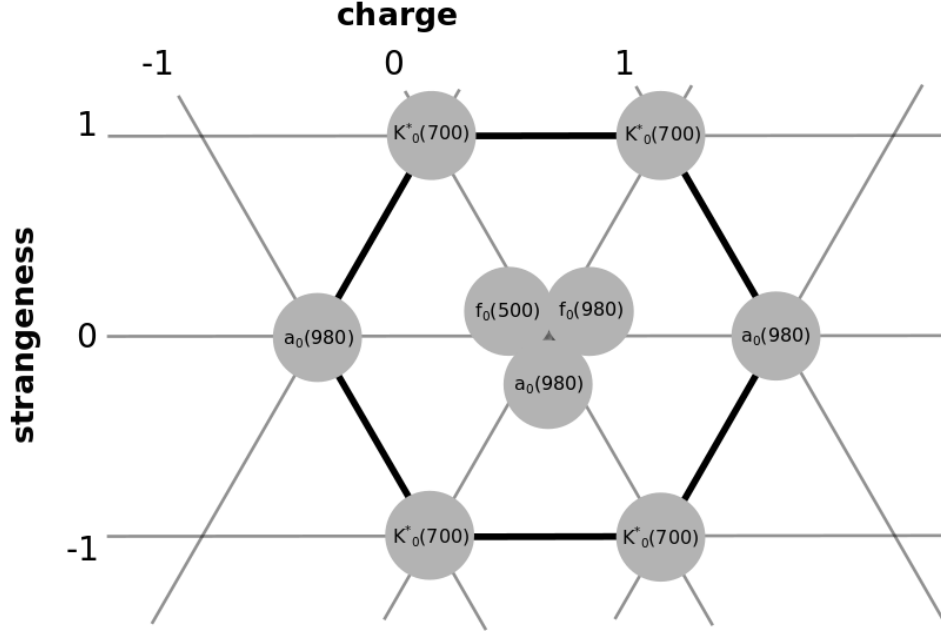
Figure 5.2: Predicted scalar nonet of four-quark states.
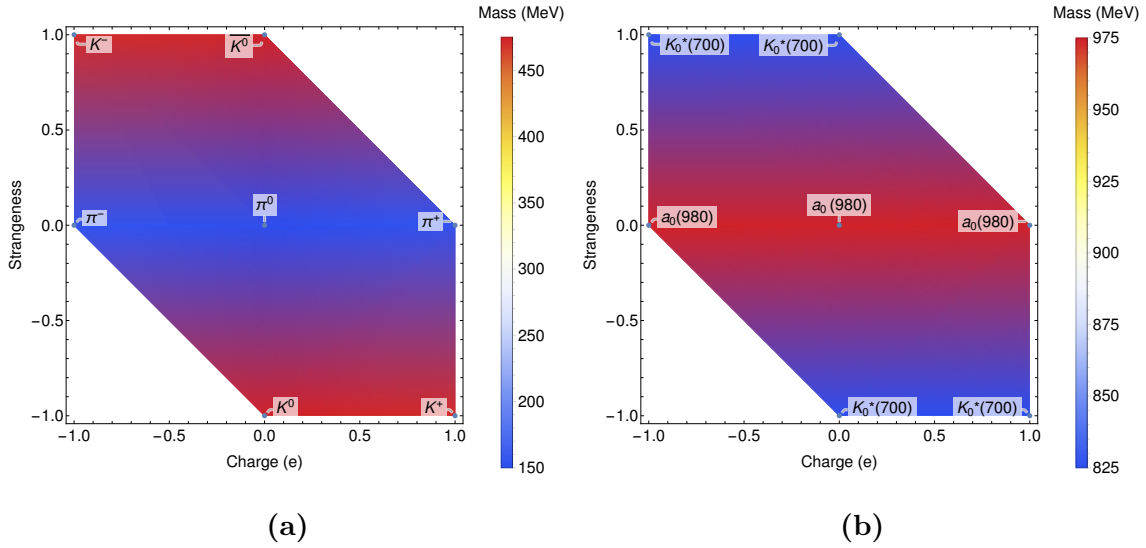
Figure 5.3: Interpolating surface mapping hadronic masses which demonstrate contrasting mass hierarchies of (a) pseudoscalars nonet in Fig. 5.1a, compared with proposed (b) scalar nonets shown in Fig 5.2. Vector nonet mass hierarchy mirrors that of the pseudoscalar nonet hierarchy.

S' of two- and four-quark states respectively

$$S = \begin{pmatrix} S_1^1 & a_0^+ & \kappa^+ \\ a_0^- & S_2^2 & \kappa^0 \\ \kappa^- & \bar{\kappa}^0 & S_3^3 \end{pmatrix} , \quad S' = \begin{pmatrix} S'^1_1 & a'^+_0 & \kappa'^+ \\ a'^-_0 & S'^2_2 & \kappa'^0 \\ \kappa'^- & \bar{\kappa}'^0 & S'^3_3 \end{pmatrix} , \tag{5.1}$$

which form chiral nonets

$$M = S + i\phi \tag{5.2}$$

$$M' = S' + i\phi', \tag{5.3}$$

where ϕ and ϕ' represent pseudoscalar meson nonets similar to S and S'. Using the transformation properties of M and M' under chiral symmetry, we related them to their quark content through scale factor matrices

$$M = I_M M_{\text{QCD}} \tag{5.4}$$

$$M' = I_{M'} M'_{\text{QCD}}. \tag{5.5}$$

where M and M' are the physical, mesonic-level nonets and M_{QCD} and M'_{QCD} are the QCD-level nonet descriptions. Here, the matrices I_M and $I_{M'}$ are scale-factor matrices

$$I_M = -\frac{m_q}{\Lambda^3} \times \mathbb{1} , \quad I_{M'} = \frac{1}{\Lambda'^5} \times \mathbb{1} , \tag{5.6}$$

where Λ and Λ' are constant scale factors with units of energy, and $m_q = (m_u + m_d)/2$. In each paper, we investigate a specific set of isopartners; in Ref. [33] the isotriplets $a_0(980) - a_0(1450)$, and in Ref. [34] the isodoublets $K_0^*(800) - K_0^*(1430)$. We find remarkable agreement between scale factors Λ and Λ' from each individual analysis indicating a consistency with the requirements of chiral symmetry, and that the scale factors demonstrate very little dependence on the energy scale, suggesting that approximating the scale factor as a constant is justified within an estimated error of 5%. These results show an emerging consistency in our

methodology, promising a robust connection between the chiral Lagrangian methodology and QCD sum-rules. My contributions to both of these works pertain to the QCDSR analysis. In the case of the isotriplet analysis, I rederived and made corrections to expressions used in the previous work, improved the optimization procedure, explored the inclusion of updated sum rule parameter values within the analysis, designed Figure 5.4, and edited the manuscript. In the case of the isodoublet analysis, I performed a full analysis and determination of scale factors from GSRs applying the optimization procedure I developed in the isotriplet case, designed the figures, and led in the writing and editing of the manuscript.

The following works may be found published in:

and

5.2   Manuscript: The Bridge Between Chiral Lagrangians and QCD Sum-Rules

Abstract: Properties of the scale-factor matrices forming a bridge between the mesonic fields of chiral Lagrangians and quark-level structures of QCD sum-rules are reviewed. The scale-factor matrices combined with mixing angles provide a physical projection of a QCD correlation function matrix that disentangles the mesonic states. This methodology is illustrated for the isotriplet $a_0(980) - a_0(1450)$ system, and the scale factors are determined from the combined inputs of QCD sum-rules and chiral Lagrangians. The resulting scale factors are shown to be in good agreement with the vacuum expectation values in the chiral Lagrangian framework. The sensitivity of the scale factors on the gluon condensate QCD sum-rule parameter is explored.

5.2.1 Introduction

The interpretation of the light scalar mesons in terms of the underlying quark and gluonic substructures is one of the most challenging aspects of hadronic physics [1, 203, 204]. Given the highly-populated scalar states below 2 GeV, the scenario of a mixture of a two-quark nonet, a four-quark nonet, and gluonium seems natural [7, 201, 205, 206, 207, 208, 209, 210, 211]. In this scenario, the inverted scalar mass spectrum for four-quark states is an important theoretical feature that emerges in the MIT bag model [212] and in QCD sum-rules [213, 214, 215, 216].

Chiral Lagrangian methods, in either the linear [7, 207, 210, 211] or non-linear models [205, 208, 217, 218, 219, 220, 221], are founded on chiral symmetry and its breakdown, and the model parameters are determined from fits to experimental data. For the scalar sector, the mixings among scalar states provides implicit information on their quark substructure, with the lighter states being primarily four-quark compositions while the heavier are primarily two-quark states [7, 219, 208]. An important feature in these chiral Lagrangian analyses is the significant mixture of gluonium in two of the states [201, 208, 222], a feature that also emerges from QCD sum-rule analyses (see e.g., [8, 167, 223, 224, 225, 226] and review of earlier results in Ref. [38]), and in other methods [227, 228].

Both chiral Lagrangian and QCD sum-rule studies of scalar mesons have their limitations. For example, although $U_A(1)$ symmetry provides a fundamental distinction between two-quark and four-quark compositions in chiral Lagrangians [7, 210, 211], there is no way to distinguish between different substructures (e.g, molecular versus diquark). This limitation can be potentially addressed by QCD sum-rules because the field-theoretical results depend on the specific four-quark composition. Similarly, QCD sum-rules are based on quark-hadron duality [36, 37, 169] and require parameterization of the spectral function. In the case of broad, light, and overlapping states such as those found in the scalar sector (e.g., the σ meson) a simple Breit-Wigner parameterization may be insufficient. This limitation can potentially be overcome by guidance on resonance shapes from chiral Lagrangian approaches that have been fitted to experimental data. A precise linkage between chiral Lagrangians and QCD sum-rules could thus lead to synergies for deeper understandings of low-energy

hadronic physics and open new insights and avenues of exploration.

In Ref. [32] this linkage between QCD sum-rules and chiral Lagrangians was developed and validated for the $I = 1$ scalar channel. The key aspect of the resulting bridge connecting QCD sum-rules and chiral Lagrangians are scale factor matrices that combine with mixing angles to form a physical projection of the QCD correlation function onto single hadronic states. In this proceedings article the properties of the scale factor matrices and the projection formalism will be reviewed along with the application to the $I = 1$ channel. The analysis of Ref. [32] is extended to study the dependence of the scale factors on the gluon condensate (a key non-perturbative parameter in QCD sum-rules) to reflect its most recent determination [229].

The generalized linear sigma model in the notation of Refs. [7, 210, 211] contains two chiral nonets M and M' respectively representing a two-quark nonet and a four-quark nonet structure. The two nonets have the same chiral transformation properties but have different $U_A(1)$ charges:

$$
\begin{aligned}
M &\rightarrow U_L \, M \, U_R^\dagger, & M &\rightarrow e^{2i\nu} M \\
M' &\rightarrow U_L \, M' \, U_R^\dagger, & M' &\rightarrow e^{-4i\nu} M' \ .
\end{aligned}
\tag{5.7}
$$

The nonets are expressed in terms of their scalar and pseudoscalar components

$$
\begin{aligned}
M &= S + i\phi \\
M' &= S' + i\phi'
\end{aligned}
\tag{5.8}
$$

where the two scalar meson nonets contain the two- and four-quark "bare" (unmixed) scalars

$$
S = \begin{pmatrix} S_1^1 & a_0^+ & \kappa^+ \\ a_0^- & S_2^2 & \kappa^0 \\ \kappa^- & \bar{\kappa}^0 & S_3^3 \end{pmatrix}, \quad
S' = \begin{pmatrix} S_1'^1 & a_0'^+ & \kappa'^+ \\ a_0'^- & S_2'^2 & \kappa'^0 \\ \kappa'^- & \bar{\kappa}'^0 & S_3'^3 \end{pmatrix}
\tag{5.9}
$$

and similar matrices for ϕ and ϕ'.

We now map M and M' to their QCD counterparts M_{QCD} and M'_{QCD} having appropriate chiral transformation properties. In particular,

$$(M_{\mathrm{QCD}})_a^b \propto (\bar{q}_R)^b (q_L)_a \Rightarrow (S_{\mathrm{QCD}})_a^b = q_a \bar{q}^b \tag{5.10}$$

where as will be seen below there is no loss of generality in the choice of the S_{QCD} proportionality constant. A similar expression exists for S'_{QCD} in terms of four-quark operators, but because of the many possible choices the specific form will be given below. The QCD operators and mesonic fields are related by scale factor matrices I_M and $I_{M'}$ that align the mass dimensions

$$M = I_M M_{\mathrm{QCD}}, \ \ M' = I_{M'} M'_{\mathrm{QCD}} . \tag{5.11}$$

The properties of the scale factor matrices are governed by chiral symmetry. Since both M and M_{QCD} have the transformation properties of (5.7), we have

$$M \to U_L I_M M_{QCD} U_R^\dagger = I_M U_L M_{QCD} U_R^\dagger$$
$$\Rightarrow [U_L, I_M] = 0 . \tag{5.12}$$

A similar analysis for the transformation of $M^\dagger$ yields

$$[U_R, I_M] = 0 . \tag{5.13}$$

Eqs. (5.12) and (5.13) must also apply to $I_{M'}$ because the chiral transformation properties of M and M' are identical

$$[U_R, I_{M'}] = 0 = [U_L, I_{M'}] = 0 . \tag{5.14}$$

Collectively Eqs. (5.12)–(5.14) imply that the scale factor matrices are multiples of the identity matrix

$$I_M = -\frac{m_q}{\Lambda^3} \times \mathbb{1}, \ \ I_{M'} = \frac{1}{\Lambda'^5} \times \mathbb{1}, \tag{5.15}$$

where the (constant) scale factor quantities Λ and Λ' have dimensions of energy that must be determined and the quark mass factor $m_q = (m_u + m_d)/2$ has been chosen to result in renormalization-group invariant currents as discussed below.

The specific example of the isotriplets $a_0(980)$ and $a_0(1450)$ illustrates the determination of the scale factors and the detailed implementation of the bridge between chiral Lagrangians and QCD sum-rules. The physical states are mixtures of the chiral Lagrangian fields S and S' which are then related to QCD operators

$$
\mathbf{A} = \begin{pmatrix} a_0^0(980) \\ a_0^0(1450) \end{pmatrix} = L_a^{-1} \begin{pmatrix} \left(S_1^1 - S_2^2\right)/\sqrt{2} \\ \left(S'^1_1 - S'^2_2\right)/\sqrt{2} \end{pmatrix}
$$
$$
= L_a^{-1} I_a J^{\mathrm{QCD}} \tag{5.16}
$$

where L_a is the rotation matrix for isovectors of Ref. [7], I_a is formed out of the scale factors defined for the two chiral nonets in (5.11) and J^{QCD} is constructed from two- and four-quark operators

$$
L_a^{-1} = \begin{pmatrix} \cos\theta_a & -\sin\theta_a \\ \sin\theta_a & \cos\theta_a \end{pmatrix} , \quad I_a = \begin{pmatrix} \frac{-m_q}{\Lambda^3} & 0 \\ 0 & \frac{1}{\Lambda'^5} \end{pmatrix} \tag{5.17}
$$

$$
J^{\mathrm{QCD}} = \frac{1}{\sqrt{2}} \begin{pmatrix} (S_{\mathrm{QCD}})_1^1 - (S_{\mathrm{QCD}})_2^2 \\ (S'_{\mathrm{QCD}})_1^1 - (S'_{\mathrm{QCD}})_2^2 \end{pmatrix} . \tag{5.18}
$$

Because Eq. (5.16) defines the physical a_0 states, the projected physical currents J^P are defined by

$$
J^P = L_a^{-1} I_a J^{\mathrm{QCD}} . \tag{5.19}
$$

A physical correlation function matrix Π^P is then constructed from a physical projection of a QCD correlation function matrix Π^{QCD}

$$
\Pi^P(Q^2) = \widetilde{\mathcal{T}}^a \Pi^{\mathrm{QCD}}(Q^2)\mathcal{T}^a , \quad \mathcal{T}^a = I_a L_a \tag{5.20}
$$

$$
\Pi_{mn}^{\mathrm{QCD}}(x) = \langle 0|\mathrm{T}\left[J_m^{\mathrm{QCD}}(x)J_n^{\mathrm{QCD}}(0)\right]|0\rangle \tag{5.21}
$$

where $\widetilde{\mathcal{T}}^a$ denotes the transpose of the matrix $\mathcal{T}^a$. Although the development of (5.20) was

123

in the context of the a_0 system, the relation for the projected physical correlator is easily generalized by the appropriate rotation matrix and scale factor matrix.

The physical correlator matrix is diagonal, providing a self-consistency condition relating elements of the QCD correlation function matrix. For example, the case of the 2×2 a_0 system leads to the following constraint from the vanishing of off-diagonal elements[1]

$$\Pi_{12}^{\text{QCD}} = - \left[\frac{\widetilde{\mathcal{T}}_{11}^a \Pi_{11}^{\text{QCD}} \mathcal{T}_{12}^a + \widetilde{\mathcal{T}}_{12}^a \Pi_{22}^{\text{QCD}} \mathcal{T}_{22}^a}{\widetilde{\mathcal{T}}_{11}^a \mathcal{T}_{22}^a + \widetilde{\mathcal{T}}_{12}^a \mathcal{T}_{12}^a} \right] . \tag{5.22}$$

The relation (5.22) can be used in different ways depending on whether it is feasible to calculate the off-diagonal QCD correlator. In the a_0 case, the leading corrections to the off diagonal correlator are a difficult four-loop topology, so (5.22) will be used as input for Π_{12}^{QCD}.

In QCD sum-rule methodologies, an integral transform is applied to a dispersion relation relating the QCD and hadronic contributions to the projected physical correlators [36, 37, 169]. The mixing angle matrix L_a must be chosen to isolate individual states so it is important to use a sum-rule method that can check whether a residual effect of multiple states is occurring because of an insufficiently accurate mixing matrix. Laplace sum-rules are not ideal for this purpose because they suppress heavier states, so Gaussian sum-rules will be employed because they provide similar weight to all states [9, 75]. The hadronic part of the Gaussian sum-rule is given by

$$G^{\text{H}}(\hat{s}, \tau) = \frac{1}{\sqrt{4\pi\tau}} \int_{s_{th}}^{\infty} dt \exp \left[\frac{-(\hat{s} - t)^2}{4\tau} \right] \rho^H(t) . \tag{5.23}$$

In (5.23), the hadronic spectral function is determined via the mesonic fields and a QCD continuum above the continuum threshold s_0.

$$\rho^H(t) = \frac{1}{\pi} \text{Im} \Pi^{\text{H}}(t) \tag{5.24}$$

$$\Pi_{ij}^{\text{H}}(q^2) = \int d^4x \, e^{iq \cdot x} \langle 0| \text{T} \left[\mathbf{A}_i(x) \mathbf{A}_j(0) \right] |0\rangle$$

$$= \delta_{ij} \left(\frac{1}{m_{ai}^2 - q^2 - im_{ai}\Gamma_{ai}} + \text{cont.} \right) \tag{5.25}$$

---

[1]Eq. (5.22) corrects a minor typographical error in Ref. [32].

The effect of final-state interactions in the $\pi\eta$ channel is not significant and therefore in the first approximation is neglected here. The last term denoted by "cont" represents the QCD continuum contribution inherent in QCD sum-rule methods [36, 37, 169]. The hadronic and QCD contributions to the Gaussians sum-rules are now equated:

$$G^H\left(\hat{s}, \tau\right) = \widetilde{\mathcal{T}}^a G^{\text{QCD}}\left(\hat{s}, \tau, s_0\right) \mathcal{T}^a \tag{5.26}$$

where the QCD continuum has been absorbed from the hadronic side into the QCD contributions. Methods for calculating the QCD prediction G^{QCD} from the underlying correlation function are reviewed in Ref. [9]. The hadronic side of (5.26) is diagonal because the states have been disentangled by the rotation matrix and the QCD side of (5.26) is diagonalized by imposing the constraint (5.22)

$$G^H = \begin{pmatrix} (G^H)_{11} & 0 \\ & \\ 0 & (G^H)_{22} \end{pmatrix} = \widetilde{\mathcal{T}}^a G^{\text{QCD}} \mathcal{T}^a. \tag{5.27}$$

The resulting diagonal elements of (5.27) are given by

$$G_{11}^H(\hat{s}, \tau) = aA G_{11}^{QCD}\left(\hat{s}, \tau, s_0^{(1)}\right) - bB G_{22}^{QCD}\left(\hat{s}, \tau, s_0^{(1)}\right) \tag{5.28}$$

$$G_{22}^H(\hat{s}, \tau) = -aB G_{11}^{QCD}\left(\hat{s}, \tau, s_0^{(2)}\right) + bA G_{22}^{QCD}\left(\hat{s}, \tau, s_0^{(2)}\right)$$

$$A = \frac{\cos^2\theta_a}{\cos^2\theta_a - \sin^2\theta_a} \ , \ \ B = \frac{\sin^2\theta_a}{\cos^2\theta_a - \sin^2\theta_a} \tag{5.29}$$

$$a = \frac{m_q^2}{\Lambda^6} \ , \ \ b = \frac{1}{(\Lambda')^{10}} \tag{5.30}$$

where the QCD continuum has been absorbed into the QCD Gaussian sum-rules, G_{11}^H and G_{22}^H respectively represent $a_0(980)$ and $a_0(1450)$, and the factor of m_q^2 is combined with G_{11}^{QCD} for renormalization-group purposes. Note that each sum-rule has its own continuum threshold represented by $s_0^{(1)}$ and $s_0^{(2)}$, and the constraint (5.22) has been used within the QCD prediction.

The QCD currents in (5.18) used to construct the QCD sum-rules are [215, 216, 9]

$$J^{QCD} = \begin{pmatrix} J_1 \\ \\ J_2 \end{pmatrix} , \ J_1 = \left(\bar{u}u - \bar{d}d \right) / \sqrt{2} \tag{5.31}$$

$$J_2 = \frac{\sin \phi}{\sqrt{2}} d_\alpha^T C \gamma_\mu \gamma_5 s_\beta \left(\bar{d}_\alpha \gamma^\mu \gamma_5 C \bar{s}_\beta^T - \alpha \leftrightarrow \beta \right)$$
$$+ \frac{\cos \phi}{\sqrt{2}} d_\alpha^T C \gamma_\mu s_\beta \left(\bar{d}_\alpha \gamma^\mu C \bar{s}_\beta^T + \alpha \leftrightarrow \beta \right) - u \leftrightarrow d \tag{5.32}$$

where C is the charge conjugation operator and $\cot \phi = 1/\sqrt{2}$ [215, 216]. Expressions for the resulting QCD sum-rules can be found in Refs. [8, 9, 215, 216] along with the necessary QCD input parameters (e.g., QCD condensates). The choice $\tau = 3\,\mathrm{GeV}^4$ has been made, consistent with the central value used in Refs. [8, 9]. The physical mass and width of the a_0 states are used along with $\cos \theta_a = 0.493$ from chiral Lagrangians [7]. Two different values of the gluon condensate are considered: $\langle \alpha G^2 \rangle = 0.07\,\mathrm{GeV}^4$ as used in Ref. [32] and $\langle \alpha G^2 \rangle = 0.06\,\mathrm{GeV}^4$ corresponding to the lower bound determined in Ref. [229]. For the strange quark condensate we use $\langle \bar{s}s \rangle = 0.8\langle \bar{q}q \rangle$ (see e.g., Refs. [169, 40]) in conjunction with $m_s/m_q = 27.3$ [1] and PCAC for $m_q\langle \bar{q}q \rangle$.

Eqs. (5.28) are solved for the (constant) scale factors Λ and Λ', and a procedure is developed to optimize the continuum thresholds that minimize the $\hat{s}$ dependence of the scale factors. Fig. 5.4 shows the $\hat{s}$ dependence of the scale factors for the optimized values of the continuum for the two values of the gluon condensate $\langle \alpha G^2 \rangle$. The remarkable independence of the scale factors on the auxiliary sum-rule parameter $\hat{s}$ clearly demonstrates validity of the bridge connecting QCD sum-rules and chiral Lagrangians.

The best-fit predictions of the scale factors and continuum thresholds are given in Table 5.1 along with the vacuum expectation value

$$\langle S_1^1 \rangle = -\frac{m_q\langle \bar{u}u \rangle}{\Lambda^3} . \tag{5.33}$$

The QCD predictions for the vacuum expectation value are in excellent agreement with the chiral Lagrangian value $\langle S_1^1 \rangle = 0.056\,\mathrm{GeV}$ [7]. The scale factor Λ' can also be related to a

vacuum expectation value using the vacuum saturation hypothesis

$$\langle S_1'^1 \rangle = 1.31 \frac{\langle \bar{d}d \rangle \langle \bar{s}s \rangle}{\Lambda'^5} \tag{5.34}$$

The QCD side of (5.34) is not a renormalization-group invariant quantity so it is not clear how to choose a renormalization scale for comparison. An estimate of the QCD value yields $\langle S_1'^1 \rangle \approx 0.08\,\text{GeV}$ which is in reasonable agreement with the chiral Lagrangian value $\langle S_1'^1 \rangle \approx 0.03\,\text{GeV}$ [7] considering that the vacuum saturation hypothesis and renormalization scale dependence effects could each introduce a factor of 2–3.

$\langle \alpha G^2 \rangle$	$s_0^{(1)}$	$s_0^{(2)}$	Λ	Λ'	$\langle S_1^1 \rangle$
0.07	1.50	3.14	0.108	0.270	0.067
0.06	1.53	3.13	0.109	0.267	0.065

Table 5.1: Values for the optimized scale factors $\{\Lambda,\ \Lambda'\}$ and continuum thresholds $\left\{ s_0^{(1)},\ s_0^{(2)} \right\}$ and vacuum expectation value $\langle S_1^1 \rangle$ for different inputs of the gluon condensate $\langle \alpha G^2 \rangle$. All quantities are in appropriate powers of GeV.

Two other aspects were explored in the analysis. Variations away from the chiral Lagrangian mixing angle $\cos \theta_a = 0.493$ were explored, and the optimized χ^2 used to measure the variations of the scale factors from a constant value increased when the mixing angle was decreased to $\cos \theta_a = 0.4$ and increased to $\cos \theta_a = 0.6$, suggesting the possibility that QCD sum-rules could help distinguish between different chiral Lagrangian mixing scenarios. The physical-projection constraint (5.22) was also explored by comparing the Gaussian sum-rule obtained from the constraint with the estimated leading-order perturbative contribution. The good agreement in the order-of-magnitudes emerging from the constraint and perturbative estimates shown in Fig. 5.5 implies that the physical projection of the full QCD sum-rule matrix would be nearly diagonal.

In summary, it has been shown how chiral symmetry governs the properties of scale factor matrices that serve as a bridge connecting QCD sum-rules and chiral Lagrangians. These scale factor matrices combine with a mixing matrix that projects QCD sum-rules onto physical mesonic states. The a_0 system was used to illustrate the extraction of the scale factors using the combined information from chiral Lagrangians and QCD sum-rules. The
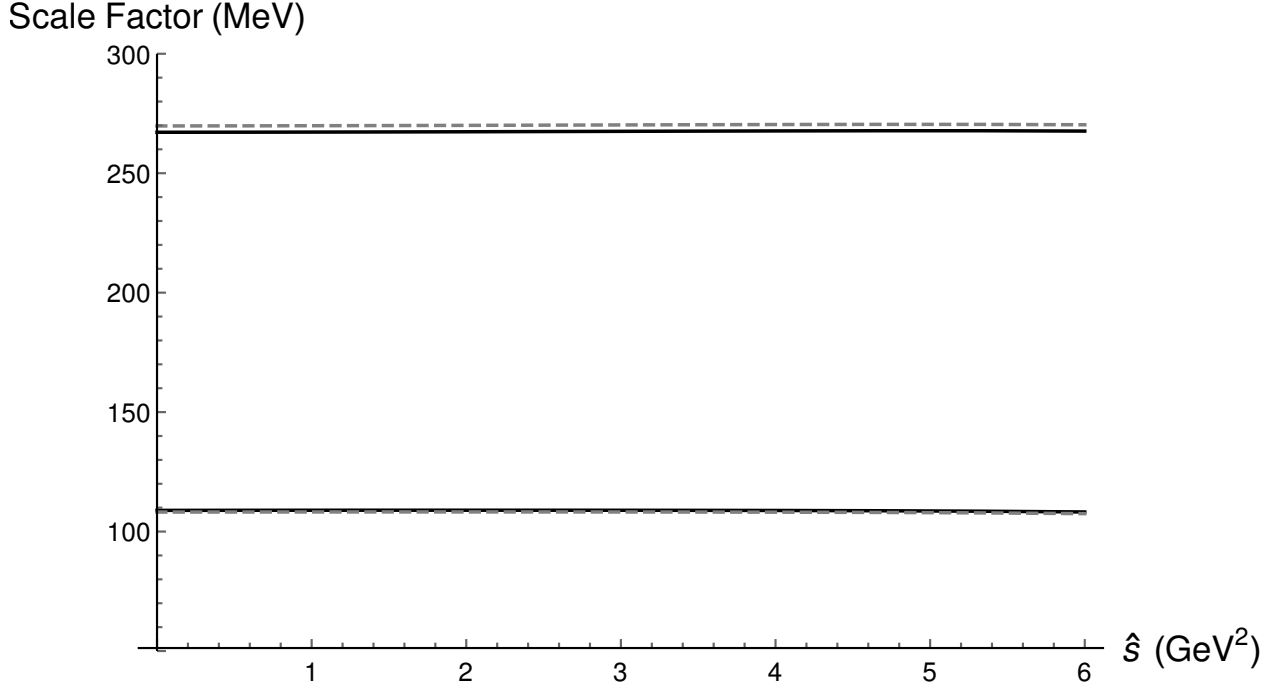
Figure 5.4: The scale factors Λ (lower pair of curves) and Λ' (upper pair of curves) are shown as a function of $\hat{s}$ for optimized continuum thresholds in Table 5.1. Solid curves use the value $\langle \alpha G^2 \rangle = 0.06 \, \text{GeV}^4$ as QCD input and the dashed curves are for $\langle \alpha G^2 \rangle = 0.07 \, \text{GeV}^4$. The mixing angle $\cos \theta_a = 0.493$ of Ref. [7] has been used along with $\tau = 3 \, \text{GeV}^4$ as in Refs. [8, 9].

extracted scale factors were remarkably independent of auxiliary sum-rule parameters and result in excellent agreement with renormalization-group invariant chiral Lagrangian vacuum expectation values, providing an important validation of the methodology to bridge QCD sum-rules and chiral Lagrangians. In future work, the connection between chiral Lagrangians and QCD sum-rules will continue to be explored for other states in the scalar nonets. A key test of the bridge connecting QCD sum-rules and chiral Lagrangians will be to establish the universality of the scale factors for other sectors of the the scalar nonet.
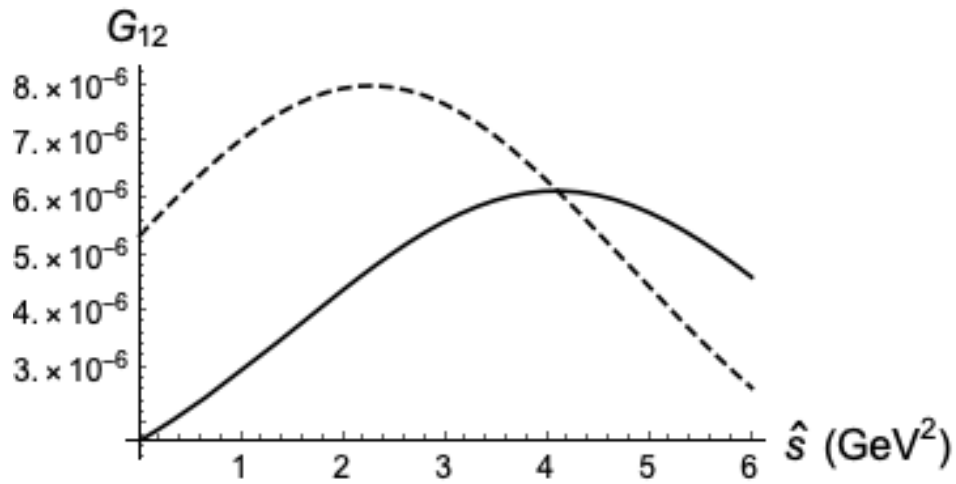
Figure 5.5: Off-diagonal Gaussian sum-rule G_{12} emerging from the QCD constraint (5.22) (solid curve) compared with the estimated leading-order perturbative QCD contribution (dashed-curve). The optimized parameters from the first row of Table 5.1 have been used along with $\tau = 3\,\text{GeV}^4$ as in Refs. [8, 9]. All scales in GeV units.

Acknowledgments

5.3 Manuscript: Universal scale factors relating mesonic fields and quark operators

Abstract: Scale factor matrices relating mesonic fields in chiral Lagrangians and quark-level operators of QCD sum-rules are shown to be constrained by chiral symmetry, resulting in universal scale factors for each chiral nonet. Built upon this interplay between chiral Lagrangians and QCD sum-rules, the scale factors relating the a_0 isotriplet scalar mesons to their underlying quark composite field were recently determined. It is shown that the same technique when applied to K_0^* isodoublet scalars reproduces the same scale factors, confirming the universality property and further validating this connection between chiral Lagrangians and QCD sum-rules which can have nontrivial impacts on our understanding of the low-energy QCD, in general, and the physics of scalar mesons in particular.

5.3.1 Introduction

In the absence of an exact solution to the strong coupling limit of QCD in terms of fundamental quarks, we are forced to accept a less ambitious viewpoint in which the light hadrons are the runner-up candidates for the appropriate low-energy degrees of freedom. Such secondary viewpoints have also been proven to be very challenging; nevertheless, the great efforts by many investigators have led to significant progress over the past several decades and resulted in development of important frameworks such as chiral perturbation theory and various effective models [1, 14, 230]. Such frameworks have enjoyed the blessing of fundamental QCD by respecting several guiding principles such as chiral symmetry (and its breakdown), $U(1)_A$ axial anomaly and various assumptions about the QCD vacuum.

However, the quest for understanding the strong interaction phenomena at low-energies based on fundamental QCD has never stopped and important attempts have been made, most important of which is the approach of the lattice QCD program, which despite all the technical challenges has made an enormous progress [1]. Still, a framework that can directly connect the low-energy strong interaction data to the fundamental quarks and gluons has not yet emerged. Particularly in the scalar meson sector of low-energy QCD, establishing such a connection is even less trivial. On the experimental side, some of these states are broad and overlap with nearby states, leaving some of their experimental properties vague. On the

theoretical side, explaining their mass spectrum and decay properties requires a description beyond the conventional quark-antiquark pattern. For the case of isosinglet scalars, the complexities are significantly greater because these states have the same quantum numbers of the QCD vacuum, which can develop a vacuum expectation value and spontaneously break the chiral symmetry. This means that understanding the substructure of isosinglet scalars, which can be composed of not only various two- and four-quark fields but also of glue, is naturally nontrivial and perhaps beyond the current reach of lattice simulations. For a full understanding of scalar sector, it is vital to seek a bridge that can connect the low-energy data all the way to fundamental QCD. Such a solid bridge currently does not exist, and awaits the exact solution to nonperturbative QCD.

In Refs. [32, 33] we demonstrated how a linkage between two existing frameworks, QCD sum-rules [36, 37, 169] (that significantly connect fundamental QCD to hadronic physics through duality relations) and chiral Lagrangians (which are appropriately designed in terms of the hadron fields and can be conveniently used to describe low-energy data) can provide an approximation of such a bridge. This linkage occurs through scale-factor matrices relating mesonic fields of chiral Lagrangians to quark-level structures of QCD sum-rules. Specifically, the scale factors were first determined for the isovector scalar sector [32, 33] by connecting the QCD sum-rules to the chiral Lagrangian described by the generalized linear sigma model [7, 211]. However, chiral symmetry requires that the scale factors must be universal for all members of the chiral nonets. In the present work, we demonstrate that the same scale factors are remarkably recovered in the isodoublet scalar sector, providing a crucial test of the universality property.

Establishing universality of these scale factors is essential for exploiting the bridge between chiral Lagrangians and QCD sum-rules to address the long-standing puzzles in the isoscalar sector. The exact relationship between the composite fields of quarks representing a mesonic state (which requires a mass dimension of three or higher), and that of a single mesonic field (of mass dimension one) is not known. We have assumed [32, 33] that this relationship is of a simple form where the underlying composite fields of quarks inside a scalar meson are linearly proportional to the meson field. If this assumption is a good approximation to the exact relationship between the meson fields and their underlying quark fields, then the

scale factor adjusting the mass dimensions should reflect certain characteristics of the meson. Chiral symmetry requires that all members of the same chiral nonet have the same scale factor [32, 33] (i.e., the universality condition), which is examined in this work, in testing the proposed bridge, by independently computing the scale factors for the K_0^* isodoublet scalar system and comparing with the previous computation of these factors for the a_0 isovector system of Refs. [32, 33].

At the mesonic level, our framework is the generalized linear sigma model of [7, 211] that we use to demonstrate the bridge between chiral Lagrangians and QCD sum-rules. This framework is formulated in terms of a quark-antiquark chiral nonet and a four-quark chiral nonet, and even though there are no direct connections to the underlying quark world, the distinction between two and four-quark nonets is made through the $U(1)_A$ anomaly. It is shown in [7, 211] (and references therein) how the framework can intake various low-energy experimental data to disentangle two- from four-quark components of each members of the scalar meson nonet. While this information is valuable it is not complete. Several four-quark composite fields, each with the same overall quantum numbers of a given scalar meson, can be formed out of different combinations of color and spin (see for example [210]), but these combinations cannot be disentangled solely on the basis of chiral symmetry – a limitation of chiral Lagrangians (such as those of [7, 211]). QCD sum-rules, on the other hand, have their own limitations — although they directly utilize the specific quark currents, but when probing a complicated scalar meson substructure for which there are numerous possibilities for mixing among two- and four-quark currents, the disentanglement of two- from four-quarks is difficult to achieve in a self contained manner within its framework. Addressing these limitations are examples of the mutual benefits that this bridge provides: The disentanglement of two- from four-quark currents that can be determined at the mesonic level can enhance (and simplify) the overall analysis of QCD sum-rules, and reciprocally, the self consistency checks within the QCD sum-rules can favor one combination of four-quark currents versus the other and remedy a gap in the chiral Lagrangian approach which, due to the lack of direct connection to the underlying quark fields, is oblivious to various four-quark currents. Establishing an interplay between chiral Lagrangians and QCD sum-rules has been the centerpiece of our proposal in Refs. [32, 33]. This idea is not limited to the scalar channel and/or a specific

type of chiral Lagrangian or a particular variant of QCD sum-rules.

We begin by defining our notation. At the mesonic level, we employ the generalized linear sigma model of [7, 211] which is formulated in terms of two chiral nonets M and M' that respectively represent a quark-antiquark nonet and a four-quark nonet (a "molecule" type and/or a diquark-antidiquark type) underlying substructure. Both chiral nonets transform in the same way under chiral transformation but differently under $U(1)_A$:

$$
\begin{aligned}
M &\rightarrow U_L M U_R^\dagger,\ M \rightarrow e^{2i\nu} M \\
M' &\rightarrow U_L M' U_R^\dagger,\ M' \rightarrow e^{-4i\nu} M'
\end{aligned}
\tag{5.35}
$$

The axial charge is the main tool for distinguishing these two nonets. Each of these two chiral nonets can be expressed in terms of a scalar and pseudoscalar meson nonet

$$
\begin{aligned}
M &= S + i\phi \\
M' &= S' + i\phi'
\end{aligned}
\tag{5.36}
$$

where the two scalar meson nonets contain the two- and four-quark "bare" (unmixed) scalars

$$
S = \begin{pmatrix} S_1^1 & a_0^+ & \kappa^+ \\ a_0^- & S_2^2 & \kappa^0 \\ \kappa^- & \bar{\kappa}^0 & S_3^3 \end{pmatrix}, \quad
S' = \begin{pmatrix} S'^1_1 & a'^+_0 & \kappa'^+ \\ a'^-_0 & S'^2_2 & \kappa'^0 \\ \kappa'^- & \bar{\kappa}'^0 & S'^3_3 \end{pmatrix}
\tag{5.37}
$$

and similar matrices for ϕ and ϕ'. The framework of Ref. [7, 211, 210] provides a detailed analysis of the mixing between these two "bare" nonets and how that results in a description of mass spectrum, decay widths and scattering analysis of scalar as well as pseudoscalar mesons below and above 1 GeV. In this picture and of specific interest in this work, the physical isodoublet scalars $K_0^*(700)$ and $K_0^*(1430)$ become a linear admixture of two- and four-quark components κ and κ' respectively. Understanding the physical characteristics of $K_0^*(700)$, particularly its substructure, has posed many challenges and has resulted in numerous investigations [1]. Particularly, the possibility of a non-quark-antiquark nature of

134

this state has been extensively studied [7, 205, 211, 231, 232, 233, 234, 235, 236, 237, 238, 239, 240].

The transformation properties (5.35) as well as the decompositions (5.36) are direct consequences of the assumed underlying quark configurations. The two mesonic-level chiral nonets M and M' can be mapped to the quark-level chiral nonets M_{QCD} and M'_{QCD}. For example, Eq. (5.35) implies

$$(M_{\mathrm{QCD}})^b_a \propto (\bar{q}_R)^b (q_L)_a \Rightarrow (S_{\mathrm{QCD}})^b_a \propto q_a \bar{q}^b \ . \tag{5.38}$$

To make the exact connection to the quark world we need to make a specific choice for the proportionality factor, and with no loss of generality we choose $(S_{\mathrm{QCD}})^b_a = q_a \bar{q}^b$. Similarly, M'_{QCD} can be mapped to quark-level composite field configurations. However, in this case there are several options, each representing a different angular momentum, spin, flavor and color configurations for diquark-antidiquark combination. Here we do not list such quark configurations and the specific form used for our analysis will be given below.

We assume a simple relationship between the quark-level nonets M_{QCD} and M'_{QCD} and the physical mesonic-level nonets M and M' via a scale-factor matrix that adjusts the mass dimensions

$$M = I_M M_{\mathrm{QCD}} \ , \ \ M' = I_{M'} M'_{\mathrm{QCD}} \ . \tag{5.39}$$

As shown in [32, 33], chiral symmetry imposes the following constraints on the scale factor matrices

$$[U_R, I_M] = [U_L, I_M] = 0 \ , \tag{5.40}$$

$$[U_R, I_{M'}] = [U_L, I_{M'}] = 0 \ , \tag{5.41}$$

implying that the scale matrices are multiples of the identity matrix

$$I_M = -\frac{m_q}{\Lambda^3} \times \mathbb{1} \ , \ \ I_{M'} = \frac{1}{\Lambda'^5} \times \mathbb{1} \ , \tag{5.42}$$

where the (constant) scale factor quantities Λ and Λ' have dimensions of energy that must be determined, and the quark mass factor $m_q = (m_u + m_d)/2$ has been chosen to result in renormalization-group invariant currents as discussed below. This methodology can be

135

generalized to include additional substructures (e.g., glueball components) through an additional scale factor. The scale factors Λ and Λ' have been determined in the study of a_0 isotriplet states [32, 33] and will be redetermined here for isodoublet system to demonstrate universality.

We now consider the specific example of the isodoublets $K_0^*(700)$ and $K_0^*(1430)$, for which the physical states are related to the QCD operators via

$$\mathbf{K} = \begin{pmatrix} K_0^*(700) \\ K_0^*(1430) \end{pmatrix} = L_\kappa^{-1} \begin{pmatrix} S_2^3 \\ (S')_2^3 \end{pmatrix} = L_\kappa^{-1} I_\kappa J^{\mathrm{QCD}} \tag{5.43}$$

where L_κ^{-1} is the rotation matrix that disentangles two- from four-quark components of isodoublets, I_κ is formed out of the scale factors defined for the two chiral nonets in (5.42), and J^{QCD} is constructed from two- and four-quark operators (the specific form will be given below):

$$L_\kappa^{-1} = \begin{pmatrix} \cos\theta_\kappa & -\sin\theta_\kappa \\ \sin\theta_\kappa & \cos\theta_\kappa \end{pmatrix} , \ I_\kappa = \begin{pmatrix} \frac{-m_q}{\Lambda^3} & 0 \\ 0 & \frac{1}{\Lambda'^5} \end{pmatrix} . \tag{5.44}$$

Since (5.43) relates the physical states to QCD operators, we define the projected physical currents $J^P = L_\kappa^{-1} I_\kappa J^{\mathrm{QCD}}$ that define a physical correlation function matrix Π^P constructed from a physically-projected QCD correlation function matrix Π^{QCD}

$$\Pi^P(Q^2) = \widetilde{\mathcal{T}}^\kappa \Pi^{\mathrm{QCD}}(Q^2) \mathcal{T}^\kappa , \quad \mathcal{T}^\kappa = I_\kappa L_\kappa \tag{5.45}$$

$$\Pi_{mn}^{\mathrm{QCD}}(x) = \langle 0| \mathrm{T} \left[J_m^{\mathrm{QCD}}(x) J_n^{\mathrm{QCD}}(0)^\dagger \right] |0\rangle \tag{5.46}$$

where $\widetilde{\mathcal{T}}^\kappa$ denotes the transpose of the matrix $\mathcal{T}^\kappa$.

The projected physical correlator matrix is diagonal, providing a self-consistency condition between elements of the QCD correlation function matrix. In our 2×2 K_0^* isodoublet system we have the following constraint from the vanishing of off-diagonal elements (A minor

136

typographical error in Ref. [32] is corrected in (5.47) and [33].)

$$\Pi_{12}^{\mathrm{QCD}} = - \left[\frac{\widetilde{\mathcal{T}}_{11}^{\kappa} \Pi_{11}^{\mathrm{QCD}} \mathcal{T}_{12}^{\kappa} + \widetilde{\mathcal{T}}_{12}^{\kappa} \Pi_{22}^{\mathrm{QCD}} \mathcal{T}_{22}^{\kappa}}{\widetilde{\mathcal{T}}_{11}^{\kappa} \mathcal{T}_{22}^{\kappa} + \widetilde{\mathcal{T}}_{12}^{\kappa} \mathcal{T}_{12}^{\kappa}} \right] . \tag{5.47}$$

The relation (5.47) will be used as input for Π_{12}^{QCD} because the QCD off-diagonal correlator is unknown and not readily calculable because of its complicated higher-loop topology.

QCD sum-rule methodologies are based on quark-hadron duality, and apply an integral transform to a dispersion relation relating the QCD and hadronic contributions to the projected physical correlators [36, 37, 169]. The mixing matrix L_{κ} must disentangle individual states so a sum-rule method is needed to check whether a residual effect of multiple states is occurring because of an insufficiently accurate mixing matrix. Laplace sum-rules are not suitable because they suppress heavier states, so Gaussian sum-rules will be employed because they provide similar weight to all states [9, 197]. The hadronic part of the Gaussian sum-rule is given by

$$G^H(\hat{s}, \tau) = \frac{1}{\sqrt{4\pi\tau}} \int_{s_{th}}^{\infty} dt \exp\left[\frac{-(\hat{s} - t)^2}{4\tau} \right] \rho^H(t) . \tag{5.48}$$

The hadronic spectral function ρ^H in (5.48) is determined from the mesonic fields and a QCD continuum above the continuum threshold s_0:

$$\rho^H(t) = \frac{1}{\pi} \mathrm{Im}\Pi^H(t) + \theta(t - s_0) \frac{1}{\pi} \mathrm{Im}\Pi^{\mathrm{QCD}}(t) \tag{5.49}$$

$$\Pi_{ij}^H(q^2) = \int d^4x\, e^{iq\cdot x} \langle 0 | \mathrm{T}\left[\mathbf{K}_i(x) \mathbf{K}_j^{\dagger}(0) \right] | 0 \rangle$$

$$= \delta_{ij} \left(\frac{1}{m_{\kappa i}^2 - q^2 - i m_{\kappa i} \Gamma_{\kappa i}} \right) . \tag{5.50}$$

The last term in (5.49) represents the QCD continuum contribution inherent in QCD sum-rule methods [36, 37, 169]. The effect of final state interactions in the πK channel is quite large near the kappa pole. Within the framework of generalized linear sigma model, these are estimated in [241].

The hadronic and QCD contributions to the Gaussian sum-rules are now equated:

$$G^H\left(\hat{s},\tau\right) = \widetilde{\mathcal{T}}^\kappa G^{\text{QCD}}\left(\hat{s},\tau,s_0\right)\mathcal{T}^\kappa \tag{5.51}$$

where the QCD continuum has been absorbed from the hadronic side into the QCD contributions. Methods for calculating the QCD prediction G^{QCD} from the underlying correlation function are reviewed in [9]. The QCD side of (5.51) is diagonalized via the constraint (5.47) and the hadronic side of (5.51) is diagonal because the rotation matrix disentangles the states

$$G^H = \begin{pmatrix} (G^H)_{11} & 0 \\ 0 & (G^H)_{22} \end{pmatrix} = \widetilde{\mathcal{T}}^\kappa G^{\text{QCD}}\mathcal{T}^\kappa. \tag{5.52}$$

The resulting diagonal elements of (5.52) are given by

$$G_{11}^H(\hat{s},\tau) = aAG_{11}^{\text{QCD}}\left(\hat{s},\tau,s_0^{(1)}\right) - bBG_{22}^{\text{QCD}}\left(\hat{s},\tau,s_0^{(1)}\right) \tag{5.53}$$

$$G_{22}^H(\hat{s},\tau) = -aBG_{11}^{\text{QCD}}\left(\hat{s},\tau,s_0^{(2)}\right) + bAG_{22}^{\text{QCD}}\left(\hat{s},\tau,s_0^{(2)}\right)$$

$$A = \frac{\cos^2\theta_a}{\cos^2\theta_a - \sin^2\theta_a}, \quad B = \frac{\sin^2\theta_a}{\cos^2\theta_a - \sin^2\theta_a} \tag{5.54}$$

$$a = \frac{m_q^2}{\Lambda^6}, \quad b = \frac{1}{(\Lambda')^{10}} \tag{5.55}$$

where G_{11}^H and G_{22}^H respectively represent $K_0^*(700)$ and $K_0^*(1430)$ contributions, and the factor of m_q^2 is combined with G_{11}^{QCD} for renormalization-group purposes. Note that each sum-rule has its own continuum threshold represented by $s_0^{(1)}$ and $s_0^{(2)}$, and the constraint (5.47) has been used within the QCD prediction.

The scale factors Λ and Λ' for the isodoublet K_0^* scalar meson system can now be calcu-

lated. The QCD currents in (5.43) are

$$
J^{\mathrm{QCD}} = \begin{pmatrix} J_1 \\ \\ J_2 \end{pmatrix} , \ J_1 = \bar{d}s \tag{5.56}
$$

$$
\begin{aligned}
J_2 &= \sin(\phi) u_\alpha^T C \gamma_\mu \gamma_5 s_\beta \left(\bar{d}_\alpha \gamma^\mu \gamma_5 C \bar{u}_\beta^T - \alpha \leftrightarrow \beta \right) \\
&+ \cos(\phi) d_\alpha^T C \gamma_\mu s_\beta \left(\bar{d}_\alpha \gamma^\mu C \bar{u}_\beta^T + \alpha \leftrightarrow \beta \right)
\end{aligned} \tag{5.57}
$$

where C is the charge conjugation operator and $\cot\phi = 1/\sqrt{2}$ [215, 216]. Given an input of $\cos\theta_\kappa = 0.4161$ from chiral Lagrangians [7, 211] and the physical mass and width of the K_0^* states, (we use $m_\kappa = 824\,\mathrm{MeV}$, $\Gamma_\kappa = 478\,\mathrm{MeV}$ for the $K_0^*(700)$ and $m_K = 1425\,\mathrm{MeV}$, $\Gamma_K = 270\,\mathrm{MeV}$ for the $K_0^*(1430)$ to be consistent with [1]) one can solve (5.53) for the (constant) scale factors Λ and Λ', and optimize the continuum thresholds to minimize the $\hat{s}$ dependence of the scale factors.

The correlation function for the two-quark current J_1 is given in [226, 242] and the methods of [9] can then be used to form the Gaussian sum-rule:

$$
G_{11}^{\mathrm{QCD}} (\hat{s}, \tau, s_0) =
$$

$$
\frac{3}{8\pi^2} \int_0^{s_0} t\,dt \left[\left(1 + \frac{17}{3}\frac{\alpha_s}{\pi} \right) - 2\frac{\alpha_s}{\pi} \log\left(\frac{t}{\sqrt{\tau}} \right) \right] W(t, \hat{s}, \tau)
$$

$$
+ \frac{\pi n_c \rho_c^2}{m_s^* m_q^*} \int_0^{s_0} t J_1 \left(\rho_c \sqrt{t} \right) Y_1 \left(\rho_c \sqrt{t} \right) W(t, \hat{s}, \tau)\,dt \tag{5.58}
$$

$$
+ \exp\left\{ \left(-\frac{\hat{s}^2}{4\tau} \right) \right\} \left[\frac{1}{2\sqrt{\pi\tau}} \langle C_4^s \mathcal{O}_4^s \rangle - \frac{\hat{s}}{4\tau\sqrt{\pi\tau}} \langle C_6^s \mathcal{O}_6^s \rangle \right] ,
$$

$$
W(t, \hat{s}, \tau) = \frac{1}{\sqrt{4\pi\tau}} \exp\left\{ \left(-\frac{(t - \hat{s})^2}{4\tau} \right) \right\} \tag{5.59}
$$

$$
\langle C_4^s \mathcal{O}_4^s \rangle = \langle m_s \bar{q}q \rangle + \frac{1}{2} \langle m_s \bar{s}s \rangle + \frac{1}{8\pi} \langle \alpha_s G^2 \rangle , \tag{5.60}
$$

$$
\begin{aligned}
\langle C_6^s \mathcal{O}_6^s \rangle &= -\frac{1}{2} \langle m_s \bar{q}\sigma Gq \rangle - \frac{1}{2} \langle m_q \bar{s}\sigma Gs \rangle \\
&- \frac{16\pi}{27} \alpha_s \left(\langle \bar{q}q \rangle^2 + \langle \bar{s}s \rangle^2 \right) - \frac{48}{9} \alpha_s \langle \bar{q}q \rangle \langle \bar{s}s \rangle ,
\end{aligned} \tag{5.61}
$$

where q denotes the non-strange u, d quarks. Because G_{11}^{QCD} is being combined with m_q^2, the

139

combination satisfies a homogenous renormalization-group equation, which requires evaluating all running quantities at the renormalization scale $\nu^2 = \sqrt{\tau}$ [9]. Similarly, the Gaussian sum-rule related to the four-quark current J_2 is obtained via

$$G_{22}^{\mathrm{QCD}}\left(\hat{s}, \tau, s_0\right) = \int_0^{s_0} dt\, W\left(t, \hat{s}, \tau\right) \rho^{\mathrm{QCD}}(t) \tag{5.62}$$

where $\rho^{\mathrm{QCD}}(t)$ is given in [215, 216]. Because this result is leading-order, renormalization of the current J_2 represents a higher-order effect and the Gaussian sum-rule G_{22}^{QCD} effectively satisfies a homogenous renormalization-group equation, allowing application of the renormalization-group results of Ref. [9]. For the QCD input parameters we use PDG values [1] (quark masses, and α_s) and the following QCD condensate [169, 174, 175, 176] and instanton liquid model parameters [243, 244]

$$\langle \alpha_s G^2 \rangle = 0.07\, \mathrm{GeV}^4\,, \tag{5.63}$$

$$\frac{\langle \bar{q}\sigma G q \rangle}{\langle \bar{q}q \rangle} = \frac{\langle \bar{s}\sigma G s \rangle}{\langle \bar{s}s \rangle} = 0.8\, \mathrm{GeV}^2 \tag{5.64}$$

$$\langle \bar{q}q \rangle = (-0.24\, \mathrm{GeV})^3\,,\ \ \langle \bar{s}s \rangle = 0.8\langle \bar{q}q \rangle \tag{5.65}$$

$$n_c = 8.0 \times 10^{-4}\, \mathrm{GeV}^4\,,\ \ \rho = 1/600\, \mathrm{MeV}\,. \tag{5.66}$$

$$m_q^* = 170\, \mathrm{MeV}\,,\ \ m_s^* = 220\, \mathrm{MeV} \tag{5.67}$$

The m_s/m_q ratio is of particular importance because it appears in both the QCD inputs and as a parameter in the chiral Lagrangian analysis. We choose $\tau = 3\, \mathrm{GeV}^4$ consistent with the central value used in Refs. [9, 165].

Fig. 5.6 shows the $\hat{s}$ dependence of the scale factors for the optimized values of the continuum for both the a_0 [32, 33] and K_0^* channels. The a_0 channel results have been updated from [32, 33] to use $\cos\theta_a = 0.6304$ consistent with the m_s/m_q mass ratio used for the K_0^* analysis. The remarkable independence of the scale factors on the auxiliary sum-rule parameter $\hat{s}$ demonstrates the validity of the scale-factor matrices connecting chiral Lagrangians mesonic fields and the quark-level operators in QCD sum-rules. As is evident from Table 5.2, the best-fit predictions of the scale factors clearly demonstrate the crucial

universality property required by chiral symmetry.

In addition to providing a bridge between chiral Lagrangians and QCD sum-rules, the scale factors can also be related to the chiral Lagrangian vacuum expectations values via $\langle S_1^1 \rangle = -m_q \langle \bar{u}u \rangle / \Lambda^3$ and $\langle S'^1_1 \rangle \approx 1.31 \langle \bar{d}d \rangle \langle \bar{s}s \rangle / \Lambda'^5$. The relation $\langle S'^1_1 \rangle$ is approximate because it depends on the renormalization scale and relies upon the vacuum saturation approximation. As discussed in [32, 33], the resulting agreement is excellent for $\langle S_1^1 \rangle$ and provides the approximate scale for $\langle S'^1_1 \rangle$.
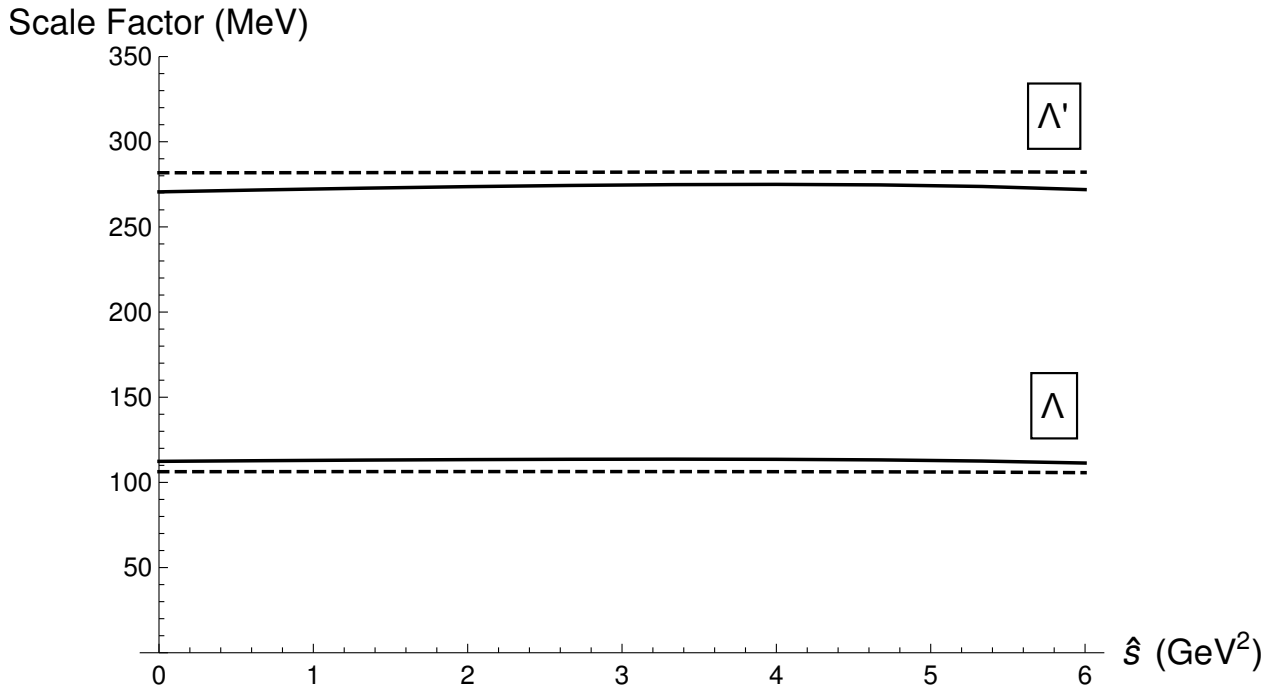
Figure 5.6: The scale factors Λ (lower pair of curves) and Λ' (upper pair of curves) are shown as a function of $\hat{s}$ for optimized continuum thresholds in Table 5.2. Solid curves are for the K_0^* channel and dashed curves are for the a_0 channel.

Channel	$s_0^{(1)}$	$s_0^{(2)}$	Λ	Λ'
K_0^*	1.61	3.04	0.114	0.276
a_0	1.68	2.88	0.106	0.282

Table 5.2: Values for the optimized scale factors Λ, Λ' and continuum thresholds $s_0^{(1)}$, $s_0^{(2)}$ for the a_0 and K_0^* channels. All quantities are in appropriate powers of GeV.

In summary, it has been shown that chiral symmetry transformation properties require

that the scale factor matrices serving as a bridge connecting QCD sum-rules and chiral Lagrangians must contain universal scale factors for all sectors of the chiral nonets. The scale factors determined in this work for the K_0^* system are in remarkable agreement with the corresponding values previously found in the a_0 channel [32, 33] (see Table 5.2), providing a key demonstration of the universality property. With evidence for universal scale factors now established, more complicated sectors of the scalar nonets can therefore be simplified by taking input of the universal scale factors from other channels in the nonet. This powerful synergy between chiral Lagrangians and QCD will enable future progress on more challenging and controversial aspects of low-energy hadronic physics.

Acknowledgments

CHAPTER 6

HYBRID BARYONS

6.1 Hybrid Baryons

As has been discussed in the preceding chapters, since the early formulation of the conventional quark model by Gell-Mann and Zweig [10, 11], hadronic states not conforming to $q\bar{q}$, qqq, or $\bar{q}\bar{q}\bar{q}$ structures have been imagined, and are allowed within QCD. Experiments have observed and confirmed some of these multi-quark state predictions [19, 20]; however, identification and confirmation of states with valence gluon content has been elusive. Experiments are now underway to search for the lowest-lying hybrid meson ($qg\bar{q}$) and scalar glueball (gg) hadronic states [25].

A less discussed variation on structures beyond the conventional quark model is the *hybrid baryon*. Analogous to the $qg\bar{q}$ structure of the hybrid meson, the hybrid baryon is a colour-singlet set of three quarks (antiquarks) and a constituent gluon. Unlike quarkonium-like hybrid mesons, the hybrid baryon spectrum does not carry the "smoking gun" exotic quantum number signatures that their hybrid meson analogues can; hybrid baryons, like their conventional counterparts, carry half-integer total angular momentum J, and parity $P \in \{-1, +1\}$. Identification of hybrid baryons must be through examining decay processes or through observation of overpopulated states i.e., more states of a certain quantum number than predicted by a conventional model. This challenge in identifying hybrid baryons is magnified by the fact that even the conventional baryon spectrum is poorly understood [245], as many states predicted by the conventional quark model have yet to be experimentally observed.

Here we examine the experimental foundation for hybrid baryons, and discuss their status in the context of the QCD sum-rule methodology.

6.1.1   Experimental Searches for Hybrid Baryons

Initial interest in hybrid baryon states was kindled by the observation of the Roper resonance [15], a $J^P = \frac{1}{2}^+$ state now known as the $N(1440)\frac{1}{2}^+$. The resonance was measured to be analogous to the proton, but with 50% more mass [246]. The Roper resonance was understood within the constituent quark model to be consistent with a $n = 2$ (where n is the radial quantum number) radial excitation of a nucleon state; however, it was observed with a mass less than the lower-energy the $n = 1$ excitation, the $N(1535)\frac{1}{2}^-$ [246]. This inconsistency between the measured mass of the Roper resonance and theoretical predictions of the excitations of the nucleon led some to later propose the Roper resonance as a possible hybrid baryon candidate [4, 247, 248]. However, in 2009 it was determined that the mass difference in the constituent quark model could be explained by pion-shielding [246], and the Roper resonance was indeed a $n = 2$ radial excitation of the nucleon.

Though the Roper resonance is no longer favoured as a hybrid baryon candidate, there still remains an active effort to refine our understanding of the baryonic spectrum, and search for hybrid baryon states in the process. Next door to the GlueX experiment at JLab, the CLAS12 collaboration has a mandate to map nucleon excitation masses for all $J \in \left\{\frac{1}{2}, \frac{3}{2}\right\}$ states of $P \in \{-1, +1\}$ for masses up to $3\,\mathrm{GeV}$ [27]. Through a detailed mapping of the baryonic mass spectrum, we should be able to identify if the hybrid baryon exists by looking for extraneous states compared to those that can be identified by the conventional quark model, strong decays, or by finding states with anomalous EM couplings [249].

6.1.2   Hybrid Baryons in QCD Sum-rules

The earliest study of hybrid baryons in QCD sum-rules [3] was based upon the original qqq baryon studies of Ioffe [250], and examined $J^P = \frac{1}{2}^+$ hybrid baryons utilizing the current

$$\eta_i = \left[u^{aT}(x)C\gamma^\mu u^b(x)\right]\gamma^\sigma G^d_{\mu\sigma}(x)\left(t^d d_i(x)\right)^c \epsilon^{abc}, \tag{6.1}$$

where i represents a spinor index, $u^T(x)$ is a transposed quark spinor, $\{a, b, c\}$ are quark color indices, d is a gluon color index, and $\{\mu, \sigma\}$ are Lorentz indices. Given the symmetries of the

current (6.1), the two-point function can be written in terms of two form-factors

$$\Pi_{ij}(q) = i \int d^d\mathrm{x}\, e^{iq\cdot x} \langle 0 | T\{\eta_i(x)\bar{\eta}_j(0)\} | 0 \rangle \tag{6.2}$$

$$= \Pi_1\left(q^2\right) \slashed{q}_{ij} + \Pi_2\left(q^2\right) \delta_{ij}. \tag{6.3}$$

Through a standard pole plus continuum modelling of the phenomenological side of the sum-rule, Ref. [3] arrives at the following relationships between Π_1 and Π_2, through the hybrid baryon resonance coupling λ_N, the hybrid baryon mass M_N, and the Borel parameter M,

$$\lambda_N^2 = \Pi_1\left(M^2\right) \frac{M^2}{M_N^{10}} e^{M_N^2/M^2} \tag{6.4}$$

$$\lambda_N^2 = \Pi_2\left(M^2\right) \frac{M^2}{M_N^{11}} e^{M_N^2/M^2}. \tag{6.5}$$

Combining these equations allows the extraction of the hybrid baryon mass M_N. Martyneko extracted a mass prediction of $M_N = 2.1\,\mathrm{GeV}$ [3].

Another paper was later published by an independent group reviewing the work of Martyneko [3], and included nucleon mixing effects [4]. Conflicts between the papers emerged; a number of correlator disagreements with [3] are highlighted in [4], including the dimension four NLO and dimension six LO gluon condensates, and the dimension five mixed condensate. The authors in [4] maintained that the Feynman diagrams calculated were identical to [3]. As well, the resulting continuum, coupling, Borel, and mass parameters between the two papers disagree considerably; the updated analysis in Ref. [4] predicted $M_N = 1.5\,\mathrm{GeV}$, though this could be accounted for through the addition of nucleon mixing.

Other methodologies give some insight into what the spectrum of hybrid baryons may look like. The earliest calculations on hybrid baryons in the literature were done using potential models, including the bag model [247, 251], large N_c QCD [252], and the flux tube model [253]. These methodologies predict similar masses for the $J^P = \frac{1}{2}^+$ hybrid baryons, with the bag model predicting masses of $1.6 - 1.8\,\mathrm{GeV}$ [247], and the flux tube model predicting degeneracy between the $J^P = \left\{\frac{1}{2}^+, \frac{3}{2}^+\right\}$ hybrid baryons with a mass of $M_N = 1.87\,\mathrm{GeV}$. More recently, LQCD calculations have predicted a preliminary spectrum of hybrid baryon states using a pion mass of $m_\pi = 396$, 524, and $702\,\mathrm{MeV}$ [28]. These calculations at heavy

pion masses put the $J^P = \left\{\frac{1}{2}^+, \frac{3}{2}^+\right\}$ hybrid baryons at $M_N = 2.5 - 2.7\,\mathrm{GeV}$, which could line up with the existing literature in the chiral limit.

6.1.3 Calculation of the Correlation Function

To resolve the tension in the current sum-rule literature, we calculated analytical forms for the leading order correlation function using dimensional regularization including non-perturbative effects up to dimension six gluon and quark condensates. A summary of our correlator calculations as well as the corresponding correlators from [3, 4] are included in Table 6.1.

Some methodological issues common to both papers bring into question the viability of the resulting predictions. In both calculations, the LO dimension four condensate does not contribute to the sum-rule. This necessitates the calculation of the NLO contribution; however, the diagrams calculated by both groups (Fig. 6.2) do not form a complete representation of the NLO dimension four gluon condensate topologies (Fig. 6.3).

As well, both calculations omit restricting the Borel window such that OPE convergence is enforced and the pole contribution is constrained. We can take the original analysis from Martynenko [3] and the subsequent analysis from Kisslinger [4] and examine the convergence of the OPE and the resulting Borel window as a way of assessing the validity of the sum rules.

A summary of the correlators in [3, 4] are presented alongside our own calculations of the leading order contributions in Table 6.1. We note that while our results follow a complete dimensional regularization prescription (including the d dependence contained in the expressions for the nonzero VEVs), neither of the previous works follow this convention. In addition, Martynenko [3] includes $\mathcal{O}(m)$ corrections, while Kisslinger $et.al$ [4] work in the chiral limit. We see, as highlighted in [4], differences emerge in the correlator calcuation, particularly in the dimension four, five, and six condensate contributions.

As reported in [3], the optimized parameters for the continuum onsets $s_0^{(1)}$ and $s_0^{(2)}$ as well
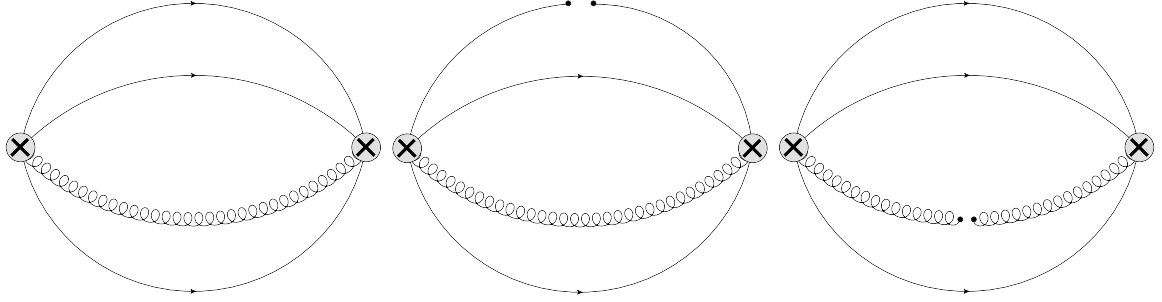
(a) Diagram I (LO perturbation theory)

(b) Diagram II (dimension-three)

(c) Diagram III (dimension-four)
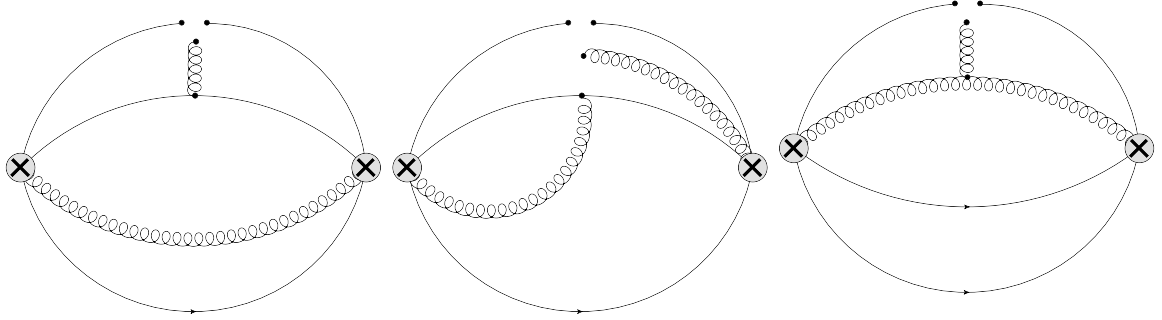
(d) Diagram IV (dimension-five)

(e) Diagram V (dimension-five)

(f) Diagram VI (dimension-five)
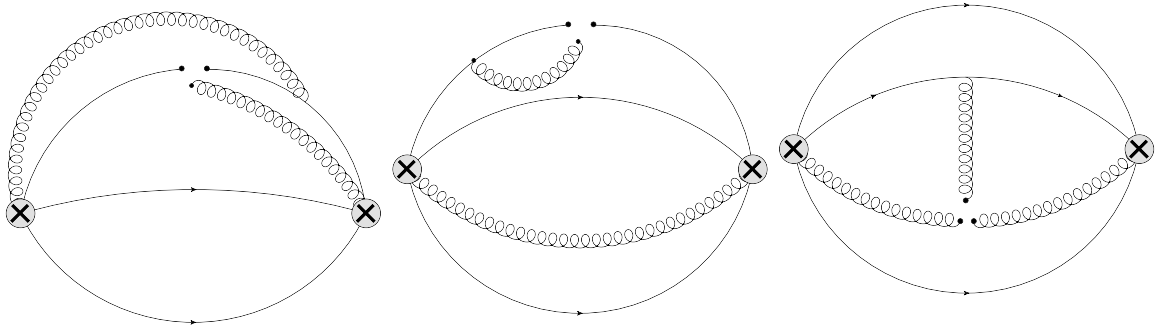
(g) Diagram VII (dimension-five)

(h) Diagram VIII (dimension-five)

(i) Diagram IX (dimension-six gluon)
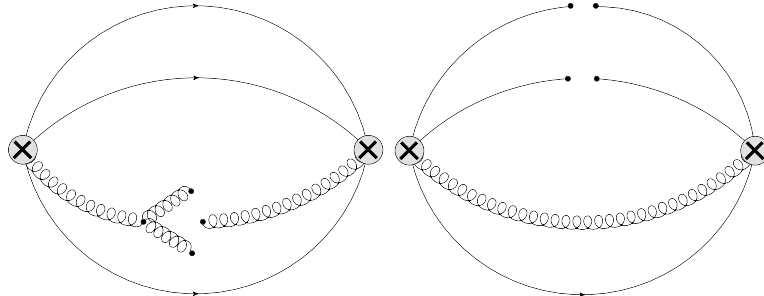
(j) Diagram X (dimension-six gluon)

(k) Diagram XI (dimension-six quark)

Figure 6.1: Leading order Feynman diagrams calculated for light hybrid baryon, up to and including dimension six condensates.
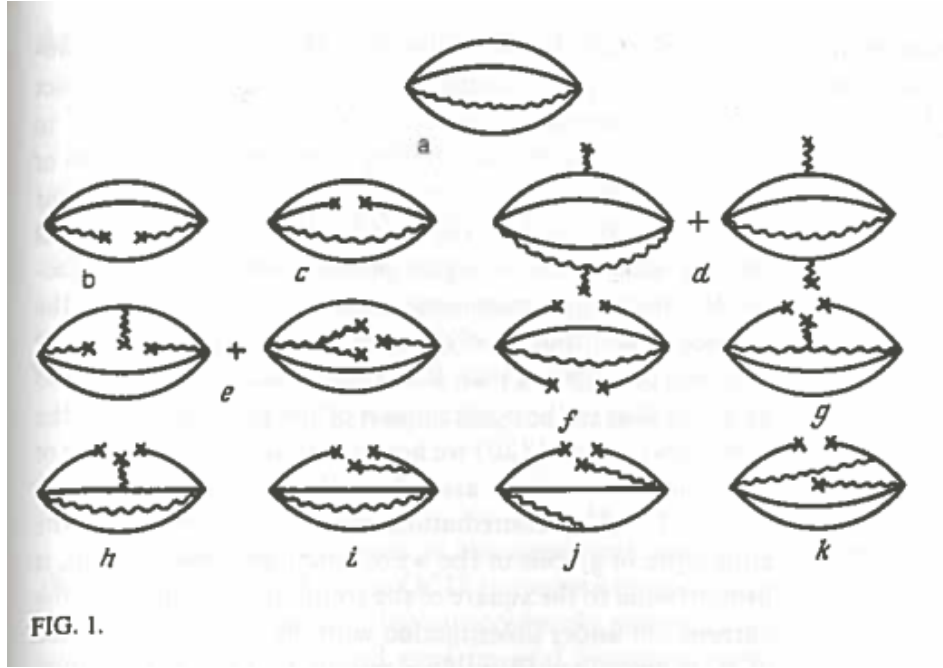
Figure 6.2: Original Feynman diagrams calculated in [3, 4]; figure taken from [3].
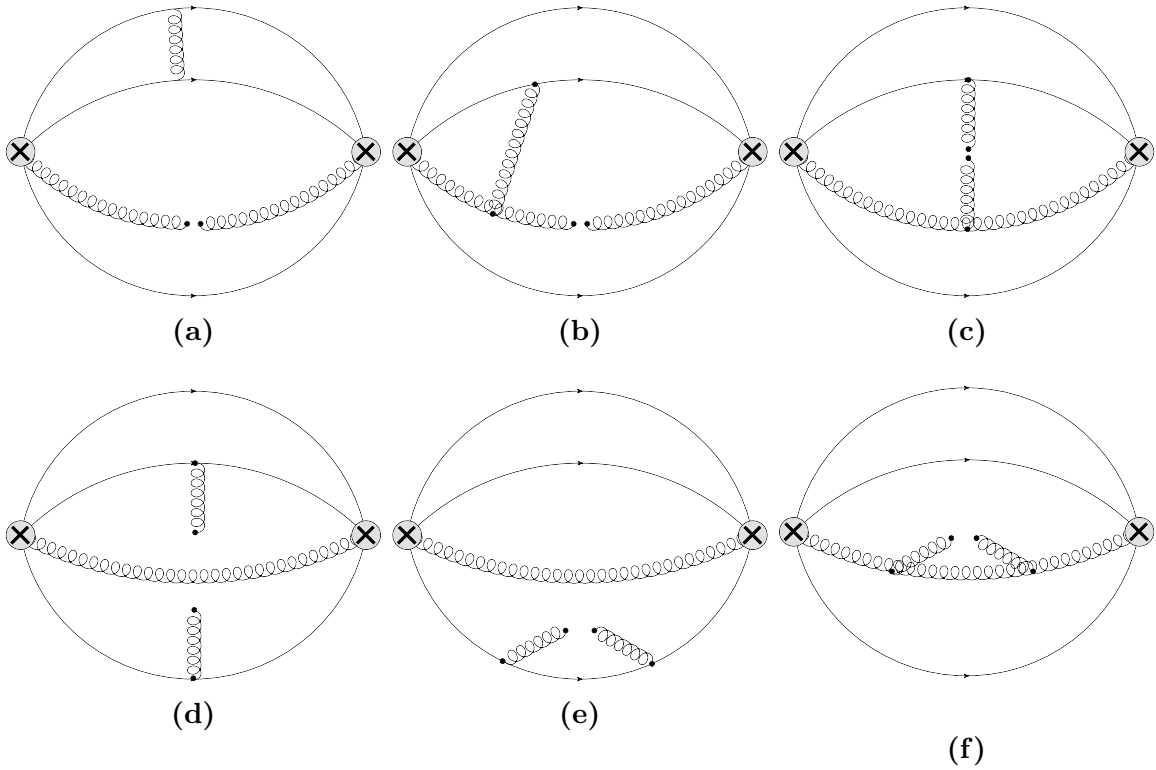
Figure 6.3: Next-to-leading order dimension four gluon condensate contributions. Topologies (a), (b), (e), and (f) are not accounted for in [3, 4].

	Martynenko [3]	Kisslinger *et.al* [4]	This work
PT	$\dfrac{q^8 \log\left(-\frac{q^2}{\nu^2}\right)(3m+\slashed{q})}{92160\pi^6}$	$\dfrac{q^8 \log\left(-\frac{q^2}{\nu^2}\right)\slashed{q}}{92160\pi^6}$	$\dfrac{q^8\slashed{q}}{276480\pi^6\epsilon} + \dfrac{q^8 \log\left(-\frac{q^2}{\nu^2}\right)\slashed{q}}{92160\pi^6}$
3D Quark	$\dfrac{\log\left(-\frac{q^2}{\nu^2}\right)\left(q^6+3mq^4\slashed{q}\right)\langle\bar qq\rangle}{1152\pi^4}$	$\dfrac{\log\left(-\frac{q^2}{\nu^2}\right)q^6\langle\bar qq\rangle}{1152\pi^4}$	$\dfrac{q^6\langle\bar qq\rangle}{4608\pi^4\epsilon} + \dfrac{\log\left(-\frac{q^2}{\nu^2}\right)q^6\langle\bar qq\rangle}{2304\pi^4}$
4D Gluon	$\dfrac{q^4\log\left(-\frac{q^2}{\nu^2}\right)\left(96\pi m\langle G^2\rangle+37\slashed{q}\langle\alpha G^2\rangle\right)}{73728\pi^5}$	$-\dfrac{17q^4\log\left(-\frac{q^2}{\nu^2}\right)\slashed{q}\langle\alpha G^2\rangle}{73728\pi^5}$	$\dfrac{q^4\slashed{q}\langle G^2\rangle}{6144\pi^4}$
5D Mixed	$-\dfrac{5\log\left(-\frac{q^2}{\nu^2}\right)\left(q^4-\frac{104}{15}mq^2\slashed{q}\right)\langle\bar q\sigma Gq\rangle}{2048\pi^4}$	$-\dfrac{5\log\left(-\frac{q^2}{\nu^2}\right)q^4\langle\bar q\sigma Gq\rangle}{1024\pi^4}$	$\dfrac{71q^4\langle\bar q\sigma Gq\rangle}{4096\pi^4\epsilon}$ $+\dfrac{71\log\left(-\frac{q^2}{\nu^2}\right)\left(q^4-\frac{104}{15}mq^2\slashed{q}\right)\langle\bar q\sigma Gq\rangle}{2048\pi^4}$
6D Gluon	$-\dfrac{q^2\log\left(-\frac{q^2}{\nu^2}\right)(39m+7\slashed{q})\langle g^3G^3\rangle}{24576\pi^5\alpha}$	$-\dfrac{q^2\log\left(-\frac{q^2}{\nu^2}\right)\slashed{q}\langle g^3G^3\rangle}{3072\pi^5\alpha}$	$-\dfrac{q^2\slashed{q}\langle g^3G^3\rangle}{2304\pi^4}$
6D Quark	$\dfrac{q^2\log\left(-\frac{q^2}{\nu^2}\right)(\slashed{q}-3m)\langle\bar q\bar qqq\rangle}{36\pi^2}$	$\dfrac{q^2\log\left(-\frac{q^2}{\nu^2}\right)\slashed{q}\langle\bar q\bar qqq\rangle}{36\pi^2}$	$\dfrac{q^2\log\left(-\frac{q^2}{\nu^2}\right)\slashed{q}\langle\bar q\bar qqq\rangle}{36\pi^2}$

Table 6.1: Summary of hybrid baryon correlators across the literature organized by contribution to the OPE, including calculations from this work. Note that our calculation only reflects leading order contributions in the dimension four gluon condensate, while [3, 4] include 4D NLO corrections.

as the calculated ground state hybrid baryon mass M_H are given to be

$$s_0^{(1)} = 6.3\,\text{GeV}^2 \tag{6.6}$$

$$s_0^{(2)} = 6.1\,\text{GeV}^2 \tag{6.7}$$

$$M_H = 2.1\text{GeV}. \tag{6.8}$$

The parameters as reported in [4] are

$$s_0^{(1)} = 2.80\,\text{GeV}^2 \tag{6.9}$$

$$s_0^{(2)} = 2.95\,\text{GeV}^2 \tag{6.10}$$

$$M_H = 1.5\,\text{GeV}. \tag{6.11}$$

In both analyses, an approximate Borel scale of $\tau \approx \frac{1}{M_H^2}$ is taken. Using these criteria, we can compare the relative contributions of the perturbative and nonperturbative components to investigate the predicted convergence of the OPE (Figures 6.4 – 6.7).
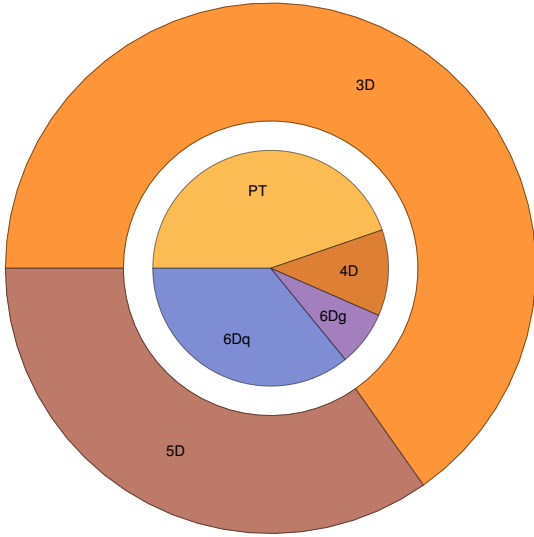
Figure 6.4: Percentage breakdown of the absolute contributions of each portion of the Π_1 (inner ring) and Π_2 (outer ring) correlators from [3] using parameters in (6.6) – (6.8)*.
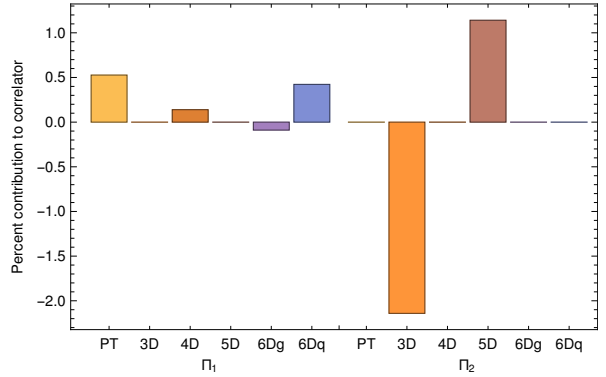
Figure 6.5: Percentage breakdown of the contributions of each portion of the Π_1 (left) and Π_2 (right) correlators from [3] with relative signs intact using parameters in (6.6) – (6.8)*.
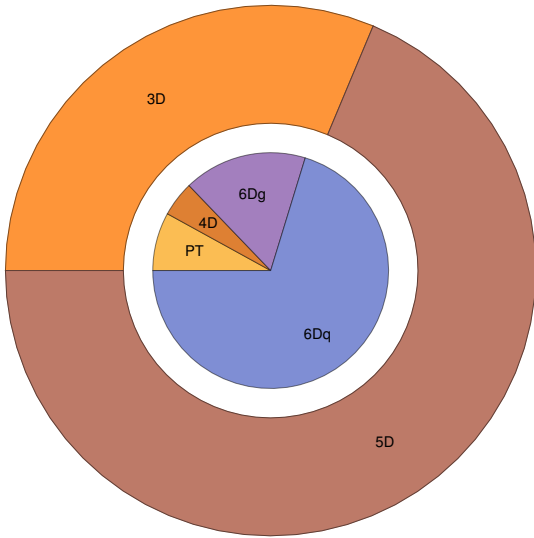
Figure 6.6: Percentage breakdown of the absolute contributions of each portion of the Π_1 (inner ring) and Π_2 (outer ring) correlators from [4] using parameters in (6.9) – (6.11)*.
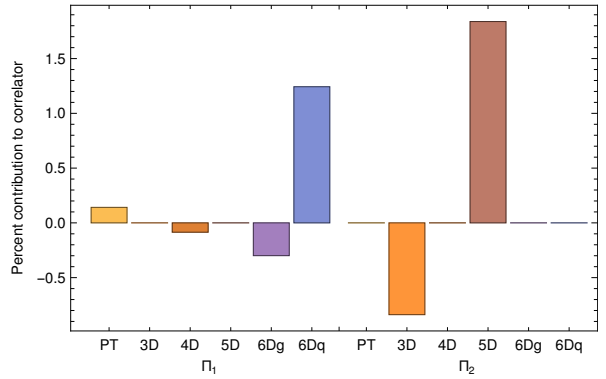
Figure 6.7: Percentage breakdown of the contributions of each portion of the Π_1 (left) and Π_2 (right) correlators from [4] with relative signs intact using parameters in (6.9) – (6.11)*.

In the Borel window specified in [3], Π_1 is predominantly composed of perturbative contributions (Fig. 6.4); however, the relative contributions between the dimension four NLO and dimension six LO condensate terms are not in line with the requirements of OPE convergence [49]. In the analysis from [4], we see that OPE convergence within the Borel window is significantly worse, with the leading order contribution to Π_1 coming from the dimension six LO gluon contribution. In both analyses, we see that Π_2 is only composed of dimension three and dimension five condensate terms (Fig. 6.4 and 6.6), carrying opposite signs in both cases (Fig. 6.5 and 6.7).

While our calculations of the correlator presented in Table 6.1 do not resolve any disagreements in correlator construction between Refs. [3, 4], our analysis of these works does raise concerns regarding the validity of these sum rules with the relative contributions indicating convergence issues in the relevant OPEs, and inconsistencies in the calculation of NLO dimension four condensate contributions. A careful treatment of a QCDSR analysis concerning the hybrid baryons is still needed.

---

*Abbreviations in Figures 6.4 to 6.7 correspond to different contributions to Π_1 (left) and Π_2 from the OPE; PT is perturbation theory, 3D is the dimension three quark condensate, 4D is the dimension four gluon condensate, 5D is the dimension five mixed condensate, 6Dg is the dimension six gluon condensate, and 6Dq is the dimension six quark condensate.

CHAPTER 7

THE END

Since the conception of quarks [10, 11, 12, 13], physicists have imagined how the constituents of mesons and baryons might behave and interact to form new, novel forms of matter. We have only recently begun to see experimental hints of such diversity of structures through the observations and confirmation of multiquark states at modern particle colliders [19, 20, 21, 122]; these results make the next chapter of hadronic physics an exciting prospect as we search for other exotic states, particularly those with explicit gluonic content [25]. Many questions within QCD are still unanswered; a deeper investigation into the nature of the strong interaction between quarks and gluons, the internal structure of hadrons (distinguishing different models of hybrid and multiquark states in particular), and the mechanism of confinement are just some of the challenges facing physicists. To overcome the challenges associated with the non-perturbative nature of QCD, multiple methodologies must be employed to ensure a complete understanding of the dynamics of the strong interaction. This includes model-based approaches, lattice QCD [28, 29, 30], the Dyson-Schwinger Bethe-Salpeter equations [31], and QCD sum rules [36, 37, 49, 51, 115, 165, 167, 254]. Our methodology follows the tradition of the last approach, and we have explored approaches that augment the sum rule methodology with computational tools and new analytic approaches to extract improved predictions of exotic hadron states to be tested against this and future generations of high-energy physics experiments [24, 25, 26].

The focus of this work on exotic hadrons began with examining hybrid meson structures [49, 51, 52] and predicting hybrid mass and multiplet structures across both closed and open-flavour hybrid mesons; this is an area of hadronic physics that still requires much experimental work. At higher masses, more sophisticated detectors are necessary to distinguish conventional states and their exotic counterparts, both in the measurement of mass and

decay properties. At lower masses, the GlueX experiment is well underway in their search for the lowest-lying hybrid multiplet [24, 25]; with any luck, their search for the exotic 1^{-+} vector will be successful, and we may begin studying properties of the gluon directly as a constituent particle. Finally, as we progress further into the non-perturbative realm of QCD, at masses lower than $1\,\text{GeV}$ the scalar meson puzzle emerges [14, 33, 34]. The behaviour of low-energy QCD at these scales suggests a tendency towards exotic four-quark structures, perhaps due to an attractive force between mesons [14]. At these energies, difficulties on both the experimental and theoretical side emerge making interpretation of the data in this domain unclear. Often, theoretical methods in these energies will approximate fundamental quark degrees of freedom with approximate hadronic degrees of freedom due to the complicated non-perturbative effects. My work at these energies focuses on joining hadron-level and quark-level methods to leverage benefits from both paradigms in an effort to understand more about the structure and composition of these exotic hadrons at low energies [33, 34]. To date, we have found excellent agreement between scale factors determined from mixing between two and four-quark nonets in both the isodoublet and isotriplet scalar mesons, indicating a robust relationship between the quark-level description of QCD sum rules, and the meson-level description from chiral Lagrangians. Finally, as we look forward to upcoming and next-generation experimental searches [27], I assess what work needs to be done in the future of QCD sum rules predicting properties of the experimentally and theoretically more complex hybrid baryon states.

QCD sum rules has had a long history with many successes in extracting bound-state predictions from the fundamental degrees of freedom of the strong interaction. While calculating masses is an important piece of identifying exotic hadron states, predictions around decay widths and mechanisms are also necessary; this could be an avenue of future work in exotic hadron theory. Computational tools are now widely available that empower the calculation of higher-order processes, both in terms of loops and number of external particles. Improving the precision of theoretical methods is vital to keep pace with the precise experimental data coming from modern experiments. By exploring different approaches and applications of QCD sum rules, modernizing the methodology with computational tools, and improving upon the existing formalism through cooperation with other approaches, perhaps we may

move closer towards a stronger understanding of quarks, gluons, and how they interact.

References

[1] Particle Data Group, M. Tanabashi *et al.*, Phys. Rev. **D98**, 030001 (2018).

[2] Particle Data Group, K. A. Olive *et al.*, Chin. Phys. **C38**, 090001 (2014).

[3] A. P. Martynenko, Sov. J. Nucl. Phys. **54**, 488 (1991), [Yad. Fiz.54,809(1991)].

[4] L. S. Kisslinger and Z. P. Li, Phys. Rev. **D51**, R5986 (1995).

[5] ATLAS - The Physics, `https://atlas.cern/discover/physics`, Accessed: 2019-12-13.

[6] D. Binosi and L. Theußl, Comput. Phys. Commun **161**, 76 (2004), 0309015.

[7] A. H. Fariborz, R. Jora, and J. Schechter, Phys. Rev. **D79**, 074014 (2009).

[8] T. G. Steele, D. Harnett, and G. Orlandini, AIP Conf. Proc. **688**, 128 (2003).

[9] G. Orlandini, T. G. Steele, and D. Harnett, Nucl. Phys. **A686**, 261 (2001), hep-ph/0007299.

[10] M. Gell-Mann, Phys. Lett. **8**, 214 (1964).

[11] G. Zweig and S. An, CERN-TH-412 (1964).

[12] M. Gell-Mann, Phys. Rev. **125**, 1067 (1962).

[13] Y. Ne'eman, Nucl. Phys. **26**, 222 (1961).

[14] J. R. Peláez, Phys. Rep. **658**, 1 (2016).

[15] L. D. Roper, Phys. Rev. Lett. **12**, 340 (1964).

[16] S. Godfrey and S. L. Olsen, Annu. Rev. Nucl. Part. Sci. **58**, 51 (2008).

[17] N. Brambilla *et al.*, (2019), arXiv:1907.07583 [hep-ph].

[18] R. M. Albuquerque *et al.*, J. Phys. **G46**, 093002 (2019).

[19] BESIII Collaboration, M. Ablikim *et al.*, Phys. Rev. Lett. **110**, 252001 (2013).

[20] Belle Collaboration, Z. Q. Liu *et al.*, Phys. Rev. Lett. **110**, 252002 (2013).

[21] LHCb Collaboration, R. Aaij *et al.*, Phys. Rev. Lett. **115**, 072001 (2015).

[22] LHCb Collaboration, R. Aaij *et al.*, Phys. Rev. Lett. **122**, 222001 (2019).

[23] S. Dobbs, (2019), arXiv:1908.09711 [hep-ph].

[24] GlueX Collaboration, A. Ali *et al.*, Phys. Rev. Lett. **123**, 072001 (2019).

[25] GlueX Collaboration, H. Al Ghoul *et al.*, AIP Conf. Proc. **1735**, 20001 (2016).

[26] PANDA Collaboration, G. Barucca *et al.*, Eur. Phys. J. **A55**, 42 (2019), 1812.05132.

[27] CLAS12 Collaboration, V. Burkert *et al.*, Jefferson Lab Report No. PR12-16-010, 2016 (unpublished).

[28] J. J. Dudek and R. G. Edwards, Phys. Rev. **D85**, 054016 (2012).

[29] J. J. Dudek, Phys. Rev. **D84**, 074023 (2011), arXiv:1106.5515 [hep-ph].

[30] J. J. Dudek, R. G. Edwards, P. Guo, and C. E. Thomas, Phys. Rev. **D88**, 094505 (2013).

[31] T. Hilger and A. Krassnigg, Eur. Phys. J. **A53**, 142 (2017).

[32] A. H. Fariborz, A. Pokraka, and T. G. Steele, Mod. Phys. Lett. **A31**, 1650023 (2016).

[33] A. H. Fariborz, J. Ho, A. Pokraka, and T. G. Steele, (2019), arXiv:1909.07243 [hep-ph].

[34] A. H. Fariborz, J. Ho, and T. G. Steele, (2019), arXiv:1911.04945 [hep-ph].

[35] R. L. Jaffe and K. Johnson, Phys. Lett. **B60**, 201 (1976).

[36] M. A. Shifman, A. I. Vainshtein, and V. I. Zakharov, Nucl. Phys. **B147**, 385 (1979).

[37] M. A. Shifman, A. I. Vainshtein, and V. I. Zakharov, Nucl. Phys. **B147**, 448 (1979).

[38] S. Narison, Nucl. Phys. **B509**, 312 (1998).

[39] P. Colangelo and A. Khodjamirian, QCD Sum Rules, a Modern Perspective, in *At The Frontier of Particle Physics*, pp. 1495–1576, World Scientific, 2001.

[40] P. Gubler and D. Satow, Prog. Part. Nucl. Phys. **106**, 1 (2019).

[41] L. Faddeev and V. Popov, Phys. Lett. **B25**, 29 (1967).

[42] P. Pascual and R. Tarrach, *QCD: Renormalization for the Practitioner*, Lecture Notes in Physics Vol. 194 (Springer, Berlin, Heidelberg, 1984).

[43] M. Chanowitz, M. Furman, and I. Hinchliffe, Nucl. Phys. **B159**, 225 (1979).

[44] D. J. Gross and F. Wilczek, Phys. Rev. Lett. **30**, 1343 (1973).

[45] H. D. Politzer, Phys. Rev. Lett. **30**, 1346 (1973).

[46] N. Isgur, R. Kokoski, and J. Paton, Phys. Rev. Lett. **54**, 869 (1985).

[47] S. Narison, *QCD as a Theory of Hadrons: From Partons to Confinement* (Cambridge University Press, 2004).

[48] D. Harnett, R. T. Kleiv, K. Moats, and T. G. Steele, Nucl. Phys. **A850**, 110 (2011).

[49] J. Ho, D. Harnett, and T. G. Steele, J. High Energy Phys. **2017**, 149 (2017).

[50] A. Palameta, J. Ho, D. Harnett, and T. G. Steele, Phys. Rev. **D97**, 034001 (2018), arXiv:1707.00063 [hep-ph].

[51] J. Ho, R. Berg, T. G. Steele, W. Chen, and D. Harnett, Phys. Rev. **D98**, 096020 (2018), arXiv:1806.02465 [hep-ph].

[52] J. Ho, R. Berg, T. G. Steele, W. Chen, and D. Harnett, Phys. Rev. **D100**, 034012 (2019).

[53] M. E. Peskin and D. V. Schroeder, *An Introduction to Quantum Field Theory* (Addison-Wesley Publishing Company, 1995).

[54] Y. Nambu, Phys. Rev. **117**, 648 (1960).

[55] J. Goldstone, Il Nuovo Cimento (1955-1965) **19**, 154 (1961).

[56] T.-P. Cheng and L.-F. Li, *Gauge Theory of Elementary Particle Physics* (Oxford University Press, Oxfordshire, 1984).

[57] M. Gell-Mann, R. J. Oakes, and B. Renner, Phys. Rev. **D175**, 2195 (1968).

[58] O. W. Greenberg, Phys. Rev. Lett. **13**, 598 (1964).

[59] N. Isgur and J. E. Paton, Phys. Rev. **D31**, 2910 (1985).

[60] E. Eichten, K. Gottfried, T. Kinoshita, K. D. Lane, and T. M. Yan, Phys. Rev. **D17**, 3090 (1978).

[61] E. Eichten, K. Gottfried, T. Kinoshita, K. D. Lane, and T. M. Yan, Phys. Rev. **D21**, 203 (1980).

[62] Y. Sumino, Phys. Lett. **B571**, 173 (2003).

[63] LHCb Collaboration, R. Aaij *et al.*, Phys. Rev. Lett. **112**, 222002 (2014).

[64] J. Govaerts, L. J. Reinders, H. R. Rubinstein, and J. Weyers, Nucl. Phys. **B258**, 215 (1985).

[65] L. J. Reinders, H. R. Rubinstein, and S. Yazaki, Phys. Rep. **127**, 1 (1984).

[66] V. Elias, T. G. Steele, and M. D. Scadron, Phys. Rev. **D38**, 1584 (1988).

[67] J. Ho, QCD Correlation Functions of Heavy-light Hybrid Mesons ($J^P = 1^-$), Master's thesis, University of Saskatchewan, 2015.

[68] M. A. Shifman, Nucl. Phys. **B173**, 13 (1980).

[69] C. Cronstrm, Phys. Lett. **B90**, 267 (1980).

[70] E. Bagan, M. R. Ahmady, V. Elias, and T. G. Steele, Z. Phys. **C61**, 157 (1994).

[71] C. Jarlskog, Paper [1952a]: On the definition of the renormalization constants in quantum electrodynamics, in *Portrait of Gunnar Källén: A Physics Shooting Star and Poet of Early Quantum Field Theory*, edited by C. Jarlskog, pp. 509–527, Springer International Publishing, 2014.

[72] H. Lehmann, Il Nuovo Cimento (1943-1954) **11**, 342 (1954).

[73] S. Narison, Phys. Lett. B **675**, 319 (2009).

[74] V. Elias, A. Fariborz, F. Shi, and T. G. Steele, Nucl. Phys. **A633**, 279 (1998).

[75] R. Bertlmann, G. Launer, and E. de Rafael, Nucl. Phys. B **250**, 61 (1985).

[76] R. A. Bertlmann, C. A. Dominguez, M. Loewe, M. Perrottet, and E. de Rafael, Z. Phys. **C39**, 231 (1988).

[77] W. Chen *et al.*, J. High Energy Phys. **1309**, 019 (2013).

[78] T. G. Steele, S. Alavian, and J. Kwan, Phys. Lett. **B392**, 189 (1997).

[79] M. Benmerrouche, G. Orlandini, and T. G. Steele, Phys. Lett. **B356**, 573 (1995).

[80] G. 't Hooft and M. Veltman, Nucl. Phys. **B44**, 189 (1972).

[81] R. Mertig and R. Scharf, Comput. Phys. Commun. **111**, 265 (1998).

[82] O. V. Tarasov, Phys. Rev. **D54**, 6479 (1996).

[83] O. V. Tarasov, Nucl. Phys. **B502**, 455 (1997).

[84] D. J. Broadhurst, J. Fleischer, and O. V. Tarasov, Z. Phys. **C60**, 287 (1993), 9304303.

[85] E. E. Boos and A. I. Davydychev, Theor. Math. Phys. **89**, 1052 (1991).

[86] A. I. Davydychev, J. Math. Phys. **33**, 358 (1992).

[87] T. Binoth and G. Heinrich, Nucl. Phys. **B585**, 741 (2000).

[88] S. Borowka *et al.*, Comput. Phys. Commun. **222**, 313 (2018).

[89] S. Borowka *et al.*, Comput. Phys. Commun. **240**, 120 (2019).

[90] J. C. Collins, *Renormalization* Cambridge Monographs on Mathematical Physics (Cambridge University Press, 1984).

[91] H.-y. Jin and J. G. Körner, Phys. Rev. **D64**, 074002 (2001).

[92] T. Hilger, M. Gómez-Rocha, and A. Krassnigg, Eur. Phys. J. **C77**, 625 (2017).

[93] W. Chen, T. G. Steele, and S.-L. Zhu, J. Phys. **G41**, 025003 (2014).

[94] C. Meyer and E. Swanson, Prog. Part. Nucl. Phys. **82**, 21 (2015).

[95] J. I. Latorre, P. Pascual, and S. Narison, Z. Phys. C **34**, 347 (1987).

[96] G.-J. Ding and M.-L. Yan, Phys. Lett. **B650**, 390 (2007), hep-ph/0611319.

[97] W. Chen *et al.*, Phys. Rev. **D88**, 045027 (2013).

[98] S.-L. Zhu, Phys. Lett. **B625**, 212 (2005), hep-ph/0507025.

[99] Belle Collaboration, S.-K. Choi *et al.*, Phys. Rev. Lett. **94**, 182002 (2005).

[100] R. Berg, D. Harnett, R. T. Kleiv, and T. G. Steele, Phys. Rev. **D86**, 034002 (2012).

[101] B. Ketzer, PoS **QNP2012**, 025 (2012), 1208.5125.

[102] D. Horn and J. Mandula, Phys. Rev. **D17**, 898 (1978).

[103] T. Barnes, F. E. Close, F. de Viron, and J. Weyers, Nucl. Phys. **B224**, 241 (1983).

[104] M. S. Chanowitz and S. R. Sharpe, Nucl. Phys. **B222**, 211 (1983), [Erratum: Nucl. Phys. B228, 588 (1983)].

[105] F. E. Close and P. R. Page, Nucl. Phys. **B443**, 233 (1995), hep-ph/9411301.

[106] T. Barnes, F. E. Close, and E. S. Swanson, Phys. Rev. **D52**, 5242 (1995).

[107] J. Govaerts, F. de Viron, D. Gusbin, and J. Weyers, Phys. Lett. **128B**, 262 (1983), [Erratum: Phys. Lett.136B,445(1984)].

[108] J. Govaerts, F. de Viron, D. Gusbin, and J. Weyers, Nucl. Phys. **B248**, 1 (1984).

[109] J. I. Latorre, S. Narison, P. Pascual, and R. Tarrach, Phys. Lett. **147B**, 169 (1984).

[110] I. Balitsky, D. Diakonov, and A. V. Yung, Z. Phys. **33**, 265 (1986).

[111] H.-y. Jin, J. G. Körner, and T. G. Steele, Phys. Rev. **D67**, 014025 (2003).

[112] Z.-R. Huang, H.-Y. Jin, and Z.-F. Zhang, J. High Energy Phys. **2015**, 4 (2015).

[113] K. Chetyrkin and S. Narison, Phys. Lett. **B485**, 145 (2000).

[114] S. L. Zhu, Phys. Rev. **D60**, 097502 (1999).

[115] D. Harnett, R. T. Kleiv, T. G. Steele, and H.-y. Jin, J. Phys. **G39**, 125003 (2012).

[116] C.-F. Qiao, L. Tang, G. Hao, and X.-Q. Li, J. Phys. **G39**, 015005 (2012).

[117] S. Perantonis and C. Michael, Nucl. Phys. **B347**, 854 (1990).

[118] L. Liu *et al.*, J. High Energy Phys. **2012**, 1 (2012).

[119] G. Moir, M. Peardon, S. M. Ryan, and C. E. Thomas, PoS **ConfinementX**, 139 (2012), arXiv:1301.3397 [hep-ph].

[120] T. Huang, H.-y. Jin, and A. Zhang, Phys. Rev. **D61**, 034016 (2000).

[121] D0 Collaboration, V. M. Abazov *et al.*, Phys. Rev. Lett. **117**, 022003 (2016).

[122] LHCb Collaboration, R. Aaij *et al.*, Phys. Rev. Lett. **117**, 152003 (2016).

[123] W. Chen, H.-X. Chen, X. Liu, T. G. Steele, and S.-L. Zhu, Phys. Rev. Lett. **117**, 022002 (2016).

[124] J. Govaerts, L. J. Reinders, and J. Weyers, Nucl. Phys. **B262**, 575 (1985).

[125] J. Govaerts, L. J. Reinders, P. Francken, X. Gonze, and J. Weyers, Nucl. Phys. **B284**, 674 (1987).

[126] E. Bagán, M. R. Ahmady, V. Elias, and T. G. Steele, Z. Phys. **61**, 157 (1994).

[127] S. Narison and E. de Rafael, Phys. Lett. **B103**, 57 (1981).

[128] J. L. Rosner, S. Stone, and R. S. Van de Water, Submitted to: Particle Data Book (2015), arXiv:1509.02220 [hep-ph].

[129] HPQCD Collaboration, B. Chakraborty *et al.*, Phys. Rev. **D91**, 054508 (2015).

[130] G. Launer, S. Narison, and R. Tarrach, Z. Phys. **C26**, 433 (1984).

[131] S. Narison, Phys. Lett. **B693**, 559 (2010), [Erratum: Phys. Lett.B705,544(2011)].

[132] S. Narison, Phys. Lett. **B605**, 319 (2005).

[133] S. Narison, Phys. Lett. **B210**, 238 (1988).

[134] S. Narison, Nucl. Part. Phys. Proc. **270-272**, 143 (2016).

[135] S. Narison, Int. J. Mod. Phys. **A30**, 1550116 (2015), 1404.6642.

[136] J. Govaerts, L. Reinders, and J. Weyers, Nucl. Phys. B **262**, 575 (1985).

[137] T. Huang, H. Jin, and A. Zhang, Eur. Phys. J. C **8**, 465 (1999).

[138] BES Collaboration, M. Ablikim *et al.*, Phys. Rev. Lett. **100**, 102003 (2008), arXiv:0712.1143 [hep-ph].

[139] D.-Y. Chen, X. Liu, and T. Matsuki, Eur. Phys. J. **C72**, 2008 (2012).

[140] S. Godfrey and N. Isgur, Phys. Rev.. **D32**, 189 (1985).

[141] T. Barnes, N. Black, and P. R. Page, Phys. Rev. **D68**, 054014 (2003), nucl-th/0208072.

[142] G.-J. Ding and M.-L. Yan, Phys. Lett. **B657**, 49 (2007), hep-ph/0701047.

[143] J. Merlin and J. E. Paton, Phys. Rev. **D35**, 1668 (1987).

[144] H.-X. Chen, C.-P. Shen, and S.-L. Zhu, Phys. Rev. **D98**, 014011 (2018), arXiv:1805.06100 [hep-ph].

[145] Z.-G. Wang, Nucl. Phys. **A791**, 106 (2007), hep-ph/0610171.

[146] H.-X. Chen, X. Liu, A. Hosaka, and S.-L. Zhu, Phys. Rev. **D78**, 034012 (2008), 0801.4603.

[147] M. Abud, F. Buccella, and F. Tramontano, Phys. Rev. **D81**, 074018 (2010), arXiv:0912.4299 [hep-ph].

[148] L. Zhao, N. Li, S.-L. Zhu, and B.-S. Zou, Phys. Rev. **D87**, 054034 (2013), arXiv:1302.1770 [hep-ph].

[149] M. Napsuciale, E. Oset, K. Sasaki, and C. A. Vaquera-Araujo, Phys. Rev. **D76**, 074012 (2007), 0706.2972.

[150] A. Martinez Torres, K. P. Khemchandani, L. S. Geng, M. Napsuciale, and E. Oset, Phys. Rev. **D78**, 074031 (2008), arXiv:0801.3635 [hep-ph].

[151] L. Alvarez-Ruso, J. A. Oller, and J. M. Alarcon, Phys. Rev. **D80**, 054011 (2009), arXiv:0906.0222 [hep-ph].

[152] S. Gomez-Avila, M. Napsuciale, and E. Oset, Phys. Rev. **D79**, 034018 (2009), arXiv:0711.4147 [hep-ph].

[153] I. I. Balitsky, D. Diakonov, and A. V. Yung, Phys. Lett. **112B**, 71 (1982).

[154] I. I. Balitsky, D. Diakonov, and A. V. Yung, Z. Phys. **C33**, 265 (1986).

[155] V. Braun and A. Kolesnichenko, Phys. Lett. B **175**, 485 (1986).

[156] J. Govaerts, L. J. Reinders, P. Francken, X. Gonze, and J. Weyers, Nucl. Phys. **B284**, 674 (1987).

[157] K. Chetyrkin and S. Narison, Phys. Lett. B **485**, 145 (2000), 0003151.

[158] H. Y. Jin, J. G. Korner, and T. G. Steele, Phys. Rev. **D67**, 014025 (2003).

[159] Z. Zhu-Feng, J. Hong-Ying, and T. G. Steele, Chin. Phys. Lett. **31**, 51201 (2014).

[160] Z.-R. Huang, H.-Y. Jin, T. G. Steele, and Z.-F. Zhang, Phys. Rev. D **94**, 054037 (2016).

[161] C. J. Burden, L. Qian, C. D. Roberts, P. C. Tandy, and M. J. Thomson, Phys. Rev. C **55**, 2649 (1997).

[162] C. J. Burden and M. A. Pichowsky, Few Body Syst. **32**, 119 (2002).

[163] T. Barnes and F. E. Close, Phys. Lett. **116B**, 365 (1982).

[164] W. Chen *et al.*, J. High Energy Phys. **09**, 019 (2013).

[165] D. Harnett and T. G. Steele, Nucl. Phys. **A695**, 205 (2001), hep-ph/0011044.

[166] A. Zhang and T. G. Steele, Nucl. Phys. A **728**, 165 (2003).

[167] D. Harnett, R. T. Kleiv, K. Moats, and T. G. Steele, Nucl. Phys. **A850**, 110 (2011), arXiv:0804.2195 [hep-ph].

[168] R. Mertig and R. Scharf, Comput. Phys. Commun. **111**, 265 (1998), hep-ph/9801383.

[169] L. J. Reinders, H. Rubinstein, and S. Yazaki, Phys. Rept. **127**, 1 (1985).

[170] Q.-N. Wang, Z.-F. Zhang, T. G. Steele, H.-Y. Jin, and Z.-R. Huang, Chin. Phys. C **41**, 074107 (2017).

[171] F. Shi *et al.*, Nucl. Phys. A **671**, 416 (2000).

[172] M. Benmerrouche, G. Orlandini, and T. G. Steele, Phys. Lett. B **366**, 354 (1996).

[173] Particle Data Group, C. Patrignani *et al.*, Chin. Phys. **C40**, 100001 (2016).

[174] S. Narison, Phys. Lett. **B707**, 259 (2012), arXiv:1105.5070 [hep-ph].

[175] M. Beneke and H. G. Dosch, Phys. Lett. **B284**, 116 (1992).

[176] V. M. Belyaev and B. L. Ioffe, Sov. Phys. JETP **56**, 493 (1982).

[177] W. Chen, H.-X. Chen, X. Liu, T. G. Steele, and S.-L. Zhu, Phys. Rev. D **96**, 114017 (2017).

[178] D. Meng-Lin, C. Wei, C. Xiao-Lin, and Z. Shi-Lin, Chin. Phys. C **37**, 33104 (2013).

[179] BaBar Collaboration, B. Aubert *et al.*, Phys. Rev. **D74**, 091103 (2006), hep-ex/0610018.

[180] BaBar Collaboration, B. Aubert *et al.*, Phys. Rev. **D76**, 012008 (2007).

[181] BaBar Collaboration, B. Aubert *et al.*, Phys. Rev. **D77**, 092002 (2008).

[182] BaBar Collaboration, J. P. Lees *et al.*, Phys. Rev. **D86**, 012008 (2012).

[183] Belle Collaboration, C. P. Shen *et al.*, Phys. Rev. **D80**, 031101 (2009), arXiv:0808.0006 [hep-ex].

[184] BESIII Collaboration, M. Ablikim *et al.*, Phys. Rev. **D91**, 052017 (2015).

[185] BESIII Collaboration, M. Ablikim *et al.*, (2017), arXiv:1709.04323 [hep-ex].

[186] J. Merlin and J. E. Paton, J. Phys. **G11**, 439 (1985).

[187] J. Govaerts, L. J. Reinders, and J. Weyers, Nucl. Phys. **B262**, 575 (1985).

[188] P. R. Page, E. S. Swanson, and A. P. Szczepaniak, Phys. Rev. **D59**, 034016 (1999), hep-ph/9808346.

[189] P. R. Page, Phys. Lett. **B402**, 183 (1997), hep-ph/9611375.

[190] H.-W. Ke and X.-Q. Li, (2018), arXiv:1810.07912 [hep-ph].

[191] Y. Dong, A. Faessler, T. Gutsche, Q. L, and V. E. Lyubovitskij, Phys. Rev. **D96**, 074027 (2017), arXiv:1705.09631 [hep-ph].

[192] BaBar Collaboration, B. Aubert *et al.*, Phys. Rev. Lett. **95**, 142001 (2005), hep-ex/0506081.

[193] BESIII Collaboration, M. Ablikim *et al.*, Phys. Rev. Lett. **118**, 092001 (2017), arXiv:1611.01317 [hep-ex].

[194] E. Kou and O. Pene, Phys. Lett. **B631**, 164 (2005), hep-ph/0507119.

[195] H.-X. Chen, W. Chen, X. Liu, and S.-L. Zhu, Phys. Rept. **639**, 1 (2016), arXiv:1601.02092 [hep-ph].

[196] M. S. Chanowitz, M. Furman, and I. Hinchliffe, Nucl. Phys. **B159**, 225 (1979).

[197] R. A. Bertlmann, G. Launer, and E. de Rafael, Nucl. Phys. **B250**, 61 (1985).

[198] S. Narison and E. de Rafael, Phys. Lett. **103B**, 57 (1981).

[199] H.-X. Chen, C.-P. Shen, and S.-L. Zhu, Phys. Rev. **D98**, 014011 (2018).

[200] BESIII Collaboration, M. Ablikim *et al.*, Phys. Rev. **D99**, 032001 (2019), arXiv:1811.08742 [hep-ex].

[201] F. E. Close and N. A. Törnqvist, J. Phys. G **28**, R249 (2002).

[202] S. Narison, N. Pak, and N. Paver, p. 77 (1984).

[203] S. Weinberg, Phys. Rev. Lett. **110**, 261601 (2013).

[204] E. Klempt and A. Zaitsev, Phys. Rep. **454**, 1 (2007).

[205] D. Black, A. H. Fariborz, and J. Schechter, Phys. Rev. **D61**, 074001 (2000).

[206] T. Teshima, I. Kitamura, and N. Morisita, J. Phys. G **28**, 1391 (2002).

[207] M. Napsuciale and S. Rodríguez, Phys. Rev. **D70**, 094043 (2004).

[208] A. H. Fariborz, Phys. Rev. **D74**, 054030 (2006).

[209] G. 't Hooft, G. Isidori, L. Maiani, A. Polosa, and V. Riquer, Phys. Lett. **B662**, 424 (2008).

[210] A. H. Fariborz, R. Jora, and J. Schechter, Phys. Rev. **D77**, 094004 (2008).

[211] A. H. Fariborz, R. Jora, and J. Schechter, Phys. Rev. **D72**, 034001 (2005).

[212] R. J. Jaffe, Phys. Rev. **D15**, 267 (1977).

[213] A. Zhang, Phys. Rev. **D61**, 114021 (2000).

[214] T. V. Brito, F. S. Navarra, M. Nielsen, and M. E. Bracco, Phys. Lett. **B608**, 69 (2005).

[215] H.-X. Chen, A. Hosaka, and S.-L. Zhu, Phys. Rev. **D76**, 094025 (2007).

[216] H.-X. Chen, A. Hosaka, and S.-L. Zhu, Phys. Lett. **B650**, 369 (2007).

[217] F. Sannino and J. Schechter, Phys. Rev. **D52**, 96 (1995).

[218] M. Harada, F. Sannino, and J. Schechter, Phys. Rev. **D54**, 1991 (1996).

[219] D. Black, A. H. Fariborz, F. Sannino, and J. Schechter, Phys. Rev. **D59**, 074026 (1999).

[220] D. Black, M. Harada, and J. Schechter, Phys. Rev. Lett. **88**, 181603 (2002).

[221] R. Escribano, P. Masjuan, and J. J. Sanz-Cillero, J. High Energy Phys. **2011**, 94 (2011).

[222] M. Albaladejo and J. A. Oller, Phys. Rev. Lett. **101**, 252002 (2008).

[223] L. Kisslinger, J. Gardner, and C. Vanderstraeten, Phys. Lett. **B410**, 1 (1997).

[224] T. Huang, H. Jin, and A. Zhang, Phys. Rev. **D59**, 034026 (1999).

[225] S. Narison, Phys. Rev. **D73**, 114024 (2006).

[226] J. Zhang, H. Y. Jin, Z. F. Zhang, T. G. Steele, and D. H. Lu, Phys. Rev. **D79**, 114033 (2009).

[227] P. Minkowski and W. Ochs, Eur. Phys. J. **C9**, 283 (1999).

[228] F. E. Close and A. Kirk, Phys. Lett. **B483**, 345 (2000).

[229] S. Narison, Int. J. Mod. Phys. **A33**, 1850045 (2018).

[230] E. Klempt and A. Zaitsev, Phys. Rept. **454**, 1 (2007), arXiv:0708.4016 [hep-ph].

[231] J. Peláez and A. Rodas, Eur. Phys. J. **C77**, 431 (2017), arXiv:1703.07661 [hep-ph].

[232] J. Peláez, Phys. Rev. Lett. **92**, 102001 (2004), hep-ph/0309292.

[233] D. Black, A. H. Fariborz, F. Sannino, and J. Schechter, Phys. Rev. **D59**, 074026 (1999), hep-ph/9808415.

[234] D. Black, A. H. Fariborz, F. Sannino, and J. Schechter, Phys. Rev. **D58**, 054012 (1998), hep-ph/9804273.

[235] J. Oller and E. Oset, Phys. Rev. **D60**, 074023 (1999), hep-ph/9809337.

[236] M. Jamin, J. A. Oller, and A. Pich, Nucl. Phys. **B587**, 331 (2000), hep-ph/0006045.

[237] J. A. Oller, Nucl. Phys. **A727**, 353 (2003), hep-ph/0306031.

[238] J. A. Oller, Phys. Rev. **D71**, 054030 (2005), hep-ph/0411105.

[239] Z.-H. Guo, J. Oller, and J. Ruiz de Elvira, Phys. Rev. **D86**, 054006 (2012), arXiv:1206.4163 [hep-ph].

[240] F. Giacosa, Phys. Rev. **D75**, 054007 (2007), hep-ph/0611388.

[241] A. H. Fariborz, E. Pourjafarabadi, S. Zarepour, and S. M. Zebarjad, Phys. Rev. **D92**, 113002 (2015), arXiv:1511.01623 [hep-ph].

[242] D.-S. Du, J.-W. Li, and M.-Z. Yang, Phys. Lett. **B619**, 105 (2005).

[243] E. V. Shuryak, Nucl. Phys. **B214**, 237 (1983).

[244] T. Schäfer and E. V. Shuryak, Rev. Mod. Phys. **70**, 323 (1998), hep-ph/9610451.

[245] E. Klempt and J.-M. Richard, Rev. Mod. Phys. **82**, 1095 (2010).

[246] V. D. Burkert and C. D. Roberts, Rev. Mod. Phys. **91**, 011003 (2019).

[247] T. Barnes and F. Close, Phys. Lett. **B128**, 277 (1983).

[248] E. Golowich, E. Haqq, and G. Karl, Phys. Rev. **D28**, 160 (1983).

[249] T. Barnes, (2000), nucl-th/0009011.

[250] B. Ioffe, Nucl. Phys. **B188**, 317 (1981).

[251] I. Duck and E. Umland, Phys. Lett. **128B**, 221 (1983).

[252] C.-K. Chow, D. Pirjol, and T.-M. Yan, Phys. Rev. **D59**, 056002 (1999).

[253] S. Capstick and P. R. Page, Phys. Rev. **D60**, 111501 (1999).

[254] D. Harnett, R. Berg, R. T. Kleiv, and T. G. Steele, Nucl. Phys. B Proc. Suppl. **234**, 154 (2013).

Appendix A

Derivation of the Hölder Inequality in Gaussian Sum-Rules

A.1 Deriving the Hölder Inequalities for Gaussian Sum-Rules

Previous investigations of hadronic systems analyzed using Laplace sum-rules have utilized Hölder inequalities to fundamentally restrict the τ window [79, 171]. Here, we derive expressions for the Hölder inequalities in the framework of Gaussian sum-rules.

The Hölder inequality is expressed generally as

$$\left| \int_{t_1}^{t_2} f\left(t\right) g\left(t\right) \mathrm{d}\mu \right| \leq \left(\int_{t_1}^{t_2} |f\left(t\right)|^p \mathrm{d}\mu \right)^{\frac{1}{p}} \left(\int_{t_1}^{t_2} |g\left(t\right)|^q \mathrm{d}\mu \right)^{\frac{1}{q}}, \tag{A.1}$$

under the condition that

$$\frac{1}{p} + \frac{1}{q} = 1. \tag{A.2}$$

We consider the Gaussian sum-rule (GSR), defined as

$$G_k\left(\tau, \hat{s}, s_0\right) = \int_{t_0}^{s_0} \mathrm{Im}\Pi\left(t\right) t^k \frac{e^{-\frac{\left(\hat{s}-t\right)^2}{4\tau}}}{\sqrt{4\pi\tau}} \mathrm{d}t. \tag{A.3}$$

Given that $\mathrm{Im}\Pi\left(t\right)$ is positive for diagonal correlators, we can define a measure, and consider inequality (A.1) with the assignments

$$\mathrm{d}\mu = \mathrm{Im}\Pi\left(t\right) \mathrm{d}t \tag{A.4}$$

$$f\left(t\right) = t^\alpha \left(\frac{e^{-\frac{\left(\hat{s}-t\right)^2}{4\tau}}}{\sqrt{4\pi\tau}} \right)^a \tag{A.5}$$

$$g\left(t\right) = t^\beta \left(\frac{e^{-\frac{\left(\hat{s}-t\right)^2}{4\tau}}}{\sqrt{4\pi\tau}} \right)^b \tag{A.6}$$

$$t_1 = t_0, \; t_2 = s_0 \tag{A.7}$$

$$a + b = 1, \; \alpha + \beta \in \mathbb{Z}. \tag{A.8}$$

166

With these definitions, our Hölder inequality becomes

$$\left| \int_{t_0}^{s_0} t^{\alpha+\beta} \left(\frac{e^{-\frac{(\hat{s}-t)^2}{4\tau}}}{\sqrt{4\pi\tau}} \right)^{a+b} \mathrm{Im}\Pi(t) \, \mathrm{d}t \right| \leq \left(\int_{t_0}^{s_0} \left| t^\alpha \left(\frac{e^{-\frac{(\hat{s}-t)^2}{4\tau}}}{\sqrt{4\pi\tau}} \right)^a \right|^p \mathrm{Im}\Pi(t) \, \mathrm{d}t \right)^{\frac{1}{p}}$$

$$\times \left(\int_{t_0}^{s_0} \left| t^\beta \left(\frac{e^{-\frac{(\hat{s}-t)^2}{4\tau}}}{\sqrt{4\pi\tau}} \right)^b \right|^q \mathrm{Im}\Pi(t) \, \mathrm{d}t \right)^{\frac{1}{q}}. \qquad (A.9)$$

We recognize the left side of this inequality as the definition of the GSR (A.3) for $k = \alpha + \beta$ subject to (A.8). Thus,

$$|G_{\alpha+\beta}(\tau, \hat{s}, s_0)| \leq \left(\int_{t_0}^{s_0} \left| t^\alpha \left(\frac{e^{-\frac{(\hat{s}-t)^2}{4\tau}}}{\sqrt{4\pi\tau}} \right)^a \right|^p \mathrm{Im}\Pi(t) \, \mathrm{d}t \right)^{\frac{1}{p}}$$

$$\times \left(\int_{t_0}^{s_0} \left| t^\beta \left(\frac{e^{-\frac{(\hat{s}-t)^2}{4\tau}}}{\sqrt{4\pi\tau}} \right)^b \right|^q \mathrm{Im}\Pi(t) \, \mathrm{d}t \right)^{\frac{1}{q}}$$

$$\leq \left(\int_{t_0}^{s_0} t^{\alpha p} \left(\frac{e^{-ap\frac{(\hat{s}-t)^2}{4\tau}}}{\sqrt{4\pi\tau}^{ap}} \right) \mathrm{Im}\Pi(t) \, \mathrm{d}t \right)^{\frac{1}{p}}$$

$$\times \left(\int_{t_0}^{s_0} t^{\beta q} \left(\frac{e^{-bq\frac{(\hat{s}-t)^2}{4\tau}}}{\sqrt{4\pi\tau}^{bq}} \right) \mathrm{Im}\Pi(t) \, \mathrm{d}t \right)^{\frac{1}{q}}, \quad \{\tau, t_0, s_0,\} > 0. \qquad (A.10)$$

We can clean this expression up by introducing a factor of $\frac{\sqrt{ap}^{ap}}{\sqrt{ap}^{ap}}$ or $\frac{\sqrt{bq}^{bq}}{\sqrt{bq}^{bq}}$ into each integral on the right side,

$$|G_{\alpha+\beta}(\tau, \hat{s}, s_0)| \leq \left(\int_{t_0}^{s_0} t^{\alpha p} \left(\frac{e^{-ap\frac{(\hat{s}-t)^2}{4\tau}}}{\sqrt{4\pi\tau}^{ap}} \frac{\sqrt{ap}^{ap}}{\sqrt{ap}^{ap}} \right) \mathrm{Im}\Pi(t) \, \mathrm{d}t \right)^{\frac{1}{p}}$$

$$\times \left(\int_{t_0}^{s_0} t^{\beta q} \left(\frac{e^{-bq\frac{(\hat{s}-t)^2}{4\tau}}}{\sqrt{4\pi\tau}^{bq}} \frac{\sqrt{bq}^{bq}}{\sqrt{bq}^{bq}} \right) \mathrm{Im}\Pi(t) \, \mathrm{d}t \right)^{\frac{1}{q}} \qquad (A.11)$$

$$\leq \frac{1}{\sqrt{ap}^{ap}} \frac{1}{\sqrt{bq}^{bq}} \left(\int_{t_0}^{s_0} t^{\alpha p} \left(\frac{e^{-ap\frac{(\hat{s}-t)^2}{4\tau}}}{\sqrt{4\pi\frac{\tau}{ap}}^{ap}} \right) \mathrm{Im}\Pi(t) \, \mathrm{d}t \right)^{\frac{1}{p}}$$

$$\times \left(\int_{t_0}^{s_0} t^{\beta q} \left(\frac{e^{-bq\frac{(\hat{s}-t)^2}{4\tau}}}{\sqrt{4\pi\frac{\tau}{bq}}^{bq}} \right) \mathrm{Im}\Pi(t) \, \mathrm{d}t \right)^{\frac{1}{q}}. \qquad (A.12)$$

167

Factoring out the appropriate power of our denominator, we can simplify the right side in terms of our GSR (A.3),

$$|G_{\alpha+\beta}(\tau,\hat{s},s_0)| \leq \frac{1}{\sqrt{ap}^a} \frac{1}{\sqrt{bq}^b} \left(\frac{1}{\sqrt{4\pi \frac{\tau}{ap}}^{a-\frac{1}{p}}} \right) \left(\frac{1}{\sqrt{4\pi \frac{\tau}{bq}}^{b-\frac{1}{q}}} \right)$$

$$\times \left(\int_{t_0}^{s_0} t^{\alpha p} \left(\frac{e^{-ap\frac{(\hat{s}-t)^2}{4\tau}}}{\sqrt{4\pi \frac{\tau}{ap}}} \right) \text{Im}\Pi(t) \, dt \right)^{\frac{1}{p}}$$

$$\times \left(\int_{t_0}^{s_0} t^{\beta q} \left(\frac{e^{-bq\frac{(\hat{s}-t)^2}{4\tau}}}{\sqrt{4\pi \frac{\tau}{bq}}} \right) \text{Im}\Pi(t) \, dt \right)^{\frac{1}{q}}$$

$$|G_{\alpha+\beta}(\tau,\hat{s},s_0)| \leq \frac{1}{\sqrt{ap}^a} \frac{1}{\sqrt{bq}^b} \left(\frac{1}{\sqrt{4\pi \frac{\tau}{ap}}^{a-\frac{1}{p}}} \right) \left(\frac{1}{\sqrt{4\pi \frac{\tau}{bq}}^{b-\frac{1}{q}}} \right)$$

$$\times G_{\alpha p}^{\frac{1}{p}} \left(\frac{\tau}{ap}, \hat{s}, s_0 \right) G_{\beta q}^{\frac{1}{q}} \left(\frac{\tau}{bq}, \hat{s}, s_0 \right). \tag{A.13}$$

We can further simplify the coefficient on the right side using (A.8),

$$|G_{\alpha+\beta}(\tau,\hat{s},s_0)| \leq \frac{1}{\sqrt{\tau}} \left(\frac{1}{\sqrt{\frac{\tau}{ap}}^{-\frac{1}{p}}} \right) \left(\frac{1}{\sqrt{\frac{\tau}{bq}}^{-\frac{1}{q}}} \right)$$

$$\times G_{\alpha p}^{\frac{1}{p}} \left(\frac{\tau}{ap}, \hat{s}, s_0 \right) G_{\beta q}^{\frac{1}{q}} \left(\frac{\tau}{bq}, \hat{s}, s_0 \right). \tag{A.14}$$

Defining $\frac{\tau}{ap} = \tau_1$ and $\frac{\tau}{bq} = \tau_2$, and recognizing that $\frac{1}{p} + \frac{1}{q} = 1$,

$$|G_{\alpha+\beta}(\tau,\hat{s},s_0)| \leq \left(\frac{\tau_1}{\tau} \right)^{\frac{1}{2p}} \left(\frac{\tau_2}{\tau} \right)^{\frac{1}{2q}} G_{\alpha p}^{\frac{1}{p}}(\tau_1,\hat{s},s_0) G_{\beta q}^{\frac{1}{q}}(\tau_2,\hat{s},s_0). \tag{A.15}$$

We can parameterize (A.15) by allowing

$$\frac{1}{p} = \omega, \ \frac{1}{q} = 1 - \omega, \ 0 < \omega < 1 \tag{A.16}$$

and consider the zero-weight GSR ($\alpha = \beta = 0$), such that

$$|G_0(\tau,\hat{s},s_0)| \leq \left(\frac{\tau_1}{\tau} \right)^{\frac{\omega}{2}} \left(\frac{\tau_2}{\tau} \right)^{\frac{1-\omega}{2}} G_0^{\omega}(\tau_1,\hat{s},s_0) G_0^{1-\omega}(\tau_2,\hat{s},s_0). \tag{A.17}$$

However, we must be certain that our assignment of τ_1 and τ_2 satisfy the requirements of

(A.8). We require that

$$a + b = 1$$

$$\Rightarrow \left(\frac{\tau\omega}{\tau_1}\right) + \left(\frac{\tau(1-\omega)}{\tau_2}\right) = 1$$

$$\Rightarrow \tau = \frac{\tau_1\tau_2}{\omega\tau_2 + (1-\omega)\tau_1}. \tag{A.18}$$

So, our final expression for the zero-weight GSR is

$$\left| G_0 \left(\frac{\tau_1\tau_2}{\omega\tau_2 + (1-\omega)\tau_1}, \hat{s}, s_0 \right) \right| \leq \left(\frac{\omega\tau_2 + (1-\omega)\tau_1}{\tau_2} \right)^{\frac{\omega}{2}} \left(\frac{\omega\tau_2 + (1-\omega)\tau_1}{\tau_1} \right)^{\frac{1-\omega}{2}}$$

$$\times G_0^\omega (\tau_1, \hat{s}, s_0) G_0^{1-\omega} (\tau_2, \hat{s}, s_0). \tag{A.19}$$